



**HAL**  
open science

# Hollow nanoparticles for low cost, high oxygen reduction reaction activity and durability for proton exchange membrane fuel cell application

Tristan Asset

## ► To cite this version:

Tristan Asset. Hollow nanoparticles for low cost, high oxygen reduction reaction activity and durability for proton exchange membrane fuel cell application. Mechanics of materials [physics.class-ph]. Université Grenoble Alpes; Université de Liège, 2017. English. NNT : 2017GREAI037 . tel-01689721

**HAL Id: tel-01689721**

**<https://theses.hal.science/tel-01689721>**

Submitted on 22 Jan 2018

**HAL** is a multi-disciplinary open access archive for the deposit and dissemination of scientific research documents, whether they are published or not. The documents may come from teaching and research institutions in France or abroad, or from public or private research centers.

L'archive ouverte pluridisciplinaire **HAL**, est destinée au dépôt et à la diffusion de documents scientifiques de niveau recherche, publiés ou non, émanant des établissements d'enseignement et de recherche français ou étrangers, des laboratoires publics ou privés.

## THÈSE

Pour obtenir les grades de

**DOCTEUR DE LA COMMUNAUTE UNIVERSITE  
GRENOBLE ALPES**

et de

**DOCTEUR EN SCIENCES DE L'INGENIEUR DE  
L'UNIVERSITE DE LIEGE**

préparée dans le cadre d'une cotutelle *entre la Communauté Uni-  
versité Grenoble Alpes et l'Université de Liège.*

Spécialité : **Matériaux, Mécanique, Génie Civil, Electrochimie**

Arrêté ministériel : le 6 janvier 2005 - 7 août 2006

Présentée par

**Tristan ASSET**

Thèse dirigée par **Laetitia DUBAU, Nathalie JOB et Frederic  
MAILLARD**

préparée au sein du **Laboratoire d'Electrochimie et de Physico-  
chimie des Materiaux et Interfaces (Grenoble)** et du **Departement de Chemical Engineering (Liège).**

dans l'**Ecole Doctorale I-MEP2 (Grenoble)** et l'**Ecole Doctorale en Chemical Engineering (Liège).**

## **Particules creuses peu onéreuses, durables et actives pour la réduction de l'oxygène dans le cadre d'une ap- plication en pile à combustible à membrane échangeuse de protons**

Thèse soutenue publiquement le **26 Septembre 2017**,  
devant le jury composé de :

Prof. Marian CHATENET

Professeur, Université de Grenoble Alpes, Président

Prof. Aliaksandr BANDARENKA

Professeur, Université de Munich, Rapporteur

Prof. Elena SAVINOVA

Professeur, Université de Strasbourg, Rapporteur

Prof. Christophe COUTANCEAU

Professeur, Université de Poitiers, Examineur

Dr. Cédric GOMMES

Research Associate, FNRS, Liège, Examineur

Dr. Laetitia DUBAU

Chargé de Recherche, CNRS, Grenoble, Co-Directrice de Thèse

Prof. Nathalie JOB

Professeur, Université de Liège, Directrice de Thèse

Dr. Frédéric MAILLARD

Chargé de Recherche, CNRS, Directeur de Thèse





« Les hommes sont prompts à forger myriades d'ouvrages,  
Armés de rien, si ce n'est de leur astuce et de leur rage. »

## Acknowledgments

I have been recently told that, for those that do not consider your PhD subject as the single most important thing in the Universe, the ‘Acknowledgments’ are an essential part of the manuscript. There, they might find something interesting (*i.e.* if they are slightly egocentric, their name) or, at least, that might be funny, fresh or fascinating. Therefore, this part of the manuscript is dedicated to those that are not fascinated by the magnificent curves of a CO<sub>ads</sub> stripping; to those that have yet to find the true beauty of this world. While looking back at the *ca.* 3 years that passed since my PhD started, I cannot but see all the wonderful moments, all the amazing memories that shine on the road behind.

I shared those instants with some of the greatest persons I might ever meet. So, thanks. To my friends, for the parties, for the talks, for being there. For the afternoons and nights, we spent playing board games, video games and chess (the king of all games). For all the discussions, serious or not, we had. For the soccer games, where you were almost always able to fill the gaps I let in the defence while running like a crazy horse all around the field. For the barbecues, especially the ones we never talk about. For sharing my passion for art (and lending me books onto Egyptian history); for reading my poetry and my texts and criticizing them wisely. For the trips, for conferences or just for fun. For the laser games, the movies we shared, the escape rooms, the *via ferrata*, the running, the ski (there, I especially thanks all the peoples that never crossed my way while descending the ski runs: I do not really know how to break on those things), the concerts or just those little moments that I do not exactly remember but that, all together, bring a smile to my face and a tear in my eyes.

To my colleagues, that often belong to the previous category. My consideration for the organisation within a scientific environment is driven by the 2<sup>nd</sup> principle of thermodynamics: ‘every transformation of a system generates entropy’. Thus, *disorder* is the natural consequence of research. First and foremost, I am grateful to the persons that do not share my state of mind and did not hesitate to lead me onto the path of sorting, organisation and cleaning. The road ahead might be long but, at least, I know it is there! On a more serious note, I could not have chosen better places to do my PhD. Experimenting was amazing: they were always someone in the lab to interact with, laugh with and make an ageing test much more interesting than it should be (except if your eyes have a point-to-point resolution of *ca.* 1 nm or if, because you did not

## Acknowledgments

sacrifice a cow to the great God of Electrochemistry, your experimental setup decided today is not a good day for experiment, nothing significant happens during an ageing test). Most of the great talks I had on my PhD, I had them in the lab while torturing a helpless, innocent electrocatalyst. To the internship students, especially those that contributed to this manuscript; while you did not stay long, you always brought something new in our lives, often for the best. To the Belgium folk, I do not know if, from all the nations of Gaul, you are the bravest but, doubtlessly, you are the kindest and I cherish the days I spent in your freezing, dark and rainy country (I am writing those lines in Belgium. The temperature is  $T = 297$  K, there is a beautiful sun and almost no clouds. But a cliché is a cliché). To my comrades from the IDS-FunMat program. We started our first meeting lost in a monastery in Germany. We ended the last in Aveiro, with an open-bar and amazing food. Thinking about it, this *might* be a deep and philosophical representation of our spiritual ascension during the last three years. To our administrative teams, both in Grenoble and Liège for their time and their patience. I would not be there without you, especially since I never filled the form A38.

To my collaborators, during the last three years. Not only our collaborations were fruitful, but all the knowledge you shared with me was among the greatest experiences of this PhD and most of this manuscript was written thanks to the discussions we had. To Laetitia, Nathalie and Frédéric. For everything. For your patience, for your devotion to the project, for your time, your motivation and your wisdom. The respect and the gratitude I have for you cannot be expressed with words. You accepted me as I was, as I am and, from this tempestuous student, you forged something greater. And, finally, to my parents, my sister and my brother. I might be the one who wrote this thesis, but you are those who created my very nature, through all those wonders we saw together and all those things you taught me.

This work is as much yours than mine.

## Table of Contents

Acknowledgments .....	4
Table of Contents .....	6
List of Figures .....	10
List of Tables.....	19
List of Abbreviations and Symbols .....	21
List of the Publications used in this Manuscript .....	26
<b>Chapter I. General Introduction.....</b>	<b>27</b>
I. 1. Nowadays Challenges .....	28
I. 2. The proton exchange membrane fuel cell .....	30
I. 3. Hydrogen Oxidation Reaction.....	32
I. 4. Oxygen Reduction Reaction.....	34
I. 4. 1. Theoretical aspects .....	34
I. 4. 2. Platinum, the ‘benchmark’ catalyst for the ORR.....	37
I. 4. 3. The d-band theory and its applications for the ORR .....	38
I. 4. 4. The ‘ensemble’ effect. ....	41
I. 4. 5. The role of the structural defects. ....	42
I. 4. 6. A comparison of the different Pt-based nanostructures.....	43
I. 5. The carbon supports .....	44
I. 6. Ageing of electrocatalysts for PEMFC applications. ....	46
I. 6. 1. Electrochemical corrosion of the carbon support .....	46
I. 6. 2. Ageing of the Pt-based nanoparticles .....	47
I. 6. 3. Ageing of Pt-based electrocatalysts and the formation of hollow nanostructures: toward a new type of electrocatalysts .....	49
I. 6. 4. The Pt-rich hollow nanoparticles.....	50
I. 7. Objectives of the PhD .....	52

## Table of Contents

<b>Chapter II. Introduction to the Techniques &amp; Experimental Section</b> .....	55
II. 1. Synthesis of porous hollow PtM nanoparticles supported on carbon .....	56
II. 1. 1. Technical aspects.....	56
II. 1. 2. In operando synthesis .....	57
II. 1. 3. Reference electrocatalysts .....	57
II. 2. Synthesis of the carbon supports.....	58
II. 2. 1. Synthesis of the carbon xerogel .....	58
II. 2. 2. Synthesis of three-dimensional (3D) graphene nanosheets.....	58
II. 2. 3. Synthesis of the carbon nanotubes .....	59
II. 3. Electrochemical methods .....	59
II. 3. 1. Preparation of the electrochemical cell .....	59
II. 3. 2. Preparation of the electrocatalyst suspensions .....	60
II. 3. 3. Cyclic voltammetry in Ar-saturated electrolyte .....	61
II. 3. 4. CO <sub>ads</sub> stripping on the Pt-based electrocatalysts .....	64
II. 3. 5. Oxygen reduction reaction on Pt-based electrocatalysts.....	66
II. 3. 6. Accelerated stress tests.....	67
II. 3. 7. In operando ageing of porous hollow PtNi/C.....	68
II. 4. Measurement of the specific surface area of the supports .....	69
II. 5. Atomic Absorption Spectroscopy .....	70
II. 6. Electron Microscopy .....	70
II. 6. 1. Transmission electron microscopy.....	70
II. 6. 2. Identical Localisation TEM.....	71
II. 6. 3. Scanning Electron Microscopy .....	72
II. 7. Raman spectroscopy .....	72
II. 8. X-ray photoelectron spectroscopy .....	73
II. 9. X-ray diffraction .....	74
II. 9. 1. Introduction .....	74

## Table of Contents

II. 9. 2. Wide angle X-ray scattering.....	75
II. 9. 3. Pair function distribution analysis.....	76
II. 9. 4. Rietveld analysis .....	76
II. 9. 5. Small angle X-ray scattering .....	77
II. 10. Membrane electrode assembly characterisation .....	78
<b>Chapter III. At the heart of the synthesis of porous hollow PtNi/C nanoparticles .....</b>	<b>81</b>
III. 1. Introduction .....	82
III. 2. Results and Discussion .....	82
III. 2. 1. Wide angle X-ray scattering and energy dispersive X-ray mapping .....	82
III. 2. 2. X-ray photoelectron spectroscopy and high-resolution TEM.....	86
III. 2. 3. Small Angle X-Ray Scattering.....	88
III. 3. Conclusion.....	91
<b>Chapter IV. Design of porous hollow PtM nanoparticles for the ORR.....</b>	<b>93</b>
IV. 1. Introduction to the structural properties of the porous hollow PtNi/C.....	95
IV. 2. The CO <sub>ads</sub> electrooxidation peak-multiplicity .....	97
IV. 3. The porous hollow PtNi/C NPs, a highly defective structure .....	106
IV. 3. 1. The effect of the temperature onto the PtNi/C NPs nanostructure .....	106
IV. 3. 2. The multiplicity of the catalytic sites onto a porous hollow PtNi/C NPs surface .....	112
IV. 4. Extending the synthesis of hollow Pt-based/C nanostructures to other transition metals.....	113
IV. 5. The influence of the carbon support.....	116
IV. 5. 1. Physico-chemical properties of the carbon supports .....	116
IV. 5. 2. Morphology and electrochemical activity of porous hollow PtNi/C catalysts .	120
IV. 6. Conclusions .....	126

## Table of Contents

<b>Chapter V. Stability of the porous hollow PtNi/C NPs during simulated PEMFC operating conditions</b> .....	131
V. 1. Introduction.....	132
V. 2. Elucidating the mechanisms driving the ageing of porous hollow PtNi/C nanoparticles by the means of CO <sub>ads</sub> stripping .....	134
V. 3. In operando study of the ageing of the porous hollow PtNi/C NPs.....	142
V. 4. Stability of the carbon supports .....	153
V. 5. Conclusions.....	163
 <b>Chapter VI. General Conclusion and Perspectives</b> .....	165
 <b>Chapter VII. References</b> .....	175
 Abstract .....	202
Résumé .....	202

## List of Figures

<b>Figure 1.</b> (A) Schematic representation of the accelerated growth in technology that followed the discovery of the steam engine and (B) Evolution of the Earth population from 1350 to nowadays. The changes in the world population has been established from Ref. <sup>9</sup> .....	28
<b>Figure 2.</b> Global stock resources for several key elements and fossil fuels, for a static consumption rate and if the Earth consumption rate is half of the US rate – i.e. an enhancement of the quality of life in the developing countries. Indicators of the global warming are provided on the graph. References: A. Reller, University of Augsburg, T. Graedel, University of Yale and Ref. <sup>12,13</sup> . The graphic does not take into consideration neither the discovery of new technologies nor a large-scale recycling of the different elements.....	29
<b>Figure 3.</b> Design of a Proton Exchange Membrane Fuel Cell (PEMFC) reprinted from Ref. <sup>17</sup> .....	30
<b>Figure 4.</b> Scanning electron micrograph of a Membrane Electrode Assembly (i.e. catalytic layers + membrane + gas diffusion layer). PEM = Proton Exchange Membrane, CL = catalytic layer, MPL = Micro-Porous Layer and GDL = Gas Diffusion Layer). Reprinted from Ref. <sup>19</sup> .....	31
<b>Figure 5.</b> Calculation of the kinetic current densities for the HOR on Pt at T = 291 K. Dashed and dotted curves represent the contributions from the TV ( $j_{TV}$ ) and HV ( $j_{HV}$ ) pathways, respectively, while $j_k$ (black line) represent their combined contribution determined by a dual pathway kinetic equation. The dashed-dotted curve shows the kinetic current ( $j_k$ ) calculated using the Butler-Volmer equation. Reprinted from Ref. <sup>24</sup> .....	33
<b>Figure 6.</b> Log $i_0$ vs. the M – H bond energy for the HER. Reprinted from Ref. <sup>33</sup> .....	34
<b>Figure 7.</b> Example of a mechanism proposed for the oxygen reduction reaction, adapted from Ref. <sup>34</sup> k corresponds to the kinetic constants of the different steps. ....	34
<b>Figure 8.</b> Theoretical plot of free energies of adsorption of $HOO_{ads}$ ( $HOO^*$ ), $HO_{ads}$ ( $HO^*$ ) and $O_{ads}$ ( $O^*$ ), $\Delta G_{HOO^*}$ , $\Delta G_{HO^*}$ and $\Delta G_{O^*}$ , respectively, as a function of $\Delta G_{OH^*}$ , for (111), (100) and (211) pure metal surfaces (filled squares) as well as Pt overlayers on Pt-alloy surfaces. Reprinted from Ref. <sup>54</sup> .....	36
<b>Figure 9.</b> Relationship between the electrocatalyst activity for the ORR and the adsorption strength of the $OH^*$ and $O^*$ intermediates – the $OOH^*$ intermediate is not considered by Nørskov et al. <sup>57</sup> . Reprinted from Ref. <sup>57</sup> .....	37
<b>Figure 10.</b> (A) Effect of insertion of a 3d transition metal in the first subsurface layer of a Pt surface on the Pt density of states (reprinted from Ref. <sup>101</sup> ) and (B) Volcano-plot of the kinetic current for the ORR (relative to Pt) as a function of the adsorption strength of the $O^*$ intermediate. The dotted line corresponds to the theoretical predictions of Rossmeisl et al. <sup>113</sup> . Reprinted from Ref. <sup>55</sup> .....	40
<b>Figure 11.</b> (A) Maximal reported value for the $PtM_x$ (x = the M/Pt atomic ratio observed for the optimal activity) for the ORR at E = 0.9 V vs. the Reversible Hydrogen Electrode (RHE), compared to the corresponding Pt electrocatalyst (the stars refer to nanoparticles) as the function of the atomic radius of the alloying element. (B) Schematic 3D representation of the relation between the ORR activity of the	

## List of Figures

electrocatalyst, the radius of the alloying element and the composition of the alloy. Reprinted from Ref. <sup>136</sup> .....	41
<b>Figure 12.</b> Enhancement of the ORR kinetics vs. Pt/C for several electrocatalysts in 0.1 M HClO <sub>4</sub> , i.e. commercial Pt/C <sup>49</sup> , nanoporous NiPt/C <sup>81</sup> , dealloyed PtNi <sub>3</sub> /C <sup>75</sup> , porous hollow PtNi/C <sup>84</sup> , octahedral PtNi/C <sup>88</sup> and Pt ultrafine nanowires <sup>143</sup> (at E = 0.90 V vs. RHE, v = 0.005 V s <sup>-1</sup> or 0.020 V s <sup>-1</sup> for Ref. <sup>143</sup> ), Pt (111) and Pt <sub>3</sub> Ni (111) <sup>138</sup> , Ni@Au@PtNi/C <sup>111</sup> , Pt <sub>3</sub> Ni/C Nanoframes <sup>129</sup> and PtNi mesostructured thin films <sup>158</sup> (at E = 0.95 V vs. RHE, v = 0.020 V s <sup>-1</sup> ). See references associated to each nanostructure for more information. ....	44
<b>Figure 13.</b> Scanning electron microscopy (SEM) micrographs of different carbon structures. (A) Graphene nanosheets, (B) carbon black (Vulcan XC72) (C) carbon nanotubes and (D) carbon xerogel. ....	45
<b>Figure 14.</b> Mechanisms for Pt NPs instability in PEMFC cathodes: (A) growth via electrochemical Ostwald ripening, i.e. dissolution of Pt NPs, production of Pt <sup>z+</sup> ionic species (z = 2, 4) and redeposition of Pt <sup>z+</sup> species onto larger Pt crystallites, (B) (in FC) dissolution of Pt NPs and precipitation in the ionomer phase and the proton-exchange membrane via chemical reduction by H <sub>2</sub> , (C) crystallite migration, agglomeration and possibly coalescence, (D) detachment of Pt NPs from carbon support. Reprinted from Ref. <sup>199</sup> .....	48
<b>Figure 15.</b> High annular angle dark field signal of NPs acquired simultaneously with the energy electron losses spectra. The elemental maps were constructed using the Pt N <sub>3</sub> (518 eV) and the Co L <sub>2,3</sub> (780 eV) edges, respectively. The Pt N <sub>3</sub> signal is shown in red, and the Co L <sub>2,3</sub> signal is shown in green. Reprinted from Ref. <sup>215</sup> .....	49
<b>Figure 16.</b> (A) Cyclic voltammogram in Ar-saturated 0.1 M HClO <sub>4</sub> of a porous hollow PtNi/C NPs (v = 0.02 V s <sup>-1</sup> , T = 298 ± 1 K) with a Ni content of ca. 15 at. %. (B) Zoom in the 0.05 – 0.45 V vs. RHE potential range showing a base CV and a CV taken after CO <sub>ads</sub> adsorption and purge of the electrolyte (CO stripping voltammogram). ....	62
<b>Figure 17.</b> Parameters extracted from CO <sub>ads</sub> stripping measurements describing the physico-chemical properties of a nanostructured, low Ni atomic content porous hollow PtNi/C electrocatalyst: (A) the electrical charge under the CO <sub>ads</sub> stripping pre-peak (Q <sub>pp,CO</sub> ), the total electrical charge of the CO <sub>ads</sub> stripping (Q <sub>T,CO</sub> ) and the position of the ‘high-potential’ peak (E <sub>p,CO</sub> ); (B) the first moment of the potential weight of the CO <sub>ads</sub> stripping voltammogram determined as the integral of E × I/Q <sub>T,CO</sub> (μ <sub>1</sub> <sup>CO</sup> ). ....	66
<b>Figure 18.</b> Linear sweep voltammogram recorded in O <sub>2</sub> -saturated 0.1 M HClO <sub>4</sub> on hollow PtNi/C NPs with and without the correction of the Ohmic drop and of the oxygen diffusion in solution (v = 0.005 V s <sup>-1</sup> , T = 298 ± 1 K, ω = 1600 rpm). ....	67
<b>Figure 19.</b> Protocols used for the ASTs discussed in this manuscript: (A) Start-stop protocol, (B) Load-cycling protocol. The ASTs temperature was T = 353 K. ....	68

## List of Figures

- Figure 20.** Scheme of the electrochemical cell used to investigate the degradation mechanisms of porous hollow PtNi/C NPs by in operando WAXS and SAXS measurements: (A) front and (B) side views.. 69
- Figure 21.** Raman spectra of Vulcan XC72 in the 1200 – 1750  $\text{cm}^{-1}$  range highlighting the position of the theoretical vibration modes of carbon. .... 73
- Figure 22.** (A) Measured SAXS pattern before the addition of the first drop of  $\text{NaBH}_4$  (background, black) and  $t = 14$  min (orange, before background correction) ( $t$  is the time after the addition of the first drop of  $\text{NaBH}_4$ ). (B) Example of a fit of SAXS pattern. Dark circles: the background-corrected SAXS pattern at  $t = 14$  min. orange curve: the fit using the core/shell NP model. .... 78
- Figure 23.** Schematic representation of the initial (i.e. metal precursors + carbon in MQ-grade water) and final (acid leaching) steps of the synthesis of porous hollow PtNi/C NPs. .... 83
- Figure 24.** (A) Variation of the external diameter of the NPs, approximated by counting between 100 and 250 NPs for each discussed time and (B) variation of the Ni content of the NPs measured on individual NPs by scanning transmission electron microscopy – energy dispersive X-ray spectroscopy. .... 84
- Figure 25.** Insights into the synthesis of porous hollow PtNi/C NPs via electron and X-ray based techniques. (A, B) X-ray energy dispersive spectroscopy elemental maps of the different nanostructures forming during the synthesis of hollow PtNi/C NPs (the Pt and Ni atoms are represented in red and green, respectively). (C) Wide angle X-ray scattering patterns of the different PtNi nanostructures forming for  $0 \text{ min} < t < 60 \text{ min}$  ( $t$  being the time after the addition of the first drop of  $\text{NaBH}_4$ ). The intensity of the X-ray patterns was normalized to the highest peak intensity measured in the  $25^\circ < 2\theta < 120^\circ$  range (C (002) from  $0 \leq t \leq 3.5 \text{ min}$  and Pt (111) for  $t < 3.5 \text{ min}$ ). .... 85
- Figure 26.** Atomic pair function distribution for  $3 \text{ min} \leq t \leq 60 \text{ min}$  ( $t$  being the time after the addition of the first drop of  $\text{NaBH}_4$  and  $r$  the distance between two atoms). .... 86
- Figure 27.** (A) High-Resolution TEM image of a  $\text{Ni}@_{\text{Ni}_x\text{B}_y\text{O}_z}$  nanostructure obtained after  $t = 2 \text{ min}$  ( $t$  being the time after the addition of the first drop of  $\text{NaBH}_4$ ). (B) XPS peak of boron (B 1s) as a function of the synthesis time. (C) XPS peak of Ni as a function of the synthesis time. (D) Relative content of boron extracted from the analysis of XP spectra acquired on samples collected during the synthesis of hollow PtNi/C NPs. .... 87
- Figure 28.** Variation of the parameters extracted from the fitting of the SAXS, i.e. the scattering light density of the core ( $\text{SLD}_{\text{core}}$ ), of the shell ( $\text{SLD}_{\text{shell}}$ ) and their ratio. The solid line is a fifth order polynomial fit of the  $\text{SLD}_{\text{shell}}/\text{SLD}_{\text{core}}$  ratio. .... 88
- Figure 29.** Electrochemical characterization of the different nanostructures formed during the synthesis of porous hollow PtNi/C NPs. (A, B) Cyclic voltammograms (in Ar-saturated 0.1 M  $\text{HClO}_4$  or 0.1 M NaOH at  $v = 0.020 \text{ V s}^{-1}$  without rotation of the electrode), (C, D) positive-going linear sweep voltammograms (in  $\text{O}_2$ -saturated 0.1 M  $\text{HClO}_4$  or 0.1 M NaOH at a potential sweep rate  $v = 0.005 \text{ V s}^{-1}$  and a rotation rate  $\omega = 1600 \text{ rpm}$ ), and (E, F) Ohmic drop and mass-transport corrected ORR specific activity. All the experiments were performed at  $T = 298 \pm 1 \text{ K}$ . The dashed line corresponds to the value

## List of Figures

of the specific activity for the ORR of a reference 20 wt. % Pt/C measured in the same experimental conditions. ....	90
<b>Figure 30.</b> Schematic representation of the different steps of the synthesis of the porous hollow PtNi/C NPs, from the formation of the Ni NPs at $t = 1$ min ( $t$ being the time after the addition of the first drop of $\text{NaBH}_4$ ) to the ‘porous hollow’ PtNi/C nanostructure obtained after acid leaching. ....	92
<b>Figure 31.</b> Morphological properties of porous hollow PtNi/C nanoparticles and its consequences in terms of surface reactivity. (A-C) Conventional and high-resolution transmission electron microscopy micrographs of the porous hollow PtNi NPs supported on XC72 (initial $\text{Pt}^2\text{:Ni}^{2+}$ atomic ratio of 1:3). (D) $\text{CO}_{\text{ads}}$ stripping voltammograms measured on the porous hollow PtNi/C electrocatalysts. The ‘pre-peak’ is believed to be due to $\text{CO}_{\text{ads}}$ electrooxidation at the structural defects (e.g. grain boundaries, highlighted in orange for the sake of clarity) and the main ‘peak’ assimilated to electrooxidation of $\text{CO}_{\text{ads}}$ that cannot diffuse to the structural defects. ....	96
<b>Figure 32.</b> Electrochemical and morphological properties of the electrocatalysts discussed in this chapter. (A) $\text{CO}_{\text{ads}}$ stripping ( $v = 0.020 \text{ V s}^{-1}$ , electrolyte = Ar-saturated 0.1 M $\text{HClO}_4$ ). (B) Linear sweep voltammetry in Tafel representation, corrected for Ohmic drop and diffusion ( $v = 0.005 \text{ V s}^{-1}$ , electrolyte = $\text{O}_2$ -saturated 0.1 M $\text{HClO}_4$ , $\omega = 1600 \text{ rpm}$ ). (C – E) TEM micrographs of (C) the commercial Pt/C, (D) the PtNi/C ‘sea-sponges’ and (E) the porous hollow PtNi/C NPs. ....	97
<b>Figure 33.</b> Changes in the $\text{CO}_{\text{ads}}$ stripping voltammograms while modifying the $\text{CO}_{\text{ads}}$ initial coverage ( $X_{\text{CO}}$ ) of (A) an electrocatalyst composed of 67 wt. % of PtNi/C ‘sea-sponges’ and 33 wt. % of commercial Pt/C and (B) a porous hollow PtNi/C electrocatalyst. The CO was adsorbed by injecting a determined volume of a CO-saturated 0.1 M $\text{HClO}_4$ solution. The remaining CO was removed after $t = 1$ min of adsorption, by bubbling Ar in the electrolyte (other conditions: $v = 0.020 \text{ V s}^{-1}$ , electrolyte = Ar-saturated 0.1 M $\text{HClO}_4$ ). All the currents were normalized to the ECSA determined for the electrocatalyst with $X_{\text{CO}} = 100 \%$ . ....	99
<b>Figure 34.</b> Changes in the $\text{CO}_{\text{ads}}$ stripping patterns after partial $\text{CO}_{\text{ads}}$ electrooxidation of a fully covered surface. The electrode potential was stepped from $E = 0.1 \text{ V vs. RHE}$ to $0.550 \text{ V} \leq E_{\text{desor}} \text{ vs. RHE} \leq 0.740 \text{ V}$ during $t = 60 \text{ s}$ , then stepped back to $E = 0.1 \text{ V vs. RHE}$ and a $\text{CO}_{\text{ads}}$ stripping voltammogram was then immediately recorded. (A) Schematic representation of the partial $\text{CO}_{\text{ads}}$ electrooxidation protocol. (B) $\text{CO}_{\text{ads}}$ stripping of the porous hollow PtNi/C (the dotted line corresponds to $\text{CO}_{\text{ads}}$ stripping recorded on a fully covered surface). (C) Focus on the $H_{\text{upd}}$ region during the first potential sweep of the $\text{CO}_{\text{ads}}$ stripping presented in (B) (the dotted lines correspond to a non-covered surface and a fully covered surface). (D) $H_{\text{upd}}$ of a non-covered porous hollow PtNi/C electrocatalyst minus the $H_{\text{upd}}$ presented in (C). ....	102
<b>Figure 35.</b> Changes in the $\text{CO}_{\text{ads}}$ stripping patterns after partial $\text{CO}_{\text{ads}}$ electrooxidation of a fully covered surface. The electrode potential was stepped from $E = 0.1 \text{ V vs. RHE}$ to $E_{\text{desor}} = 0.625 \text{ V vs. RHE}$ during $t = 60 \text{ s}$ , then stepped back to $E = 0.1 \text{ V vs. RHE}$ and a $\text{CO}_{\text{ads}}$ stripping voltammogram was then recorded after $0 \text{ min} \leq t \leq 90 \text{ min}$ . ....	103

## List of Figures

- Figure 36.** (A) Normalised  $\text{CO}_{\text{ads}}$  stripping patterns voltammograms for hollow PtNi/C nanoparticles at different potential sweep rates, i.e.  $0.002 \text{ V s}^{-1} < v < 0.200 \text{ V s}^{-1}$ . (B) Focus on the  $\text{CO}_{\text{ads}}$  stripping ‘low-potential’ peak – the peaks were aligned in current and potential. All the currents were normalized by the charge under the peaks ( $Q_{\text{CO}}$ ) – other conditions: electrolyte = Ar-saturated 0.1 M  $\text{HClO}_4$ . ..... 104
- Figure 37.** Description of the different sites observed for  $\text{CO}_{\text{ads}}$  stripping on PtNi/C porous hollow NPs and their associated  $\text{CO}_{\text{ads}}$  stripping peak. .... 105
- Figure 38.** Electrochemical and physico-chemical properties of the porous hollow PtNi/C electrocatalysts synthesized at  $T = 278, 293, 313, 333$  and  $353 \text{ K}$ . (A)  $\text{CO}_{\text{ads}}$  stripping measurements on the electrocatalysts in Ar-saturated 0.1 M  $\text{HClO}_4$  at  $v = 0.02 \text{ V s}^{-1}$ . (B) Tafel plot of Ohmic drop and mass-transport corrected linear sweep voltammograms in  $\text{O}_2$ -saturated 0.1 M  $\text{HClO}_4$  at  $v = 0.005 \text{ V s}^{-1}$  and  $\omega = 1600 \text{ rpm}$  ( $T = 298 \text{ K}$ , Pt loading =  $20 \mu\text{g cm}^{-2}$ ). (C) Nickel atomic content determined by atomic adsorption spectroscopy (AAS). (D) External ( $d_{\text{ext}}$ ) and inner ( $d_{\text{in}}$ ) diameter of the porous hollow PtNi/C NPs synthesized at different temperatures – due to its dual morphology, i.e. agglomerates + isolated NPs, only the diameter of the isolated NPs was given for the electrocatalyst synthesized at  $T = 353 \text{ K}$ . (E) HR-TEM micrograph of the electrocatalyst synthesized at  $T = 278 \text{ K}$ . The grain boundaries are highlighted in orange. (F) HR-TEM micrograph of the electrocatalyst synthesized at  $T = 333 \text{ K}$ . The grain boundaries are highlighted in orange. .... 106
- Figure 39.** Variation of the specific activity for the ORR measured at  $E = 0.95 \text{ V}$  vs. RHE on the porous hollow PtNi/C electrocatalysts synthesized at  $T = 278, 293, 313, 333$  and  $353 \text{ K}$  vs. (A) the ratio of the electrical charge under the ‘low-potential’ peak ( $Q_{\text{pp,CO}}$ ) to the total  $\text{CO}_{\text{ads}}$  stripping charge ( $Q_{\text{T,CO}}$ ), (B) the potential of the ‘high-potential’ peak of the  $\text{CO}_{\text{ads}}$  stripping ( $E_{\text{p,CO}}$ ), (C) the first moment of the potential weight of the  $\text{CO}_{\text{ads}}$  stripping ( $\mu_1^{\text{CO}}$ ). .... 109
- Figure 40.** Variation of (A) the potential of the high-potential peak of the  $\text{CO}_{\text{ads}}$  stripping voltammogram ( $E_{\text{p,CO}}$ ) on the porous hollow PtNi/C electrocatalysts synthesized at  $T = 278, 293, 313, 333$  and  $353 \text{ K}$  vs. the nickel atomic content determined by AAS and (B) potential of the ‘high-potential’ peak of the  $\text{CO}_{\text{ads}}$  stripping ( $E_{\text{p,CO}}$ ) vs. the lattice parameter of the electrocatalysts discussed in this work. .... 110
- Figure 41.** Variation of the specific activity for the ORR measured at  $E = 0.95 \text{ V}$  vs. RHE on the porous hollow PtNi/C electrocatalysts synthesized at  $T = 278, 293, 313, 333$  and  $353 \text{ K}$ , vs. the microstrain determined by Rietveld refinement from XRD patterns ( $\mu_{\epsilon}$ ). .... 111
- Figure 42.** (A) Bottom and side view of a 5-layer Pt (111) slab after relaxation for 40% of vacancies randomly introduced. (B) Map of the inner deformation of the defective plane. (C) Deformation index plotted as a function of the coordination number (CN) for each atomic site of the surface displayed in (A). Adapted from Ref. <sup>157</sup> ..... 113
- Figure 43.** Extension of the synthesis of hollow PtM/C NPs to other sacrificial metals, with  $M = \text{Ni, Co, Cu, Zn}$  and  $\text{Fe}$ . (A) Pt weight fraction and M content determined by Atomic Absorption Spectroscopy after acid leaching; (B) Specific and mass activity for the ORR at  $E = 0.95 \text{ V}$  vs. RHE ( $\text{SA}_{0.95}$  and  $\text{MA}_{0.95}$ , respectively) The measurements were performed in an  $\text{O}_2$ -saturated 0.1 M  $\text{HClO}_4$  electrolyte, at a sweep

## List of Figures

rate $v = 0.005 \text{ V s}^{-1}$ and a rotation speed $\omega = 1600 \text{ rpm}$ . All currents are corrected for Ohmic drop and mass transport. (C) TEM and STEM-EDX micrographs of the PtNi/C, PtCo/C and PtCu/C electrocatalysts (Pt atoms and M atoms are represented in red and green, respectively).....	115
<b>Figure 44.</b> (A) XRD patterns measured on the porous hollow PtNi/C NPs synthesized in this work and (B) Raman patterns of the various carbon supports. ....	118
<b>Figure 45.</b> (A) Transmission Electron Microscopy micrographs of the porous hollow PtNi/C NPs synthesized on CNT, GNS, XC72 and KJB. (B) Variation of the external and inner diameters of the porous hollow PtNi/C NPs as a function of the BET surface area (micropores excluded) of the different carbons supports.....	121
<b>Figure 46.</b> $\text{CO}_{\text{ads}}$ stripping in Ar-saturated 0.1 M $\text{HClO}_4$ on porous hollow PtNi/C NPs synthesized on different carbon supports, namely: Vulcan XC72 (XC72), carbon nanotubes (CNT), YS (YS), graphene nanosheets (GNS), acid leached graphene nanosheets (GNS – AL), carbon xerogels (CX) and Ketjenblack (KJB) – other conditions: $v = 0.020 \text{ V s}^{-1}$ , $T = 298 \pm 1 \text{ K}$ .....	124
<b>Figure 47.</b> Specific activity (SA) and mass activity (MA) in $\text{O}_2$ -saturated 0.1 M $\text{HClO}_4$ at (A) $E = 0.95 \text{ V vs. RHE}$ and (B) $E = 0.9 \text{ V vs. RHE}$ , corrected for diffusion in solution and Ohmic drop, for the porous hollow PtNi/C NPs synthesized on different carbon supports – other conditions: $T = 298 \pm 1 \text{ K}$ , $\omega = 1600 \text{ rpm}$ , $v = 0.005 \text{ V s}^{-1}$ . (C) Pt specific surface area values determined from the $\text{CO}_{\text{ads}}$ stripping measurements. ....	125
<b>Figure 48.</b> Controlling the morphological properties of hollow PtNi/C NPs. The graphs display variations of the mean crystallite size ( $d_{\text{XRD}}$ ), the mean outer ( $d_{\text{ext}}$ ) and the mean inner ( $d_{\text{in}}$ ) diameters measured on hollow PtNi/C NPs synthesized at different temperatures ( $T = 278, 293, 313, 333$ or $353 \text{ K}$ ), with different $\text{Pt}^{2+} : \text{Ni}^{2+}$ atomic ratios (1:1, 1:3, 1:5), or supported onto different carbons: carbon black (XC72), Ketjenblack 600 JD (KJB), graphitized carbon (YS), carbon nanotubes (CNT), graphene nanosheets doped with nitrogen before (GNS) or after acid treatment in $\text{HNO}_3$ (GNS – AL) and carbon xerogel (CX). The reference synthesis conditions were: initial $\text{Pt}^{2+} : \text{Ni}^{2+}$ atomic ratio of 1:3 and room temperature (RT). (A) Mean crystallite size ( $d_{\text{XRD}}$ ), (B) External ( $d_{\text{ext}}$ ) and inner ( $d_{\text{in}}$ ) diameter of the hollow Pt-based/C NPs synthesized in this work. No inner diameter is given for the commercial solid Pt/C and the solid PtNi/C, as for the electrocatalyst synthesized at $T = 353 \text{ K}$ , since they present an agglomerated structure. (C) TEM micrographs of the hollow Pt-based/C NPs synthesized in this work and correlations to the synthesis parameters: the initial $\text{Pt}^{2+} : \text{Ni}^{2+}$ atomic ratio in the synthesis reactor, the synthesis temperature $T_s$ , the specific surface area of the support, micropores excluded ( $S_{\text{BET}} - S_{\text{micropores}}$ ). ....	127
<b>Figure 49.</b> Specific and mass activity at $E = 0.95 \text{ V vs. RHE}$ of porous hollow PtM/C NPs. (A) Specific activity and (B) mass activity measured at $E = 0.95 \text{ V vs. RHE}$ ( $\text{SA}_{0.95}$ and $\text{MA}_{0.95}$ , respectively). The measurements were performed in an $\text{O}_2$ -saturated 0.1 M $\text{HClO}_4$ electrolyte, at a sweep rate $v = 0.005 \text{ V s}^{-1}$ and a rotation speed $\omega = 1600 \text{ rpm}$ . All currents are corrected for Ohmic drop and mass transport. ....	128

## List of Figures

- Figure 50.** (A) Ratio of the specific activity for the ORR measured at  $E = 0.95$  V vs. RHE for the electrocatalysts synthesized at  $T = 278, 293, 313, 333$  and  $353$  K before ( $SA_{0.95}(0k)$ ) and after ( $SA_{0.95}$ ) 5,000 and 20,000 potential cycles with linear profile between  $E = 0.6$  V vs. RHE and  $E = 1.0$  V vs. RHE at  $v = 0.05$  V s<sup>-1</sup> and  $T = 353$  K in Ar-saturated 0.1 M HClO<sub>4</sub>; (B – C) Background-subtracted CO<sub>ads</sub> stripping voltammograms measured before and after 5,000 and 20,000 potential cycles with linear profile for the porous hollow PtNi/C electrocatalysts synthesized at (B)  $T = 278$  K and (C)  $T = 333$  K; (D – E) Ohmic drop corrected polarization curves in O<sub>2</sub> saturated 0.1 M HClO<sub>4</sub> before and after 5,000 and 20,000 potential cycles with linear profile for the porous hollow PtNi/C electrocatalysts synthesized at (D)  $T = 278$  K and (E)  $T = 333$  K..... 134
- Figure 51.** Representative TEM micrographs of the porous hollow PtNi/C electrocatalysts studied in this work before and after 20,000 potential cycles between  $E = 0.6$  V vs. RHE and  $E = 1.0$  V vs. RHE at  $v = 0.05$  V s<sup>-1</sup> and  $T = 353$  K in Ar-saturated 0.1 M HClO<sub>4</sub> electrolyte. The particle size distributions have been built from the external dimeters ( $d_{ext}$ ) of the NPs before and after 20,000 potential cycles (note that the electrocatalyst synthesized at  $T = 353$  K initially presented a partly agglomerated shape: only the  $d_{ext}$  of the isolated particles is provided in the particle size distribution). ..... 137
- Figure 52.** Variation of the specific activity for the ORR measured at  $E = 0.95$  V vs. RHE for the porous hollow PtNi/C electrocatalysts synthesized at  $T = 278, 293, 313, 333$  and  $353$  K before (Fresh) and after 5,000 and 20,000 potential cycles with linear profile between  $E = 0.6$  V vs. RHE and  $E = 1.0$  V vs. RHE in Ar-saturated 0.1 M HClO<sub>4</sub> at  $v = 0.05$  V s<sup>-1</sup> and  $T = 353$  K vs. (A) the potential of the ‘high-potential’ peak in CO<sub>ads</sub> stripping voltammograms ( $E_{p,CO}$ ); (B) the ratio of the electrical charge under the ‘low-potential’ ( $Q_{pp,CO}$ ) to the total electrical charge of the CO<sub>ads</sub> stripping voltammogram ( $Q_{T,CO}$ ); (C) the first moment of the potential weight of the CO<sub>ads</sub> stripping ( $\mu_1^{CO}$ )..... 138
- Figure 53.** Variation of the composition measured by STEM-EDX for the electrocatalysts synthesized at  $T = 278$  K and  $T = 333$  K before and after 20,000 potential cycles between  $E = 0.6$  V vs. RHE and  $E = 1.0$  V vs. RHE at  $v = 0.05$  V s<sup>-1</sup>,  $T = 353$  K in an Ar-saturated 0.1 M HClO<sub>4</sub> electrolyte. .... 139
- Figure 54.** Variation of the CO<sub>ads</sub> stripping voltammograms performed in an Ar-saturated 0.1 M HClO<sub>4</sub> electrolyte ( $v = 0.020$  V s<sup>-1</sup>,  $T = 298$  K) before and after measurement of the ORR activity for the electrocatalysts synthesized at (A)  $T = 298$  K and (B)  $T = 333$  K. .... 141
- Figure 55.** Electrochemical properties of the porous hollow PtNi/C electrocatalyst discussed in this section before and after 5,000 potential cycles in Ar-saturated 0.1 M HClO<sub>4</sub> between 0.6 and 1.0 V vs. RHE or 1.1 V vs. RHE ( $v = 0.05$  V s<sup>-1</sup> and  $T = 353 \pm 1$  K). (A) CO<sub>ads</sub> stripping ( $v = 0.020$  V s<sup>-1</sup>, electrolyte = Ar-saturated 0.1 M HClO<sub>4</sub>,  $T = 298 \pm 1$  K). (B) Linear sweep voltammograms in O<sub>2</sub>-saturated 0.1 M HClO<sub>4</sub> in Tafel representation, corrected from the diffusion in solution and the Ohmic drop ( $v = 0.005$  V s<sup>-1</sup>,  $\omega = 1600$  rpm)..... 143
- Figure 56.** TEM micrographs of the gas diffusion electrode (GDE) (A) before and after 5,000 cycles in Ar-saturated 0.1 M HClO<sub>4</sub> between 0.6 and (B) 1.0 V vs. RHE or (C) 1.1 V vs. RHE. Other conditions:  $v = 0.050$  V s<sup>-1</sup> and  $T = 353 \pm 1$  K..... 145

## List of Figures

- Figure 57.** EDX elemental mapping of the gas diffusion electrode (A) before and after 5,000 cycles in Ar-saturated 0.1 M HClO<sub>4</sub> between 0.6 and (B) 1.0 V vs. RHE or (C - D) 1.1 V vs. RHE. Other conditions:  $v = 0.050 \text{ V s}^{-1}$  and  $T = 353 \pm 1 \text{ K}$ . ..... 146
- Figure 58.** High resolution TEM of the gas diffusion electrode (A) before and after 5,000 cycles in Ar-saturated 0.1 M HClO<sub>4</sub> between 0.6 and (B) 1.0 V vs. RHE or (C) 1.1 V vs. RHE. Other conditions:  $v = 0.050 \text{ V s}^{-1}$  and  $T = 353 \pm 1 \text{ K}$ . ..... 147
- Figure 59.** Variations of the X-ray patterns recorded onto a porous hollow PtNi/C electrocatalyst during 5,000 cycles in Ar-saturated 0.1 M HClO<sub>4</sub> between (A) 0.6 and 1.0 V vs. RHE or (B) 1.1 V vs. RHE ( $v = 0.050 \text{ V s}^{-1}$  and  $T = 353 \pm 1 \text{ K}$ ). ..... 150
- Figure 60.** Variations of structural parameters extracted from Rietveld refinement of XRD patterns measured on porous hollow PtNi/C electrocatalyst during 5,000 potential cycles in Ar-saturated 0.1 M HClO<sub>4</sub> between 0.6 and 1.0 V vs. RHE or 1.1 V vs. RHE ( $v = 0.050 \text{ V s}^{-1}$  and  $T = 353 \pm 1 \text{ K}$ ). (A) Normalized variation of the contraction (vs. the lattice parameter of Pt/C) of the lattice parameter,  $a_{\text{Pt-Pt}}$  vs. the lattice parameter of Pt/C, in the low radiation area, (B) normalized variation of the average crystallite size,  $d_{\text{XRD}}$  and (C) normalized variation of the microstrain,  $\mu_{\text{e}}$ . Since the number of potential cycles was kept constant, the AST between 0.6 and 1.1 V vs. RHE was 20% longer than the AST between 0.6 and 1.0 V vs. RHE..... 151
- Figure 61.** Cyclic voltammograms measured between  $E = 0.05$  and  $1.23 \text{ V vs. RHE}$  at  $v = 0.020 \text{ V s}^{-1}$  and  $T = 298 \pm 1 \text{ K}$  in Ar-saturated 0.1 M HClO<sub>4</sub>, normalized to the geometric surface of the electrode ( $0.196 \text{ cm}^2$ ), for the porous hollow PtNi/C electrocatalysts synthesized on different carbon supports: (A) Vulcan XC72, (B) carbon nanotubes, (C) YS, (D) graphene nanosheets, (E) acid leached graphene Nanosheets, (F) carbon xerogels, (G) Ketjenblack. All the results were obtained before and after an accelerated stress test protocol mimicking potential variations during start-up/shutdown of a PEMFC cathode (500 steps at  $T = 353 \text{ K}$  between  $1.0 \text{ V vs. RHE}$  ( $t = 3 \text{ s}$ ) and  $1.5 \text{ V vs. RHE}$  ( $t = 3 \text{ s}$ )). ..... 154
- Figure 62.** Electrooxidation of a CO<sub>ads</sub> monolayer between  $E = 0.05$  and  $1.23 \text{ V vs. RHE}$  at  $v = 0.020 \text{ V s}^{-1}$  and  $T = 298 \pm 1 \text{ K}$  in Ar-saturated 0.1 M HClO<sub>4</sub>, normalized by the geometric surface of the electrode ( $0.196 \text{ cm}^2$ ), for the porous hollow PtNi/C electrocatalysts synthesized on different carbon supports: (A) Vulcan XC72, (B) carbon nanotubes, (C) YS, (D) graphene nanosheets, (E) acid leached graphene nanosheets, (F) carbon xerogels, (G) Ketjenblack. All the results were obtained before and after an accelerated stress test protocol mimicking potential variations during start-up/shutdown of a PEMFC cathode (500 steps at  $T = 353 \text{ K}$  between  $1.0 \text{ V vs. RHE}$  ( $t = 3 \text{ s}$ ) and  $1.5 \text{ V vs. RHE}$  ( $t = 3 \text{ s}$ )). ..... 155
- Figure 63.** IL-TEM for the porous hollow PtNi/C NPs synthesized on on different carbon supports: Vulcan XC72, carbon nanotubes, YS, graphene nanosheets, acid leached graphene nanosheets, carbon xerogels and Ketjenblack before and after an accelerated stress test protocol mimicking potential variations during start-up/shutdown of a PEMFC cathode (500 steps at  $T = 353 \text{ K}$  between  $1.0 \text{ V vs. RHE}$  ( $t = 3 \text{ s}$ ) and  $1.5 \text{ V vs. RHE}$  ( $t = 3 \text{ s}$ )). ..... 157

## List of Figures

- Figure 64.** (A) Specific and (B) Mass activity for the ORR in O<sub>2</sub>-saturated 0.1 M HClO<sub>4</sub> at E = 0.95 V vs. RHE, (C) specific and (D) mass activity in O<sub>2</sub>-saturated 0.1 M HClO<sub>4</sub> at E = 0.90 V vs. RHE – corrected for diffusion in solution and Ohmic drop, T = 298 ± 1 K, ω = 1600 rpm, ν = 0.005 V s<sup>-1</sup> and (E) Pt specific surface area determined from the CO<sub>ad</sub> stripping experiments for the porous hollow PtNi/C NPs synthesized on different carbon supports before and after an accelerated stress test protocol mimicking potential variations during start-up/shutdown of a PEMFC cathode (500 steps at T = 353 K between 1.0 V vs. RHE (t = 3 s) and 1.5 V vs. RHE (t = 3 s))..... 158
- Figure 65.** Linear sweep voltammograms corrected from the Ohmic drop and from oxygen diffusion in solution measured at ν = 0.005 V s<sup>-1</sup> in O<sub>2</sub>-saturated 0.1 M HClO<sub>4</sub> on porous hollow PtNi/C electrocatalysts synthesized on different carbon supports: (A) Vulcan XC72, (B) carbon nanotubes, (C) YS, (D) graphene nanosheets, (E) acid leached graphene nanosheets, (F) xerogels, (G) Ketjenblack. The kinetic current is normalized to the Pt ECSA. All the results were obtained before and after an accelerated stress test protocol mimicking potential variations during start-up/shutdown of a PEMFC cathode (500 steps at T = 353 K between 1.0 V vs. RHE (t = 3 s) and 1.5 V vs. RHE (t = 3 s))..... 160
- Figure 66.** Linear fits of the difference of potential (ΔE) as a function of the kinetic current (j<sub>k</sub>) for the porous hollow PtNi/C electrocatalysts synthesized on (A) Vulcan XC72, (B) carbon nanotubes, (C) YS, (D) graphene nanosheets, (E) acid leached graphene nanosheets, (F) Xerogel and (G) Ketjenblack before and after an accelerated stress test protocol mimicking potential variations during start-up/shutdown of a PEMFC cathode (500 steps at T = 353 K between 1.0 V vs. RHE (t = 3 s) and 1.5 V vs. RHE (t = 3 s))..... 161
- Figure 67.** Variation of CO<sub>ads</sub> stripping voltammograms before and after 20,000 potential cycles between 0.6 and 1.0 V vs. RHE at T = 353 K and ν = 50 mV s<sup>-1</sup> for porous hollow PtNi/C nanoparticles with a crystallite size (A) d<sub>XRD</sub> < 2 nm and (B) d<sub>XRD</sub> > 3 nm. .... 169
- Figure 68.** Electrochemical properties of porous hollow PtNi/C NPs synthesized at LEPMI or in large-scale reactors by CEA (from ca. 350 mg to ca. 10 g), with an initial ratio Pt<sup>2+</sup>:Ni<sup>2+</sup> of 1:5. (A) CO<sub>ads</sub> stripping voltammogram (ν = 0.020 V s<sup>-1</sup>, Ar-saturated 0.1 M HClO<sub>4</sub>). (B) Ohmic drop corrected linear sweep voltammograms (ν = 0.005 V s<sup>-1</sup>, electrolyte = O<sub>2</sub>-saturated 0.1 M HClO<sub>4</sub>, ω = 1600 rpm). Mass-transport and Ohmic drop corrected specific activity (SA) and mass activity (MA) measured in O<sub>2</sub>-saturated 0.1 M HClO<sub>4</sub> at (C) E = 0.95 V vs. RHE and (D) E = 0.9 V vs. RHE..... 171
- Figure 69.** Performances of MEA (anode: 50 wt. % commercial Pt/C – 0.2 mg cm<sub>geo</sub><sup>-2</sup>, cathode: porous hollow PtNi/C or commercial Pt/C – 0.2 mg cm<sub>geo</sub><sup>-2</sup>, surface of the MEA: 25 cm<sup>2</sup>) at T = 353 K, with a relative humidity of 50 % both for the H<sub>2</sub> (P = 1.5 bar, stoichiometry 1.5) and the air (P = 1.5 bar, stoichiometry 2). (A) Beginning of life, after activation, (B) after 1,000 potential cycles between 0.6 and 1.0 V at ν = 0.050 V s<sup>-1</sup> (C) after 10,000 potential cycles and (D) after 30,000 potential cycles. .... 172
- Figure 70.** Evolution of the Pt specific surface (in cm<sub>Pt</sub><sup>2</sup> cm<sub>geo</sub><sup>-2</sup>) in MEA for a commercial Pt/C cathode or a porous hollow PtNi/C cathode (0.20 mg cm<sub>geo</sub><sup>-2</sup>). .... 173

## List of Tables

<b>Table 1.</b> External diameter ( $d_{\text{ext}}$ ) measured by TEM and crystallite diameter measured by X-Ray Diffraction for the electrocatalysts discussed in this chapter. ....	98
<b>Table 2.</b> Crystallite size ( $d_{\text{XRD}}$ ) for the electrocatalysts synthesized at different temperatures.....	107
<b>Table 3.</b> Activity for the oxygen reduction reaction – corrected from the Ohmic losses and the diffusion in solution – at $E = 0.95$ V and $E = 0.90$ vs. RHE for the electrocatalysts synthesized at $T = 278, 293, 313, 333$ and $353$ K and the Pt/C and PtNi/C references. The activities were either given with respect to the electrochemical surface area of the electrocatalysts (specific activity, SA) or to the mass of platinum in the electrocatalyst (mass activity, MA). The Pt specific surface area of the electrocatalysts ( $S_{\text{Pt,CO}}$ in $\text{m}^2 \text{g}_{\text{Pt}}^{-1}$ ) is also provided.....	108
<b>Table 4.</b> Standard potential of the $M^{2+}/M$ pair for the 3d transition metal discussed in this work. ....	115
<b>Table 5.</b> Specific surface area values of the carbon supports discussed in this work, calculated by the Brunauer, Emmett and Teller equation, ( $S_{\text{BET}}$ ), surface developed by micropores ( $S_{\text{micropores}}$ ) calculated by the t-plot method, and difference between the two surfaces ( $S_{\text{BET}} - S_{\text{micropores}}$ ). ....	117
<b>Table 6.</b> In-plane crystallite size ( $L_a$ ) and size of the graphitic domains perpendicular to the graphite plane ( $L_c$ ), determined by Raman and XRD, respectively, for the different carbon supports discussed in this work.....	118
<b>Table 7.</b> Surface composition of the different carbon substrates as derived from the XPS analysis..	119
<b>Table 8.</b> Morphological, physical and electrochemical properties of the porous hollow PtNi/C NPs synthesized on the different carbon supports, i.e. the external ( $d_{\text{ext}}$ ) and inner ( $d_{\text{in}}$ ) diameter of the NPs, the Pt weight fraction (Pt wt. %) on the carbon surface, the Ni content (Ni at. %) measured by AAS, the lattice parameter ( $a_{\text{Pt-Pt}}$ ), the mean crystallite size ( $d_{\text{XRD}}$ ) and the first moment of the potential weight of the $\text{CO}_{\text{ads}}$ stripping voltammogram ( $\mu_1^{\text{CO}}$ ).....	122
<b>Table 9.</b> Specific and mass activities for the ORR (corrected for the Ohmic losses and oxygen diffusion in solution) measured at $E = 0.95$ V vs. RHE or $E = 0.90$ vs. RHE for the electrocatalysts synthesized at $T = 278, 293, 313, 333$ and $353$ K before and after 5,000 and 20,000 potential cycles between $E = 0.6$ V vs. RHE and $E = 1$ V vs. RHE at $v = 0.05$ $\text{V s}^{-1}$ , $T = 353$ K in an Ar-saturated 0.1 M $\text{HClO}_4$ electrolyte. The electrocatalytic activities are normalized by the electrochemically active surface area (specific activity, SA) or by the mass of Pt (mass activity, MA).....	136
<b>Table 10.</b> Variation of the microstrain ( $\mu_\varepsilon$ ), the mean crystallite size ( $d_{\text{XRD}}$ ) for the electrocatalysts synthesized at $T = 278$ and $333$ K before (prior to the electrochemical characterisation, i.e. ‘Fresh’) and after electrochemical characterisation (‘Fresh + ORR’) and after 5,000 and 20,000 potential cycles between $E = 0.6$ V vs. RHE and $E = 1.0$ V vs. RHE in Ar-saturated 0.1 M $\text{HClO}_4$ at $v = 0.05$ $\text{V s}^{-1}$ and $T = 353$ K. ....	140
<b>Table 11.</b> Physical, chemical and electrochemical properties of the hollow PtNi/C electrocatalyst used in the in operando WAXS measurements. ....	144

## List of Tables

<b>Table 12.</b> Slopes ( $R_k$ ) determined from the fits of the curves presented in Figure 66 by a linear equation for the different carbon substrates and effective resistances ( $R_{\text{eff}}$ ) determined from the cyclic voltammetry using Equation 41.....	162
---	-----

## List of Abbreviations and Symbols

**AAS:** Atomic Absorption Spectroscopy.

**AB:** Acetylene Black.

**AST(s):** Accelerated Stress Test(s).

**B:** Boron.

**BET:** Brunauer, Emmett and Teller.

**BP:** Black Pearl.

**C:** Carbon.

**CE:** Counter Electrode.

**CEA:** Alternative Energy and Atomic Energy Commission.

**CL:** Catalytic Layer.

**CNT(s):** Carbon Nanotube(s).

**CV(s):** Cyclic Voltammetry (the method) or Cyclic Voltammogram(s) (the plot(s)).

**CX:** Carbon Xerogel.

**CO<sub>ads</sub>:** Carbon monoxide adsorbed onto the platinum surface.

**CO<sub>surf</sub>:** Carbon surface oxides.

**COR:** Carbon Oxidation Reaction.

**$\overline{CN}$ :** Generalized coordination number.

**cn:** Coordination number of an active site.

**DI:** De-Ionized.

**EIS:** Electrochemical Impedance Spectroscopy.

**ESRF:** European Synchrotron Radiation Facility.

**F:** Formaldehyde.

**FC(s):** Fuel Cell(s).

**GB(s):** Grain Boundary(ies).

**G-band:** Ideal graphite lattice band (Raman pattern).

**GC:** Glassy Carbon.

**GDE:** Gas Diffusion Electrode.

**GDL:** Gas Diffusion Layer.

**GNS(s):** 3-dimensionnal Graphene Nano-Sheet(s)

**GNS – AL:** Acid Leached 3-dimensionnal Graphene Nano-Sheet.

**GO:** Graphene Oxide.

## List of Abbreviations and Symbols

**HER:** Hydrogen Evolution Reaction.

**HOR:** Hydrogen Oxidation Reaction.

**HPP:** High Potential Peak for the CO<sub>ads</sub> stripping.

**HR-TEM:** High-Resolution Transmission Electron Microscopy.

**H<sub>upd</sub>:** Underpotentially-deposited Hydrogen.

**HV:** Heyrovsky Volmer.

**IL-TEM:** Identical-Location Transmission Electron Microscopy.

**LASER:** Light Amplification by Stimulated Emission of Radiation.

**LPP:** Lowest Potential Peak for the CO<sub>ads</sub> stripping.

**LSV(s):** Linear Sweep Voltammetry (the technique) or Linear Sweep Voltammogram(s) (the plot(s)).

**M (Ni, Co, Cu, Fe, Zn, Cr, *etc.*):** 3d transition metals (Nickel, Cobalt, Copper, Iron, Zinc, Chromium, *etc.*).

**MEA:** Membrane Electrode Assembly.

**MilliQ H<sub>2</sub>O:** Ultrapure water (R = 18.2 MΩ).

**MPL:** Micro-Porous Layer.

**MPP:** Medium Potential Peak for the CO<sub>ads</sub> stripping.

**MYRTE:** Mission hYdrogen & Renewable for the inTegration on the Electrical grid.

**SC:** Na<sub>2</sub>CO<sub>3</sub>.

**NC(s):** Nanocrystallite(s).

**NP(s):** Nanoparticle(s)

**ORR:** Oxygen Reduction Reaction.

**PDF:** Pair Distribution Function.

**PEM:** Proton Exchange Membrane.

**PEMFC:** Proton Exchange Membrane Fuel Cell.

**Pt:** Platinum.

**Pt(pc):** Polycrystalline Pt.

**PSD:** Particle Size Distribution.

**Q/HQ:** Quinone / Hydroquinone.

**R:** Resorcinol.

**RRDE:** Rotating Ring Disk Electrode.

**RHE:** Reversible Hydrogen Electrode.

**r.d.s.:** Rate determining step.

**rpm:** Rotation per minutes.

## List of Abbreviations and Symbols

- SAXS:** Small-Angle X-ray Scattering.
- SEM:** Scanning Electron Microscopy.
- SHE:** Standard Hydrogen Electrode.
- SLD:** Scattering Length Density.
- SSM:** Sacrificial Support Method.
- STEM-EDX:** Scanning Transmission Electron Microscopy – Energy Dispersive X-ray.
- TEM:** Transmission Electron Microscopy.
- TV:** Tafel Volmer.
- XPS:** X-ray Photoelectron Spectroscopy.
- XRD:** X-Ray Diffraction.
- WAXS:** Wide-Angle X-ray Scattering.
- WE:** Working Electrode.
- Z:** Atomic number.
- 
- FWHM:** Full width at half maximum of X-ray diffraction patterns (in radians).
- $\Delta E$ :** Potential difference (V).
- $\Delta G$ :** activation free energy (eV).
- $\lambda$ :** Wavelength (nm).
- $\rho$ :** Electronic or ionic resistivity ( $\Omega$  cm).
- $\nu$ :** Scan rate ( $V s^{-1}$ ).
- $\mu_1^{CO}$ :** First moment of the potential weight of the  $CO_{ads}$  stripping (V vs. RHE).
- $\mu_\epsilon$ :** Microstrain (%%).
- $a_{Pt-Pt}$ :** Average lattice parameter of the Pt-based crystalline structure (nm).
- at. %:** Atomic percentage.
- $C_{dl}$ :** Double layer capacitance (C).
- $d_{002}$ :** Average inter-planar spacing between the graphene domains (nm).
- $d_{ext}$ :** External diameter (nm).
- $d_{id}$ :** Interplanar distance in the crystalline system (nm).
- $d_{in}$ :** Inner diameter (nm).
- $\bar{d}_N$ :** Number-averaged diameter (nm).
- $d_{porosities}$ :** Diameter of the carbon porosities (nm).
- $\bar{d}_S$ :** Surface-averaged diameter (nm).
- $\bar{d}_V$ :** Volume-averaged diameter (nm).

## List of Abbreviations and Symbols

$d_{\text{XRD}}$ : Crystallite size (nm).

$E$ : Potential (V vs. RHE).

$E^{\circ}_{\text{CO}(2)/\text{C}}$ : Standard potential of the  $\text{CO}_2/\text{C}$  couple (V vs. SHE).

$E^{\circ}_{\text{H}^+/\text{H}_2}$ : Standard potential of the  $\text{H}^+/\text{H}_2$  couple (V vs. SHE).

$E^{\circ}_{\text{Ni}^{2+}/\text{Ni}}$ : Standard potential of the  $\text{Ni}^{2+}/\text{Ni}$  couple (V vs. SHE).

$E^{\circ}_{\text{O}_2/\text{H}_2\text{O}}$ : Standard potential of the  $\text{O}_2/\text{H}_2\text{O}$  couple (V vs. SHE).

$E_{\text{p,CO}}$ : Potential of the ‘high-potential’ peak of the  $\text{CO}_{\text{ads}}$  stripping (V vs. RHE)

$E^{\circ}_{\text{Pt}^{2+}/\text{Pt}}$ : Standard potential of the  $\text{Pt}^{2+}/\text{Pt}$  couple (V vs. SHE).

$E^{\circ}(\text{Pt}(\text{NH}_3)_4^{2+} / \text{Pt})$ : Standard potential of the  $\text{Pt}(\text{II})/\text{Pt}$  couple (V vs. SHE).

$E_{\text{a,QHQ}}$ : Potential of the anodic peak of the Q/HQ couple (V vs. RHE).

$E_{\text{c,QHQ}}$ : Potential of the cathodic peak of the Q/HQ couple (V vs. RHE).

**ECSA**: ElectroChemically active Surface Area ( $\text{cm}^2_{\text{Pt}}$ ).

$e_{\text{shell}}$ : Thickness of the NPs shell (nm).

$I$ : Current (A).

$I_{\text{D1}}$ : Integrated intensity of the D1-band peak of the Raman pattern.

$I_{\text{G}}$ : Integrated intensity of the G-band peak of the Raman pattern.

$I_{\text{lim}}$ : Diffusion-limited current density for the ORR ( $\text{mA cm}^{-2}_{\text{Pt}}$ )

$I_{\text{k}}$ : Kinetic current density for the ORR ( $\text{mA cm}^{-2}_{\text{Pt}}$ ).

$I(q)$ : Scattering intensity of the SAXS patterns.

$j_{\text{a,QHQ}}$ : Current density of the anodic peak of the Q/HQ couple ( $\text{mA cm}^{-2}_{\text{geo}}$ ).

$j_{\text{c,QHQ}}$ : Current density of the cathodic peak of the Q/HQ couple ( $\text{mA cm}^{-2}_{\text{geo}}$ ).

$L_{\text{a}}$ : Average crystallite size in the graphene plane of the carbon (nm).

$L_{\text{c}}$ : Average size of the graphitic domains out of the graphene plane (nm).

**MA**: Mass Activity ( $\text{A g}^{-1}_{\text{Pt}}$ ) for the ORR.

**MA<sub>0.95</sub>**: Specific Activity ( $\mu\text{A cm}^{-2}_{\text{Pt}}$ ) for the ORR at  $E = 0.95$  V vs. RHE.

$n_{\text{Pt(II)}}$ : Number of moles of the Pt precursor (mmol).

$n_{\text{Ni(II)}}$ : Number of moles of the Ni precursor (mmol).

$P$ : Pressure (Pa).

$P(q)$ : Form factor (see **Equation 26** for full description).

$q$ : Normalized total structure factor (see **Equation 24** for full description).

$Q_{1,\text{CO}}$ : Charge used to electrooxidize a monolayer of  $\text{CO}_{\text{ads}}$  ( $420 \mu\text{C cm}^{-2}_{\text{Pt}}$ ).

$Q_{1,\text{Hupd}}$ : Charge used to adsorb a monolayer of  $\text{H}_{\text{upd}}$  ( $210 \mu\text{C cm}^{-2}_{\text{Pt}}$ ).

$Q_{\text{Hupd}}$ : Charge under the  $\text{H}_{\text{upd}}$  peaks (C).

$Q_{\text{pp,CO}}$ : Charge under the ‘low-potential’ peak of the  $\text{CO}_{\text{ads}}$  stripping (C).

**$Q_{T,CO}$** : Total  $CO_{ads}$  stripping charge (C).

**$R_{eff}$** : Effective resistance of the system (resistance of the glassy carbon + resistance of the electrolyte + resistance of the catalytic layer,  $\Omega \text{ cm}^2_{geo}$ ).

**$R_k$** : Increase of the system resistance during ageing ( $\Omega \text{ cm}^2_{Pt}$ ).

**$R_{el}$** : Resistance of the electrolyte ( $\Omega$ ).

**SA**: Specific Activity ( $\mu\text{A cm}^{-2}_{Pt}$ ) for the ORR.

**SA<sub>0.95</sub>**: Specific Activity ( $\mu\text{A cm}^{-2}_{Pt}$ ) for the ORR at  $E = 0.95 \text{ V vs. RHE}$ .

**S<sub>BET</sub>**: Specific surface area determined by BET ( $\text{m}^2 \text{ g}^{-1}$ ).

**S<sub>Pt,CO</sub>**: Pt specific surface area calculated from  $CO_{ads}$  stripping measurements ( $\text{m}^2 \text{ g}^{-1}_{Pt}$ ).

**T**: Temperature (K).

**T<sub>s</sub>**: Temperature of the synthesis (K).

**$u/RT$** : Energy of interaction between the hydrogen atoms.

**wt. %**: Weight percentage.

## List of the Publications used in this Manuscript

This thesis is based on the following publications in international peer-reviewed journals. Some of them have been published, and others will be published:

(1) Asset, T.; Chattot, R.; Nelayah, J.; Job, N.; Dubau, L. and Maillard, F. Structure-Activity Relationships for the Oxygen Reduction Reaction in Porous Hollow PtNi/C Nanoparticles. *ChemElectroChem* 2016, 3 (10), 1591–1600.

(2) Chattot, R.; Asset, T.; Drnec, J.; Bordet, P.; Dubau, L.; Maillard, F.; Drnec, J.; Dubau, L.; and Maillard, F. Atomic Scale Snapshots of the Growth Mechanism of Hollow PtNi/C Nanocatalysts for Oxygen Reduction Reaction. *Nano Lett* 2017, 17 (4), 2447–2453.

(3) Asset, T.; Fontana, M.; Mercier-Guyon, B.; Martin, V.; Chattot, R.; Job, N.; Dubau, L. and Maillard, F. Rational Design of Hollow Pt-based Nanoparticles for the Oxygen Reduction Reaction, *submitted in ChemPhysChem*.

(4) Asset, T.; Chattot, R.; Drnec, J.; Bordet, P.; Job, N.; Maillard, F. and Dubau, L. Elucidating the Mechanisms Driving the Ageing of Porous Hollow PtNi/C Nanoparticles by the Means of CO<sub>ads</sub> stripping, **DOI:** 10.1021/acsami.7b05782.

(5) Asset, T.; Busby, Y.; Crisci, A.; Martin, V.; Stergiopoulos, V.; Serov, A.; Atanassov, P.; Chattot, R.; Dubau, L.; Maillard, F. and Job, N. Influence of the Carbon Support on the Morphology and Stability of Porous hollow PtNi/C electrocatalysts, *to be submitted*.

(6) Asset, T.; Chattot, R.; Martens, I.; Drnec, J.; Bordet, P.; Nelayah, J.; Job, N.; Maillard, F. and Dubau, L.; *In Operando* Study of the ageing of porous hollow PtNi/C NPs, *to be submitted*.

# **Chapter I. General Introduction**

## I. 1. Nowadays Challenges

6.3 million years ago, the human – chimpanzee speciation progressively occurred <sup>1</sup>, resulting in the appearance of the genus homo, which ultimately evolved in *homo sapiens*. The *homo sapiens*, *i.e.* the intelligent man, has lived from 200,000 years ago <sup>1</sup> (or *ca.* 300,000 years ago, according to the recent discovery of a characteristic *homo sapiens* skull in Morocco <sup>2</sup>) to nowadays but strikingly, it is only during the last three centuries that we discovered most of the technologies commonly used in our modern society. If the control of fire by our humans ancestor has been reported up to one million years ago <sup>3</sup>, *i.e.* during the *homo erectus* era <sup>4</sup>, the premises of metallurgy were only observed 7,000 years ago <sup>5</sup> (copper smelting) and the utilization of coal 3,500 years ago <sup>6</sup> for household and metalworking <sup>7</sup>. The use of the latter to power steam engines was unveiled in 1712 by Tomas Newcomen <sup>8</sup>. This discovery was the dawn of the industrial revolution and led to an accelerated growth in technologies (see **Figure 1A**) that resulted in (i) an enhanced quality of live and (ii) a diminished mortality rate and, thus, a dramatic rise of the Earth population (see **Figure 1B**), from *ca.* one billion in 1800 <sup>10</sup> to 7.5 billion in 2017.

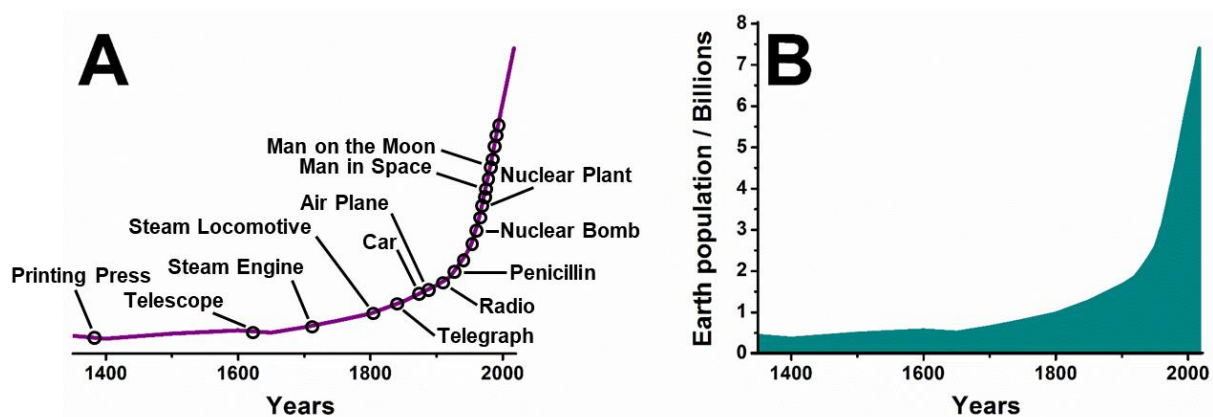


**Figure 1.** (A) Schematic representation of the accelerated growth in technology that followed the discovery of the steam engine and (B) Evolution of the Earth population from 1350 to nowadays. The changes in the world population has been established from Ref. <sup>9</sup>.

Increased population means increased consumption of goods and energy. To sustain the needs of the modern society, non-renewable resources as fossil fuels (coal, petroleum, natural gas, *etc.*) and key metals (cobalt, uranium, lead, platinum, *etc.*) were extensively consumed and are soon to be depleted (**Figure 2**). Furthermore, CO<sub>2</sub> molecules, mostly produced by the oxidation of carbon atoms present in fossil fuels, contribute to the global warming (see **Figure 2**). According to the International Energy Agency <sup>10,11</sup>, *ca.* 68 % of the greenhouse gas emissions arise

from energy (the other sources of greenhouse gas emissions being the agriculture, the industrial processes, *etc.*). In this specific domain, *ca.* 66 % of the CO<sub>2</sub> production result from electricity production, heat production and transports.

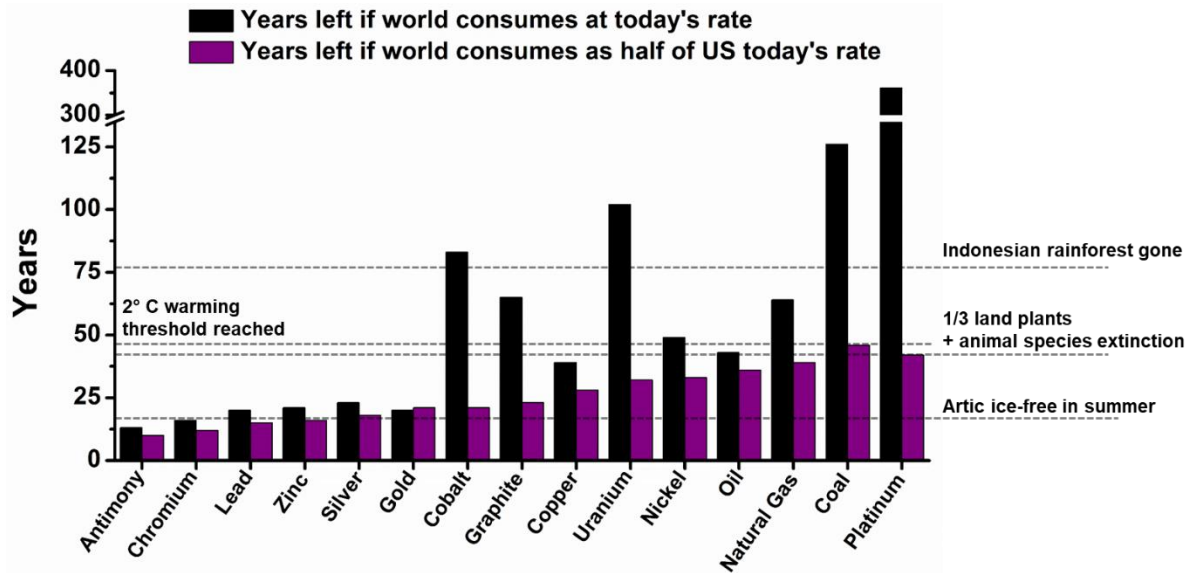


**Figure 2.** Global stock resources for several key elements and fossil fuels, for a static consumption rate and if the Earth consumption rate is half of the US rate – *i.e.* an enhancement of the quality of life in the developing countries. Indicators of the global warming are provided on the graph. References: A. Reller, University of Augsburg, T. Graedel, University of Yale and Ref. <sup>12,13</sup>. The graphic does not take into consideration neither the discovery of new technologies nor a large-scale recycling of the different elements.

Decreasing the CO<sub>2</sub> emissions, along with a reduction of the human need for fossil fuels, is essential. To this goal, the use of renewable energies (*i.e.* geothermal, hydroelectric, solar, wind *etc.*) has been widely promoted but these remain intermittent, as their energy production is highly dependent on their environment (*e.g.* weather for the wind turbines and the solar panels). Compensation for the intermittency can be achieved by storing the excess energy in batteries or in chemical bonds, as achieved in the MYRTE platform, in Ajaccio, Corsica <sup>14</sup>. The MYRTE platform combines an electrolyser which transforms H<sub>2</sub>O in H<sub>2</sub> and O<sub>2</sub> (*i.e.* converts the electrical energy produced by solar panels into chemical energy) stored in high pressure tanks. The H<sub>2</sub> and O<sub>2</sub> can be later recombined in a fuel cell (FC) to produce electrical energy.

## I. 2. The proton exchange membrane fuel cell

The fuel cell discovery was ascribed to C. F. Schönbein (who first described the so-called fuel cell effect, *i.e.* the voltage of the hydrogen/oxygen chain between two platinum (Pt) foils connected by acidified water and fed with  $H_2$  and  $O_2$ ) and Sir W. R. Grove (who first described and designed a complete fuel cell system)<sup>15,16</sup>. Nowadays, fuel cells cover a wide range of systems and applications (portable devices, stationary power generation, transportation, *etc.*) and, although some do not use  $H_2$  as a fuel or an acid solution as an electrolyte, they all present a similar design (see **Figure 3**). The latter consists of:

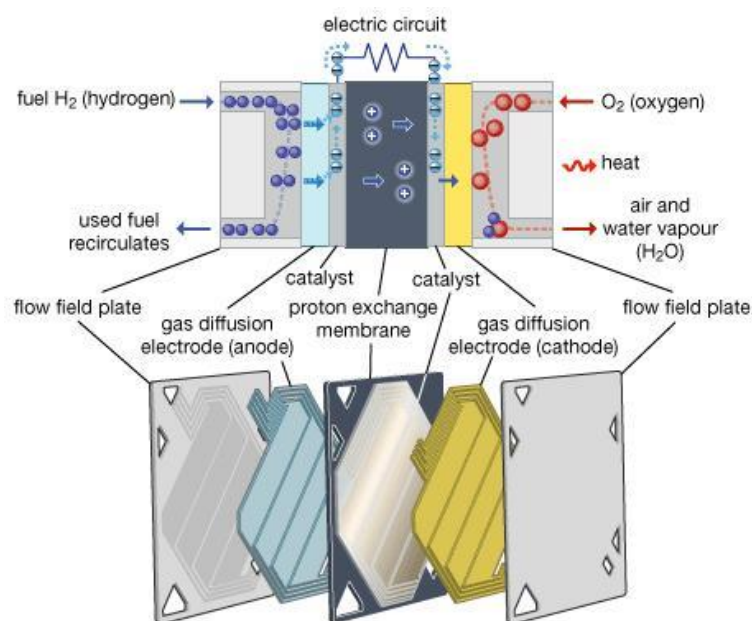


**Figure 3.** Design of a Proton Exchange Membrane Fuel Cell (PEMFC) reprinted from Ref. <sup>17</sup>.

- (i) two catalytic layers (CLs), the cathode and the anode, where the Oxygen Reduction Reaction (ORR) and the oxidation of a fuel ( $H_2$  or an alcohol in direct alcohol fuel cells) occur, respectively;
- (ii) an electronic separator, also acting as a ionic conductor between the two catalytic layers, either solid (in solid oxide fuel cells or molten carbonate fuel cells<sup>18</sup>), polymer-based (in proton exchange membrane fuel cells, *e.g.* **Figure 3**, or direct alcohol fuel cells) or liquid (in alkaline fuel cells);
- (iii) flow-field plates, which act as electronic conductor for the electrons produced/consumed by the electrochemical reactions and allow distribution of gases first to the Gas Diffusion Layers (the GDLs, *i.e.* the macroporous – microporous carbon layer which supplies a homogeneous flux of gases and removes the water produced by the

electrochemical reactions, see **Equation 1 – 3**), and then ultimately to the catalytic layers. A Scanning Electron Microscope picture of a whole membrane electrode assembly (MEA) sandwiched between two GDLs is displayed in **Figure 4**).

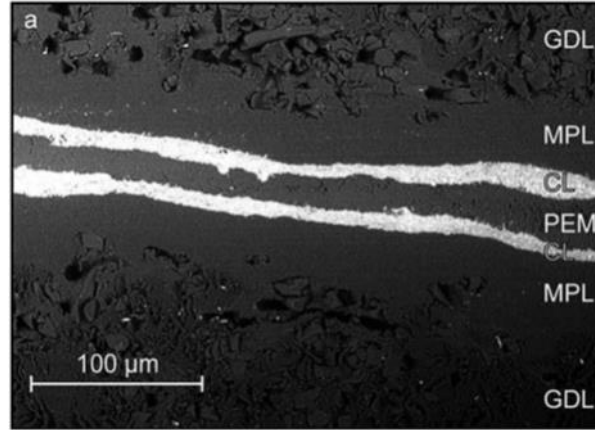
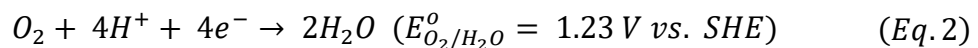
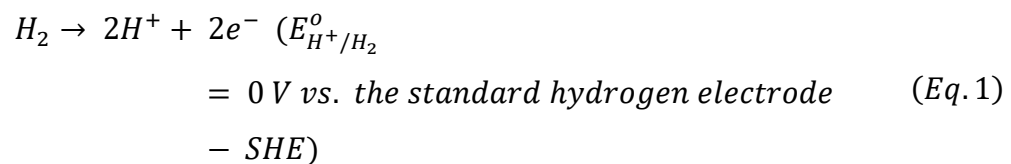


**Figure 4.** Scanning electron micrograph of a Membrane Electrode Assembly (*i.e.* catalytic layers + membrane + gas diffusion layer). PEM = Proton Exchange Membrane, CL = catalytic layer, MPL = Micro-Porous Layer and GDL = Gas Diffusion Layer). Reprinted from Ref. <sup>19</sup>.

The present manuscript focuses on Proton Exchange Membrane Fuel Cell (PEMFC, see **Figure 3**), a type of fuel cells which oxidizes hydrogen at the anode (as described by **Equation 1**), the electrons and protons produced by this reaction being transported to the cathode where they participate to the ORR (**Equation 2**). The global equation of the PEMFC is provided in **Equation 3** (at  $T = 298 \text{ K}$ ).



### I. 3. Hydrogen Oxidation Reaction

The Hydrogen Oxidation Reaction (HOR, **Equation 1**) on Pt extended surfaces involves two different mechanisms, *i.e.* the Heyrovsky – Volmer sequence (HV, **Equation 4** and **Equation 6**) and the Tafel – Volmer sequence (TV, **Equation 5** and **Equation 6**):



In the HV pathway, two successive one-electron oxidations occur, the first during the chemisorption (**Equation 4**), the second from the adsorbed hydrogen atom. By contrast, the TV pathway consists of the H<sub>2</sub> dissociative adsorption (**Equation 5**) followed by the independent oxidation of the two adsorbed hydrogen atoms (**Equation 6**). As the two pathways are observed during the HOR, the global mechanism is often referred to as Tafel – Heyrovsky – Volmer (THV) sequence. The kinetics and the favoured pathways are highly dependent on:

- (i) the surface coverage ( $\theta$ ) by adsorbed hydrogen<sup>20,21</sup> and the nature of the isotherm being related to the latter (*e.g.* for  $0.2 < \theta < 0.8$ , a Frumkin<sup>22</sup> isotherm is observed);
- (ii) the overpotential ( $\eta$ ). The TV pathway is predominant at low overpotential values, while presenting a maximal kinetic current ( $j_{\max}$ )  $\ll$  the diffusion-limited current ( $j_L$ ) (see **Figure 5**)<sup>23–25</sup>. At higher overpotentials, the HV pathway becomes predominant and  $j_{\max} \sim j_L$  (see **Figure 5**)<sup>23–25</sup>. This potential dependence is specific to Pt-based electrodes, as the HOR follows only the HV pathway on Pd electrodes (except at potential values close to the equilibrium)<sup>26,27</sup>.

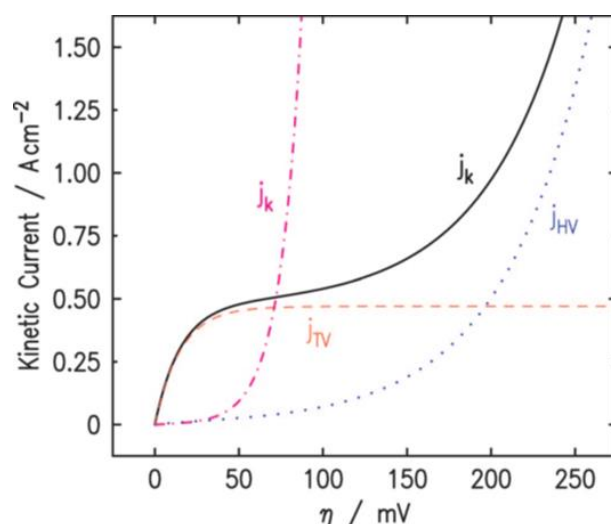


**Figure 5.** Calculation of the kinetic current densities for the HOR on Pt at  $T = 291$  K. Dashed and dotted curves represent the contributions from the TV ( $j_{TV}$ ) and HV ( $j_{HV}$ ) pathways, respectively, while  $j_k$  (black line) represent their combined contribution determined by a dual pathway kinetic equation. The dashed-dotted curve shows the kinetic current ( $j_k$ ) calculated using the Butler-Volmer equation. Reprinted from Ref. <sup>24</sup>.

The kinetics rate in acid electrolyte are extremely fast compared to the diffusion rate of the reactive species, therefore the determination of the kinetics parameters is difficult to perform <sup>28,29</sup>. The inverse reaction (the Hydrogen Evolution Reaction, HER, *i.e.*  $\text{H}_2\text{O} \rightarrow \text{H}_2$ ) is also driven by the THV mechanism. The nature of the hydrogen intermediate ( $\text{H}_{\text{ads}}$ ) was assessed by Quaino *et al.* <sup>30</sup>, as the overpotentially deposited hydrogen ( $\text{H}_{\text{opd}}$ ). The latter presents a far lower energy of interaction ( $u/RT$ ) between the hydrogen atoms and the surface than the  $\text{H}_{\text{upd}}$  atoms <sup>30–32</sup> ( $0.338 < u/RT < 1.35$  vs.  $u/RT \sim 11$  for underpotentially deposited hydrogen,  $\text{H}_{\text{upd}}$ , on Pt), as a result of the nature of their adsorption sites <sup>31,32</sup>.

The nature of the electrocatalyst greatly impacts the kinetics of the HER, as evidenced in **Figure 6**. Indeed, different metal – H bond strengths are observed, depending on the surface <sup>33</sup>. Interestingly, a too strong binding of the  $\text{H}_{\text{ads}}$  species is as detrimental as a too weak binding (*e.g.* Ti and Pb). This is rationalized by the Sabatier principle, *i.e.* a catalyst should bind an adsorbate neither too strongly nor too weakly.

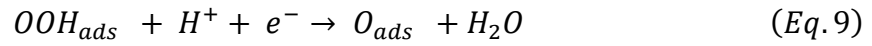


this first step was later described by Shao *et al.*<sup>39</sup> in alkaline media, *i.e.* O<sub>2</sub> reducing into O<sub>2</sub> superoxide, O<sub>2</sub><sup>-</sup>. Until the works of Durand's group<sup>40-43</sup> and Stamenkovic *et al.*<sup>34</sup>, the ORR was mostly studied by RRDE on extended surface, using a wide range of parameters to determine the nature of the intermediate steps of the ORR<sup>35,44</sup>, *i.e.* NI<sub>D</sub>/I<sub>R</sub> vs.  $\omega^{-1/2}$  plot (ratio of the disk and the ring current vs. the rotation speed,  $\omega$  being the rotation speed and N a geometric factor) or the J-S plot (which establish the mechanism based on the slope and the y-axis intercept of the NI<sub>D</sub>/I<sub>R</sub> vs.  $\omega^{-1/2}$  plot). However, as evidenced by Anastasijević *et al.*<sup>45,46</sup>, RRDE plots cannot provide a full explanation of the ORR mechanism, but only indicate that (i) all the intermediate reactions are of the first order (*i.e.* one electron exchanged), (ii) the ORR involves weakly and strongly bounded species and (iii) the O<sub>2</sub> species diffusion on the surface is negligible. The study of the ORR on Pt nanoparticles (NPs)<sup>41-43</sup> and on different crystallite facets<sup>40,47</sup> provided further insights, on the essential role of the NPs size (the decrease of the NPs resulted in depreciated specific activity, *i.e.* the *so-called* particle size effect<sup>41-43,48-50</sup>) and of the coordination number of the facets<sup>40,47</sup> (as the Pt (110) surface, *i.e.* a fully stepped surface, presented an enhanced activity toward the ORR compared to Pt (111) surface). The origin of the H<sub>2</sub>O<sub>2</sub> production was also evidenced, as it increased with the diminution of the NPs size. This is due to a different binding of the O<sub>2</sub> (end-on conformation, *i.e.* one oxygen bonded, instead of side-on – bridged – conformation, *i.e.* two oxygen bonded) which favoured its production instead of the O – O bond breaking<sup>42</sup>. This was confirmed by Stamenkovic *et al.*<sup>51</sup> and Markovic *et al.*<sup>52</sup> on extended surfaces, *i.e.* that the rate of the H<sub>2</sub>O<sub>2</sub> production is dependent on the surface availability (and, therefore, of the ability of O<sub>2</sub> to bind in bridge side-on conformation). As such, the presence of H<sub>ads</sub>, Cl<sub>ads</sub> or Br<sub>ads</sub> (*i.e.* partly blocking the active sites) would result in an enhanced production of H<sub>2</sub>O<sub>2</sub><sup>51,52</sup>. Interestingly, the O<sub>2</sub> adsorption in side-on conformation is required for the O – O bond splitting (*i.e.* the H<sub>2</sub>O formation)<sup>42,51,52</sup>. This suggest that H<sub>2</sub>O<sub>2</sub> originates from a parallel reaction where the O<sub>2</sub> adsorbs in end-on conformation, as first assumed by Damjanovic *et al.*<sup>35-37</sup> on polycrystalline surfaces. To be involved in the 4e<sup>-</sup> pathway as assumed by Ref.<sup>34</sup> (see **Figure 7**), the H<sub>2</sub>O<sub>2</sub> should (i) desorb from the end-on conformation and (ii) re-adsorb in side-on conformation.

The r.d.s. of the ORR (on platinum) is widely assumed as being the first protonation step (**Equation 7**), *i.e.*



However, the r.d.s. highly depends on the surface coverage (Temkin *vs.* Langmuir), on the pH, on the electrode potential, *etc.* <sup>41,53</sup>. Due to the ORR complexity, its mechanism is often discussed using several elementary electrochemical reactions as suggested by Stephens *et al.* <sup>54</sup> and Greeley *et al.* <sup>55</sup>:



An aspect stemming from the works of Stephens *et al.* <sup>54</sup> and Rossmeisl *et al.* <sup>56</sup> (on H<sub>2</sub>O electrolysis) is that the free energies of adsorption ( $\Delta G$ ) of the intermediates species ( $O_{ads}$ ,  $HO_{ads}$  and  $HOO_{ads}$ ) are correlated to each other (see **Figure 8**). According to **Figure 8**, optimizing an electrocatalyst for **Equation 8**, which needs a strong binding of the  $HOO_{ads}$ , is detrimental to **Equation 11**, which requires a weak binding of the  $HO_{ads}$  species (the difference of  $\Delta G$  between the  $HO_{ads}$  and the  $HOO_{ads}$  is constant and  $\Delta G_{HOO^*} - \Delta G_{HO^*} \sim 3.2$  eV <sup>54</sup>). Consequently, an ideal electrocatalyst for the ORR should bind *every* intermediate absorbed species neither too strongly, nor too weakly.

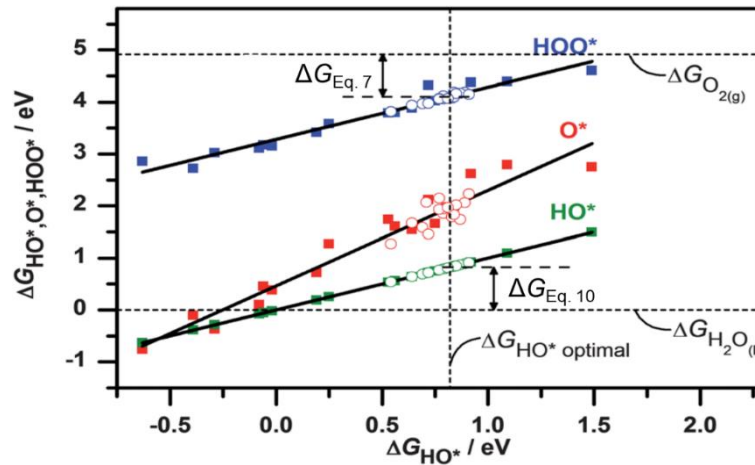


**Figure 8.** Theoretical plot of free energies of adsorption of  $HOO_{ads}$  ( $HOO^*$ ),  $HO_{ads}$  ( $HO^*$ ) and  $O_{ads}$  ( $O^*$ ),  $\Delta G_{HOO^*}$ ,  $\Delta G_{HO^*}$  and  $\Delta G_{O^*}$ , respectively, as a function of  $\Delta G_{OH^*}$ , for (111), (100) and (211) pure metal surfaces (filled squares) as well as Pt overlayers on Pt-alloy surfaces. Reprinted from Ref. <sup>54</sup>.

### I. 4. 2. Platinum, the ‘benchmark’ catalyst for the ORR

**Figure 9** shows that Au presents, among all the elements, the weakest binding not only for the O\* intermediates but also for the OH\* intermediates. As such, it does not present the highest activity for the ORR. Indeed, the optimal electrocatalyst for the ORR features a compromise between the adsorption strength of all the adsorbates (see **Section I. 4. 1**). According to **Figure 9**, Pt presents the ‘closest-to-optimum’ adsorption strength.

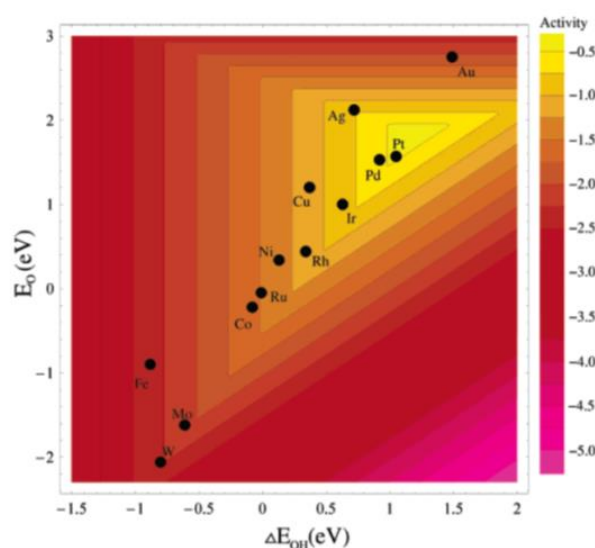


**Figure 9.** Relationship between the electrocatalyst activity for the ORR and the adsorption strength of the OH\* and O\* intermediates – the OOH\* intermediate is not considered by Nørskov *et al.*<sup>57</sup>. Reprinted from Ref.<sup>57</sup>.

Pt is considered as the ‘benchmark’ electrocatalyst for PEMFCs<sup>58</sup> and, more specifically, Pt NPs of diameter ( $d$ )  $\sim 2 - 3$  nm (*i.e.* the optimal size for the ORR specific and mass activity<sup>49,50</sup>) supported on high surface area carbon (non-precious metal electrocatalysts, *e.g.* Me/N/C electrocatalysts<sup>59–63</sup> are not discussed in this manuscript). In the FCs, the catalytic layer (CL) is active only at the ‘three-phase boundary’, *i.e.* where the Pt NPs are in contact with:

- (i) the CL pores, as the latter have a porous network to allow the reactant transport and the evacuation of the products from/to the GDL;
- (ii) the carbon support, which ensures electron transport from the flow-field plates to the Pt NPs and *vice versa*;

- (iii) the ionomer phase, as the CL is impregnated with ionomer (*e.g.* Nafion<sup>®</sup>) to ensure efficient ionic conduction, *i.e.* connection with the PEM. In FCs, the weight percentage (wt. %) of Nafion<sup>®</sup> in the catalytic layer must be carefully established as a too low wt. % results only in a partial coverage of the carbon support while a too high wt. % results in a thick Nafion<sup>®</sup> layer that limits the reactant diffusion<sup>64</sup>, the optimal loading being  $27 \pm 6$  wt. % on Vulcan XC72<sup>65</sup>.

Unfortunately, platinum is a rare and not evenly distributed (88 wt. % of the Pt resources are found in South Africa<sup>66</sup>) and, therefore, expensive element. An increased consumption of Pt would accelerate its depletion (*ca.* 42 years if considering **Figure 2**). If all the global annual production of Pt was devoted to fuel cell vehicles, *ca.* only 10 million vehicles will be produced per year, *i.e.* 10 % of the annual automotive vehicles production<sup>67</sup>. Increasing the Pt mass activity (*i.e.* the electrocatalytic activity normalized to a gram of Pt – MA) and the Pt specific activity (*i.e.* the electrocatalytic activity normalized to a cm<sup>2</sup> of platinum – SA) has therefore been one of the key challenges of the PEMFC for the past 20 years. To this extent, lots of efforts have been devoted to study a wide range of Pt-based nanomaterials (*e.g.* Pt-based alloys<sup>68–71</sup>, M@Pt core@shell NPs<sup>72–75</sup>, multi-layered (noble and non-noble metals) core@Pt-monolayer shell NPs<sup>76–80</sup>, Pt-rich nanoporous structures<sup>81–86</sup>, preferentially oriented NPs<sup>87–92</sup>, *etc.*) with an enhanced activity for the ORR. The mechanisms driving this activity enhancement (*i.e.* the lattice – strain effect, the ensemble effect and the effect of the structural defects) are widely discussed in the following sections.

#### I. 4. 3. The *d*-band theory and its applications for the ORR

Based on the *d*-band theory established by Hammer and Nørskov<sup>93,94</sup>, the specific activity for the ORR of Pt can be tuned by alloying Pt with another element (a 3d transition metal or a rare-earth element<sup>55,69,70,95,96</sup>). According to **Section I. 4. 1**, the r.d.s. of the ORR is the first protonation of the O<sub>2</sub> molecule (see **Equation 7**), *i.e.* O<sub>2</sub> → OOH<sub>ads</sub>. This kinetics of this reaction can be rationalized using the Butler-Volmer equation (**Equation 12** and **Equation 13**)<sup>97–99</sup>:

$$j_k = nFkC_{O_2}C_{H^+}(1 - \theta_{ads})^x \exp\left(-\frac{\alpha FE}{RT}\right) \times \exp\left(-\frac{\Delta G_{ads}^\ddagger}{RT}\right) \quad (Eq. 12)$$

$$\Delta G_{ads}^\ddagger = \Delta G_0^\ddagger - \beta u \theta_{ox,ads} \quad (Eq. 13)$$

where  $F$  is the faraday constant ( $96,485 \text{ C mol}^{-1}$ ),  $k$  the kinetic constant of the r.d.s.,  $n$  the number of exchanged electrons,  $C_{\text{O}_2}$  the coverage by adsorbed  $\text{O}_2$  that is the partial pressure in  $\text{O}_2$ ,  $C_{\text{H}^+}$  the concentration of  $\text{H}^+$  near the electrode,  $x$  the number of sites occupied by the  $\text{OOH}_{\text{ads}}$ , *i.e.*  $x = 1$  or  $2$ ,  $\alpha$  and  $\beta$  the symmetry factors,  $R$  the gas constants ( $8.314 \text{ J mol}^{-1} \text{ K}^{-1}$ ),  $E$  the electrode potential and  $T$  the temperature.  $\theta_{\text{ads}}$  corresponds to the total surface coverage by adsorbed species, *i.e.* dioxygen molecules and intermediate adsorbed species,  $\theta_{\text{ox,ads}}$ , spectator species and oxides formed by water splitting,  $\theta_{\text{OH,ads}}$ . The Gibbs free energy of the reaction  $\Delta G_{\text{ads}}^\ddagger$ , depends on  $\Delta G_0^\ddagger$ , the Gibbs free energy of oxygen adsorption of a zero coverage, on  $u$ , the lateral interaction factor between the oxygen molecules, and on  $\theta_{\text{ox,ads}}$  (see **Equation 13**). As evidenced by Dubau *et al.*<sup>97</sup> on  $\text{Pt}_3\text{Co}$  NPs, **Equation 12** can be transformed into **Equation 14** assuming (i)  $\theta_{\text{ads}} \sim \theta_{\text{OH,ads}} \gg \theta_{\text{ox,ads}}$ , (ii)  $\beta = 0.5$  and (iii)  $u/RT = 6$ <sup>52</sup>.

$$j_k = nFk'C_{\text{O}_2}C_{\text{H}^+}(1 - \theta_{\text{OH,ads}})^x \exp\left(-\frac{\alpha FE}{RT}\right) \times \exp(-3\theta_{\text{ox,ads}}) \quad (\text{Eq. 14})$$

$$k' = k \exp\left(\frac{\Delta G_0^\ddagger}{RT}\right) \quad (\text{Eq. 15})$$

The terms  $(1 - \theta_{\text{OH,ads}})$  and  $\exp(-3\theta_{\text{ox,ads}})$  show that diminishing the surface coverage in oxygen species (and especially the  $\text{OH}_{\text{ads}}$  coverage) would result in faster kinetics for the first protonation of the  $\text{O}_2$  molecule (**Equation 7**), *i.e.* that the  $\text{OH}_{\text{ads}}$  binding strength should be reduced for increased performances. **Figure 9** shows that Pt bind the  $\text{OH}_{\text{ads}}$  *ca.*  $0.2 - 0.3 \text{ eV}$  too strongly. The binding strength can be modified by alloying Pt with another element. The alloying modifies the density of states of the Pt 5d band (see **Figure 10A**), and its centre relative to the Fermi-level. The change of the Pt 5d band structure in turn modifies the adsorption strength of the oxygen-containing ORR intermediates<sup>100–104</sup>, leading to a volcano-plot relationship between the specific activity for the ORR and the chemisorption energy of oxygenated species (*i.e.* a too weak binding of the  $\text{OH}_{\text{ads}}$  species would negatively impact the kinetics of the other ORR steps, see **Figure 10B**). The modification of the Pt 5d band centre by the alloying element is due to (i) the strain effect<sup>105–108</sup>, *i.e.* the contraction of the lattice parameter of Pt at the surface of the electrocatalyst (*e.g.* the skin/skeleton structures<sup>109–112</sup>) and/or (ii) the ligand effect<sup>108</sup>, *i.e.* the direct modification of the electronic structure of Pt by the neighbouring atoms of the alloying element.

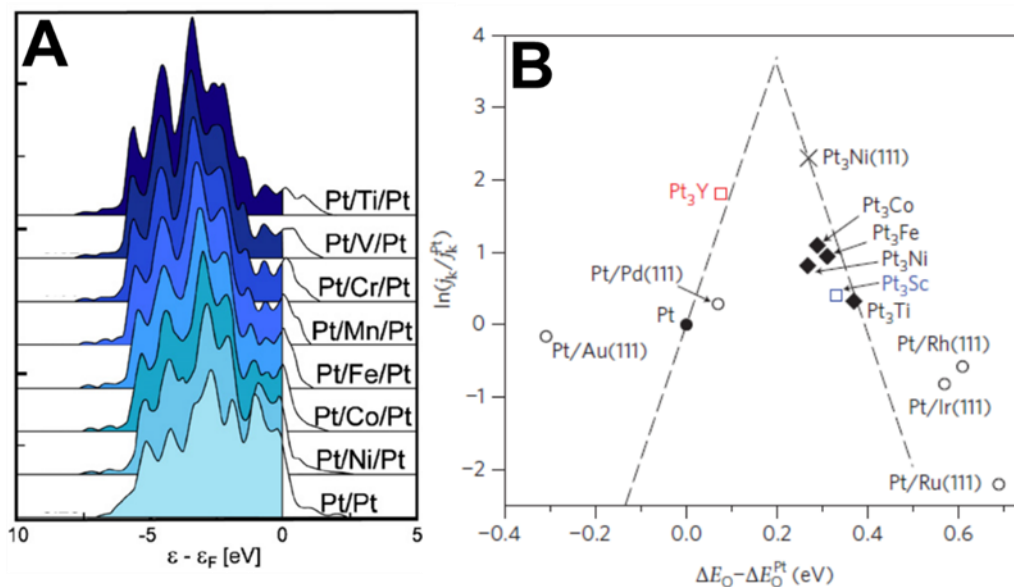


**Figure 10.** (A) Effect of insertion of a 3d transition metal in the first subsurface layer of a Pt surface on the Pt density of states (reprinted from Ref. <sup>101</sup>) and (B) Volcano-plot of the kinetic current for the ORR (relative to Pt) as a function of the adsorption strength of the O\* intermediate. The dotted line corresponds to the theoretical predictions of Rossmeisl *et al.* <sup>113</sup>. Reprinted from Ref. <sup>55</sup>.

The strain and ligand effects opened the way to the synthesis of highly active materials for the ORR, such as

- (i) Pt-based alloys <sup>70,71</sup>,
- (ii) Pt-monolayers on non-noble / noble core <sup>114,115</sup> and
- (iii) M@Pt (M = Ni, Co, Cu) core@shell NPs <sup>116,117</sup>

The latter presented an higher mass activity (because of the non-noble metal core and the strain effect) for the ORR <sup>73–75,118–125</sup>. The formation of nanoporosities was observed in core@shell NPs with an external diameter  $d_{\text{ext}} > 30$  nm after de-alloying (see Oezaslan *et al.* <sup>126</sup>) or in smaller NPs ( $d_{\text{ext}} > 10$  nm) after electrochemical ageing (see Gan *et al.* <sup>127,128</sup>). Nanoporosities imply a higher ElectroChemically active Surface Area (ECSA) for the ORR, therefore opening a second path for the synthesis of electrocatalysts for the ORR: the nanoporous NPs, *i.e.* highly porous NPs with a diameter of 10 – 15 nm <sup>81,82</sup>, such as the Pt<sub>3</sub>Ni nanoframes introduced by Chen *et al.* <sup>129</sup>. As a result of the low stability of the 3d transition metals in acid electrolyte <sup>97,130–132</sup>, a positive use of the ligand effect is not often observed for PtM<sub>x</sub> electrocatalysts (M, a 3d transition metal). Indeed, the PtM surface tends to form a skeleton structure <sup>97,110,130,133</sup>, *i.e.* a rough Pt surface where the 3d transition metal has been oxidized.

Using rare-earth elements instead of 3d transition metals presents the advantage of (i) modifying the electronic properties of Pt (ligand effect), (ii) obtaining an higher theoretical stability as the Pt – rare-earth element alloy has a negative heat of formation<sup>55</sup> and of (iii) contracting the lattice parameter of Pt by the means of a *so-called* kagomé layer, *i.e.* a contracted Pt structure with surface vacancies to accommodate the presence of the rare earth element<sup>95,96,134,135</sup>. As summarized by Čolić and Bandarenka<sup>136</sup> (see **Figure 11**), the activity of the Pt-based alloy can then be enhanced either by using 3d transition metals (*e.g.* Ni, Co, Cu or Cr) or rare-earth elements (*e.g.* Tb, Y, Gd, *etc.*)

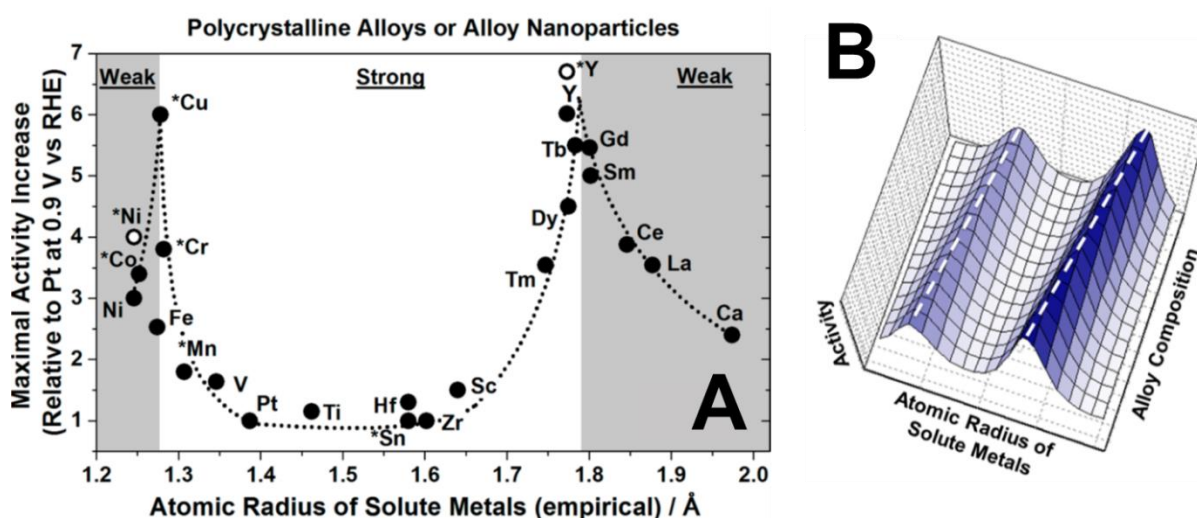


**Figure 11.** (A) Maximal reported value for the  $\text{PtM}_x$  ( $x$  = the M/Pt atomic ratio observed for the optimal activity) for the ORR at  $E = 0.9$  V vs. the Reversible Hydrogen Electrode (RHE), compared to the corresponding Pt electrocatalyst (the stars refer to nanoparticles) as the function of the atomic radius of the alloying element. (B) Schematic 3D representation of the relation between the ORR activity of the electrocatalyst, the radius of the alloying element and the composition of the alloy. Reprinted from Ref.<sup>136</sup>

#### I. 4. 4. The ‘ensemble’ effect.

As discussed in **Section I. 4. 1.**, the ORR activity is highly dependent on the crystallite orientation. This phenomenon was first evidenced by El Kadiri *et al.*<sup>40</sup> and Markovic *et al.*<sup>137</sup> on Pt extended surfaces and was studied on  $\text{Pt}_3\text{Ni}$  (hkl) by Stamenkovic *et al.*<sup>138</sup>. On  $\text{Pt}_3\text{Ni}$  (hkl) surfaces, the ORR specific activity varies as  $\text{Pt}_3\text{Ni}$  (111) >  $\text{Pt}_3\text{Ni}$  (110) >  $\text{Pt}_3\text{Ni}$  (100), due to the modification of the 5d-band centre on the different facets. The ‘ensemble’ effect, *i.e.* the impact of the surface texturation, plays a predominant role (in addition to the strain – ligand effect) in the preferentially shaped electrocatalysts activity for the ORR, *i.e.* octahedra<sup>88,89,139–141</sup>, truncated octahedra<sup>90</sup>, *etc.* These octahedral nanostructures were synthesized to replicate, at the

nanoscale, the phenomena observed on extended surfaces and presented an enhanced activity, resulting of their increased density of (111) facets. However, these nanostructures also suffered from a low durability, due to Ni segregation onto the NPs facets and the resulting loss in activity<sup>89,139</sup>. Fortunelli *et al.*<sup>142</sup> recently reported that low-coordinated – strained surface rhombi (*i.e.* four atoms arrangements in two equilateral triangles sharing one side) resulted in a decreased activation barrier for the O\* hydration reaction (**Equation 7**) and thus, enhanced kinetics for the ORR, similarly to (111) extended surfaces. Taking advantage of these specific kind of active sites, ultrafine jagged nanowires were synthesized and presented an SA at 0.90 V *vs.* RHE of 11.5 mA cm<sup>-2</sup><sub>Pt</sub>, *i.e.* 33 times higher than the commercial Pt/C characterized in the same study<sup>143</sup>. This enhancement in SA is also explained by the highly defective structure of the nanowires (see **Section I. 4. 5.**).

### **I. 4. 5. The role of the structural defects.**

The density of steps has a notorious impact on the reactivity of Pt extended surfaces, both for electrooxidation (*e.g.* CO<sub>ads</sub> oxidation) and electroreduction (*e.g.* ORR) reactions. Lebedeva *et al.*<sup>144-147</sup> found that the oxidation potential of a CO<sub>ads</sub> layer varies as Pt (553) < Pt (554) < Pt (111)<sup>147</sup>, *i.e.* increases with the decrease of the number of steps on stepped surfaces. This was ascribed to the capability of steps to nucleate OH<sub>ads</sub> species from water at lower potential than terraces atoms<sup>144</sup>. The impact of structural defects on Pt/C NPs on CO electrooxidation was discussed by Cherstiouk *et al.*<sup>148</sup> and Maillard *et al.*<sup>149</sup>. It was shown that the presence of agglomerates (nanocrystallites interconnected by grain boundaries) causes the appearance of a ‘pre-peak’ at  $E \sim 0.6 - 0.7$  V *vs.* the Reversible Hydrogen Electrode (RHE) in CO<sub>ads</sub> stripping voltammograms, *i.e.* at lower potential than observed for isolated monocrystalline Pt/C NPs ( $E \sim 0.8$  V *vs.* RHE). Hitotsuyanagi *et al.*<sup>150</sup>, Kuzume *et al.*<sup>151</sup>, Bandarenka *et al.*<sup>152</sup> and Pohl *et al.*<sup>153</sup> evidenced the crucial role of steps for the ORR activity of stepped Pt surfaces. An optimal density of steps of  $n = 5$  has been found for Pt [n(111) × (100)], resulting in a *ca.* 3-fold improvement in specific activity for the ORR *vs.* Pt(111)<sup>150</sup> (an optimum at  $n = 3$  was also found for stepped Pt [n(111) × (111)]<sup>151</sup>).

This can be rationalized as follows:

- (i) The steps interrupt the network of adsorbed OH\* and H<sub>2</sub>O\*, resulting in a non-hydrated OH\*<sup>154</sup> at the terrace sites adjacent to the steps, with a much weaker binding energy<sup>152</sup>, a diminished surface coverage (see **Equation 13**) and, thus, an enhanced activity for the ORR;

- (ii) High coordination sites are observed under the steps, with an enhanced activity for the ORR. According to Calle-Vallejo *et al.*,<sup>155,156</sup> the ORR activity of a Pt catalytic site depends on its generalized coordination number, see **Equation 16**:

$$\overline{CN} (i) = \sum_{j=1}^{n_i} \frac{cn(j)}{cn_{max}} \quad (\text{Eq. 16})$$

where  $\overline{CN}$  is the generalized coordination number of a Pt atom,  $cn(j)$  the coordination number of the first neighbours ( $j$ ) of this atom and  $cn_{max}$  the highest coordination number observed among the first neighbours. An optimal activity for the ORR should be achieved for catalytic sites presenting a  $\overline{CN} = 8.3$ <sup>156</sup>, *i.e.* slightly higher than a Pt(111) surface ( $\overline{CN} = 7.5$ ). Increasing the  $\overline{CN}$  on nanomaterials is possible by (i) synthesizing concave structures (*e.g.* the inner cavity of porous hollow NPs or the interior of porosities) and (ii) increasing the density of structural defects (*e.g.* missing surface atoms, grain boundaries, *etc.*) that results in high coordination sites near the structural defects. Recently, Le Bacq *et al.*<sup>157</sup> showed that, in addition to under-coordinated ( $\overline{CN} < 8.3$ ) and over-coordinated ( $\overline{CN} > 8.3$ ) sites, highly defective Pt surface presented a combination of relaxed and contracted lattice parameters, resulting in electrocatalysts active for both oxidation reactions ( $\text{CO}_{\text{ads}}$  oxidation, alcohol oxidation reaction) and reduction reactions (ORR). This topic is extensively discussed in **Section IV. 3**. The co-existence of relaxed and contracted domains onto a nanostructure surface was also recently discussed by Bu *et al.* on highly active PtPb@Pt core@shell nanoplates<sup>87</sup>.

#### I. 4. 6. A comparison of the different Pt-based nanostructures

Other materials (*e.g.* nanostructured and mesostructured thin films<sup>158</sup>, ultrafine nanowires<sup>143</sup>, Pt-based aerogels<sup>159–162</sup> *etc.*) were also synthesized and presented tremendous activity for the ORR. The enhancement factor in specific and mass activity for the ORR observed for some relevant electrocatalysts *vs.* the commercial Pt/C, for the ORR at  $E = 0.90$  V *vs.* RHE or  $E = 0.95$  V *vs.* RHE (both were not provided by all the authors) are presented in **Figure 12**, along with Transmission Electron Microscopy (TEM) micrographs or schematic representation of their nanostructures. Because of the difference between the scan rate ( $0.005$  V  $\text{s}^{-1}$ <sup>75,81,84,88</sup> or  $0.020$  V  $\text{s}^{-1}$ <sup>111,129,138,143,158</sup>) and the potential range of the ORR measurement ( $0.06 - 1.05$  V *vs.* RHE<sup>75,88</sup> *vs.*  $0.2 - 1.05$  V *vs.* RHE<sup>84</sup>), the absolute values of the specific and mass activity were not considered as meaningful and, therefore, not provided in **Figure 12**.

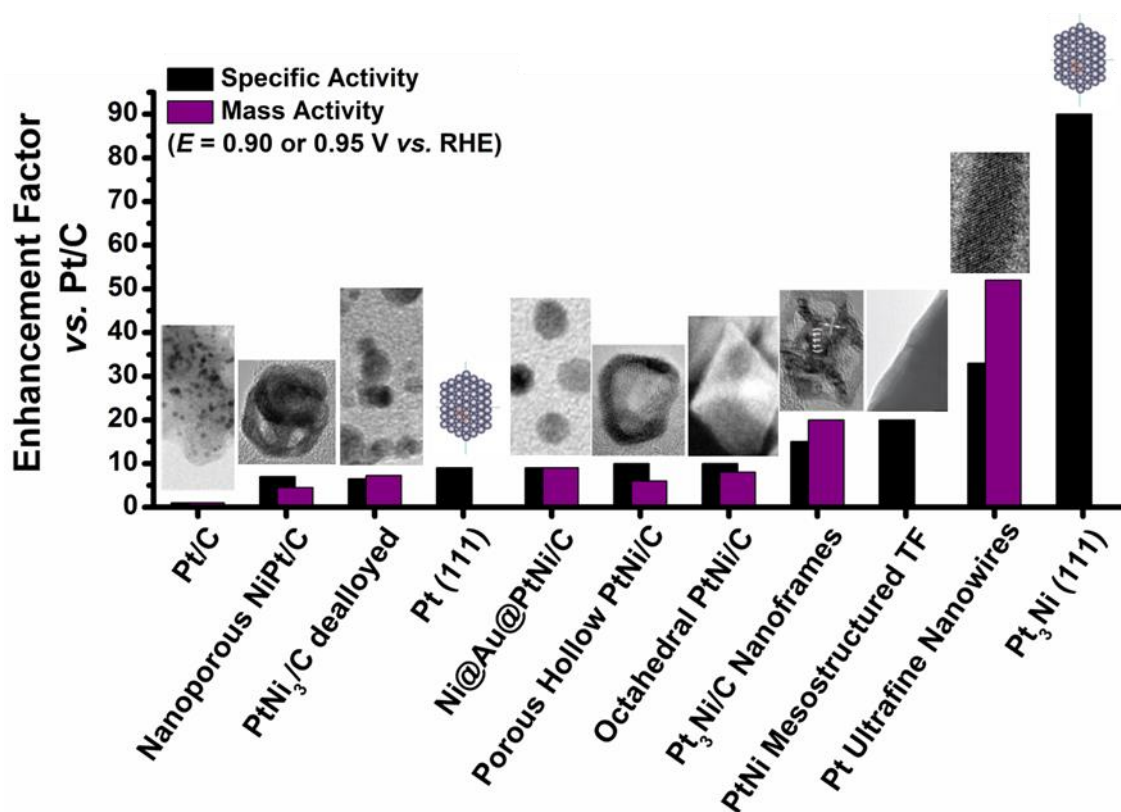


**Figure 12.** Enhancement of the ORR kinetics vs. Pt/C for several electrocatalysts in 0.1 M HClO<sub>4</sub>, *i.e.* commercial Pt/C<sup>49</sup>, nanoporous NiPt/C<sup>81</sup>, dealloyed PtNi<sub>3</sub>/C<sup>75</sup>, porous hollow PtNi/C<sup>84</sup>, octahedral PtNi/C<sup>88</sup> and Pt ultrafine nanowires<sup>143</sup> (at  $E = 0.90$  V vs. RHE,  $\nu = 0.005$  V s<sup>-1</sup> or 0.020 V s<sup>-1</sup> for Ref. 143), Pt(111) and Pt<sub>3</sub>Ni(111)<sup>138</sup>, Ni@Au@PtNi/C<sup>111</sup>, Pt<sub>3</sub>Ni/C Nanoframes<sup>129</sup> and PtNi mesostructured thin films<sup>158</sup> (at  $E = 0.95$  V vs. RHE,  $\nu = 0.020$  V s<sup>-1</sup>). See references associated to each nanostructure for more information.

## I. 5. The carbon supports

The presence of a support is essential to minimize agglomeration of Pt-based NPs and, thus maintain a high dispersion (a high ECSA) in real PEMFC electrodes. Several examples of non-supported Pt-based nanostructures can be found in Ref. 158,163–166 although they are not discussed in this manuscript. The NPs supports can be (i) carbon-free (*e.g.* metal oxide nanotubes<sup>167,168</sup> or aerogels<sup>169,170</sup>) or (ii) carbon-based. Carbon-based supports can be classified according to their physical and morphological properties such as (i) the specific surface area (in m<sup>2</sup> g<sup>-1</sup>), (ii) the surface of the mesopores ( $2 \text{ nm} < d_{\text{pore}} < 50 \text{ nm}$ <sup>171</sup>) and micropores ( $d_{\text{pore}} < 2 \text{ nm}$ <sup>171</sup>), (iii) the average crystallite size in the graphene plane ( $L_a$ , in nm), the average size of the graphitic domains perpendicular to the graphene plane ( $L_c$ , in nm), and (iv) the average inter-planar

distance between the graphene domains ( $d_{002}$ , in nm). Items (iii) and (iv) are used to characterize the structure of partially graphitized carbons<sup>172</sup>, *i.e.* their long-range order. Low  $L_a$  and  $L_c$  are typical of amorphous or quasi-amorphous carbon materials, whereas high  $L_a$  and  $L_c$  indicate larger crystallites and more organized materials<sup>173</sup>.

Nowadays, carbon supports are found under various morphologies (see **Figure 13**), including, but not limited to:

- (i) graphene nanosheets (**Figure 13A**), composed of one or several stacked graphene layers (*i.e.*  $sp^2$  bonded carbon atoms<sup>174,175</sup>);
- (ii) carbon blacks (**Figure 13B**), *i.e.* several graphene clusters combined in near-spherical particles (5 – 100 nm), connected by van der Waals bonds to form aggregates of diverse morphologies, organization and sizes<sup>176–179</sup>. Their specific surface area ranges from  $S_{BET} = 60 \text{ m}^2 \text{ g}^{-1}$  (Acetylene Black – AB) to  $1500 \text{ m}^2 \text{ g}^{-1}$  (Black Pearl – BP);
- (iii) Carbon nanotubes<sup>180,181</sup> (**Figure 13C**), *i.e.* graphene nanosheets rolled in a tubular form (single walled) or several graphene nanosheets rolled and connected by van der Waals bonds (multi-walled)<sup>182,183</sup>. Carbon nanotubes are usually mesoporous with  $70 \text{ m}^2 \text{ g}^{-1} < S_{BET} < 300 \text{ m}^2 \text{ g}^{-1}$  and  $L_a - L_c \sim 6 - 7 \text{ nm}$ <sup>178</sup>;
- (iv) Carbon xerogels, aerogels or cryogels (**Figure 13D**), *i.e.* highly amorphous carbon materials produced from resorcinol, formaldehyde and  $\text{Na}_2\text{CO}_3$ <sup>184</sup>, composed of covalently bonded near-spherical nodules with highly tuneable nodules and pore size<sup>185–187</sup>.

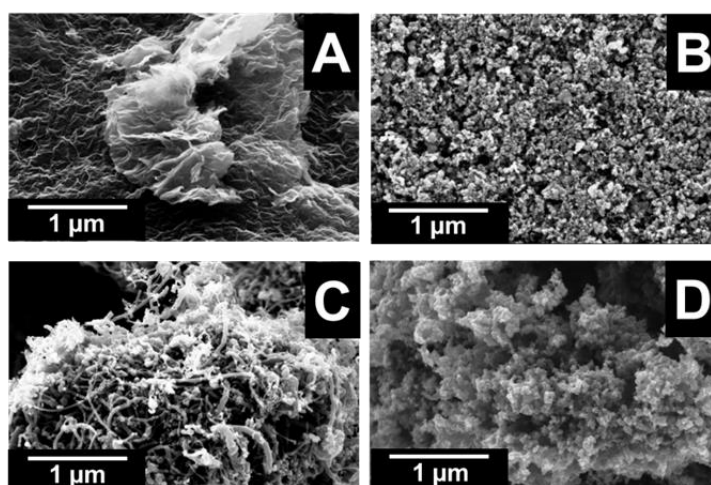


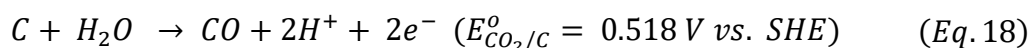
**Figure 13.** Scanning electron microscopy (SEM) micrographs of different carbon structures. (A) Graphene nanosheets, (B) carbon black (Vulcan XC72) (C) carbon nanotubes and (D) carbon xerogel.

The ideal carbon support for PEMFC electrocatalysts should meet several ‘antagonistic’ requirements, *i.e.* (i) allow a high dispersion of the Pt-based NPs to avoid agglomeration *i.e.* a high specific surface area with a minimal microporous surface (where the diffusion is limited<sup>178</sup>) (ii) be chemically inert and pure (to avoid parasitic electrochemical reactions arising from heteroatoms coming from the support), (iii) have a high electronic conductivity and (iv) feature an adequate pore size distribution to allow efficient transport of reactants and evacuation of water, (v) be compatible with the ionomer (*e.g.* Nafion<sup>®</sup>) and (vi) be resistant to electrochemical corrosion<sup>178</sup>.

## I. 6. Ageing of electrocatalysts for PEMFC applications.

### I. 6. 1. Electrochemical corrosion of the carbon support

The equilibrium potential of the CO<sub>2</sub>/C couple (*i.e.* the potential above which carbon is thermodynamically oxidized) is  $E^{\circ}_{\text{CO}(2)/\text{C}} = 0.207 \text{ V vs. SHE}$ . According to the Pourbaix diagram of carbon<sup>176</sup>, the following reactions (**Equations 17 – 18**) should be observed at higher potential values (at  $T = 298 \text{ K}$ ).



The CO molecules formed by **Equation 18** are not stable at potential values higher than  $-0.103 \text{ V vs. SHE}$  and are directly oxidized into CO<sub>2</sub>. In addition to the direct CO<sub>2</sub> formation, Kinoshita and Bett<sup>188</sup> and Donnet *et al.*<sup>189</sup> observed a second reaction pathway, occurring simultaneously and independently of the first one: the formation of carbon surface oxides, which ultimately are transformed into CO<sub>2</sub> (**Equation 19**):



where CO<sub>surf</sub> is a CO surface oxide. The kinetics of these reactions are highly dependent on the physical and chemical properties of the carbon support (degree of graphitisation, presence of heteroelements, functionalization, *etc.*) and on the external conditions (temperature, electrode potential, *etc.*)<sup>190–193</sup>. The presence of Pt NPs on the surface catalyses the electrochemical carbon corrosion (*i.e.* the carbon oxidation reaction, COR) as the CO<sub>surf</sub> formed by the carbon

corrosion might adsorb on the Pt surface ( $\text{CO}_{\text{surf}} \rightarrow \text{CO}_{\text{ads}}$ ) and be oxidized at lower potential than the same Pt-free carbon support<sup>194–196</sup>. Obviously, high Pt loadings used at PEMFC cathodes to circumvent the sluggish ORR kinetics emphasize the catalysis of the COR by Pt. Note however that the Pt catalytic effect is depreciated at  $E > 1.0 \text{ V vs. RHE}$ , due to the formation of Pt oxides<sup>195</sup>.

According to Artyushkova *et al.*,<sup>192</sup> a carbon with an ‘optimal’ resistance to corrosion should present (i) a small % of surface oxides (*i.e.* a low degree functionalization – the oxygen functions are involved in a carbon degradation mechanism proposed by Sihvonen<sup>197</sup>, resulting in a faster corrosion if the surface is highly functionalized), (ii) and a high graphitization (high  $L_a$  and  $L_c$  values). The essential role of the graphitization was recently underlined by Castanheira *et al.*<sup>193</sup>, *i.e.* the disordered and amorphous domains of the high active surface area carbons are preferentially oxidized between  $E = 0.4$  and  $1.0 \text{ V vs. RHE}$  while the graphitized domains are stable until  $E > 1.0 \text{ V vs. RHE}$ . Therefore, the COR essentially occurs at the PEMFC cathode (that mostly operates at  $0.6 \text{ V vs. RHE} < E < 1.0 \text{ V vs. RHE}$ ) and is promoted by the extremely harsh operating conditions, *i.e.*  $\text{pH} < 1$ , oxidizing atmosphere (increase in the carbon functionalization), high temperature, *etc.*

### I. 6. 2. Ageing of the Pt-based nanoparticles

The sintering of Pt nanoparticles occurs concomitantly to the carbon support degradation. Several mechanisms account for this ageing (see **Figure 14**). First, the partial or total dissolution of the Pt smallest nanocrystallites (NCs) and their redeposition by electrochemical Ostwald ripening, resulting from the Gibbs-Thompson effect (**Figure 14A**)<sup>198–201</sup>. In PEMFCs, the Pt redeposition can occur into the membrane via the chemical reduction by the  $\text{H}_2$  produced at the anode and crossing over the membrane<sup>199</sup>, see **Figure 14B**. The dissolution of the Pt NPs and NCs depends on several parameters such as their size<sup>202</sup>, the potential range, the intermediate characterizations<sup>203</sup>, the sweep rate<sup>201,204,205</sup>, the atmosphere<sup>206</sup>, the temperature and the pH<sup>198</sup>. It occurs through direct oxidation into  $\text{Pt}^{2+}$  or by the formation of a Pt surface oxide and its further oxidation / reduction into  $\text{Pt}^{2+}$  ( $\text{Pt} \rightarrow \text{PtO}_x \rightarrow \text{Pt}^{2+}$ )<sup>207</sup>. Then, the NPs coalescence / agglomeration, as the result of the migration of the NCs onto the carbon support (see **Figure 14C**) and the NPs detachment from the carbon support, due to the corrosion of the carbon support (see **Figure 14D**).

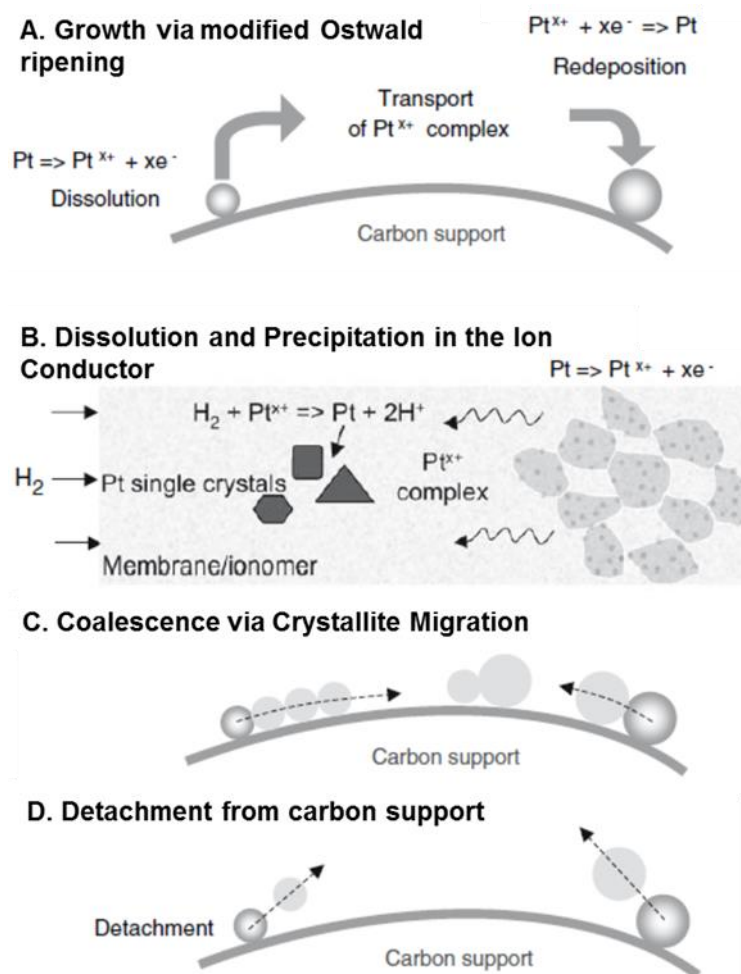


**Figure 14.** Mechanisms for Pt NPs instability in PEMFC cathodes: **(A)** growth *via* electrochemical Ostwald ripening, *i.e.* dissolution of Pt NPs, production of  $Pt^{z+}$  ionic species ( $z = 2, 4$ ) and redeposition of  $Pt^{z+}$  species onto larger Pt crystallites, **(B)** (in FC) dissolution of Pt NPs and precipitation in the ionomer phase and the proton-exchange membrane *via* chemical reduction by  $H_2$ , **(C)** crystallite migration, agglomeration and possibly coalescence, **(D)** detachment of Pt NPs from carbon support. Reprinted from Ref. <sup>199</sup>.

These degradation mechanisms occur during a PEMFC cathode operation (*i.e.* 0.6 – 1.0 V *vs.* RHE) and, as such, the accelerated stress tests (AST, see **Section II. 2. 4.**) are often performed within this potential range <sup>84,143</sup>. However, an upper potential of 1.0 V *vs.* RHE is not representative of the highest potentials that are reached by the cathode (*ca.* 1.5 V *vs.* RHE during fuel starvation events <sup>208</sup>) and, therefore, does not include a degradation mechanism observed at  $E \geq 1.05$  V *vs.* RHE <sup>209,210</sup>: the place-exchange mechanism. The latter was first observed by Conway <sup>211</sup> on Au and Pt surfaces. It originates from the formation of a Pt-oxide layer onto the Pt surface at  $E > 0.85$  V *vs.* RHE. At  $E \geq 1.05$  V *vs.* RHE, this oxide layer induces the formation of a place-exchanged structure <sup>209–212</sup> where the first layer of the Pt surface contains place-

exchanged oxygen (*i.e.* oxygen atoms enter the Pt lattice to minimize the lateral repulsive interactions between the  $O_{ads}$ <sup>212</sup>). This results in the presence, at the NP surface, of low-coordinated Pt atoms, which are prone to dissolution during the reduction of the  $PtO_x$  oxides<sup>211–213</sup>.

### I. 6. 3. Ageing of Pt-based electrocatalysts and the formation of hollow nanostructures: toward a new type of electrocatalysts

The degradation mechanisms depicted above are also observed on PtM (M being a 3d transition metal) nanostructures<sup>214–217</sup>. In addition, because of its high oxophilicity, the alloying element is prone to segregate at the NPs surface and, because of its low standard potential values, is prone to dissolve in the acidic electrolyte of a PEMFC<sup>97,130,215–218</sup>, resulting in a diminution of the strain and ligand effects and, thus, of the electrocatalyst activity for the ORR. Dubau *et al.*<sup>215,216,218</sup> first reported the formation of Pt<sub>3</sub>Co-rich core@Pt-rich shell/C, hollow PtCo/C and hollow Pt/C NPs from initially Pt<sub>3</sub>Co/C NPs after operation in real PEMFC operating conditions (Figure 15).

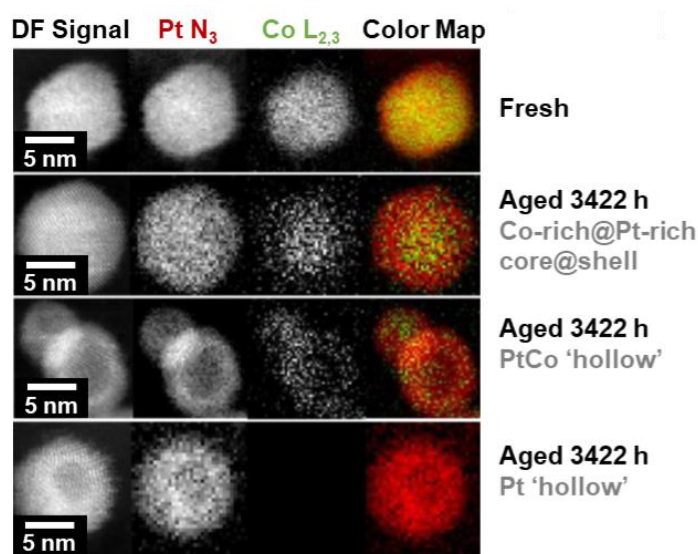


**Figure 15.** High annular angle dark field signal of NPs acquired simultaneously with the energy electron losses spectra. The elemental maps were constructed using the Pt N<sub>3</sub> (518 eV) and the Co L<sub>2,3</sub> (780 eV) edges, respectively. The Pt N<sub>3</sub> signal is shown in red, and the Co L<sub>2,3</sub> signal is shown in green. Reprinted from Ref.<sup>215</sup>.

The latter were formed under specific conditions (*i.e.* at low current, *ca.*  $0.24 \text{ A cm}^{-2}_{geo}$ , *i.e.* high electrode potential<sup>216</sup>), due to the nanoscale Kirkendall effect<sup>219–222</sup>. The nanoscale Kirkendall effect is a vacancy-mediated interdiffusion mechanism occurring in binary alloys or core@shell materials. It is driven by the different interdiffusion coefficients of the involved elements *i.e.*

the Co atoms interdiffuse to the NPs surface, whereas the Pt atoms interdiffuses more slowly to the NPs core, thereby causing the appearance of atomic vacancies to compensate for the inequality in the atomic fluxes. Interestingly, Dubau *et al.*<sup>131</sup> disassembled the MEA after ageing and investigated the intrinsic electrocatalytic activity for the ORR of the different nanostructures with rotating disk electrode in liquid electrolyte. It was found that the formation of hollow Pt/C NPs yields an increase in SA for the ORR. Moreover, as the hollow Pt/C NPs were obtained upon degradation of the fresh Pt<sub>3</sub>Co/C NPs, they are believed to be more stable than the latter<sup>215,218</sup>. In practice, hollow PtM/C NPs may be synthesized using a combination of galvanic replacement and the nanoscale Kirkendall effect, which are very close to the processes at stake in a real PEMFC cathode.

### I. 6. 4. The Pt-rich hollow nanoparticles

The synthesis of hollow NPs by Kirkendall effect was first evidenced by Yin *et al.*<sup>219</sup> on Co<sub>x</sub>S<sub>y</sub>, CoO and CoSe nanostructures at  $T = 455$  K. The CoSe hollow nanocrystals were formed in less than  $t = 30$  min upon injection of a suspension of Se in *o*-dichlorobenzene into a Co nanocrystals solution. Later, Wang *et al.*<sup>223</sup> used a combination of galvanic replacement (formation of Ni-cores by electrodeposition and reduction of the Pt<sup>2+</sup> ions by galvanic replacement) and Kirkendall effect (induced by electrochemical cycling between 0.2 and 1.05 V vs. RHE) to synthesize ~ 5 nm hollow Pt NPs. Using galvanic replacement, non-noble metal corrosion and Kirkendall effect, Gonzalez *et al.*<sup>224</sup> also synthesized hollow Pt NPs, using silver NPs synthesized by the polyol method as a sacrificial template. Since then, the Kirkendall effect became a simple route to synthesize bimetallic hollow shaped NPs composed of a noble-element (*e.g.* platinum, gold) and a less-noble element (*e.g.* cobalt, palladium, nickel or silver) without the use of a surfactant such as citrate<sup>225</sup>, poly(vinylpyrrolidone)<sup>226</sup>, *etc.* The non noble element acts as the sacrificial template for the galvanic replacement before being etched from the nanostructure by Kirkendall effect, often in combination with its dissolution<sup>224,226–230</sup>. Many parameters such as (i) the nature of the sacrificial element<sup>230</sup>, (ii) the stoichiometry between the noble and less-noble element<sup>84,231</sup>, (iii) the temperature of the synthesis<sup>232</sup> and (iv) the shape of the sacrificial template<sup>224</sup> play determining roles in the morphology of the NPs and, thus, their activity for various electrochemical reactions. The resulting hollow structures presented an enhanced activity (with respect to commercial Pt/C) both for oxidation reaction (*e.g.* alcohol oxidation reaction)<sup>225,229,233</sup> and reduction reactions (*e.g.* ORR)<sup>85,231</sup>.

In 2012, Bae *et al.*<sup>231</sup> introduced a ‘one-pot’ method for the synthesis of hollow Pt-rich NPs that presented a 4-fold increase in mass activity toward commercial Pt/C. The synthesis only consisted of mixing the Pt and Ni (the sacrificial metal) precursors with the carbon support, before adding a reducing agent. The resulting electrocatalyst was acid leached and then electrochemically characterized. Owing to their superior activity, their propensity to form during ageing test<sup>218</sup> and the simplicity of their synthesis process<sup>231</sup>, the carbon supported hollow PtNi NPs synthesized by the ‘one-pot’ method became of major interest as an electrocatalyst for the ORR in PEMFC applications. During the past four years, our group<sup>83,84,218,234</sup>, and, consequently, this manuscript, have focused on understanding and optimizing the ‘one-pot’ synthesis. Dubau *et al.*<sup>83</sup> synthesized hollow PtNi/C NPs with a 1:1 ratio between the metallic precursors ( $\text{Pt}^{2+}:\text{Ni}^{2+}$ ) that presented a 3-fold increase in SA for the ORR in 0.1 M  $\text{H}_2\text{SO}_4$ , ascribed to a *ca.* 1.2 % contraction of the lattice parameter *vs.* the lattice parameter of a Pt cubic-face-centered crystallite ( $a_{\text{Pt-Pt}} = 0.3924$  nm). By carefully controlling the synthesis parameters (*e.g.* the addition time of the reducing agent, *etc.*), SA and MA enhancements up to 9-fold and 6-fold, respectively<sup>84</sup>, *vs.* Pt/C were achieved in 0.1 M  $\text{HClO}_4$  electrolyte. The decrease of the  $\text{Pt}^{2+}:\text{Ni}^{2+}$  ratio resulted in a diminution of the shell thickness (*i.e.* a 1:5  $\text{Pt}^{2+}:\text{Ni}^{2+}$  ratio resulted in a shell thickness  $e_{\text{shell}} = 2.6 \pm 0.7$  nm *vs.* a  $e_{\text{shell}} = 3.9 \pm 1.0$  nm for a 1:1  $\text{Pt}^{2+}:\text{Ni}^{2+}$  ratio) and an increase of the electrocatalyst SA and MA for the ORR at  $E = 0.95$  V *vs.* RHE ( $\text{SA}_{0.95} = 141 \pm 21$   $\mu\text{A cm}^{-2}_{\text{Pt}}$  for the 1:5 ratio *vs.*  $\text{SA}_{0.95} = 114 \pm 11$   $\mu\text{A cm}^{-2}_{\text{Pt}}$  for the 1:1 ratio). The NPs were found to be porous allowing the contribution of the inner central cavity and of the porous nano channel located in the shell to the total Pt specific surface area.

Their activity enhancement for the ORR was, as in Dubau *et al.*<sup>83</sup>, first ascribed to the strain effect (*i.e.* the contraction of the lattice parameter due to the residual Ni content of the shell). However, it was also found to be 3-fold and 4-fold higher in SA and MA, respectively, over solid PtNi/C NPs with similar crystallite size and Ni content. Thus, other effects (*e.g.* the structural defects<sup>234</sup>) positively impact the activity of the porous hollow PtNi/C NPs for the ORR. This aspect is widely discussed in **Chapter IV**. Their activity was found to be stable after 30,000 potential cycles between  $E = 0.6$  V *vs.* RHE and  $E = 1.0$  V *vs.* RHE at  $T = 298$  K.

## I. 7. Objectives of the PhD

In **Section I. I.**, we discussed the environment-related challenges that mankind is facing, nowadays, *i.e.* depletion in fossil resources, global warming, *etc.* and the need for renewable sources of energy that resulted. The PEMFC is a promising replacement for fossil fuels engines in cars, but its large-scale commercialization faces several challenges *i.e.* hydrogen storage<sup>235–237</sup> and production<sup>238–240</sup>, the membrane cost and fuel crossover<sup>241,242</sup>, the electrocatalysts activity, cost and durability<sup>67,243</sup>, *etc.* To enhance the latter, the scientific community went from classical Pt/C NPs ( $d \sim 2 - 3$  nm) to Pt-based nanostructured electrocatalysts (*e.g.* PtNi octahedra<sup>88</sup>, Ni-rich@Pt-rich core@shell NPs<sup>244</sup>, nanowires<sup>143</sup>, nanoframes<sup>129</sup>, nanoplates<sup>87</sup>, *etc.*). These structures, in addition to optimize the utilization of the Pt-atoms, take advantage of:

- (i) the strain-ligand effect, *i.e.* the contraction of the lattice parameter induced by the presence of a 3d transition metal;
- (ii) the ensemble effect, *i.e.* the enhanced activity of crystallite facets such as Pt<sub>3</sub>Ni (111)<sup>138</sup> or Pt (110)<sup>47</sup>;
- (iii) the impact of the structural defects, *i.e.* the presence at the electrocatalyst surface, of a wide variety of active sites (*i.e.* low / high coordination, extended / contracted lattice) and, thus, of ‘optimal’ sites onto the NPs surface for the ORR (see **Section I. 4.**).

The porous hollow PtNi/C NPs are in line with this philosophy. As reported by Dubau *et al.*<sup>84</sup>, they feature a 9-fold and a 6-fold enhancement in SA and MA for the ORR, respectively, for the ORR, subsequent to the positive effect of which are due to several parameters:

- (i) the presence of pores yielding enhanced specific surface area (*ca.* 40 – 50 m<sup>2</sup> g<sup>-1</sup><sub>Pt</sub> instead of 25 – 35 m<sup>2</sup> g<sup>-1</sup><sub>Pt</sub> for hollow NPs with the same diameter / shell thickness but without opened porosities<sup>84</sup>);
- (ii) the presence of non-noble metal (*i.e.* Ni, Co, *etc.*) at a *ca.* 15 – 20 at. %, inducing a contraction of the lattice parameter and, thus, a shift of the Pt 5d-band centre<sup>57,93,101,110</sup>. This results in a decreased chemisorption energy of oxygenated species (Pt binds oxygenated species *ca.* 0.2 – 0.3 eV too strongly) and enhances the ORR kinetics<sup>54,55</sup>.

These structural aspects alone cannot fully explain the activity enhancement for the ORR (*i.e.* the 3-fold and 4-fold enhancement in SA and MA, respectively, over solid PtNi/C NPs with similar crystallite size and Ni content) which are partly due to other physical parameters (*e.g.* the structural defects<sup>155,156</sup>) that requires further investigation.

Little is known of the mechanisms that drive the synthesis of the hollow porous PtNi/C NPs: if the latter is simple (*i.e.* the ‘one-pot’ method), the exact contribution of the non-noble metal corrosion, of the galvanic replacement and of the Kirkendall effect are yet to be determined. The Pt<sup>2+</sup>:Ni<sup>2+</sup> ratio has been discussed as a parameter that impacts the final morphology of the porous hollow PtNi/C NPs<sup>84</sup> but the effect of (i) the temperature of the synthesis, (ii) the nature of the carbon support and (iii) the nature of the non-noble metal (*e.g.* Co, Cu, Fe and Zn) must be addressed. The durability of the porous hollow PtNi/C NPs has only been investigated in (i) liquid electrolyte (0.1 M H<sub>2</sub>SO<sub>4</sub> for 9,000 cycles, between  $E = 0.60$  and 1.05 V *vs.* RHE<sup>83</sup> and 0.1 M HClO<sub>4</sub> for 10,000 and 30,000 cycles, between  $E = 0.60$  and 1.00 V *vs.* RHE<sup>84</sup> at  $T = 293$  K) and (ii) PEMFC (5,000 cycles at  $T = 353$  K, between  $E = 0.60$  and 1.05 V *vs.* RHE<sup>83</sup>). The variation of the parameters responsible for their enhanced activity (*e.g.* the Ni content, *etc.*) under ageing and the stability of their carbon support require further studies to be fully understood.

After the presentation of the different techniques and procedures used throughout this PhD (**Chapter II**), the manuscript addresses the following subjects:

- In **Chapter III**, the synthesis of the hollow-porous PtNi/C NPs is discussed. The latter has been monitored by a combination of *in operando* X-ray measurements as well as electrochemical, physical and microscopy methods. The sequential contribution of the galvanic replacement and the Kirkendall effect has been evidenced, as well as the nature of the intermediate nanostructures formed during the synthesis.
- In **Chapter IV**, the different parameters driving the morphology of the porous hollow Pt-based/C NPs (*i.e.* the nature of the sacrificial metal, the carbon support and the temperature of the synthesis) are investigated. The structure/activity relationships are established by means of electrochemical, physical and microscopy methods.
- In **Chapter V**, the electrochemical stability of the NPs and of their support is discussed, by ageing the electrocatalysts during (i) 500 cycles between  $E = 1.0$  and 1.5 V *vs.* RHE at  $T = 353$  K (*i.e.* the operating temperature of PEMFC) to focus on the carbon support, (ii) 5,000 and 20,000 cycles between  $E = 0.6$  and 1.0 V *vs.* RHE at  $T = 353$  K, to follow the density of structural defects and the Ni-content, and thus assess their stability and (iii) 5,000 cycles between  $E = 0.6$  and 1.0 or 1.1 V *vs.* RHE using *in operando* X-ray at  $T = 353$  K to obtain further insights on the physical changes of the NPs and highlight the contribution of the place-exchange mechanism to their ageing.

## Chapter I. General Introduction

- In **Chapter VI**, we present, in addition to the general conclusion of the manuscript, some results related to the ‘scale-up’ of the synthesis, (*i.e.* the increase of the amount of electrocatalyst produced by synthesis, from 0.385 g to 10 g). The activity and the durability tests in membrane electrode assembly and single-cell configuration is also reported. This study has been performed in collaboration with the French Alternative Energy and Atomic Energy Commission (CEA).

# **Chapter II. Introduction to the Techniques & Experimental Section**

## II. 1. Synthesis of porous hollow PtM nanoparticles supported on carbon

### II. 1. 1. Technical aspects

In this work, porous hollow Pt-based NPs supported on carbon were synthesized by a one-pot process first introduced by Bae *et al.*<sup>231</sup>. In contrast to syntheses involving numerous steps and addition of surfactants (*e.g.* synthesis of hollow NPs in presence of citrate<sup>225,245,246</sup> or electrochemical formation of hollow NPs<sup>85,223</sup>), the synthesis of the porous hollow PtM NPs only consists of:

- (i) the dissolution of the metal precursors in the solvent (water) in the presence of a carbon support (see **Section II. 3.** for the nature of the carbon supports). The platinum precursor is  $\text{Pt}(\text{NH}_3)_4\text{Cl}_2 \cdot \text{H}_2\text{O}$  (Alfa Aesar Premion 99.995 % metal basis) while the sacrificial metal precursors are  $\text{MCl}_2$ , *i.e.* Ni(II) Chloride, Alfa Aesar 99.99 %, Zn(II) Chloride hydrate, Alfa Aesar Puratronic 99.999 %, Cu(II) Chloride hexahydrate, Alfa Aesar Puratronic 99.999 %, Fe(II) Chloride anhydrous Alfa Aesar (99.5 %), Co(II) Chloride hexahydrate, Alfa Aesar Puratronic 99.998 %);
- (ii) the drop-wise addition of a sodium borohydride (Sigma Aldrich,  $\text{NaBH}_4$ , 99.99 %, 5.5 mmol,  $V = 25 \text{ mL}$ ) solution at a  $5 \text{ mL min}^{-1}$  rate.

The mechanisms driving the synthesis of the porous hollow NPs are extensively discussed in **Section III. 2.** In brief, the galvanic replacement (an electrochemical process in which a metal, often referred to as a sacrificial template, is oxidized producing the electrons that are required for the deposition of  $\text{Pt}^{\text{Z}+}$  ionic species) and the nanoscale Kirkendall effect are playing a key role in the formation of porous hollow PtM/C NPs. The synthesis of porous hollow PtNi/C NPs was performed on different carbon supports (see **Section IV. 5.**), at different temperatures (see **Section IV. 3.**), with different sacrificial cores (see **Section IV. 4.**) and different molar ratios between the Pt precursor and the sacrificial Ni precursor (see **Section I. 6. 4.** and Ref.<sup>84</sup>).

A determined amount of  $\text{Pt}(\text{NH}_3)_4\text{Cl}_2 \cdot \text{H}_2\text{O}$  ( $n_{\text{Pt(II)}} = 0.440 \text{ mmol}$  for a 1:3 ratio between the Pt precursor and the M precursor, aiming for a theoretical weight fraction in Pt of 23 wt. %) and of  $\text{MCl}_2$  precursor ( $n_{\text{M(II)}} = 1.320 \text{ mmol}$ , M being a 3d transition metal, *i.e.* Ni, Co, Cu, Zn or Fe) are first dissolved in 140 mL of MilliQ water (Millipore,  $\rho = 18.2 \text{ M}\Omega \text{ cm}$ ) and 10 mL of ethanol (Absolute Ethanol VWR chemicals 99.92 %, except in **Chapter III**) in presence of 0.3 g of high surface area carbon. An aqueous solution of  $\text{NaBH}_4$  (Aldrich 99.99 %, 208 mg dissolved in 25 mL for a 1:3 ratio) is added at a  $5 \text{ mL min}^{-1}$  rate while the solution is magnetically stirred. No temperature management was used for the synthesis at room temperature, while the

syntheses at controlled temperature ( $T = 278, 293, 313, 333$  and  $353$  K) were performed in a double envelope beaker with water at the adequate temperature circulating between the two envelopes. After  $t = 1$  h, the solution was filtered, the powder thoroughly washed with Milli-Q water and dried for  $t = 45$  min at  $T = 383$  K. The resulting electrocatalyst was then acid leached under magnetic stirring in a  $1$  M  $\text{H}_2\text{SO}_4$  solution at room temperature for  $t = 22$  h, and filtered, washed and dried for  $t = 45$  min at  $T = 383$  K.

### II. 1. 2. *In operando* synthesis

The mechanism of formation and growth of porous hollow PtNi/C NPs was investigated *in operando* in **Section III. 2**. For the Wide-Angle X-ray Scattering (WAXS) and Small-Angle X-ray Scattering (SAXS) measurements, the synthesis was performed in a poly (methyl methacrylate) cuvette of  $4.5$  cm  $\times$   $1.25$  cm  $\times$   $1.25$  cm (Plastibrand), placed perpendicularly to the X-ray beam, and used as reactor. The amount of metal precursors and the solution volume were adapted to the reduced volume of the reactor. For Transmission Electron Microscopy (TEM) images and electrochemical measurements of/on the intermediates structures formed after  $t = 1, 2, 3, 4, 5, 7, 10, 20, 40$  and  $60$  min, a volume of the synthesis solution was pipetted ( $10$   $\mu\text{L}$  for the TEM analysis,  $10$  mL for the electrochemical measurements) and (i) for the TEM analysis, deposited on a gold TEM grid and dried with a heat gun, (ii) for the electrochemical measurements, immediately dried a  $T = 383$  K during  $t = 45$  min.

### II. 1. 3. Reference electrocatalysts

A  $20$  wt. % Pt/Vulcan XC72 catalyst purchased from E-TEK was used as reference material without any treatment. The number averaged Pt NP size was  $2.9 \pm 0.6$  nm. A solid PtNi/C catalyst was prepared by a modified polyol method by Ms. Sc. Raphaël Chattot. Calculated amounts of  $\text{H}_2\text{PtCl}_6 \cdot 6\text{H}_2\text{O}$  (Alfa Aesar, 99.9%) and  $\text{NiCl}_2$  (Alfa Aesar Puratonic, 99.9995%) were first dissolved in a  $20$  mL vial of deionised water ( $\text{H}_2\text{O}$ ) and ethylene glycol (EG) (EG: $\text{H}_2\text{O} = 1:1$  volume ratio). Meanwhile, the appropriate amount of Vulcan XC72 was dispersed by sonication in a separate  $20$  mL vial of EG: $\text{H}_2\text{O}$  (1:1). The contents of each vial were then mixed with  $20$  mL of pure EG. The pH of the obtained mixture was adjusted to  $10$  by using a  $0.5$  M NaOH solution (diluted in EG: $\text{H}_2\text{O}$  1:1). The suspension was continuously stirred while heating to reflux at  $T = 433$  K for  $t = 3$  h under argon and then cooled to room temperature under air over  $t = 12$  h. The pH was then adjusted to  $3$  with a  $0.5$  M aqueous solution of  $\text{H}_2\text{SO}_4$ . After  $t = 24$  h, the suspension was filtered and the solid phase washed with MQ-grade water before being dried at  $T = 383$  K for  $t = 1$  h. More information on the synthesis of the reference

PtNi/C sample can be found in Ref. <sup>247</sup> under the name ‘A-PtNi/C’. The PtNi/C ‘sea-sponges’ discussed in **Section IV. 2.** were synthesized by Ms. Sc. Raphaël Chattot following the protocol described in Ref. <sup>247</sup>.

### **II. 2. Synthesis of the carbon supports**

Porous hollow PtNi NPs were synthesized on seven different carbon supports (see **Section IV. 5.**) mostly differing by their extent of graphitization: carbon blacks, multi-walled carbon nanotubes, graphene nanosheets and carbon xerogels. The carbon blacks, *i.e.* Vulcan XC72 (XC72 – Cabot), YS (YS – Société du Noir d’Acétylène de l’Aubette) and Ketjenblack EC-600JD (KJB – Akzo Nobel) were used as purchased.

#### **II. 2. 1. Synthesis of the carbon xerogel**

The synthesis of the carbon xerogel (CX) was performed by Dr. Vaios Stergiopoulos from the University of Liège (Belgium), according to the procedure described in Ref. <sup>186</sup>. Na<sub>2</sub>CO<sub>3</sub> (SC), Resorcinol (R) and Formaldehyde (F) were first mixed with Milli-Q water ( $\rho = 18.2 \text{ M}\Omega \text{ cm}$ ). The molar ratios were  $R/F = 0.5$ ,  $R/SC = 1500$  and  $\text{water} / \text{reactants} = 5.7$ . The formation of the xerogel took place in an oven at  $T = 358 \text{ K}$  for  $t = 72 \text{ h}$ , followed by two drying steps under vacuum: (i) at  $T = 333 \text{ K}$  for  $t = 24 \text{ h}$ , and (ii) at  $T = 423 \text{ K}$  for another  $t = 24 \text{ h}$ . The dried xerogel was grinded in a planetary mill for  $t = 30 \text{ min}$  at  $\omega = 400 \text{ rpm}$ , using agate balls of  $d = 10 \text{ mm}$ . The powder was then pyrolysed at  $T = 1073 \text{ K}$  under N<sub>2</sub> atmosphere, for  $t = 2 \text{ h}$ .

#### **II. 2. 2. Synthesis of three-dimensional (3D) graphene nanosheets**

The 3D graphene nanosheets (GNS) were synthesized by Dr. Alexey Serov from the University of New Mexico (United States of America) using a modified Sacrificial Support Method (SSM) <sup>248–252</sup>. The SSM is a templating strategy, where the precursors are mixed with (or deposited on) silica and then pyrolysed, before chemical etching of silica. A Graphene Oxide (GO) was synthesized by a modified Hummers method <sup>253</sup>. The synthesized GO was exfoliated in distilled water ( $\rho = 15 \text{ M}\Omega \text{ cm}$ ) by a high power ultrasonic probe (700 kJ was delivered to 12.5 g of GO dispersed in 1 L of De-Ionized (DI) water for  $t = 3 \text{ h}$ ) followed by the addition of 25 g of silica sacrificial support (Cab-O-Sil ® EH-5, surface area  $\sim 400 \text{ m}^2 \text{ g}^{-1}$ ). The colloidal mixture of GO-SiO<sub>2</sub> was ultrasonicated with the probe for  $t = 1 \text{ h}$  ( $\sim 300 \text{ kJ}$ ) and dried overnight at  $T = 358 \text{ K}$ . The dry powder was ball-milled at  $\omega = 375 \text{ rpm}$  for  $t = 25 \text{ min}$  and subjected to reduction in 7 at. % H<sub>2</sub> (flow rate =  $100 \text{ cm}^3 \text{ min}^{-1}$ ) at  $T = 1073 \text{ K}$  for  $t = 1 \text{ h}$ . After reduction, the GNS-SiO<sub>2</sub>

was additionally ball-milled at  $\omega = 375$  rpm for  $t = 25$  min. The silica support was leached in 40 wt. % HF for  $t = 24$  h, followed by continuous filtration until a neutral pH was reached. The resulting GNS was dried overnight at  $T = 358$  K. To obtain an oxidized surface of GNS, 5 g were soaked in 8 M HNO<sub>3</sub> for  $t = 8$  h at room temperature. The wet powder was filtrated with DI water until the pH reached  $\sim 6.5$ . The powder was dried at  $T = 358$  K for  $t = 8$  h, resulting in the carbon support discussed as GNS – AL.

### II. 2. 3. Synthesis of the carbon nanotubes

The carbon nanotubes (CNTs) were synthesized by Dr. Alexey Serov from the University of New Mexico (United States of America), using the SSM<sup>183</sup> and the thermal decomposition of C<sub>2</sub>H<sub>4</sub> on iron NPs (seeds). Fe(NO<sub>3</sub>)<sub>3</sub>·9H<sub>2</sub>O was mixed with a water colloidal suspension of a silica sacrificial support (Cab-O-Sil ® EH-5), dried and ball milled for  $t = 4$  h at  $\omega = 350$  rpm and placed in a furnace. The amount of iron nitrate was calculated to have  $\sim 20$  wt. % of reduced iron seeds on the silica support. The powder sample was further subjected to reduction at  $T = 773$  K in a H<sub>2</sub> atmosphere for  $t = 30$  min, leading to the CNTs growth at  $T = 1043$  K in a C<sub>2</sub>H<sub>4</sub> atmosphere for  $t = 60$  min. The material was removed from the furnace, leached with 40 wt. % HF and washed with DI water to reach a neutral pH. Concentrated nitric acid was introduced, resulting in CNTs with high degree of ordering and increased concentration of carbon surface oxides.

## II. 3. Electrochemical methods

### II. 3. 1. Preparation of the electrochemical cell

Shinozaki *et al.*<sup>254</sup> have recently underlined the importance of the electrochemical half-cell preparation to obtain optimal performances for the ORR and state-of-the-art base voltammograms. The authors reported that the SA for the ORR measured at  $E = 0.9$  V vs. RHE is increased by *ca.* 3 on polycrystalline Pt (Pt(pc)) if the electrochemical cell was vigorously rinsed with MQ-grade water + boiled at least one time compared to a superficial cleaning. In this work, all the glassware used for the electrochemical experiments was cleaned by (i) soaking overnight in H<sub>2</sub>SO<sub>4</sub>/H<sub>2</sub>O<sub>2</sub> mixture, (ii) thorough washing with Milli-Q water, (iii) boiling in Milli-Q water at least once and (iv) washing with fresh electrolyte prior to any electrochemical experiment. A perchloric acid solution (0.1 M HClO<sub>4</sub>) was chosen as electrolyte instead of a sulfuric acid solution to minimize strong adsorption of (bi)sulfate anions contained in sulfuric acid<sup>255,256</sup>. Indeed, these ions ‘poison’ the Pt catalytic sites and diminish the activity for the ORR. A special

attention was given to the quality of the electrolyte, as a low-quality electrolyte results in depreciated SA values for the ORR <sup>254</sup>. Thus, all the electrolyte solutions were prepared using a 96 wt. % HClO<sub>4</sub> (70 % Merck, Suprapur). For the experiment in alkaline electrolyte described in **Section III. 2. 5**, *i.e.* in 0.1 M NaOH, the electrolyte was prepared from NaOH powder, 99.99 % Merck, Suprapur and Milli-Q water (Millipore, 18.2 MΩ cm). The electrolyte solution was stored at  $T = 278$  K. The electrochemical measurements were performed with an Autolab PGSTAT302N potentiostat controlled by the Nova<sup>®</sup> software. The temperature of the electrochemical cell was thermostatically controlled at  $T = 298 \pm 1$  K. A four-electrode electrochemical cell containing *ca.* 20 mL of electrolytic solution was used. It was composed of the following electrodes:

- (i) the reference electrode was a commercial RHE (Hydroflex, Gaskatel GmbH), except for the measurements in alkaline media described in **Section III. 2. 5**, where the reference electrode was a mercury – mercury oxide (Hg/HgO) reference;
- (ii) the counter electrode (CE) was a glassy carbon plate connected to the potentiostat by a gold wire. This forbids any release of Pt<sup>z+</sup> ionic species, which might have been produced if a Pt CE had been used;
- (iii) the fourth electrode was a platinum wire connected to the reference electrode to filter the high-frequency noise and to avoid any low-frequency disturbance of the electrochemical measurements <sup>257</sup>;
- (iv) the working electrode (WE) was a rotating disk electrode composed of a glassy carbon disk (0.196 cm<sup>2</sup>, Sigradur) on which a fixed volume of the electrocatalyst suspension was drop casted.

### II. 3. 2. Preparation of the electrocatalyst suspensions

The electrocatalyst suspensions were composed of (i) 10 mg of the electrocatalyst powder (for a Pt weight fraction of 20 wt. %), (ii) 54 μL of a Nafion<sup>®</sup> 5 wt. % solution (Sigma-Aldrich), *i.e.* 2.36 mg, therefore achieving an ionomer / carbon mass ratio of 0.3, (iii) 3600 μL of Milli-Q water and (iv) 1446 μL of isopropyl alcohol (99.5% Acros Organics). The electrocatalyst inks were first homogenised for  $t = 20$  s using an ultrasonic probe and then placed  $t = 15$  min in an ultrasonic bath. The catalytic inks were not used more than 2 weeks after their preparation, thus ensuring reproducible electrocatalytic measurements as described in Ref. <sup>258</sup>. The uniformity and the homogeneity of the catalytic layer are pivotal for reproducible electrocatalytic measurements <sup>259,260</sup>. Therefore, 10 μL of the electrocatalyst suspension were deposited (targeting a loading of 20 μg of Pt per geometrical cm<sup>2</sup>) on the working electrode while rotating at  $\omega = 500$

rpm and drying under a heat flux. Prior to any electrochemical measurement, the fresh working electrode was immersed in the deaerated electrolyte at  $E = 0.1 \text{ V vs. RHE}$ .

The electrochemical experiments were then performed in the following order:

- (i) 50 cyclic voltammograms (CVs) between 0.05 and 1.23 V vs. RHE at a scan rate  $\nu = 0.500 \text{ V s}^{-1}$ ;
- (ii) 3 CVs between 0.05 and 1.23 V vs. RHE at  $\nu = 0.020 \text{ V s}^{-1}$ ;
- (iii) the  $\text{CO}_{\text{ads}}$  stripping in which the CO was bubbled in the electrolytic solution for  $t = 6 \text{ min}$  followed by a purge of the solution by Ar during  $t = 29 \text{ min}$  at  $E = 0.1 \text{ V vs. RHE}$  and the recording of 3 CVs at  $\nu = 0.02 \text{ V s}^{-1}$  between 0.05 and 1.23 V vs. RHE;
- (iv) 6 linear sweep voltammograms (LSVs) from 0.20 to 1.05 V vs. RHE in  $\text{O}_2$ -saturated electrolytic solution at  $\nu = 0.005 \text{ V s}^{-1}$  and at different revolution rates ( $\omega = 400, 900, 1600$  and  $2500$  rotation per minutes – rpm) to determine the electrocatalytic activity of the thin-film electrodes for the ORR.

### II. 3. 3. Cyclic voltammetry in Ar-saturated electrolyte

CVs in Ar-saturated 0.1 M  $\text{HClO}_4$  were performed to achieve a better understanding of the surface reactivity of the different hollow electrocatalysts. CVs consists in sweeping the potential between two values (*i.e.*  $E_1 \rightarrow E_2 \rightarrow E_1$ ) at a determined scan rate while recording the current (i). An example of a CV on a porous hollow PtNi/C electrocatalyst with a Ni content of *ca.* 15 at. % is provided in **Figure 16**. Note that the current can be separated into two additive contributions: (i) the capacitive current resulting from the specific adsorption of  $\text{H}_{\text{ads}}$  and  $\text{OH}_{\text{ads}}$  species at the surface of the electrode (*e.g.*  $\text{H}_{\text{ads}} \rightarrow \text{H}^+ + \text{e}^-$ ) and (ii) the capacitive current resulting of the rearrangement of ions in the double layer (Helmholtz and Gouy-Chapman layers).

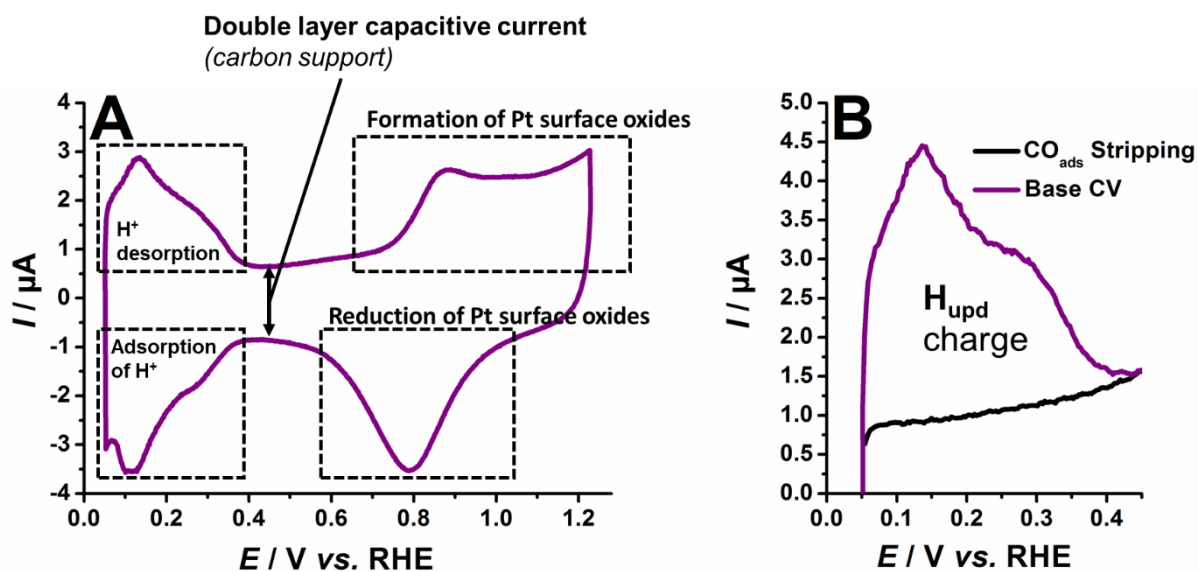


**Figure 16.** (A) Cyclic voltammogram in Ar-saturated 0.1 M HClO<sub>4</sub> of a porous hollow PtNi/C NPs ( $v = 0.02 \text{ V s}^{-1}$ ,  $T = 298 \pm 1 \text{ K}$ ) with a Ni content of *ca.* 15 at. %. (B) Zoom in the 0.05 – 0.45 V vs. RHE potential range showing a base CV and a CV taken after CO<sub>ads</sub> adsorption and purge of the electrolyte (CO stripping voltammogram).

Due to the structural and chemical sensitivity of Pt to hydrogen<sup>51,261,262</sup> and oxygen adsorption/desorption and CO electrooxidation<sup>149,263–265</sup>, CVs are a powerful tool to gain insights on the Pt:Ni atomic ratio, crystallographic orientation of the exposed facets, the degree of defectivity of the exposed PtNi/C surfaces and their ECSA. Note that, before being probed with CV, all the electrocatalysts discussed in this manuscript have been acid leached, except in **Section III. 2**. According to Durst *et al.*<sup>133</sup>, this treatment yields the formation of a Pt-skeleton structure with a 2-3 monolayer thick Pt shell covering a PtNi core; therefore, it is assumed that no Ni atoms are present on the surface of the hollow PtNi/C NPs. In the 0.05 V vs. RHE  $< E < 0.45$  V vs. RHE region, the desorption (adsorption) of H<sup>+</sup> from (on) the Pt surface is observed (see **Figure 16A**). According to the works of Yeager *et al.*<sup>266</sup>, Clavilier *et al.*<sup>267–269</sup> and Markovic *et al.*<sup>47,51,256,261,270</sup> on extended Pt surfaces. The peaks observed on the CV at 0.05 V vs. RHE  $< E < 0.45$  V vs. RHE positive scan can be ascribed to the hydrogen desorption from Pt (111) and Pt (110) (0.05 V vs. RHE  $\leq E \leq 0.25$  V vs. RHE), and Pt (111) and Pt (100) (0.25 V vs. RHE  $< E \leq 0.40$  V vs. RHE). Snyder *et al.*<sup>81</sup> and Chattot *et al.*<sup>247</sup> proposed that, on highly defective nanostructures, the 0.25 V vs. RHE  $< E \leq 0.40$  V vs. RHE shoulder results from the H<sub>ads</sub> adsorption on the structural defects at the surface of the electrocatalyst.

Assuming the charge used to adsorb/desorb a monolayer of  $H_{upd}$  is  $Q_{1,H_{upd}} = 210 \mu\text{C cm}^{-2}_{Pt}$ , the ECSA can be determined from the CVs in Ar-saturated electrolyte, by integrating the coulometry required to desorb a monolayer of  $H_{upd}$  after subtraction of the capacitive current associated with the carbon support only ( $Q_{H_{upd}}$ ). As  $H_{upd}$  adsorption is completely suppressed on a surface fully covered by  $CO_{ads}$ , the first cycle of the  $CO_{ads}$  stripping can be used to this purpose (see **Figure 16B**), and ECSA determined using **Equation 20**:

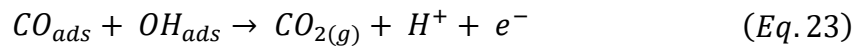
$$ECSA_H(cm^2) = \frac{Q_{H_{upd}}}{Q_{1,H_{upd}}} \quad (Eq. 20)$$

The sum of the specific and non-specific currents observed in the  $0.45 \text{ V vs. RHE} < E < 0.70 \text{ V vs. RHE}$  potential range is proportional to the specific surface area of the electrocatalyst and mostly originates from the high surface area carbon support. The faradaic current at  $E > 0.80 \text{ V vs. RHE}$  corresponds to the formation of platinum surface oxides as a result of the water dissociation<sup>212</sup>. Their reduction is observed at  $E \sim 0.80 \text{ V vs. RHE}$  (see **Figure 16A**). Note that CVs in Ar-saturated electrolyte also provide essential information during ageing protocols, *i.e.* ECSA losses (diminution of the coulometry required to adsorb/desorb  $H_{upd}$ ), possible occurrence of the COR, *etc.* An increase of the double layer capacitance ( $C_{dl}$ ) usually translates into increased specific surface area and formation of carbon surface oxides ( $C \rightarrow CO_{surf}$ ) while a diminution is representative of losses in specific surface area (severe carbon corrosion resulting in  $CO_{surf} \rightarrow CO_2$  and  $C \rightarrow CO_2$ ). In that respect, the quinone / hydroquinone (Q/HQ) redox peaks located at *ca.*  $0.6 \text{ V vs. RHE}$  (oxidation) and  $0.5 \text{ V vs. RHE}$  (reduction) are particularly instructive<sup>176</sup>.

To limit the impact of the ohmic losses (*i.e.* the potential shift due to the electrolyte resistance,  $\Delta E = IR_{el}$ , with  $\Delta E$  the potential shift and  $R_{el}$  the electrolyte resistance, detrimental at high-current values), the resistance of the electrolyte was determined by electrochemical impedance spectroscopy (EIS) and was always found to be equal to *ca.*  $20 \Omega$  in acid electrolyte and *ca.*  $25 \Omega$  in alkaline electrolyte. The potential values of the CVs in Ar-saturated electrolyte and of the  $CO_{ads}$  stripping were then automatically corrected by the potentiostat by *ca.* 85 % of the electrolyte resistance (the correction was made manually on the LSV in  $O_2$ -saturated electrolyte, after the measurement, by 100 % of the electrolyte resistance).

### II. 3. 4. CO<sub>ads</sub> stripping on the Pt-based electrocatalysts

The CO<sub>ads</sub> stripping consists in (i) the adsorption of a monolayer of CO onto the electrocatalyst surface at 0.10 V vs. RHE, (ii) the removal of all remaining CO<sub>ads</sub> from the solution and (iii) the stripping of the CO<sub>ads</sub> monolayer from the surface by electrochemical means. CO is bubbled in an Ar-saturated solution during  $t = 6$  min, followed by  $t = 29$  min of Ar bubbling at 0.10 V vs. RHE). After the purge, the solution is CO-free and the electrode is covered by a CO<sub>ads</sub> monolayer, which can further be oxidized by CVs between 0.05 and 1.23 V vs. RHE. It is well-established that the electrooxidation of a CO<sub>ads</sub> monolayer adsorbed on Pt (also known as CO<sub>ads</sub> stripping voltammograms) provides important information on the contraction of the lattice parameter<sup>271</sup>, the defectivity<sup>232,234,247</sup>, the crystallite size and agglomeration degree<sup>149,264</sup> of Pt-based/C NPs. The CO<sub>ads</sub> monolayer has been studied on monocrystalline stepped Pt surfaces<sup>144,146,147,272,273</sup>. The CO<sub>ads</sub> electrooxidation proceeds along a Langmuir-Hinshelwood mechanism. Water molecules are dissociated into OH<sub>ads</sub> species (**Equation 20**) and CO molecules are adsorbed (**Equation 21**), before recombination with the OH<sub>ads</sub> species.



The reaction onset is related to the dissociation of water molecules into OH<sub>ads</sub> species from water (**Equation 20**). There are numerous evidences in the literature that this reaction is more facile at surface defects. According to Lebedeva *et al.*<sup>144</sup>, an increase in the density of steps on Pt (111) surfaces yields a negative shift of both the onset and the peak potential of CO<sub>ads</sub> stripping voltammograms in acidic electrolyte. This is explained by fast surface diffusion of CO<sub>ads</sub> molecules adsorbed on the terraces to the bottom of steps where they are oxidized. The CO<sub>ads</sub> electrooxidation mechanism on Pt surfaces introduced by Koper *et al.*<sup>274</sup> and Lebedeva *et al.*<sup>144,146,147</sup> was extrapolated to real-life PEMFC electrocatalysts, such as isolated or agglomerated Pt/C NPs by Maillard *et al.*<sup>149,264,265,275,276</sup>. It was shown that grain boundaries present on such nanostructures enable the CO<sub>ads</sub> electrooxidation to occur at lower potentials, therefore playing a similar role than the steps on monocrystalline Pt surfaces. On highly defective Pt/C electrocatalysts, the CO<sub>ads</sub> stripping voltammograms either feature a ‘low-potential’ peak at  $E \sim 0.70$  V vs. RHE or two electrooxidation peaks, *i.e.* the ‘low-potential’ peak and a ‘high-potential’

peak at  $E \sim 0.78$  V vs. RHE (see **Figure 17**). The nature of the two peaks is discussed in **Section IV. 2.** for porous hollow PtNi/C NPs.

As it will be shown in this thesis, several characteristics of  $\text{CO}_{\text{ads}}$  stripping voltammograms provide structural and chemical insights on the different electrocatalysts:

- (i) the position of the high-potential peak of the  $\text{CO}_{\text{ads}}$  stripping ( $E_{\text{p,CO}}$ ) depends on contraction of the lattice parameter induced by the transition metal (**Figure 17A**). A diminution of  $E_{\text{p,CO}}$  indicates an increased contraction of the lattice parameter;
- (ii) the presence of a low-potential  $\text{CO}_{\text{ads}}$  stripping peak indicates that the electrocatalysts contains structural defects. Hence, the ratio of the electrical charge under the ‘low-potential’ peak to the total electrical charge of the  $\text{CO}_{\text{ads}}$  stripping,  $Q_{\text{pp,CO}} / Q_{\text{T,CO}}$  (**Figure 17A**) provides semi-quantitative information on the density of structural defects contained in the different electrocatalysts<sup>232</sup>.
- (iii) the first moment of the potential weight of the  $\text{CO}_{\text{ads}}$  stripping,  $\mu_1^{\text{CO}}$ , first introduced by Chattot *et al.*<sup>247</sup>, combines the effect of the contraction of the lattice parameter and of the density of the structural defects. A diminution of  $\mu_1^{\text{CO}}$  indicates an increase of the contraction of the lattice parameter and/or an increase in the surface density of structural defects (**Figure 17A**).  $\mu_1^{\text{CO}}$  is described by **Equation 24**;

$$\mu_1^{\text{CO}} = \int_{0.55}^1 \frac{E \times I}{\int_{0.55}^1 I \times dE} \times dE = \int_{0.55}^1 \frac{E \times I}{Q_{\text{T,CO}}} \times dE \quad (\text{Eq. 24})$$

- (iv) the ECSA can be determined considering that the charge required for the electrooxidation of a monolayer of  $\text{CO}_{\text{ads}}$  is  $Q_{1,\text{CO}} = 420 \mu\text{C cm}^{-2}_{\text{Pt}}$  (**Equation 25**).

$$\text{ECSA}_{\text{CO}} (\text{cm}^2) = \frac{Q_{\text{T,CO}}}{Q_{1,\text{CO}}} \quad (\text{Eq. 25})$$

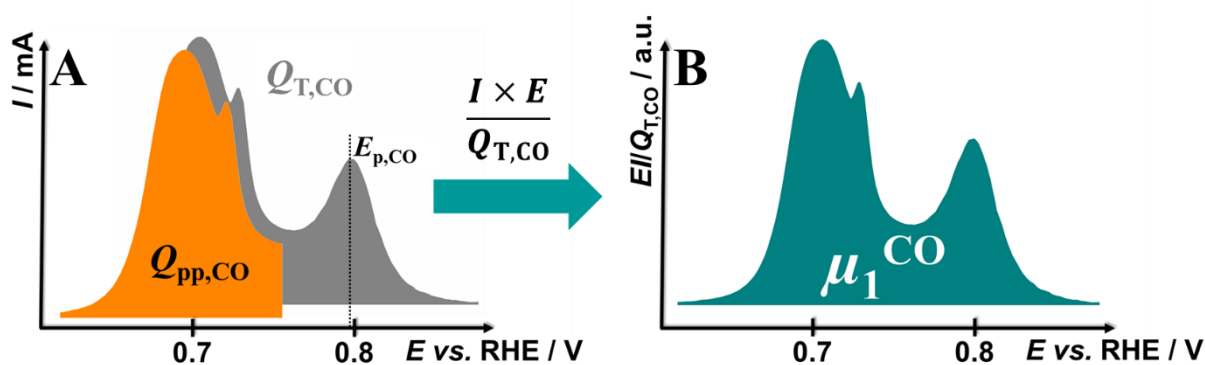


**Figure 17.** Parameters extracted from  $\text{CO}_{\text{ads}}$  stripping measurements describing the physico-chemical properties of a nanostructured, low Ni atomic content porous hollow PtNi/C electrocatalyst: **(A)** the electrical charge under the  $\text{CO}_{\text{ads}}$  stripping pre-peak ( $Q_{\text{pp,CO}}$ ), the total electrical charge of the  $\text{CO}_{\text{ads}}$  stripping ( $Q_{\text{T,CO}}$ ) and the position of the ‘high-potential’ peak ( $E_{\text{p,CO}}$ ); **(B)** the first moment of the potential weight of the  $\text{CO}_{\text{ads}}$  stripping voltammogram determined as the integral of  $E \times I/Q_{\text{T,CO}}$  ( $\mu_1^{\text{CO}}$ ).

These parameters will be used in **Chapter V** to gain insights into the degradation mechanism of hollow Pt-based nanostructures.

### II. 3. 5. Oxygen reduction reaction on Pt-based electrocatalysts

The electrocatalytic activity for the ORR of the different electrocatalysts discussed in this manuscript has been investigated by rotating disk electrode (RDE) measurements at a sweep rate of  $\nu = 0.005 \text{ V s}^{-1}$ . This low sweep rate allows minimizing capacitive currents associated with the various carbon supports and better simulates steady-state PEMFC conditions. Note however that low  $\nu$  values yields depreciated specific activities for the ORR by a factor *ca.* 1.5 compared to  $\nu = 20 \text{ mVs}^{-1}$ <sup>277</sup>. This reflects the time-dependency of the surface oxides coverage: high sweep rate promotes low coverage with surface oxides and thus increased number of catalytic sites that may adsorb and dissociate oxygen molecules. In this study, the activity for the ORR has been determined on the positive-going potential scan between 0.20 and 1.05 V vs. RHE, *i.e.* on an oxide-free Pt surface. Since Pt surface oxides form at  $E > 0.80 \text{ V vs. RHE}$ , ORR measurements on the negative-going potential scan would have resulted in a much lower SA value (the Pt surface would have been highly oxidized)<sup>254</sup>. The electrochemical activity of the different electrocatalysts was determined at  $E = 0.90 \text{ V vs. RHE}$  and at  $E = 0.95 \text{ V vs. RHE}$ , after correction of the Ohmic drop in the electrolyte (determined by Electrochemical Impedance Spectroscopy – EIS) and of the oxygen diffusion in solution by the Koutecky-Levich equation (**Equation 26**).

$$I_k = \frac{I \times I_{lim}}{I_{lim} - I} \quad (Eq. 26)$$

Where  $I$  is the measured current,  $I_k$  is the kinetic current and  $I_{lim}$  is the diffusion-limited current. The kinetic current at  $E = 0.95$  V vs. RHE is comprised between  $0.1 \times I_{lim} < I_k < 0.5 \times I_{lim}$ , *i.e.* the oxygen diffusion in solution is efficiently corrected<sup>278,279</sup>. The kinetic current at  $E = 0.90$  V vs. RHE is noticeably higher than  $0.5 \times I_{lim}$  (see **Figure 18**) for the porous hollow PtNi/C NPs, therefore resulting in non-negligible impact of the oxygen diffusion in solution and in the catalytic layer<sup>278,279</sup>. The SA and the MA values were determined by dividing the kinetic current by the ECSA and the mass of platinum deposited on the electrode (*ca.* 3.92  $\mu\text{g}$ ), respectively. An example of a linear sweep voltammetry (LSV) in  $\text{O}_2$ -saturated electrolyte on a porous hollow PtNi/C electrocatalyst, with and without the correction of the Ohmic drop and the diffusion in solution is provided in **Figure 18**.

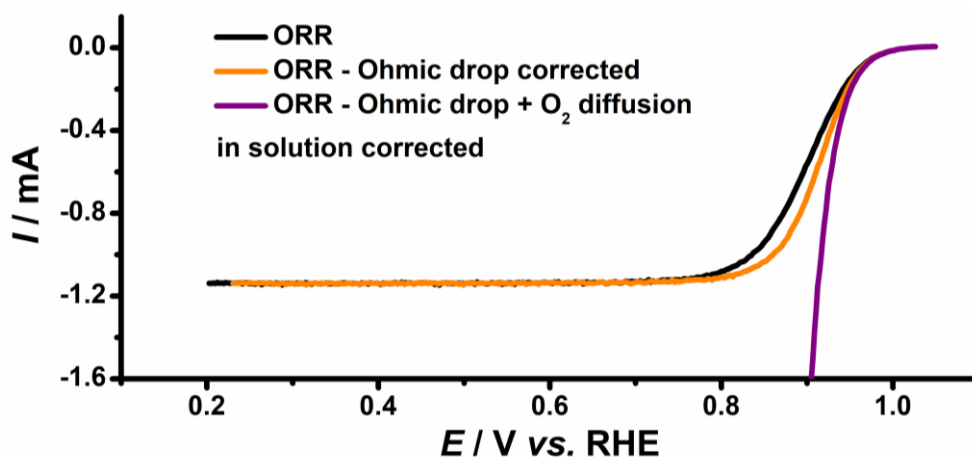


**Figure 18.** Linear sweep voltammogram recorded in  $\text{O}_2$ -saturated 0.1 M  $\text{HClO}_4$  on hollow PtNi/C NPs with and without the correction of the Ohmic drop and of the oxygen diffusion in solution ( $\nu = 0.005$  V  $\text{s}^{-1}$ ,  $T = 298 \pm 1$  K,  $\omega = 1600$  rpm).

### II. 3. 6. Accelerated stress tests

To assess the stability of the porous hollow PtNi/C NPs and of their carbon support, ASTs extrapolated from the FCCJ recommendations<sup>208</sup> were performed (see **Figure 19**). Two protocols were defined and used:

- (i) a start-stop protocol, *i.e.* a square potential ramp between 1.0 and 1.5 V vs. RHE with  $t = 3$  s at each potential, to mimic the start-up and the shutdown of a PEMFC (**Section V. 4.**);

- (ii) A load-cycling protocol, *i.e.* triangular potential ramp between 0.6 and 1.0 (or 1.1) V vs. RHE, with a scan rate of  $0.050 \text{ V s}^{-1}$ , to mimic the potential experienced by the PEMFC during its operation (**Section V. 2.** and **V. 3.**).

All the AST were performed at  $T = 353 \text{ K}$ . Dubau and Maillard<sup>280</sup> showed that the AST temperature plays a predominant role onto the degradation of the electrocatalysts and, on commercial Pt/C, that an AST at  $T = 353 \text{ K}$  (in  $0.1 \text{ M H}_2\text{SO}_4$ ) adequately reproduces the structural changes observed in PEMFCs. The electrochemical cell was also thoroughly washed before the intermediate and final characterization and the aged electrolyte (contaminated by dissolved  $\text{Pt}^{\text{Z+}}$  and  $\text{Ni}^{\text{Z+}}$  species<sup>280</sup>) was replaced by fresh electrolyte.

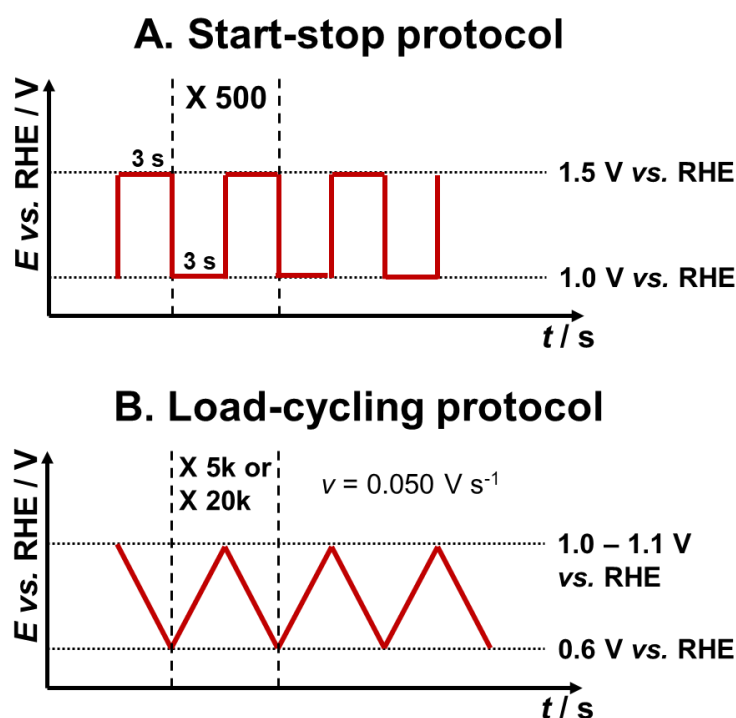


**Figure 19.** Protocols used for the ASTs discussed in this manuscript: **(A)** Start-stop protocol, **(B)** Load-cycling protocol. The ASTs temperature was  $T = 353 \text{ K}$ .

### II. 3. 7. *In operando* ageing of porous hollow PtNi/C

*In operando* WAXS measurements were performed at the ID31 beamline of the European Synchrotron Radiation Facility (ESRF) in Grenoble, France, to investigate the degradation mechanisms of porous hollow PtNi/C NPs. A home-made cell (see **Figure 20**), made of Kel-F (homopolymer of chlorotrifluoroethylene), was used to characterize a gas-diffusion electrode (GDE), *i.e.* a commercial GDL (Sigracet 25BC, SGL Carbon) coated with a suspension of po-

rous hollow PtNi/C ink, and hot-pressed on a Nafion<sup>®</sup> membrane (N115, Ionpower). The theoretical Pt loading was  $250 \mu\text{g}_{\text{Pt}} \text{cm}^{-2}_{\text{geo}}$ . The cell was designed to minimize the thickness of the electrolyte layer on the beam path. The GDE was connected to the potentiostat by a circular gold current collector (WE). The counter electrode was a circular Pt wire (CE) and the reference was a commercial RHE (Hydroflex, Gaskatel GmbH) connected to a Pt wire (used to avoid any low-frequency disturbance of the electrochemical measurements). The current collector and the CE were maintained out of the beam trajectory. For more information on the cell geometry and composition, please refer to **Figure 20**. The electrocatalysts were aged by a load-cycle protocol (see **Figure 19A**) during 5,000 cycles between 0.6 and 1.0 V vs. RHE or 1.1 V vs. RHE at  $v = 0.050 \text{ V s}^{-1}$  after 5 cycles at  $v = 0.020 \text{ V s}^{-1}$  between 0.10 V and 1.23 V vs. RHE at a targeted temperature  $T_{\text{theo}} = 353 \text{ K}$  (a loss of *ca.* 10 – 20 K was assumed during the circulation of the electrolyte from the thermostatic bath to the electrochemical cell).

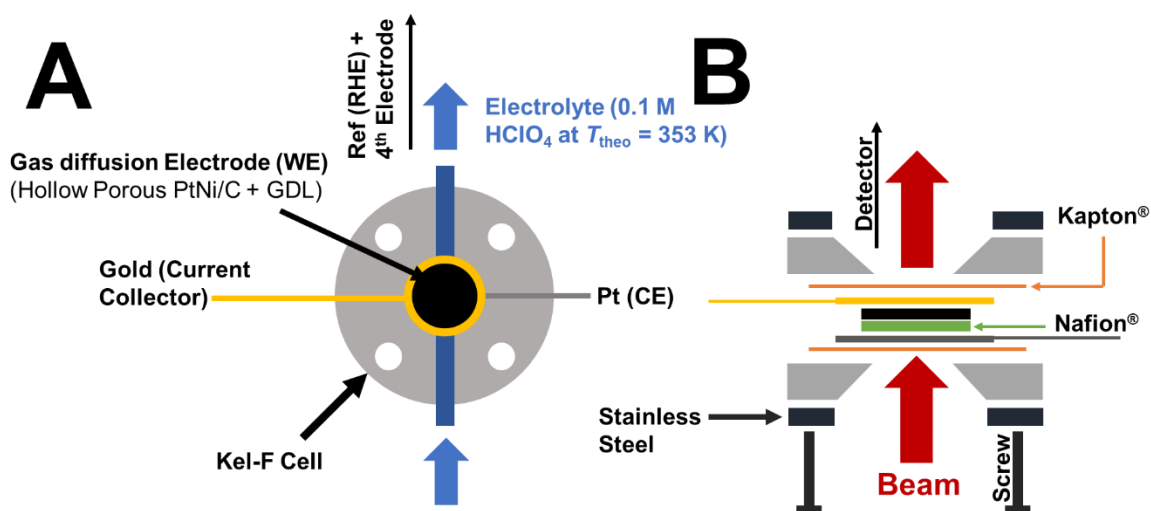


**Figure 20.** Scheme of the electrochemical cell used to investigate the degradation mechanisms of porous hollow PtNi/C NPs by *in operando* WAXS and SAXS measurements: (A) front and (B) side views.

## II. 4. Measurement of the specific surface area of the supports

The specific surface area of the carbon supports was determined by N<sub>2</sub> adsorption using the BET equation<sup>281</sup>. The measurements were performed by Mr. Vincent Martin (LEPMI, St Martin d'Hères, France) at  $T = 77 \text{ K}$  using a Micromeritics ASAP2020 apparatus. The cell was emptied (at a rate of  $6.7 \text{ kPa s}^{-1}$ ) before the N<sub>2</sub> adsorption until reaching a pressure ( $P$ ) of 66.7 Pa while increasing the temperature to  $T = 363 \text{ K}$ , at a speed of  $10 \text{ K min}^{-1}$ . The temperature was then increased at  $T = 623 \text{ K}$  at a  $10 \text{ K min}^{-1}$  rate and maintained at  $T = 623 \text{ K}$  during  $t = 4 \text{ h}$  to desorb any specie previously adsorbed on the surface before bringing the cell to  $T = 77 \text{ K}$

by immersion in liquid N<sub>2</sub>. The adsorption isotherm is then measured by injecting controlled volume of gaseous N<sub>2</sub> into the cell. When  $P = P_0$  ( $P_0$  being the atmospheric pressure), N<sub>2</sub> is desorbed by emptying the cell until  $P = 66.7$  Pa. The total specific surface area was calculated in the relative pressure domain  $0.06 < P/P_0 < 0.2$  using the BET equation. The microporous specific surface area was determined using the  $t$ -plot method<sup>282,283</sup>.

### II. 5. Atomic Absorption Spectroscopy

The M (Ni, Cu, Co, Fe and Zn) and Pt content of each electrocatalyst was established by Atomic Absorption Spectroscopy (AAS – PinAACle 900F, PerkinElmer). The electrocatalyst ( $5 \pm 1$  mg) was first digested in aqua regia (HCl:HNO<sub>3</sub> 3:1 volumic ratio) made from high-purity acids (37 vol. % ACS Reagent Sigma Aldrich and 65 vol. % Sigma-Aldrich) for  $t = 72$  h at  $T = 298 \pm 1$  K. The solution was then diluted sevenfold to reach the AAS range for Pt and Ni, Cu, Co, Fe and Zn. The metals contents were then determined using three series of three measurements. The wavelengths considered for Pt, Ni, Cu, Co, Fe and Zn were  $\lambda = 266.0$  nm,  $\lambda = 232.0$  nm,  $\lambda = 327.4$  nm,  $\lambda = 240.7$  nm,  $\lambda = 327.4$  nm,  $\lambda = 248.3$  nm and  $\lambda = 213.9$  nm, respectively.

### II. 6. Electron Microscopy

#### II. 6. 1. Transmission electron microscopy

The TEM is a microscopy technique based on the wave-like properties of the electrons. The wavelength of an electron beam accelerated close to the light speed is extremely small, *ca.*  $\lambda = 2.5$  pm at 200 kV, allowing a point-to-point resolution of *ca.* 0.2 nm. The electrons are generated from a LaB<sub>6</sub> single crystal or a tungsten filament, accelerated by a potential field and focused by electrostatic and electromagnetic lenses before reaching the sample. As the electrons considered must be transmitted through the sample, the latter is usually thinner than 100 nm. Variations in thickness and electronic density of the sample regions result in clearer and darker areas on the TEM micrographs in bright field imaging mode, thus creating a contrast between the NPs (high  $Z$  value,  $Z$  being the proton number) and their support (low  $Z$  value).

Since the porous hollow PtM/C NPs display an irregular shape, the Feret diameter was estimated for each NP, *i.e.*  $0.5 \times (d_{\max} + d_{\min})$ , from the TEM micrographs, to determine the number-averaged NPs diameter ( $\bar{d}_N$  – **Equation 26**). 200 NPs were measured to build a particle size distribution (PSD). For comparison purposes, the surface-averaged diameter ( $\bar{d}_S$  – **Equation 27**) and the volume-averaged diameter ( $\bar{d}_V$  – **Equation 28**) were also determined:

$$\bar{d}_N = \frac{\sum_{i=1}^n n_i d_i}{\sum_{i=1}^n n_i} \quad (\text{Eq. 26})$$

$$\bar{d}_S = \frac{\sum_{i=1}^n n_i d_i^3}{\sum_{i=1}^n n_i d_i^2} \quad (\text{Eq. 27})$$

$$\bar{d}_V = \frac{\sum_{i=1}^n n_i d_i^4}{\sum_{i=1}^n n_i d_i^3} \quad (\text{Eq. 28})$$

where  $n_i$  is the number of NPs of diameter  $d_i$ . The bright field imaging was used with a JEOL 2010 TEM operating at 200 kV with a point-to-point resolution of 0.19 nm. The PSD of the hollow Pt-based/C electrocatalysts was built from the TEM micrographs obtained at low/medium magnification ( $\times 80,000 / \times 150,000$ ). To obtain an accurate imaging of the atomic structure (*e.g.* deformations in the lattice parameter or presence of structural defects such as grain boundaries or few nanometers porosities) of the porous hollow PtNi/C NPs, high-resolution TEM (HR-TEM) micrographs were acquired by Dr. Jaysen Nelayah (University Paris Diderot, Paris, France) using a JEM-ARM 200F (JEOL) microscope equipped with a cold-field emission gun and an image aberration corrector (the operating voltage was 200 kV). The analysed electrocatalysts were deposited onto carbon-coated lacey copper or gold grids (Agar).

A scanning transmission electron microscope (STEM, *i.e.* the electron beam is focused on a fine spot and scans over the selected area) was used to analyse the chemical composition of single NPs before and after AST (see **Section V. 2.**) in energy dispersive X-ray (EDX) mode. The EDX mapping was obtained using a JEOL 2100F microscope operated at 200 kV and equipped with a retractable large angle silicon drift detector (Centurio). EDX is an analytic technique where the energy of the X-rays emitted by the sample upon interaction with the electron beam is analysed: it allows the determination of the nature and the chemical composition of the samples. The quantitative analyses were performed on Pt L line and Ni, Co and Cu K lines using the K factor provided by the JEOL software.

### II. 6. 2. Identical Localisation TEM

This technique, first introduced by Mayrhofer *et al.*<sup>284</sup>, was used to gain insights into the morphological and structural changes of the porous hollow PtNi/C NPs and of their carbon supports during a ‘start-stop’ protocol<sup>203,285,286</sup> (see **Figure 19** and **Section V. 4.**). In practice, 10  $\mu\text{L}$  of a 10-time diluted catalytic ink (1 mg of electrocatalysts in 5.4  $\mu\text{L}$  of Nafion 5 wt. % + 1446  $\mu\text{L}$  of IPA + 3600  $\mu\text{L}$  of H<sub>2</sub>O MilliQ) were deposited on a gold TEM grid. Different zones of a

carbon-coated lacey Au TEM grid were located and imaged (in this study, eighteen in six different areas) at different magnifications prior to the AST. The grid was then used as a working electrode in a conventional electrochemical cell and the exact same zones were imaged after the ‘start-stop’ procedure.

### II. 6. 3. Scanning Electron Microscopy

Micrographs of the different carbon supports discussed in this manuscript (see **Figure 13**) were obtained by Scanning Electron Microscopy (SEM). The SEM pictures were acquired on a SEM Ultra 55 operating at an accelerating voltage of 5 kV and a working distance of *ca.* 5 mm.

### II. 7. Raman spectroscopy

Raman spectroscopy is a non-destructive technique that provides insights into the molecular structure, the chemical composition and the nature of the analysed compounds. It was used to determine the structure of the different carbon materials used in this work<sup>172,176,287,288</sup>. Raman spectroscopy is based on the inelastic scattering of monochromatic light (here, an argon LASER (light amplification by stimulated emission of radiation) with  $\lambda = 514$  nm was operated at  $\sim 5$  mW). The interaction between the light and the sample results in an up-shift (down-shift) of the energy of the LASER photons, the shift being related to the vibrational modes of the studied system. Thus, the Raman patterns are plotted as a function of the frequency difference from the incident radiation (a Raman shift = 0  $\text{cm}^{-1}$  is observed for the band resulting of the elastic scattering of the monochromatic light, *i.e.* the Rayleigh band). The scattered radiations were collected by a Peltier-cooled charge detector coupled with a camera (spectral resolution = 1  $\text{cm}^{-1}$ ). The analysis was performed by Mr. Alexandre Crisci (SIMAP, Grenoble, France) with a  $\times 50$  ULWD objective and a 100  $\mu\text{m}$  confocal aperture for the sample illumination and the collection of the scattered photons. To compare the structure of the different carbon supports discussed in **Section IV. 5. 1.**, the Raman spectra were fitted using the LabSpec software and the 4 bands described in **Figure 21**. Such fitting allowed determination of the carbon crystallite size in the plane of the graphene layers ( $L_a$ ) using the Knight and White formula<sup>289</sup> (**Equation 29**):

$$L_a \text{ (nm)} = 4.4 \times \frac{I_G}{I_{D1}} \quad (\text{Eq. 29})$$

where  $I_G$  and  $I_{D1}$  stand for the integrated intensity of the  $G$  and the  $D_1$  bands, respectively (see **Figure 21**). **Equation 29** was established for  $\lambda = 514$  nm: the position<sup>290,291</sup> and the intensity

<sup>292</sup> of the  $D_1$ -band are highly dependent on the laser wavelength. Furthermore, it is only valid for non-amorphous carbons.  $I_{D_1} / I_G$  is proportional to  $L_a^2$  for amorphous carbons but no quantitative description of this relationship was provided in the literature <sup>172</sup>. For the sake of clarity, all the Raman spectra were normalized to the intensity of the band at  $\sim 1585 \text{ cm}^{-1}$ , which corresponds to the ideal graphite lattice band ( $G$ -band) of carbon (see **Figure 21**). The carbon crystallite size perpendicular to the graphene layers ( $L_c$ ) and the inter-planar distance ( $d_{002}$ ) were determined by fitting the XRD patterns (see **Section II. 9.**) and thereby complement the information derived from Raman spectra.

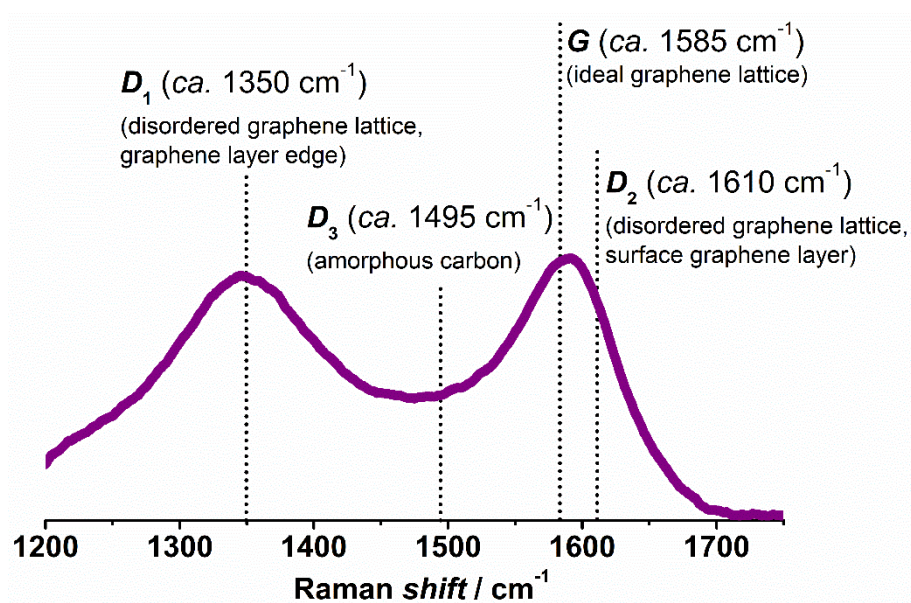


**Figure 21.** Raman spectra of Vulcan XC72 in the  $1200 - 1750 \text{ cm}^{-1}$  range highlighting the position of the theoretical vibration modes of carbon.

## II. 8. X-ray photoelectron spectroscopy

X-ray Photoelectron Spectroscopy (XPS) was used in **Section III. 2. 2.** to determine the boron atomic content of the porous hollow PtNi/C electrocatalysts during their synthesis, and in **Section IV. 5. 1.** to gain insights on the functionalization of the carbon surface (*i.e.* the atomic content in oxygen- and nitrogen-containing groups). The XPS patterns were obtained by irradiating the samples with an X-ray beam and analysing the kinetic energy of the electrons ejected from its first atomic layers. Each element of the sample gives rise to a characteristic set of peaks at kinetic energies determined by the photon energy and the respective binding energies. Moreover, the intensity of the peaks is proportional to the concentration of the element within the probed region of the sample (note that the depth of analysis depends on the mean inelastic free

path of the electrons, and is linked to the sample nature). Hence, XPS provides a qualitative and a quantitative analysis of the first atomic layers of a given sample.

In **Section III. 2. 2.**, the XPS measurements were acquired in an ultra-high vacuum chamber (Omicron,  $10^{-8}$  Pa base pressure,  $10^{-6}$  Pa during the measurements) equipped with a hemispherical analyser (VSW H100) and a monochromatic X-ray source (Al  $K_{\alpha}$ , 1486.6 eV) operating at 270 W (13.5 kV, 20 mA). The hemispherical analyzer was working in the constant pass energy mode (44 eV). The angle between the sample surface and the analyser axis was  $60^{\circ}$ . Increments of 0.25 eV and dwelling times of 10 s were used to record the XPS signals. The electrodes were prepared by depositing a non-quantified amount of catalytic powder on carbon tape, which was then glued onto a boron nitride block formerly covered with carbon tape. The samples were introduced into the XPS chamber 3 h before the measurements. The XPS patterns were analyzed using the CasaXPS software from CasaSoftware LTD. The reference was a partially oxidized Ni foil. The change of the Pt, Ni, and B contents during the synthesis were monitored by dividing the integrated areas of the Pt 4f, the Ni  $2p^{3/2}$  and the B1s peaks, after proper background subtraction, by their respective atomic sensitivity factors (4.044 for Ni, 0.159 for B, 5.575 for Pt). In **Section IV. 5. 1.**, the XPS data were acquired by Dr. Yan Busby, from the University of Namur (Namur, Belgium) on a spectrometer ESCALAB 250Xi (Thermo Scientific) equipped with a 500  $\mu\text{m}$  monochromatic Al  $K_{\alpha}$  (1486.6 eV) X-ray beam. The atomic composition was evaluated on survey spectra acquired in scan mode with a pass energy of 150 eV, while the chemical analysis was performed by fitting high-resolution spectra acquired in scan mode with a pass energy of 20 eV (to obtain the lowest peak width). Shirley background was used in peak fitting.

## II. 9. X-ray diffraction

### II. 9. 1. Introduction

The porous hollow PtNi/C NPs were analysed by X-Ray Diffraction (XRD) to determine structural parameters of interest, such as the PtNi lattice parameter ( $a_{\text{Pt-Pt}}$ ), the PtNi crystallite size ( $d_{\text{XRD}}$ ) and the microstrain (*i.e.* the shift of the lattice parameter from its average value ( $\mu_{\varepsilon} \propto \Delta a_{\text{Pt-Pt}}/a_{\text{Pt-Pt}}$ )<sup>293,294</sup>). In powder XRD experiments, a monochromatic X-ray beam interacts with the atoms of a sample, that are arranged periodically resulting in an elastic scattering (*i.e.* waves emanate from the excited structure without up-shift / down-shift as observed in the Raman patterns). The waves are emitted for a wide range of  $2\theta$  angles,  $\theta$  being the angle between the

resultant and the incident beam and often cancel each other, except for a few diffraction angles where they add constructively, according to the Bragg's law (**Equation 30**):

$$2d_{id} \times \sin \theta = \lambda \quad (\text{Eq. 30})$$

where  $d_{id}$  is the interplanar distance in the crystalline system and  $\lambda$  is the wavelength of the monochromatic beam. The 'constructive interferences' are detected, resulting in a XRD pattern. The lattice parameter can be derived from the Bragg law (**Equation 31**) and the crystallite size perpendicularly to a crystalline plane ( $d_{hkl}$ ,  $d_{XRD}$  being defined as the average value of the crystallite size perpendicularly to the (111), (110) and (100) crystallites planes) from the Scherrer equation (**Equation 32**):

$$d_{id} = \frac{a_{Pt-Pt}}{\sqrt{h^2 + k^2 + l^2}} \quad (\text{Eq. 31})$$

$$d_{hkl} = \frac{0.89 \times \lambda}{FWHM \times \cos \theta} \quad (\text{Eq. 32})$$

where (hkl) are the Miller indices of the crystalline plane corresponding to the observed peak and FWHM is the broadening at half the maximum intensity of the observed peak (in radians). The XRD patterns of the electrocatalysts presented in **Chapter IV** were determined with a PANalytical X'Pert Pro MPD vertical goniometer/diffractometer with a diffracted-beam monochromator (Cu  $K_\alpha$  radiation,  $\lambda = 0.15406$  nm) operating at 45 kV and 40 mA. The  $2\theta$  range was  $10 - 125^\circ$  and the step size  $0.033^\circ$ .

### II. 9. 2. Wide angle X-ray scattering

To obtain more information on the fine nanostructure of the electrocatalysts (*e.g.* microstrain), X-ray scattering (here often referred as WAXS) was also performed at the ID31 beamline of the ESRF. Depending of the sample, the high-energy X-ray radiation (60 keV or  $\lambda = 0.207 \text{ \AA}$ ) was focused on:

- (i) a poly (methyl methacrylate) cuvette of  $4.5 \times 1.25 \times 1.25$  cm (Plastibrand) where the synthesis occurred (see **Section III. 2.** for the results relative to this measurement);
- (ii) a Kapton capillary of  $d = 1$  mm, containing the sample powder for the *ex situ* electrocatalysts (**Section IV.2. – IV.5.**);

- (iii) a glassy carbon electrode covered by the post-ageing electrocatalyst ink (**Chapter V**);
- (iv) the home-made cell described in **Section II. 3. 7.** and **Figure 20 (Section V. 4.)**.

The WAXS measurements were performed in collaboration with Dr. Jakub Drnec, from the ESRF (Grenoble, France). The X-ray beam was focused with two transfocators to a size of  $4 \mu\text{m} \times 30 \mu\text{m}$  (vertical  $\times$  horizontal) at the sample position. The flux was  $5 \times 10^{12}$  photons  $\text{s}^{-1}$  at the sample position. The scattered signal was collected with Dectris Pilatus CdTe 2M detector positioned 300 mm behind the sample. The energy, detector distance and tilts were calibrated using a standard  $\text{CeO}_2$  powder and the 2D diffraction patterns were reduced to 1D curves using pyFAI software package <sup>295</sup>.

### II. 9. 3. Pair function distribution analysis

Pair-Function Distribution (PDF) analysis refers to the probability of finding two atoms at a given inter-atomic distance  $r$  <sup>296</sup>. Hence, PDF analysis provides information on the short / medium range order in crystalline structures. The PDF can be obtained from the XRD data as the Fourier transformed of the normalized total structure factor ( $q$ , see **Equation 33**).

$$q = \frac{4\pi \times \sin \theta}{\lambda} \quad (\text{Eq. 33})$$

PDF analysis was conducted by Dr. Pierre Bordet, from the Louis Néel Institute (Grenoble, France) using PDFGetX3 <sup>297</sup>. The data were considered up to  $q_{\text{max}} = 19.9 \text{ \AA}^{-1}$ . The scattering associated with the poly (methyl methacrylate) cuvette and the carbon support (**Section III. 2.**) was subtracted from the data. The PDF of a  $\text{CeO}_2$  standard was used to determine the instrumental parameters (damping and broadening of PDF peaks due to experimental resolution), which were then fixed during the PDF refinements, carried out with PDFgui <sup>298</sup>.

### II. 9. 4. Rietveld analysis

The WAXS patterns were refined by Dr. Pierre Bordet, from the Louis Néel Institute (Grenoble, France) by the Rietveld method (a refinement method using the least square method, *i.e.* minimization of the square of the error between the experimental and the theoretical data). This method allows an accurate determination of the physical parameters ( $a_{\text{Pt-Pt}}$ ,  $\mu_{\text{E}}$ ,  $d_{\text{XRD}}$ ). The Rietveld refinements were carried using the Fullprof software, considering the Fm-3m structure

of a cubic closed-packed metal ( $a \sim 3.9 \text{ \AA}$ ). The instrumental resolution function was determined by the refinement of the  $\text{CeO}_2$  standard sample. The Thomson-Cox-Hastings profile function was adopted with possibility for uniaxial anisotropic broadening from size origin.

### II. 9. 5. Small angle X-ray scattering

To obtain information on the structural changes of the NPs during their synthesis (see **Section III. 2.**), small angle X-ray scattering (SAXS) was performed in collaboration with Dr. Jakub Drnec (ESRF, Grenoble, France). The scattered signal was collected with Dexela 2923 positioned 6 m behind the sample. A long flight tube inserted between the detector and the sample was used to limit the air scattering of the direct beam. The beam stop was positioned at the end of the flight tube, about 150 mm from the detector. The size of the beam at the sample position was  $4 \mu\text{m} \times 30 \mu\text{m}$  (vertical  $\times$  horizontal). The energy, detector distance and tilts were calibrated using a standard Ag behenate powder and the 2D diffraction patterns were reduced to 1D curves using pyFAI software package<sup>295</sup>. SAXS focuses on the very low diffraction angles of the elastic scattering of the X-ray and provides information into the shape and composition of the nanostructure. As such, it is extremely useful to probe the morphological changes of the growing NPs. At small angles (for diluted solutions), the scattering intensity of spherical and identical particles,  $I(q)$ , is described as (**Equation 34**):

$$I(q) \sim P(q) \quad (\text{Eq. 34})$$

where  $P(q)$  is the form factor that describe the shape of the individual growing NPs. Here, the form factor is a Fourier transform of the autocorrelation function and therefore the square of the form factor amplitudes (**Equation 35**)<sup>299</sup>:

$$P(q) = \langle |F(\vec{q})|^2 \rangle = \left\langle \left| \int_V \Delta \rho e^{-i\vec{q}\vec{r}} d\vec{r} \right|^2 \right\rangle \quad (\text{Eq. 35})$$

where  $\Delta\rho$  is the scattering length density (SLD – *i.e.* the scattering power of the materials, that increases with (i) the density of the material and (ii) the atomic number of the atoms) difference between the NPs and the solvent. Since the studied nanomaterials feature an inhomogeneous SLD distribution, a monodisperse spherical NP with a core@shell structure was considered and  $P(q)$  was substituted by an analytical expression<sup>300</sup>. This idealized model was used to fit the SAXS data. The SLD of the core and of the shell absolute values are arbitrary since they depend

on the fitting parameter, *i.e.* the scaling. Technically, the *in operando* SAXS data were analysed using a SAXS utilities package. The raw images were radially integrated with the PyFAI software package. The last SAXS pattern measured before the adjunction of the NaBH<sub>4</sub> solution (*i.e.* the background, see **Figure 22A**) was subtracted from the subsequent patterns. The background-corrected patterns were fitted using SAXS utilities package and a core@shell NP model (**Figure 22B**). To avoid considering the peak at  $q = 0.13 \text{ nm}^{-1}$  resulting from the carbon support (that was not eliminated by the background subtraction, therefore suggesting modifications of the carbon support during the first minutes of the synthesis) only the region shown in **Figure 22B** was used to fit the form factor.

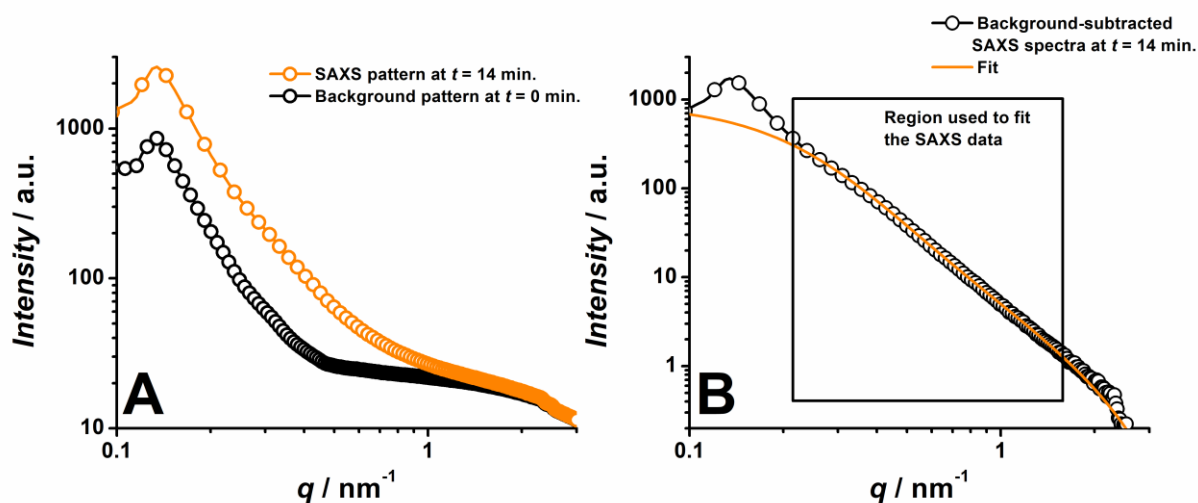


**Figure 22.** (A) Measured SAXS pattern before the addition of the first drop of NaBH<sub>4</sub> (background, black) and  $t = 14$  min (orange, before background correction) ( $t$  is the time after the addition of the first drop of NaBH<sub>4</sub>). (B) Example of a fit of SAXS pattern. Dark circles: the background-corrected SAXS pattern at  $t = 14$  min. orange curve: the fit using the core/shell NP model.

## II. 10. Membrane electrode assembly characterisation

The porous hollow PtNi/C NPs were characterized in membrane electrode assembly (MEA) in collaboration with the French Alternative Energy and Atomic Energy Commission (CEA).

The MEA was composed of:

- (i) an anode (commercial Pt/C, 50 wt. % loading,  $0.2 \text{ mg cm}_{\text{geo}}^{-2}$ );
- (ii) a membrane (Nafion<sup>®</sup> HP 20  $\mu\text{m}$ );
- (iii) a cathode (porous hollow PtNi/C –  $0.20 \text{ mg cm}_{\text{geo}}^{-2}$  or commercial Pt/C –  $0.20 \text{ mg cm}_{\text{geo}}^{-2}$ ). The porous hollow PtNi/C used for the MEA characterisation had a  $\text{Pt}^{2+}:\text{Ni}^{2+}$  ratio of 1:5 and a theoretical loading of 23 wt. %.

The electrocatalyst was deposited by a spraying method and hot pressed onto the GDL (24 BC (SLG) used both at the anode and cathode sides). The MEA geometric surface was  $25 \text{ cm}^2$ . Before characterisation, the MEA was activated and conditioned at  $T = 353 \text{ K}$ , with  $\text{H}_2$  ( $P = 1.5 \text{ bar}$ ) at the anode and air at the cathode. The stoichiometry for  $\text{H}_2$  and air was set to 1.5 and 2 respectively. The relative humidity (RH) was 80 % for both gases. The MEA characterization by polarization curves was performed at  $T = 353 \text{ K}$ , with a relative humidity of 50 % both for the  $\text{H}_2$  ( $P = 1.5 \text{ bar}$ ) and the air. The MEAs were aged up to 30,000 potential cycles between 0.6 and 1.0 V at  $T = 353 \text{ K}$  and  $\nu = 0.050 \text{ V s}^{-1}$  under  $\text{H}_2/\text{N}_2$  atmosphere.



# Chapter III. At the heart of the synthesis of porous hollow PtNi/C nanoparticles

**All the results discussed in this chapter have been published in:**

Chattot, R.; Asset, T.; Drnec, J.; Bordet, P.; Dubau, L.; Maillard, F.; Drnec, J.; Dubau, L.; and Maillard, F. Atomic Scale Snapshots of the Growth Mechanism of Hollow PtNi/C Nanocatalysts for Oxygen Reduction Reaction. *Nano Lett.* **2017**, *17* (4), 2447–2453.

In this article, the author of this thesis contributed to (i) the preparation, acquisition, analysis and treatment of the *in operando* WAXS spectra, (ii) the preparation and acquisition of the *in operando* SAXS spectra, (ii) the preparation of the samples, the acquisition of the TEM micrographs and the determination of the particle size distribution, (iii) the synthesis of the porous hollow PtNi/C for the electrochemical characterisation, the electrochemical characterisation in acidic and alkaline media and the data analysis, (iv) the acquisition of the XPS patterns, (v) the acquisition of the EDX elemental maps and (vi) the preparation of the manuscript for publication.

### III. 1. Introduction

Knowledge of the mechanisms driving the formation of the porous hollow PtNi/C NPs<sup>83,84,301</sup> and of the intermediate structures observed during their synthesis (for technical details on the synthesis process, please refer to **Section II. 1. 1.**) is fundamental to efficiently design this class on nanomaterials. Liang *et al.*<sup>245</sup> have first reported the synthesis of *ca.* 20 nm hollow Pt/C NPs by galvanic replacement using Co NPs as sacrificial templates. They observed a 2-fold enhancement of the methanol electrooxidation kinetics relative to solid Pt/C NPs. Improved methanol<sup>245,302</sup> or formic acid<sup>303</sup> electrooxidation kinetics was later reported on similar electrocatalytic materials based on Pt. More recently, Wang *et al.*<sup>223</sup> electrodeposited Ni NPs on glassy carbon, and deposited a controlled number of Pt-shells on their surface via galvanic replacement. Due to nanoscale Kirkendall effect, they obtained hollow Pt/C NPs with enhanced ORR kinetics relative to their solid counterpart. Using Co/C, Cu/C or Ni/C as sacrificial templates, Bae *et al.*<sup>231</sup> and Dubau *et al.*<sup>83,84,218</sup> synthesized efficient Pt-based/C ORR electrocatalysts with enhancement of the SA for the ORR by a factor of 9. However, to date, the atomic scale details of the mechanism and the kinetics of formation of hollow Pt-rich nanoalloys remain elusive. Moreover, the nature and the electrocatalytic activity for the ORR of the different nanostructures forming during the synthesis are unknown. In this chapter, the mechanism of formation and growth of hollow Pt-rich nanocatalysts synthesized by a ‘one-pot’ method<sup>83,84,231</sup> is investigated, using a combination of *in operando* synchrotron WAXS and SAXS, TEM, HR-TEM, STEM-EDX, XPS and electrochemical techniques. For the technical details of the different methods, please refer to **Chapter II.**

### III. 2. Results and Discussion

#### III. 2. 1. Wide angle X-ray scattering and energy dispersive X-ray mapping

The porous hollow PtNi/C NPs were synthesized by a ‘one-pot’ method where all the precursors (Pt(NH<sub>3</sub>)<sub>4</sub>Cl<sub>2</sub>·H<sub>2</sub>O, NiCl<sub>2</sub> and Vulcan XC72) are mixed and dissolved / dispersed in 150 mL of Milli-Q grade H<sub>2</sub>O (18.2 MΩ), before the drop-wise addition (in *t* = 5 min) of 208 mg of NaBH<sub>4</sub> dissolved in 25 mL of MilliQ H<sub>2</sub>O. 60 min after the addition of the first drop of NaBH<sub>4</sub>, the electrocatalyst was filtered, thoroughly washed, dried and acid-leached during *t* = 22 h in a 1 M H<sub>2</sub>SO<sub>4</sub> solution, resulting in the formation of porous hollow PtNi/C NPs (as schematized in **Figure 23**)<sup>83,84,231</sup>.

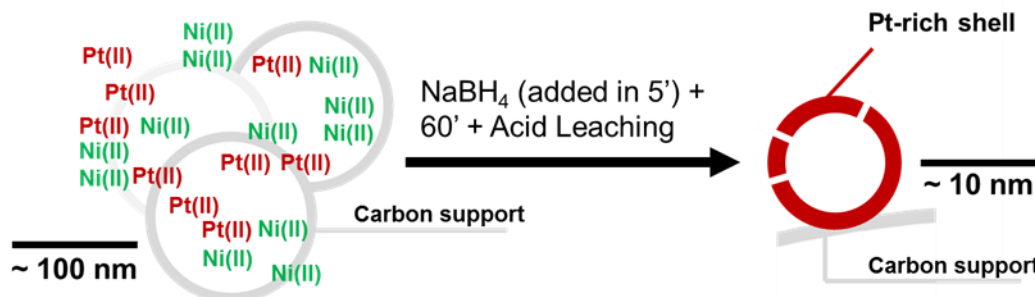
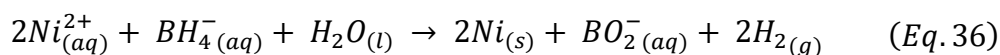


**Figure 23.** Schematic representation of the initial (*i.e.* metal precursors + carbon in MQ-grade water) and final (acid leaching) steps of the synthesis of porous hollow PtNi/C NPs.

The addition of  $\text{NaBH}_4$  initiates the synthesis (*i.e.* before adding it, Pt and Ni are at an oxidation state of +II, see **Figure 23**). According to its low standard potential ( $E^\circ = -0.82 \text{ V vs. SHE}$  at  $\text{pH} = 7$ <sup>304,305</sup> for the  $\text{BO}_2/\text{BH}_4^-$  couple),  $\text{NaBH}_4$  can reduce both precursors ( $E^\circ_{\text{Pt}^{2+}/\text{Pt}} = 1.19 \text{ V vs. SHE}$  and  $E^\circ_{\text{Ni}^{2+}/\text{Ni}} = -0.25 \text{ V vs. SHE}$ ) but  $\text{Pt}^{2+}$  ions should be reduced first and then be followed by the reduction of  $\text{Ni}^{2+}$ , thereby promoting the formation of a Pt-rich@Ni-rich core@shell and avoiding the formation of hollow NPs. However, using  $\text{Pt}(\text{NH}_3)_4^{2+}$  salts induces a lower reduction potential for Pt(II) ( $E^\circ(\text{Pt}(\text{NH}_3)_4^{2+}/\text{Pt}) = 0.76 \text{ V vs. RHE}$ ), slower reduction kinetics and a slower decomposition in  $\text{H}_2\text{O}$ <sup>83,84</sup> resulting in a preferential reduction of Ni atoms as described by **Equation 36**.



After the addition of the first drop of  $\text{NaBH}_4$ , (i) the external diameter of the Ni NPs rapidly increases to be close to the final diameter of the hollow PtNi/C at  $t = 2 \text{ min}$  ( $d_{\text{ext}}(2 \text{ min}) = 11.1 \pm 4.7 \text{ nm vs. } d_{\text{ext}}(60 \text{ min}) = 14.0 \pm 2.9 \text{ nm}$ , see **Figure 24A**) and (ii) the Ni content measured by STEM-EDX decreases rapidly from 94 at. % at  $t = 1 \text{ min}$  to 69 at. % at  $t = 4 \text{ min}$  (**Figure 24B** and **Figure 25B**). Slower variations are monitored at  $t > 4 \text{ min}$ , the final Ni content being 49 at. % after  $t = 60 \text{ min}$ . This non-monotonic variation of the Ni content reflects the occurrence of two sequential processes:

- (i) the galvanic replacement which is most effective in the deposition of the first Pt atoms on the Ni-rich/C NPs;
- (ii) the nanoscale Kirkendall effect<sup>219,221</sup> that allows the transformation of solid Ni-rich core@Pt-rich shell NPs (at  $t = 20 \text{ min}$ , see **Figure 25A**) into hollow PtNi/C NPs.

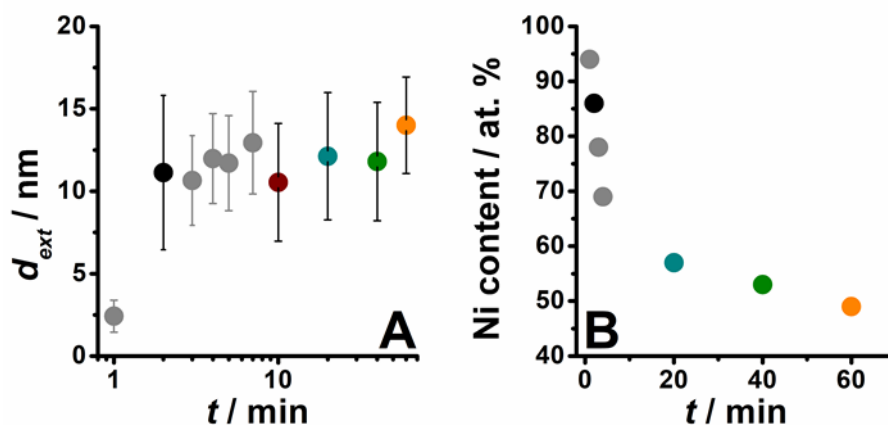


**Figure 24.** (A) Variation of the external diameter of the NPs, approximated by counting between 100 and 250 NPs for each discussed time and (B) variation of the Ni content of the NPs measured on individual NPs by scanning transmission electron microscopy – energy dispersive X-ray spectroscopy.

Deeper insights into the structure of the growing PtNi/C NPs were obtained using *in operando* WAXS (see **Figure 25C**). Note that for the sake of comparison with classical X-ray diffraction, the data obtained in synchrotron ( $\lambda = 0.207 \text{ \AA}$ ) were converted into Cu  $K\alpha$  radiation ( $\lambda = 1.5406 \text{ \AA}$ ). At  $t \leq 10$  min, diffraction from (i) the (002) planes of the carbon support at  $2\theta = 26.4^\circ$ , (ii) Pt(111) at  $2\theta = 39.8^\circ$  and (iii) Ni(111) at  $2\theta = 44.5^\circ$  are visible in **Figure 25C**. The diffraction peak at  $2\theta = 36.6^\circ$  (detected between  $1 < t < 4$  min, **Figure 25C**) was ascribed to monoclinic  $\text{NiB}_3$  and/or tetragonal  $\text{Ni}_2\text{B}$ ,<sup>306,307</sup> in agreement with the EDX elemental maps of **Figure 25B**, where the formation of a Ni-based shell is observed at  $t = 2$  min. According to the WAXS spectra, this  $\text{Ni}_x\text{B}_y\text{O}_z$  shell (the exact nature of the shell is established in **Section III. 2. 2.**) is formed before Ni(111) planes appear, and disappears before Pt(111) diffraction peaks become visible ( $t \geq 4$  min 30, **Figure 25C**). This suggests that the  $\text{Ni}_x\text{B}_y\text{O}_z$  shell protects, at least to some extent, the metallic Ni-rich cores from the deposition of  $\text{Pt}^{2+}$  ions *via* galvanic replacement. At  $t \geq 10$  min, the disappearance of the Ni(111) signal (see **Figure 25C**) suggests that the Ni cores are amorphized, corroded or alloyed, leaving behind a WAXS signal that is typical of a slightly contracted face centered cubic PtNi structure<sup>84</sup>. A negative shift of the peaks ascribed to diffraction from (002) planes of the Vulcan support at  $2\theta \sim 26^\circ$  is also visible, similarly to what has been observed for graphite oxide (the crystalline structure of graphite is not retained upon insertion of oxygen, resulting in an increased interplanar distance and, thus, smaller diffraction angles<sup>176</sup>). We believe that this result signs the intercalation of boron atoms in the carbon black structure.

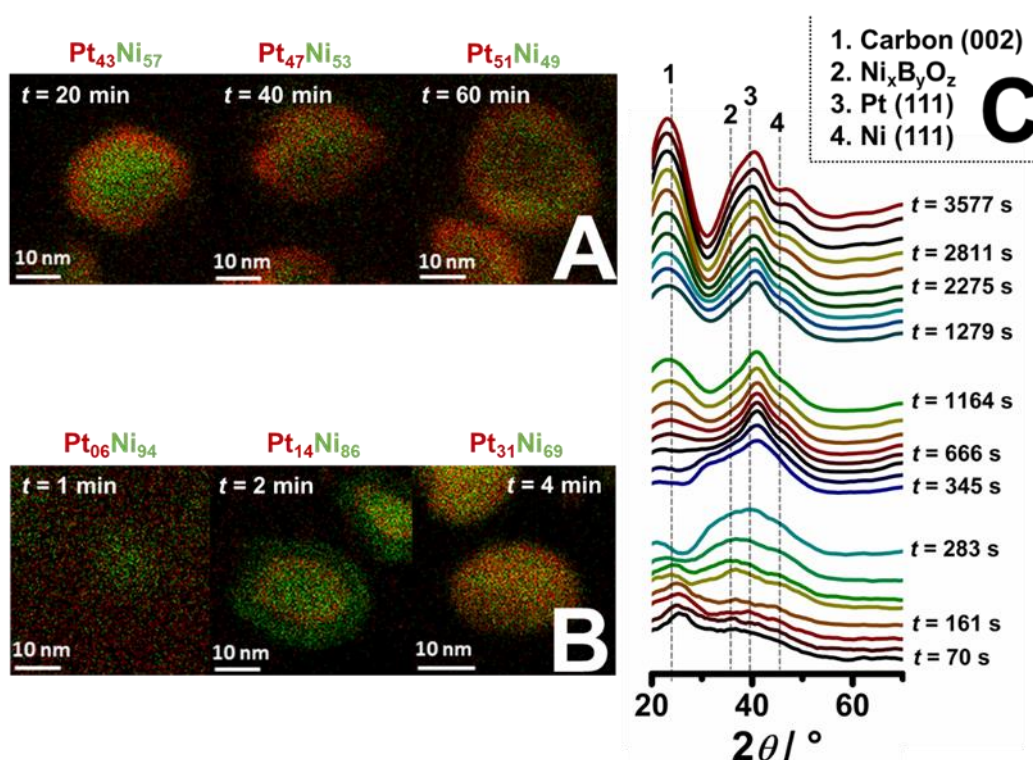


**Figure 25.** Insights into the synthesis of porous hollow PtNi/C NPs *via* electron and X-ray based techniques. (A, B) X-ray energy dispersive spectroscopy elemental maps of the different nanostructures forming during the synthesis of hollow PtNi/C NPs (the Pt and Ni atoms are represented in red and green, respectively). (C) Wide angle X-ray scattering patterns of the different PtNi nanostructures forming for  $0 \text{ min} < t < 60 \text{ min}$  ( $t$  being the time after the addition of the first drop of  $\text{NaBH}_4$ ). The intensity of the X-ray patterns was normalized to the highest peak intensity measured in the  $25^\circ < 2\theta < 120^\circ$  range (C (002) from  $0 \leq t \leq 3.5 \text{ min}$  and Pt (111) for  $t < 3.5 \text{ min}$ ).

These structural changes are confirmed by the experimental PDF extracted from the WAXS patterns (**Figure 26**). The first atomic coordination shells are distinguishable at  $t \geq 3 \text{ min}$  and the peak at  $0.249 \text{ nm}$  dominated the PDF signal for  $3 \text{ min} \leq t \leq 4 \text{ min}$  (see **Section II. 9. 3** for the technical details concerning the determination of the PDF from the WAXS patterns). This suggests the presence of Ni-rich NPs on the carbon support for  $t \leq 4 \text{ min}$ . For  $t \geq 4.5 \text{ min}$ , the peak at  $0.271 \text{ nm}$  becomes predominant, relevant for an enrichment of the nanostructure in platinum, as observed by STEM-EDX (**Figure 24B** and **Figure 25B**). At  $t \sim 10 \text{ min}$ , the PDF signal can be fitted with a single PtNi phase with a lattice parameter of  $a = 0.385 \text{ nm}$ . At longer times, the lattice parameter relaxes. This phenomenon agrees with the losses in nickel monitored by STEM-EDX (**Figure 24B** and **Figure 25B**).

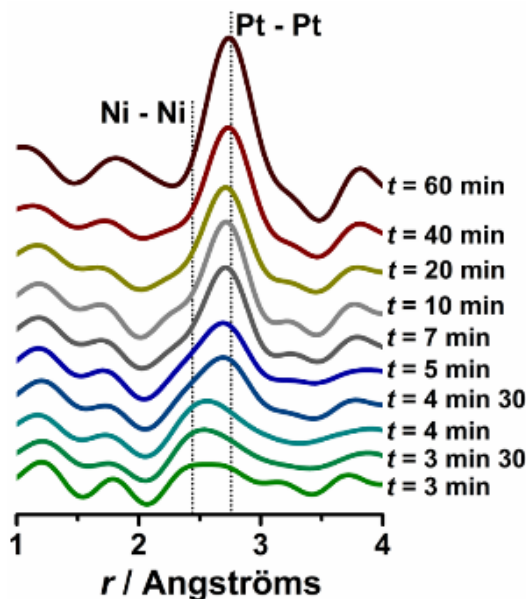
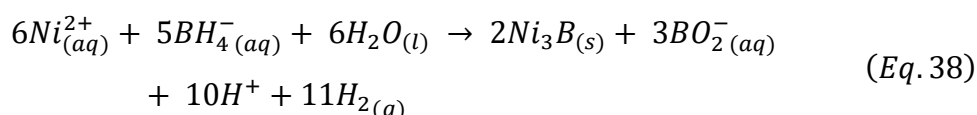
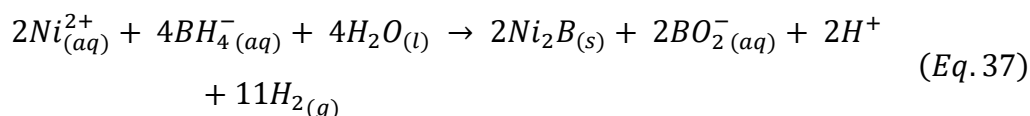


**Figure 26.** Atomic pair function distribution for  $3 \text{ min} \leq t \leq 60 \text{ min}$  ( $t$  being the time after the addition of the first drop of  $\text{NaBH}_4$  and  $r$  the distance between two atoms).

### III. 2. 2. X-ray photoelectron spectroscopy and high-resolution TEM

The formation of the  $\text{Ni}_x\text{B}_y\text{O}_z$  matrix observed by STEM-EDX and WAXS was confirmed by HR-TEM and XPS (see **Figure 26**). The amorphous shell surrounding the Ni NPs is observed by HR-TEM at  $t = 2 \text{ min}$  (**Figure 27A**) and is composed of atoms with, in average, a smaller atomic number than Ni (as evidenced by the contrast between the Ni core, darker, and the shell, lighter). The evolution of the boron relative content within the NPs was followed by XPS. It is higher at  $t = 2 \text{ min}$  ( $15.8 \pm 5 \text{ at. } \%$ ) than during the rest of the synthesis, *i.e.* from  $9.8 \pm 8.6 \text{ at. } \%$  at  $t = 20 \text{ min}$  to  $5.2 \pm 15.3 \text{ at. } \%$  at  $t = 40 \text{ min}$  (the boron content observed at  $t > 2 \text{ min}$  is at the detection limit of the XPS, see the standard deviation observed on **Figure 27D**), therefore confirming the nature of the lighter element present in the NPs shell. These results are coherent with the affinity of boron with most of the transition metals, resulting in the spontaneous formation of the transition metal borides<sup>307–312</sup>. Nickel borides (*e.g.*  $\text{Ni}_2\text{B}$ ,  $\text{Ni}_3\text{B}$ , *etc.*, *i.e.* the most common phases formed *via* the reduction of  $\text{Ni}^{2+}$  in  $\text{BH}_4^-$  containing solutions<sup>312–314</sup>) develop during the synthesis according to **Equation 37** and **Equation 38**.



The presence of oxygen in the  $\text{Ni}_x\text{B}_y\text{O}_z$  shell was also evidenced by XPS (**Figure 27B** and **Figure 27C**), by the *ca.* 5 eV positive shift of the B 1s binding energy relative to elemental boron<sup>315,316</sup> and the presence of the Ni 2p<sub>3/2</sub> satellite peak (at 859.3 eV) in the XP spectra, that correspond to Ni(OH)<sub>2</sub> or NiO.  $\text{Ni}_x\text{B}_y\text{O}_z$  phases (*e.g.* Ni(BO<sub>2</sub>)<sub>2</sub>) can be formed either by the reaction between the BO<sub>2</sub><sup>-</sup> ions produced by **Equation 36**, **Equation 37** and **Equation 38** or by homogenous hydrolysis of the NaBH<sub>4</sub> solution (see **Equation 39**) and Ni<sup>2+</sup>, as described in **Equation 40**.

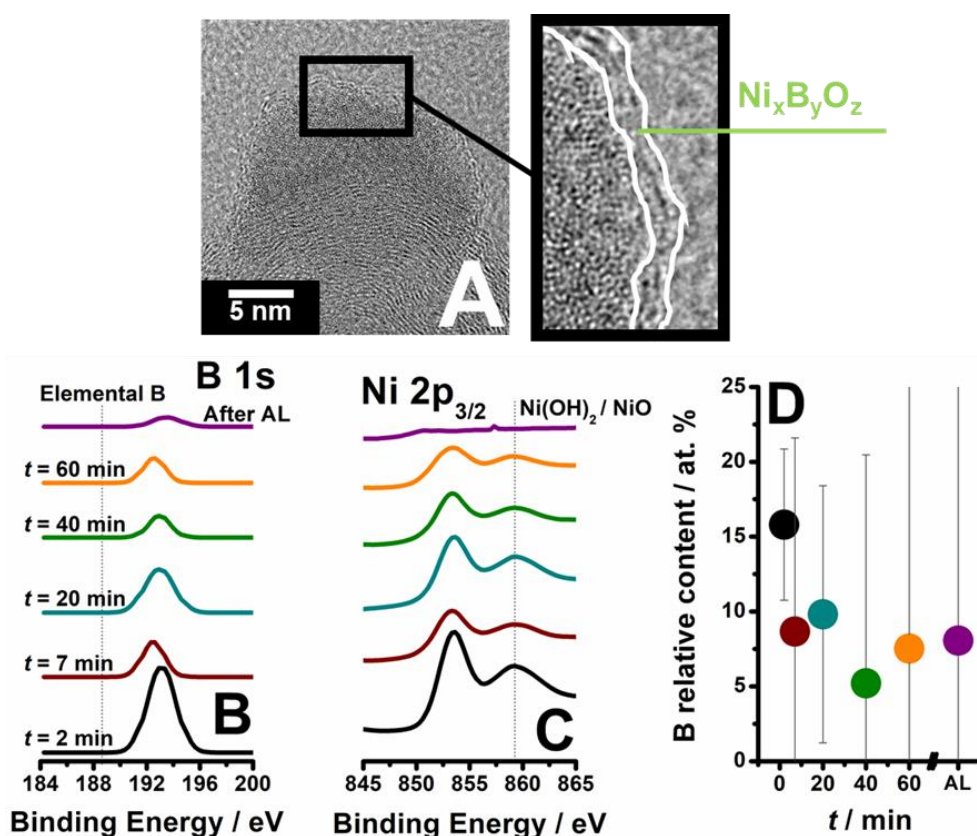
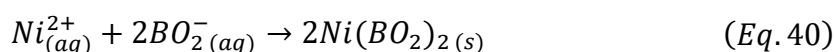
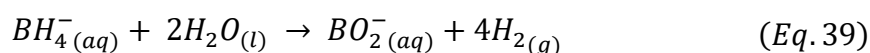


**Figure 27.** (A) High-Resolution TEM image of a Ni@Ni<sub>x</sub>B<sub>y</sub>O<sub>z</sub> nanostructure obtained after  $t = 2$  min ( $t$  being the time after the addition of the first drop of NaBH<sub>4</sub>). (B) XPS peak of boron (B 1s) as a function of the synthesis time. (C) XPS peak of Ni as a function of the synthesis time. (D) Relative content of boron extracted from the analysis of XP spectra acquired on samples collected during the synthesis of hollow PtNi/C NPs.

### III. 2. 3. Small Angle X-Ray Scattering

The slow transformation of the Ni-rich@Pt-rich core@shell structure observed at  $t = 20$  min in a hollow PtNi/C nanostructure at  $t = 60$  min (see **Figure 25**) was supported by *in operando* SAXS. The variations of the SLD of the core and the shell are presented in **Figure 28**. For the calculation, the structure of the core@shell Ni-rich@Pt-rich (that ultimately becomes a hollow PtNi NP) was ascribed to a monodisperse spherical core@shell structure (the core being, at  $t = 20$  min, the Ni-rich core and at  $t = 60$  min, the internal cavity observed on **Figure 25**). All the technical details concerning the fitting and the analysis are provided in **Section II. 9. 5**. The  $SLD_{\text{shell}}/SLD_{\text{core}}$  ratio (*i.e.* the ratio of the electron density between the shell and the core) was plotted in **Figure 28**. The  $SLD_{\text{shell}}/SLD_{\text{core}}$  ratio increased during the first 20 min of the synthesis, due to the enrichment of the shell in platinum by galvanic replacement (*i.e.* a heavier element with an increased atomic number), before flattening out (at  $3.2 \pm 0.5$ ) for  $20 \text{ min} < t \leq 35 \text{ min}$  and steeply increase for  $t \geq 35 \text{ min}$ .

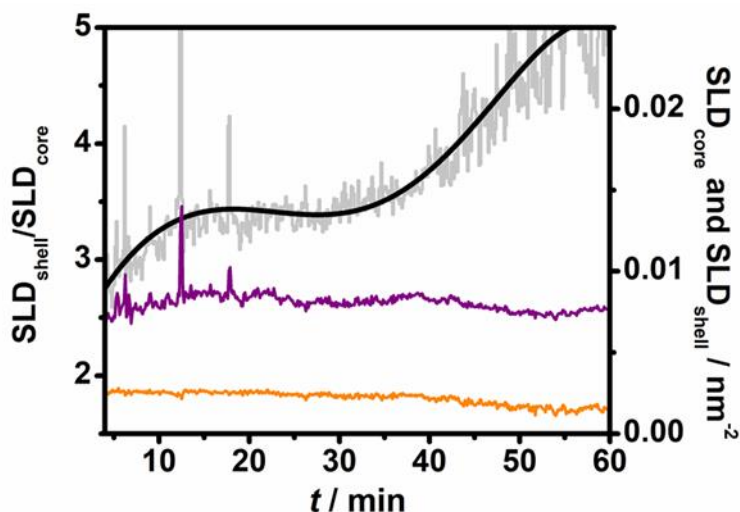


**Figure 28.** Variation of the parameters extracted from the fitting of the SAXS, *i.e.* the scattering light density of the core ( $SLD_{\text{core}}$ ), of the shell ( $SLD_{\text{shell}}$ ) and their ratio. The solid line is a fifth order polynomial fit of the  $SLD_{\text{shell}}/SLD_{\text{core}}$  ratio.

This abrupt variation signs the diffusion of the Ni atoms contained in the core of the NPs toward the surface of the Pt-rich shell, due to their oxophilicity, at a rate faster than the Pt atoms diffusion into the NPs. According to the Kirkendall effect<sup>219–221</sup>, vacancies are formed into NPs to compensate the Ni atoms departure and condensate into voids yielding ultimately to hollow PtNi/C NPs. At  $t = 60$  min, the core of the NPs is partly depleted in nickel, thus explaining the high values of the  $SLD_{\text{shell}}/SLD_{\text{core}}$  ratio ( $> 5$  – **Figure 28**). Note that the final structure of the

NPs is porous and that the formation of those porosities could either have occurred (i) during the galvanic replacement, *i.e.* a heterogenous nucleation of the Pt-rich shell resulting in a non-full coverage of the Ni-core or (ii) during the acid leaching of the electrocatalyst in 1 M H<sub>2</sub>SO<sub>4</sub> during  $t = 22$  h. Therefore, the diminution of SLD<sub>core</sub> at  $t > 35$  min can also be ascribed to leaching of the Ni-rich core.

### III. 2. 4. Electrochemical characterization of the different nanostructures.

Carbon supported Ni-rich@Pt-rich shell<sup>72,75,317</sup>, solid and hollow PtNi NPs<sup>83–85,223</sup> are extremely interesting for the oxygen reduction reaction (ORR). The surface reactivity and the ORR activity of the different synthesis intermediates was investigated in acidic (0.1 M HClO<sub>4</sub>) and alkaline (0.1 M NaOH) media and benchmarked to the performances of a commercial Pt/C electrocatalyst. The cyclic voltammograms (CVs) in Ar-saturated electrolyte (**Figure 29A** and **Figure 29B**), the linear sweep voltammetries (LSVs) in O<sub>2</sub>-saturated electrolyte (**Figure 29C** and **Figure 29D**) and the specific activity (*i.e.* the activity normalized by the active surface of platinum) measured at  $E = 0.95$  V vs. RHE (in acidic medium, see **Figure 29E**) and  $E = 0.90$  V vs. RHE (in alkaline medium, see **Figure 29F**) are reported in **Figure 29**. The CVs (**Figure 29A** and **Figure 29B**) feature the underpotential deposition of protons (in acid) and water (in alkaline) for  $0.05 < E < 0.40$  V vs. RHE and the surface oxide formation and reduction for  $E < 0.60$  V vs. RHE. The difference in reactivity toward the water and the protons provides evidences that the surface layers are Ni-rich at  $t = 2$  min and Pt-rich at  $t \geq 7$  min in agreement with *in operando* WAXS and STEM-EDX (see **Figure 25**).

The enrichment of the surface and near surface layers in Pt translates into an increased specific activity for the ORR in alkaline and acidic media, as evidenced by the positive shift of the half wave potential and of the ORR onset (**Figure 29C – Figure 29F**): the Ni@Ni<sub>x</sub>B<sub>y</sub>O<sub>z</sub> core@shell NPs ( $t = 2$  min) present the worst specific activity in alkaline and acidic media, due to their Ni-rich surface. At  $t \geq 7$  min, the electrocatalysts present a 2-fold enhancement in specific activity compared to Pt/C. Note that the electrocatalysts discussed in **Figure 29F** were not acid leached to maintain a similar structure to the ones observed by STEM-EDX (**Figure 25**), inducing lower performances for the ORR<sup>231</sup>.

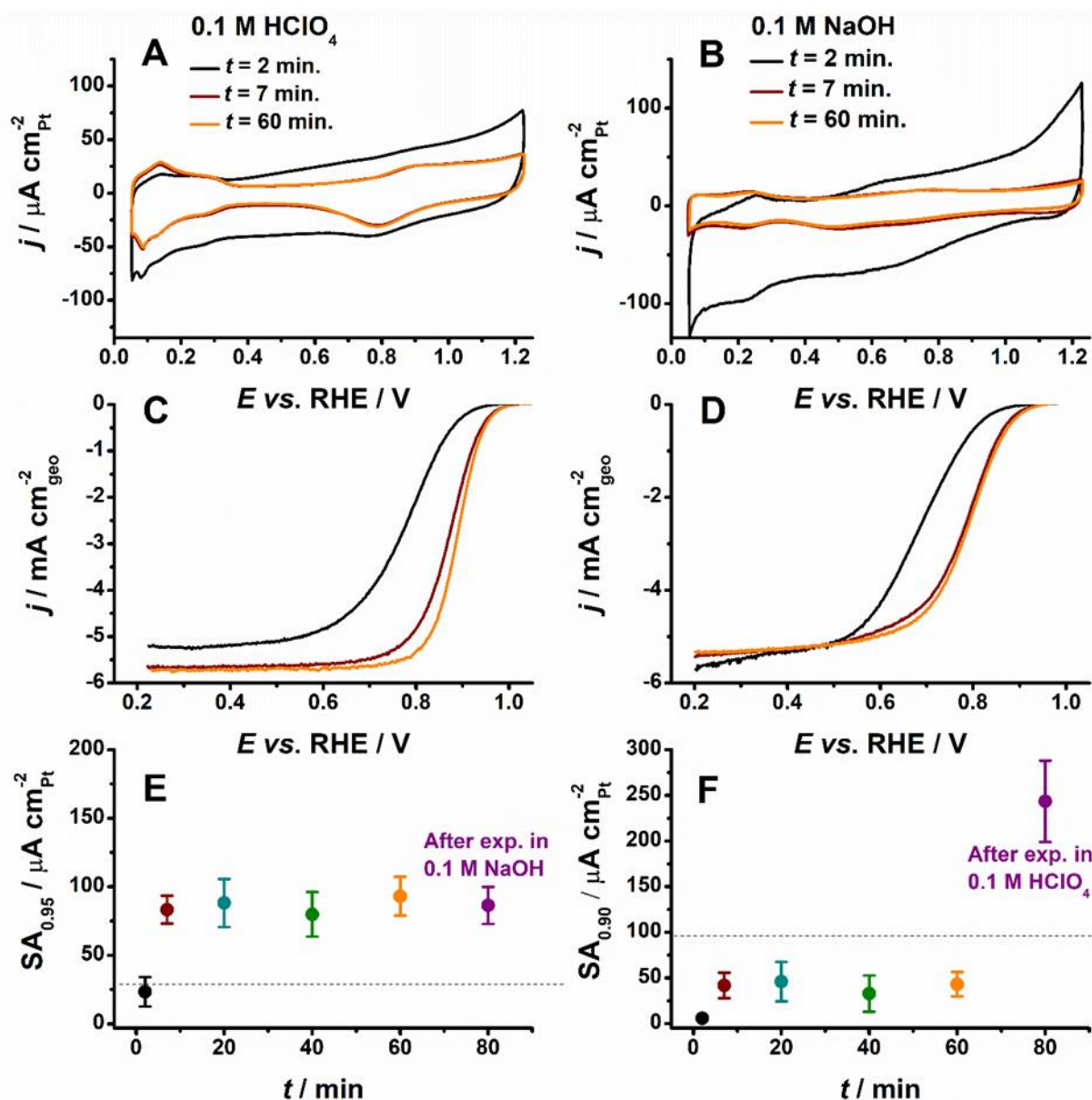


**Figure 29.** Electrochemical characterization of the different nanostructures formed during the synthesis of porous hollow PtNi/C NPs. (A, B) Cyclic voltammograms (in Ar-saturated 0.1 M HClO<sub>4</sub> or 0.1 M NaOH at  $\nu = 0.020 \text{ V s}^{-1}$  without rotation of the electrode), (C, D) positive-going linear sweep voltammograms (in O<sub>2</sub>-saturated 0.1 M HClO<sub>4</sub> or 0.1 M NaOH at a potential sweep rate  $\nu = 0.005 \text{ V s}^{-1}$  and a rotation rate  $\omega = 1600 \text{ rpm}$ ), and (E, F) Ohmic drop and mass-transport corrected ORR specific activity. All the experiments were performed at  $T = 298 \pm 1 \text{ K}$ . The dashed line corresponds to the value of the specific activity for the ORR of a reference 20 wt. % Pt/C measured in the same experimental conditions.

The specific activity of the synthesis intermediates in alkaline media was always lower than the performances of the commercial Pt/C. The latter could be improved if the electrocatalyst is first characterized in acidic medium before being characterized in alkaline medium (as evidenced on the intermediate structure at  $t = 60$  min, see **Figure 29E** and **Figure 29F**). This phenomenon is rationalized by the formation of a Pt-skeleton nanostructure upon exposure of the surface to an acidic electrolyte<sup>133</sup> (*i.e.* an electrolyte that rapidly etches the surface nickel), resulting in an increased surface area and the removal of the Ni atoms and of the  $\text{Ni}_x\text{B}_y\text{O}_z$  residual species that were formed according to **Equation 40** and poisoned the electrocatalytic sites.

### III. 3. Conclusion

In summary, this chapter introduced a methodology based on advanced electrons, X-ray and electrochemistry techniques (STEM-EDX, SAXS, WAXS, XPS, HR-TEM, *etc.*) capable of identifying the formation and growth mechanisms of various nanomaterials synthesized in aqueous electrolyte, as the porous hollow PtNi/C NPs. The different steps may be summarized as follows (see **Figure 30** for a graphical representation):

- (i) at  $t \leq 1$  min, the  $\text{Ni}^{2+}$  ions are preferentially reduced into solid Ni/C NPs ( $d \sim 3$  nm) by  $\text{NaBH}_4$ ;
- (ii) Ni-rich@ $\text{Ni}_x\text{B}_y\text{O}_z$  core@shell NPs then form (1 min  $< t < 2$  min after the addition of the first drop of the  $\text{NaBH}_4$  solution);
- (iii) the  $\text{Ni}_x\text{B}_y\text{O}_z$  shell acts as a sacrificial template for the deposition of Pt atoms by galvanic replacement (Ni atoms are oxidized and  $\text{Pt}^{2+}$  ions are reduced), resulting in an increase of the Pt at. % from 6 at. % to 31 at. % for 2 min  $< t < 4$  min;
- (iv) from 4 min  $< t < 20$  min, the Ni cores are corroded or alloyed with Pt. At  $t \sim 10$  min, the PDF signal (**Figure 26**) obtained could be fitted assuming a face centred cubic PtNi structure. The lattice parameter relaxes;
- (v) finally, for 20 min  $< t < 60$  min, the Ni-rich@Pt-rich core@shell NPs are transformed into hollow PtNi/C NPs *via* the nanoscale Kirkendall, as evidenced by the fast increase of the  $\text{SLD}_{\text{shell}}/\text{SLD}_{\text{core}}$  ratio at  $t \geq 35$  min and the diminution of the nickel content.

These changes in morphology were correlated to the changes in ORR specific activity, *i.e.* the Ni@ $\text{Ni}_x\text{B}_y\text{O}_z/\text{C}$  core@shell NPs (with a Ni-rich surface and near surface layers) show a depreciated ORR activity compared to commercial Pt/C, by opposition to the Ni-rich@Pt-rich/C core@shell NPs and the hollow PtNi/C NPs.

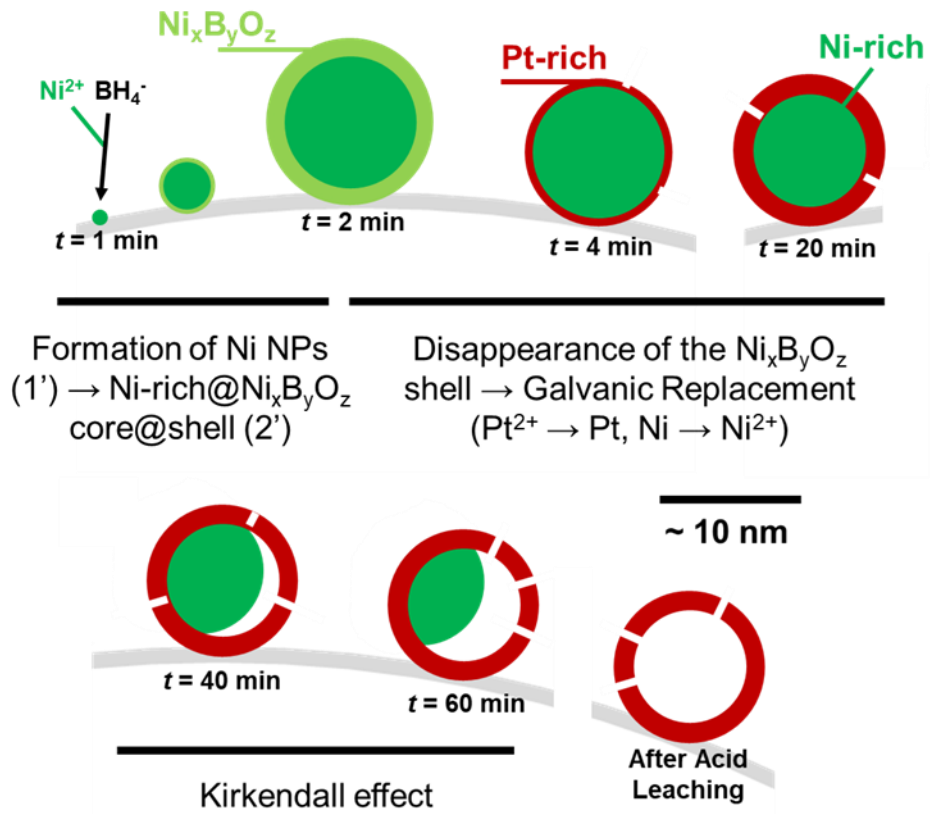


**Figure 30.** Schematic representation of the different steps of the synthesis of the porous hollow PtNi/C NPs, from the formation of the Ni NPs at  $t = 1 \text{ min}$  ( $t$  being the time after the addition of the first drop of  $\text{NaBH}_4$ ) to the ‘porous hollow’ PtNi/C nanostructure obtained after acid leaching.

# Chapter IV. Design of porous hollow PtM nanoparticles for the ORR

**All the results discussed in this chapter have been (or will be) published in:**

(1) Asset, T.; Chattot, R.; Nelayah, J.; Job, N.; Dubau, L. and Maillard, F. Structure-Activity Relationships for the Oxygen Reduction Reaction in Porous Hollow PtNi/C Nanoparticles. *ChemElectroChem* 2016, 3 (10), 1591–1600.

In this article, the contribution of the author of this thesis was (i) the synthesis of the porous hollow PtNi/C NPs at different temperature, (ii) the analysis of the XRD patterns, (iii) the acquisition and analysis of the SAA, of the electrochemical characterization and of the TEM micrographs and (iv) the preparation of the manuscript for publication.

(2) Asset, T.; Fontana, M.; Mercier-Guyon, B.; Martin, V.; Chattot, R.; Job, N.; Dubau, L. and Maillard, F. Rational Design of Hollow Pt-based Nanoparticles for the Oxygen Reduction Reaction, *submitted to ChemPhysChem*.

In this article, the contribution of the author of this thesis was (i) the synthesis of the porous hollow PtNi/C NPs with different cores, different temperatures, different carbon supports and different Pt<sup>2+</sup>.Ni<sup>2+</sup>, (ii) the analysis of the XRD patterns, (iii) the acquisition and analysis of the SAA, of the electrochemical characterization (for the CO<sub>ads</sub> electrooxidation and the ORR) and of the TEM micrographs and (iv) the preparation of the manuscript for publication.

(3) Asset, T.; Chattot, R.; Drnec, J.; Bordet, P.; Job, N.; Maillard, F. and Dubau, L. Elucidating the Mechanisms Driving the Ageing of Porous Hollow PtNi/C Nanoparticles by the Means of CO<sub>ads</sub> stripping, **DOI:** 10.1021/acsami.7b05782.

In this article, the contribution of the author of this thesis was (i) the synthesis of the porous hollow PtNi/C NPs at different temperatures, (ii) the analysis of the XRD patterns, (iii) the acquisition and analysis of the SAA, of the electrochemical characterization and of the TEM micrographs, (iv) the preparation of the samples for the WAXS measurements and the acquisition of the WAXS patterns and (v) the preparation of the manuscript for publication.

(4) Asset, T.; Busby, Y.; Crisci, A.; Martin, V.; Stergiopoulos, V.; Serov, A.; Atanassov, P.; Chattot, R.; Dubau, L.; Maillard, F. and Job, N. Influence of the Carbon Support on the Morphology and Stability of Porous hollow PtNi/C electrocatalysts, *to be submitted*.

In this article, the contribution of the author of this thesis was (i) the synthesis of the porous hollow PtNi/C NPs on different carbon supports, (ii) the acquisition and analysis of the SAA, of the electrochemical characterization and of the TEM micrographs, (iii) the analysis of the XRD patterns, of the XPS spectra and of the BET specific surface, (iv) the IL-TEM measurements (observation and electrochemical protocol) and (v) the preparation of the manuscript for publication.

In this chapter are also mentioned results published in several papers in which the author was involved in (i) the synthesis of the porous hollow PtNi/C NPs and (ii) the preparation of the manuscript for publication and, for (1), (iii), the determination of the porous nature of the hollow porous PtNi/C NPs using the works of Montejano-Carrizales *et al.*<sup>318,319</sup>.

(1) Dubau, L.; Asset, T.; Chattot, R.; Bonnaud, C.; Vanpeene, V.; Nelayah, J. and Maillard, F. Tuning the Performance and the Stability of Porous Hollow PtNi/C Nanostructures for the Oxygen Reduction Reaction. *ACS Catal.* 2015, 5 (9), 5333–5341.

(2) Dubau, L.; Nelayah, J.; Moldovan, S.; Ersen, O.; Bordet, P.; Drnec, J.; Asset, T.; Chattot, R. and Maillard, F. Defects Do Catalysis: CO Monolayer Oxidation and Oxygen Reduction Reaction on Hollow PtNi/C Nanoparticles. *ACS Catal.* 2016, 6 (7), 4673–4684.

(3) Le Bacq, O.; Pasturel, A.; Chattot, R.; Previdello, B.; Nelayah, J.; Asset, T.; Dubau, L. and Maillard, F. Effect of Atomic Vacancies on the Structure and the Electrocatalytic Activity of Pt-rich/C Nanoparticles: A Combined Experimental and Density Functional Theory Study. *ChemCatChem* 2017. **DOI:** 10.1002/cctc.201601672

(4) Chattot, R.; Asset, T.; Bordet, P.; Drnec, J.; Dubau, L. and Maillard, F. Beyond Alloying Effects: Microstrain-Induced Enhancement of the Oxygen Reduction Reaction Kinetics on Various PtNi/C Nanostructures. *ACS Catal.* 2017, 7 (1), 398–408.

(5) Dubau, L.; Nelayah, J.; Asset, T.; Chattot, R. and Maillard, F. Implementing Structural Defects as a New Direction to Improve the Durability of PtNi/C Nanoparticles. *ACS Catal.* 2017. **DOI:** 10.1021/acscatal.7b00410

## IV. 1. Introduction to the structural properties of the porous hollow PtNi/C

In **Section I. 6. 4.** and **I. 7.**, the porous hollow PtNi/C were introduced and their activity enhancement for the ORR (*i.e.* 9-fold and 6-fold *vs.* Pt/C in SA<sub>0.95</sub> and MA<sub>0.95</sub>, respectively) was ascribed to several parameters, *i.e.* (i) the Ni-induced contraction of the lattice parameter<sup>83,84</sup>, (ii) the presence of structural defects<sup>234</sup> and (iii) the open-porous architecture<sup>84</sup>. The present chapter aims at going further in the understanding of the crucial role of Ni and of structural defects on the electrochemical reactivity of this class of electrocatalysts.

The porous nature of the hollow PtNi/C NPs was established by Dubau *et al.*<sup>84</sup>. Insights were provided by HR-TEM and electrochemical measurements coupled to theoretical calculations of the Pt specific surface area<sup>318,319</sup>: these studies showed that nanopores exist in the PtNi shell thereby providing a Pt specific surface area of *ca.* 40 – 50 m<sup>2</sup> g<sup>-1</sup><sub>Pt</sub> despite the large  $d_{\text{ext}}$  values of the hollow PtNi/C NPs<sup>84</sup>. Indeed, the Pt specific surface should only be of *ca.* 25 – 35 m<sup>2</sup> g<sup>-1</sup> if the external surface only was active<sup>84</sup> (for comparison purposes, the Pt specific surface of Pt/C NPs with  $d \sim 2 - 3$  nm is *ca.* 80 – 100 m<sup>2</sup> g<sup>-1</sup><sub>Pt</sub>).

In addition to their porous architecture, the porous hollow PtNi/C NPs also present a highly defective surface, as firstly evidenced by Dubau *et al.*<sup>234</sup> by HR-TEM and CO<sub>ads</sub> electrooxidation (see **Figure 31**). The HR-TEM evidenced that (i) the porous hollow PtNi/C NPs are composed of several PtNi nanocrystallites interconnected by grain boundaries (GBs) (highlighted by an orange pencil in HR-TEM images displayed in **Figure 31C**) and (ii) the interplanar distance between the Pt atoms columns feature extended and contracted domains<sup>234</sup>. Structural disorder largely impacts the surface reactivity of the NPs (*e.g.* for the CO<sub>ads</sub> electrooxidation, see **Section II. 3. 4.**). CO<sub>ads</sub> stripping voltammograms measured on porous hollow PtNi/C NPs (see **Figure 31D**) feature two electrooxidation peaks: a ‘low-potential’ peak located at  $E \sim 0.70$  V *vs.* RHE and a ‘high-potential’ peak at  $E \sim 0.78$  V *vs.* RHE. The ‘pre-peak’ is related to CO<sub>ads</sub> electrooxidation on catalytic sites neighbouring GBs and the main ‘peak’ to CO<sub>ads</sub> electrooxidation in regions that are far from GBs<sup>149,234,264</sup>. This assignment is further discussed in the **Section IV. 2.** According to Dubau *et al.*<sup>234</sup>, an increased density of structural defects results in enhanced kinetics for the ORR.

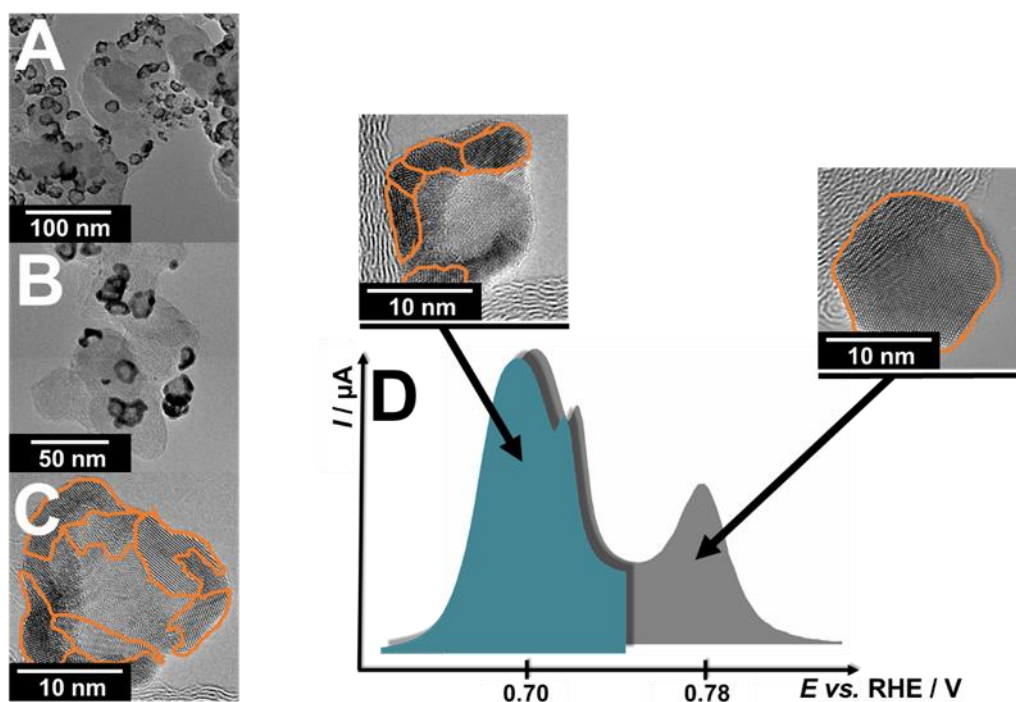


**Figure 31.** Morphological properties of porous hollow PtNi/C nanoparticles and its consequences in terms of surface reactivity. (A-C) Conventional and high-resolution transmission electron microscopy micrographs of the porous hollow PtNi NPs supported on XC72 (initial Pt<sup>2+</sup>:Ni<sup>2+</sup> atomic ratio of 1:3). (D) CO<sub>ads</sub> stripping voltammograms measured on the porous hollow PtNi/C electrocatalysts. The ‘pre-peak’ is believed to be due to CO<sub>ads</sub> electrooxidation at the structural defects (*e.g.* grain boundaries, highlighted in orange for the sake of clarity) and the main ‘peak’ assimilated to electrooxidation of CO<sub>ads</sub> that cannot diffuse to the structural defects.

In this chapter, we present our recent progresses on the synthesis and the characterization of porous hollow Pt-based NPs supported on carbon and provide rationale for their electrocatalytic activity enhancement. This chapter discusses:

- (i) the significance of the CO<sub>ads</sub> stripping peak multiplicity observed for the porous hollow PtNi/C NPs (**Section IV. 2.**);
- (ii) the determination of the surface density of structural defects and the nickel atomic content of the porous hollow PtNi/C NPs synthesized at different temperatures using a combination of CO<sub>ads</sub> stripping and X-ray based methods (**Section IV. 3.**) completed by *ab initio* calculations;
- (iii) the effect of the nature of sacrificial metal (*i.e.* Cu, Co, Ni, Fe and Zn) on the morphology and electrocatalytic activity of the ORR of the porous hollow PtNi NPs (**Section IV. 4.**);

- (iv) the effect of physical and chemical properties of the support, determined by XPS, Raman, SEM and N<sub>2</sub> adsorption on the morphology and electrocatalytic activity for the ORR of the porous hollow PtNi NPs (**Section IV. 5.**);
- (v) A general conclusion onto the parameters that control the final morphology of the porous hollow PtNi/C NPs and a comparison of the activity for the ORR of the different structures synthesized by the ‘one-pot’ method (**Section IV. 6.**).

## IV. 2. The CO<sub>ads</sub> electrooxidation peak-multiplicity

In **Section II. 3. 4.**, we briefly presented the CO<sub>ads</sub> stripping mechanism (**Equation 21 – 23**) on extended surfaces and polycrystalline NPs. As observed on **Figure 31D** and **Figure 32A**, the CO<sub>ads</sub> stripping of porous hollow PtNi/C NPs features two main peaks. This peak multiplicity was observed in the literature<sup>149</sup> and explained by the presence of (i) polycrystalline nanostructures (*e.g.* Pt NPs agglomerates<sup>149</sup>) and (ii) monocrystalline structures (*e.g.* monocrystalline NPs).

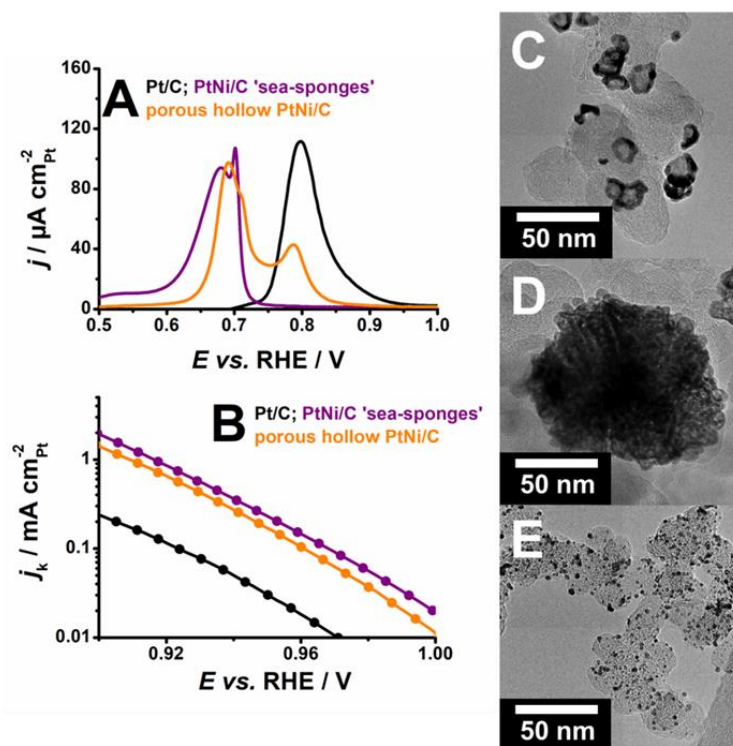


**Figure 32.** Electrochemical and morphological properties of the electrocatalysts discussed in this chapter. **(A)** CO<sub>ads</sub> stripping ( $\nu = 0.020 \text{ V s}^{-1}$ , electrolyte = Ar-saturated 0.1 M HClO<sub>4</sub>). **(B)** Linear sweep voltammetry in Tafel representation, corrected for Ohmic drop and diffusion ( $\nu = 0.005 \text{ V s}^{-1}$ , electrolyte = O<sub>2</sub>-saturated 0.1 M HClO<sub>4</sub>,  $\omega = 1600 \text{ rpm}$ ). **(C – E)** TEM micrographs of **(C)** the commercial Pt/C, **(D)** the PtNi/C ‘sea-sponges’ and **(E)** the porous hollow PtNi/C NPs.

To better explain the CO stripping peak-multiplicity, three materials of interest has been chosen, *i.e.* (i) a commercial Pt/C electrocatalyst, composed of monocrystalline NPs (and thus with only one CO<sub>ads</sub> stripping peak at  $E \sim 0.78$  V *vs.* RHE), (ii) the PtNi/C ‘sea-sponges’, *i.e.* a polycrystalline and highly defective nanostructure, without any monocrystalline NPs and thus only a ‘low-potential’ peak for the CO<sub>ads</sub> electrooxidation<sup>247</sup> (see **Figure 32A**) and (iii) the porous hollow PtNi/C.

**Table 1.** External diameter ( $d_{\text{ext}}$ ) measured by TEM and crystallite diameter measured by X-Ray Diffraction for the electrocatalysts discussed in this chapter.

	Pt/C	PtNi/C ‘sea-sponges’	porous hollow PtNi/C NPs
$d_{\text{ext}} / \text{nm}$	$2.0 \pm 0.5$	$61 \pm 21$	$11.4 \pm 1.9$
$d_{\text{XRD}} / \text{nm}$	$1.3 \pm 0.2$	$4.5 \pm 0.9$	$2.4 \pm 0.2$

The physical and electrochemical properties of the porous hollow PtNi/C NPs and of the materials discussed in **Figure 33A** (PtNi/C ‘sea-sponges’<sup>247</sup> and Pt/C) are summarized in **Figure 32** and **Table 1**. The PtNi/C ‘sea-sponges’ are Pt-based NPs with  $d_{\text{ext}} = 61 \pm 21$  nm, a Ni-content of *ca.* 15 at. %, an open-porous architecture and a 10-fold increase in SA for the ORR at  $E = 0.95$  V *vs.* RHE *vs.* commercial Pt/C (see **Figure 32** and Ref.<sup>247</sup>). All the PtNi structures present a pure Pt surface: the electrocatalysts were acid leached during their synthesis ( $t = 22$  h in a 1 M H<sub>2</sub>SO<sub>4</sub> solution<sup>84,232,247</sup>). The porous hollow PtNi/C NPs (**Figure 32C**) and the PtNi/C ‘sea-sponges’ (**Figure 32D**) present a notable difference between their external diameter ( $d_{\text{ext}}$ ) and their crystallite size ( $d_{\text{XRD}}$ ) (see **Table 1**). This is relevant of their polycrystalline structure, *i.e.* each nanostructure contains several nanocrystallites (NCs) interconnected by grain boundaries (GBs). This explains the presence of, (i) for the PtNi/C ‘sea-sponges’, a main and single peak at  $E < 0.7$  V *vs.* RHE (*i.e.* the ‘low-potential’ peak) in CO<sub>ads</sub> stripping voltammograms and (ii) for the PtNi/C porous hollow NPs, a ‘low-potential’ peak at  $E \sim 0.7$  V *vs.* RHE. This however does not explain the ‘high-potential’ peak observed at  $E \sim 0.78$  V *vs.* RHE as the porous hollow PtNi/C NPs are, in theory, composed of polycrystalline NPs<sup>84,232</sup>.

To assess the origin of the ‘high-potential’ peak observed on porous hollow PtNi/C NPs, different CO<sub>ads</sub> coverages were achieved and the sub monolayers were stripped similarly to what is done for a full CO<sub>ads</sub> monolayer (**Figure 33**). To this aim, a volume ( $0.1 \text{ mL} < V < 2 \text{ mL}$ ) of CO-saturated 0.1 M HClO<sub>4</sub> solution was introduced in the electrolyte, before quickly removing

the CO molecules present in solution by Ar bubbling. If the two peaks were induced by two different structures (*e.g.* independent polycrystalline and monocrystalline NPs), the charge under the CO<sub>ads</sub> stripping peaks should grow simultaneously as a function of the CO<sub>ads</sub> coverage<sup>276</sup>. This is the case in **Figure 33A** where a mixture of PtNi/C ‘sea-sponges’ (one CO stripping contribution at low potential) NPs and commercial Pt/C NPs (one CO stripping contribution at high potential), (see **Figure 33** and **Figure 32A**) was used. The two peaks are clearly visible for CO<sub>ads</sub> coverage ( $X_{CO}$ )  $\geq$  19 %. An interesting feature from their growth is that, if the ‘low-potential’ peak ( $E_{U1}$ ) (ascribed to the ‘sea-sponges’) potential remain constant, the ‘high-potential’ ( $E_{U2}$ ) peak potential increases, from  $E_{U2} = 0.74$  V *vs.* RHE to  $E_{U2} = 0.79$  V *vs.* RHE. This is due to an increased coverage in CO<sub>ads</sub> which decreases the density of adsorption sites for the OH<sub>ads</sub> species on the monocrystalline NPs. CO<sub>ads</sub> electrooxidation (**Equation 23**) consequently proceeds at higher potentials.

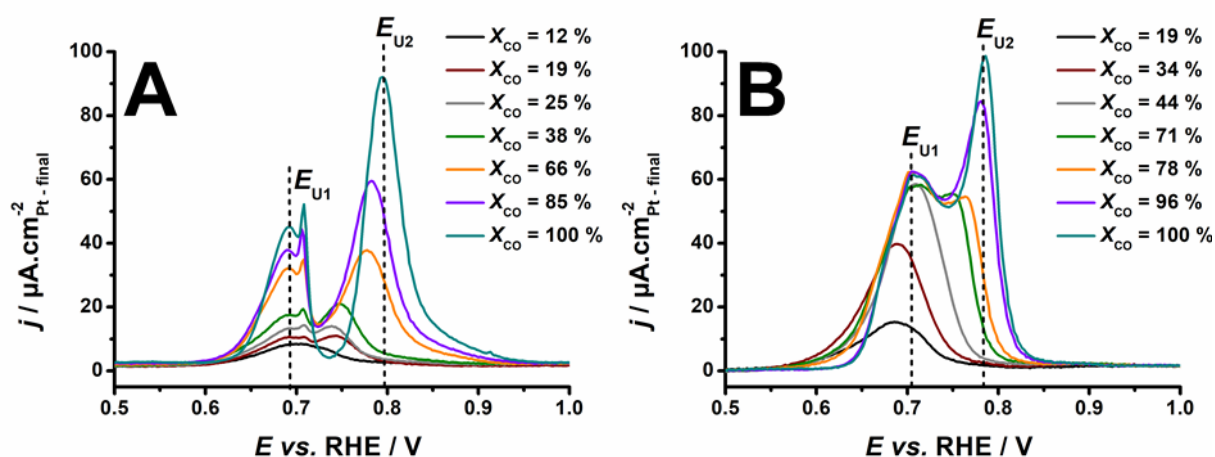


**Figure 33.** Changes in the CO<sub>ads</sub> stripping voltammograms while modifying the CO<sub>ads</sub> initial coverage ( $X_{CO}$ ) of (A) an electrocatalyst composed of 67 wt. % of PtNi/C ‘sea-sponges’ and 33 wt. % of commercial Pt/C and (B) a porous hollow PtNi/C electrocatalyst. The CO was adsorbed by injecting a determined volume of a CO-saturated 0.1 M HClO<sub>4</sub> solution. The remaining CO was removed after  $t = 1$  min of adsorption, by bubbling Ar in the electrolyte (other conditions:  $\nu = 0.020$  V s<sup>-1</sup>, electrolyte = Ar-saturated 0.1 M HClO<sub>4</sub>). All the currents were normalized to the ECSA determined for the electrocatalyst with  $X_{CO} = 100$  %.

Urchaga *et al.*<sup>320</sup> reported a 3-peak profile for CO<sub>ads</sub> stripping voltammograms measured on different nanostructures (cubic, octahedral, cuboctahedra NPs) in 0.5 M H<sub>2</sub>SO<sub>4</sub>. They ascribed the lowest potential peak (LPP), the medium potential peak (MPP) and the high potential peak (HPP) to CO<sub>ads</sub> electrooxidation on:

- (i) well-ordered surfaces (100) and (111) containing surface defects;
- (ii) (111) facets and, at higher potential, low coordination sites;
- (iii) (100) facets.

This is well in line with results reported in **Figure 33A**: (i) the LPP observed at  $E_{U1} = 0.69 - 0.71$  V vs. RHE, corresponds to the  $\text{CO}_{\text{ads}}$  electrooxidation on highly disordered facets or NPs ('sea-sponges') while (ii) the HPP observed at  $E_{U2} = 0.74 - 0.79$  V vs. RHE corresponds to the  $\text{CO}_{\text{ads}}$  electrooxidation on commercial Pt/C. Note however that the 3<sup>rd</sup>  $\text{CO}_{\text{ads}}$  electrooxidation peak (*i.e.* (100) facets) was not observed by Urchaga *et al.*<sup>320</sup> on small spherical Pt/C NPs.

The  $\text{CO}_{\text{ads}}$  undercoverage observed for the porous hollow NPs consists of (i) the 'low-potential' peak appearance and growth for  $X_{\text{CO}} < 71$  % and (ii) the appearance and potential shift (from  $E = 0.75$  V vs. RHE to  $E = 0.78$  V vs. RHE) of the 'high-potential' peak for  $X_{\text{CO}} \geq 71$  % (see **Figure 33B**).  $\text{CO}_{\text{ads}}$  adsorbs sequentially on the adsorption sites responsible for the 'low-potential' and the 'high-potential'  $\text{CO}_{\text{ads}}$  stripping peaks. It means that, by opposition to an 'agglomerated + non-agglomerated' structure such as presented in **Figure 33A**, the  $\text{CO}_{\text{ads}}$  stripping sites are connected (*i.e.* that they belong to the same NPs). According to Maillard *et al.*<sup>276</sup>, the  $\text{CO}_{\text{ads}}$  binds first on the low coordination sites (*i.e.* the sites that strongly bind  $\text{CO}_{\text{ads}}$ ) before the medium / high coordination sites. Thus, we inferred from those results that, on porous hollow PtNi/C NPs, (i) the CO adsorbs first on sites with a medium coordination number, before (ii) binding to sites that weakly bind  $\text{CO}_{\text{ads}}$ , *i.e.* the high coordination sites (*e.g.* concavities, *etc.*) These sites present a depreciated activity for the  $\text{CO}_{\text{ads}}$  electrooxidation since they bind  $\text{OH}_{\text{ads}}$  weakly<sup>156</sup>, the reaction being thus limited by the OH adsorption, *i.e.* **Equation 21**. To determine the nature of the different CO adsorption sites,  $\text{CO}_{\text{ads}}$  was oxidized at different potentials ( $0.550 \text{ V} \leq E_{\text{desor}} \leq 0.740$  V vs. RHE) during  $t = 60$  s before the  $\text{CO}_{\text{ads}}$  stripping (see **Figure 34A**), to obtain insights on the different peaks of the  $\text{CO}_{\text{ads}}$  stripping. The  $\text{CO}_{\text{ads}}$  oxidation can be divided into three phases:

- (i) for  $E_{\text{desor}} = 0.550$  and  $0.575$  V vs. RHE, the decrease of the  $\text{CO}_{\text{ads}}$  stripping lowest potential peak ( $E_{D1}$ , see **Figure 34B**). This suggests that the low potential peak can be divided into two peaks, with a peak potential of  $E_{D1} = 0.680$  V vs. RHE and  $E_{D2} = 0.700$  V vs. RHE;

- (ii) for  $0.600 \text{ V} \leq E_{\text{desor}} < 0.640 \text{ V}$  vs. RHE, the disappearance of a  $\text{CO}_{\text{ads}}$  stripping shoulder in the  $E_{\text{D2}}$  potential range;
- (iii) for  $E_{\text{desor}} \geq 0.640 \text{ V}$  vs. RHE the decrease and disappearance of the high potential peak ( $E_{\text{D3}}$ ) of the  $\text{CO}_{\text{ads}}$  stripping.

If considering the  $\text{H}_{\text{upd}}$  behaviour (see **Figure 34C** and **Figure 34D**), these phases correspond to (i) the decrease of the ‘low-potential’ (*i.e.*  $0.05 \text{ V} < E < 0.26 \text{ V}$  vs. RHE)  $\text{H}_{\text{upd}}$ , (ii) the decrease of the ‘high-potential’ (*i.e.*  $0.26 \text{ V} < E < 0.40 \text{ V}$  vs. RHE)  $\text{H}_{\text{upd}}$  and (iii) a global diminution and disappearance of the  $\text{H}_{\text{upd}}$ , the ‘high potential’  $\text{H}_{\text{upd}}$  disappearing at  $E = 0.71 \text{ V}$  vs. RHE. According to the works of Snyder *et al.*<sup>81</sup> and Chattot *et al.*<sup>247</sup>, an enhanced  $\text{H}_{\text{upd}}$  in the  $0.26 \text{ V} < E < 0.40 \text{ V}$  vs. RHE potential range is relevant for electrocatalysts presenting an important density of structural defects. Therefore, the peak  $E_{\text{D2}}$  (see **Figure 34B**) is representative of the population of structural defects (*i.e.* grain boundaries, *etc.*) that have an enhanced reactivity for  $\text{CO}_{\text{ads}}$  electrooxidation while the peak  $E_{\text{D1}}$  represents the population of active sites that are connected to those defects, *i.e.* where the  $\text{CO}_{\text{ads}}$  can diffuse from the active site to the structural defects to be oxidized into  $\text{CO}_2$  (see **Equation 22**), according to the mechanism proposed by Lebedeva *et al.*<sup>144,146,147</sup> on extended surfaces.

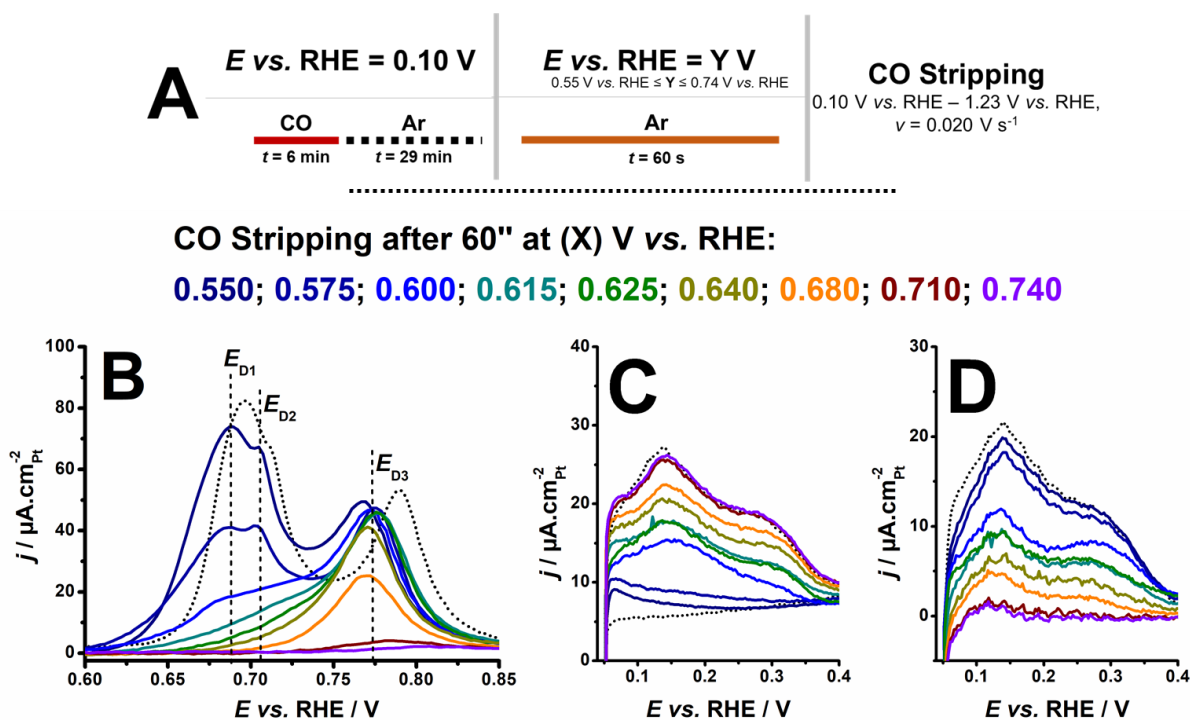


**Figure 34.** Changes in the  $\text{CO}_{\text{ads}}$  stripping patterns after partial  $\text{CO}_{\text{ads}}$  electrooxidation of a fully covered surface. The electrode potential was stepped from  $E = 0.1 \text{ V vs. RHE}$  to  $0.550 \text{ V} \leq E_{\text{desor}} \text{ vs. RHE} \leq 0.740 \text{ V}$  during  $t = 60 \text{ s}$ , then stepped back to  $E = 0.1 \text{ V vs. RHE}$  and a  $\text{CO}_{\text{ads}}$  stripping voltammogram was then immediately recorded. **(A)** Schematic representation of the partial  $\text{CO}_{\text{ads}}$  electrooxidation protocol. **(B)**  $\text{CO}_{\text{ads}}$  stripping of the porous hollow PtNi/C (the dotted line corresponds to  $\text{CO}_{\text{ads}}$  stripping recorded on a fully covered surface). **(C)** Focus on the  $H_{\text{upd}}$  region during the first potential sweep of the  $\text{CO}_{\text{ads}}$  stripping presented in **(B)** (the dotted lines correspond to a non-covered surface and a fully covered surface). **(D)**  $H_{\text{upd}}$  of a non-covered porous hollow PtNi/C electrocatalyst minus the  $H_{\text{upd}}$  presented in **(C)**.

The position of  $E_{\text{D3}}$  is independent on the potential chosen for the partial  $\text{CO}_{\text{ads}}$  electrooxidation (see **Figure 34B**) demonstrating that  $\text{CO}_{\text{ads}}$  cannot diffuse (or its diffusion rate is too low, *i.e.* the diffusion is impossible between the *ca.* 30 s between the end of the potential step at  $0.550 \text{ V} \leq E_{\text{desor}} \text{ vs. RHE} \leq 0.740 \text{ V}$  and the remaining  $\text{CO}_{\text{ads}}$  electrooxidation during the  $\text{CO}_{\text{ads}}$  stripping). To gain further insights on the  $\text{CO}_{\text{ads}}$  diffusion from the high coordination sites and its subsequent oxidation at the structural defects, the  $\text{CO}_{\text{ads}}$  monolayer was partially stripped during  $t = 60 \text{ s}$  at  $E = 0.625 \text{ V vs. RHE}$  (to remove  $E_{\text{D1}}$  and  $E_{\text{D2}}$ ) and the  $\text{CO}_{\text{ads}}$  stripping was performed after  $0 \text{ min} \leq t \leq 90 \text{ min}$ . The results are presented in **Figure 35**.

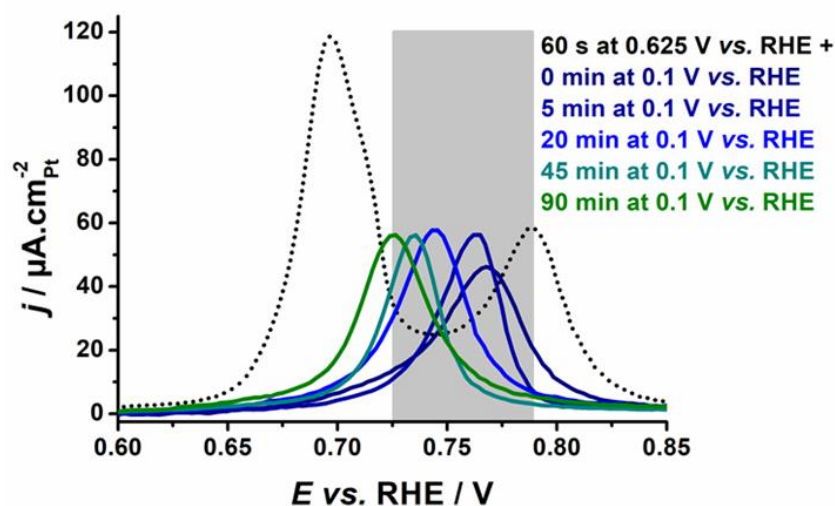


**Figure 35.** Changes in the  $\text{CO}_{\text{ads}}$  stripping patterns after partial  $\text{CO}_{\text{ads}}$  electrooxidation of a fully covered surface. The electrode potential was stepped from  $E = 0.1 \text{ V vs. RHE}$  to  $E_{\text{desor}} = 0.625 \text{ V vs. RHE}$  during  $t = 60 \text{ s}$ , then stepped back to  $E = 0.1 \text{ V vs. RHE}$  and a  $\text{CO}_{\text{ads}}$  stripping voltammogram was then recorded after  $0 \text{ min} \leq t \leq 90 \text{ min}$ .

$E_{\text{D3}}$  shifts from  $E_{\text{D3}} = 0.767 \text{ V vs. RHE}$  for  $t = 0 \text{ min}$  after the partial  $\text{CO}_{\text{ads}}$  electrooxidation to  $E_{\text{D3}} = 0.727 \text{ V vs. RHE}$  after  $t = 90 \text{ min}$  (for higher times,  $E_{\text{D3}}$  stabilize between  $0.730$  and  $0.740 \text{ V vs. RHE}$ ). This provides two essential informations about the  $\text{CO}_{\text{ads}}$  stripping on porous hollow PtNi/C NPs:

- (i) the CO adsorbed onto the high coordination sites can partly diffuse to sites with a stronger  $\text{CO}_{\text{ads}}$  binding. However, this diffusion is noticeably slow. Considering a crystallite size of *ca.*  $2.5 \text{ nm}$  (see **Table 1**) and that only GBs are structural defects favourable for a  $\text{CO}_{\text{ads}}$  electrooxidation at low potential, the  $\text{CO}_{\text{ads}}$  covered *ca.*  $1.25 \text{ nm}$  in *ca.*  $90 \text{ min}$ , *i.e.* a diffusion rate of  $\sim 2 \times 10^{-18} \text{ cm}^2 \text{ s}^{-1}$ , *i.e.* 2 orders of magnitude lower than determined by Maillard *et al.*<sup>265</sup> on  $2 \text{ nm}$  Pt NPs ( $\sim 10^{-16} \text{ cm}^2 \text{ s}^{-1}$ ). The surface diffusion of  $\text{CO}_{\text{ads}}$  thus appears to be extremely difficult on highly defective NPs surfaces for the CO adsorbed onto the high coordination sites;
- (ii)  $E_{\text{D3}}$  does not diminish to  $E_{\text{D2}}$  or  $E_{\text{D1}}$  potentials, *i.e.* the  $\text{CO}_{\text{ads}}$  adsorbed onto the high coordination sites does not fully diffuse to the structural defects or their neighbouring sites. Therefore, some  $\text{CO}_{\text{ads}}$  cannot diffuse from their initial adsorption site.

**Figure 36** presents the effect of the scan rate ( $\nu$ ) on the  $\text{CO}_{\text{ads}}$  stripping. The shape of the ‘low-potential’ peak changes dramatically with the potential sweep rate. Indeed,  $E_{\text{D2}}$  (see **Figure 36B**) shifts from potentials close to  $E_{\text{D1}}$  potential range at  $\nu = 0.002 \text{ V s}^{-1}$  to higher potentials)

for  $\nu > 0.002 \text{ V s}^{-1}$ ; the potential difference increasing with the increase of the scan rate. On stepped single crystals, Lebedeva *et al.*<sup>144</sup> observed that the CO adsorbed at the (100) or (110) steps had to be first converted into ‘terrace’  $\text{CO}_{\text{ads}}$  before diffusing to the steps to be oxidized. A similar phenomenon is observed in **Figure 36**: the  $\text{CO}_{\text{ads}}$  on the structural defects have first to diffuse out of the latter before being electrooxidized, resulting in an electrooxidation at the same potential at  $\nu \leq 0.005 \text{ V s}^{-1}$ , but at higher potentials at  $\nu > 0.005 \text{ V s}^{-1}$ . The charge under the ‘high-potential’ peak ( $E_{\text{D3}}$ ) remains roughly constant (25 % to 40 % of the charge is under  $E_{\text{D3}}$ , without dependence to the scan rate) with the scan rate (see **Figure 36**). According to **Figure 35**, the position of the  $E_{\text{D3}}$  peak remain almost identical from  $t = 0 \text{ min}$  to  $t = 5 \text{ min}$  ( $E_{\text{D3}} = 0.767 \text{ V vs. RHE}$  and  $E_{\text{D3}} = 0.762 \text{ V vs. RHE}$ , respectively) and  $E_{\text{D3}}$  never merge with  $E_{\text{D1}}$  and  $E_{\text{D2}}$ . This explains why no dramatic changes of the  $E_{\text{D3}}$  charge and position are observed.

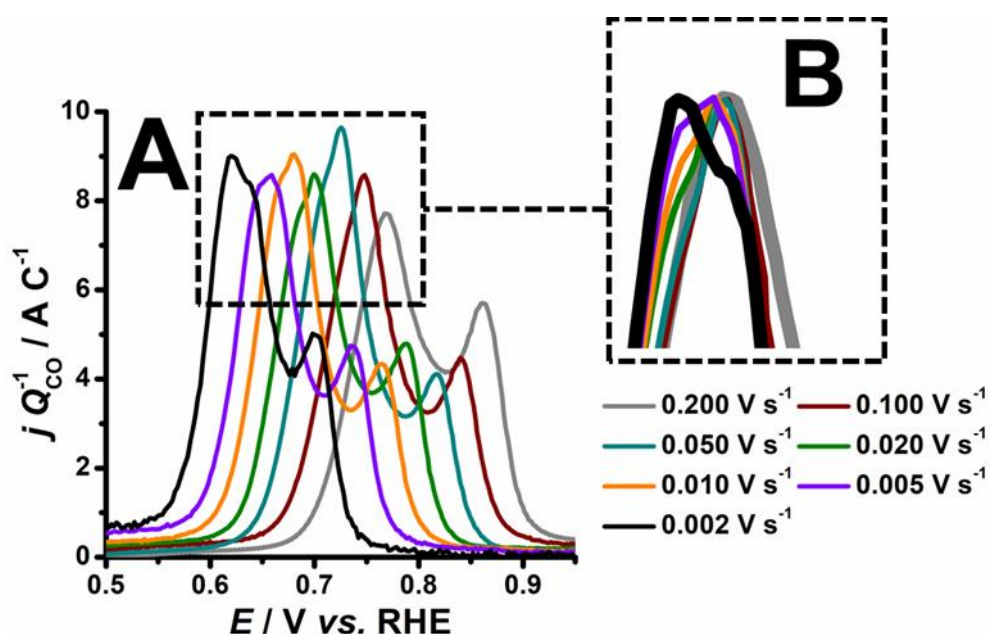


**Figure 36.** (A) Normalised  $\text{CO}_{\text{ads}}$  stripping patterns voltammograms for hollow PtNi/C nanoparticles at different potential sweep rates, *i.e.*  $0.002 \text{ V s}^{-1} < \nu < 0.200 \text{ V s}^{-1}$ . (B) Focus on the  $\text{CO}_{\text{ads}}$  stripping ‘low-potential’ peak – the peaks were aligned in current and potential. All the currents were normalized by the charge under the peaks ( $Q_{\text{CO}}$ ) – other conditions: electrolyte = Ar-saturated 0.1 M  $\text{HClO}_4$ .

Le Bacq *et al.*<sup>157</sup> showed that disordered Pt-based structures, such as the porous hollow PtNi/C NPs, are composed of a combination of low and high coordinated active sites (and contracted and relaxed lattices<sup>157,234</sup>). Calle-Vallejo *et al.*<sup>273</sup> recently evidenced that the optimal generalized coordination number ( $\overline{CN}$ <sup>155,156</sup>) was 5.4 for the  $\text{CO}_{\text{ads}}$  electrooxidation on Pt surfaces. Catalytic sites with a higher coordination number bind  $\text{OH}_{\text{ads}}$  species too weakly; thereby, the

$\text{CO}_{\text{ads}}$  electrooxidation kinetics becomes limited by  $\text{OH}_{\text{ads}}$  adsorption (**Equation 21**) while  $\text{CO}$  molecules are bound too strongly on catalytic sites with a low coordination number, thus limiting the  $\text{CO}_{\text{ads}}$  electrooxidation (**Equation 22**). Therefore, as observed by Lebedeva *et al.*<sup>144,146,147</sup>, the most active sites for the  $\text{CO}_{\text{ads}}$  electrooxidation on monocrystalline structures should be the steps with  $\overline{\text{CN}} \sim 5 - 6$  (as in the Pt(221) and Pt(331) surfaces<sup>152,153,273</sup>), where the  $\text{OH}$  adsorbs at the top before oxidizing the  $\text{CO}_{\text{ads}}$ . Here, we extrapolate this mechanism to highly defective polycrystalline NPs (see **Figure 37**). The ‘low-potential’ peak of the  $\text{CO}_{\text{ads}}$  stripping was ascribed to the  $\text{CO}_{\text{ads}}$  electrooxidation on the beneficial surface defects with a  $\overline{\text{CN}} \sim 5 - 6$ , the  $\text{CO}_{\text{ads}}$  being originally adsorbed on these sites ( $E_{\text{D2}}$ , see **Figure 34**) or diffusing from the neighbouring sites ( $E_{\text{D1}}$ , see **Figure 34**). The ‘high-potential’ peak ( $E_{\text{D3}}$ ) was ascribed to  $\text{CO}_{\text{ads}}$  electrooxidation ‘trapped’ in sites that presented a too high coordination number (*e.g.* concave sites, as likely observed on the inner surface of the porous hollow PtNi/C, see **Figure 37**) no sign of their presence (*i.e.*  $\text{CO}_{\text{ads}}$  adsorbing at high potentials before adsorbing at low potentials, *etc.*) has been observed throughout this section, thus inducing that (i) their contribution to the  $\text{CO}_{\text{ads}}$  stripping is negligible or that (ii) they also contain structural defects beneficial for the  $\text{CO}_{\text{ads}}$  stripping and, as such, contribute to the ‘low-potential’ peak.

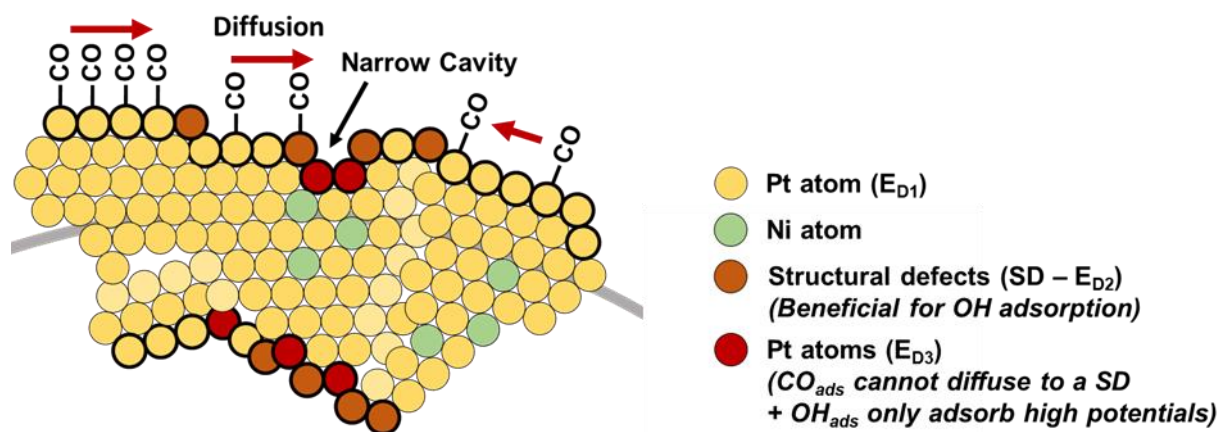


**Figure 37.** Description of the different sites observed for  $\text{CO}_{\text{ads}}$  stripping on PtNi/C porous hollow NPs and their associated  $\text{CO}_{\text{ads}}$  stripping peak.

### IV. 3. The porous hollow PtNi/C NPs, a highly defective structure

#### IV. 3. 1. The effect of the temperature onto the PtNi/C NPs nanostructure

In Section IV. 1., the beneficial role of the structural defects for the ORR was introduced. To control their density, porous hollow PtNi/C NPs were synthesized at different temperatures, *i.e.*  $T = 278, 293, 313, 333$  and  $353$  K (see Figure 38). The porous hollow PtNi/C electrocatalysts synthesized at different temperature feature a similar Ni content (Figure 38C), similar external and inner diameters (Figure 38D) and are composed of 1.5 – 3.5 nm crystallites agglomerated to form the shell of the hollow structure (Figure 38E, Figure 38F and Table 2).

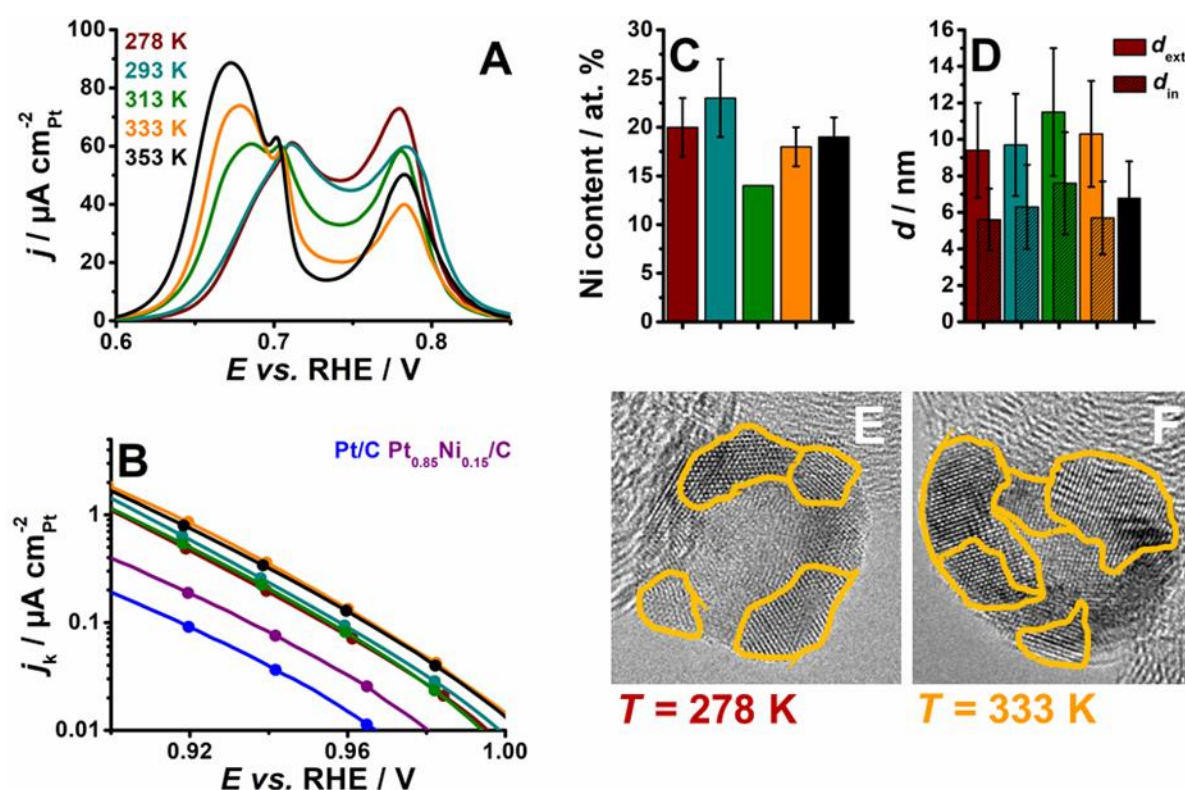


**Figure 38.** Electrochemical and physico-chemical properties of the porous hollow PtNi/C electrocatalysts synthesized at  $T = 278, 293, 313, 333$  and  $353$  K. (A)  $\text{CO}_{\text{ads}}$  stripping measurements on the electrocatalysts in Ar-saturated 0.1 M  $\text{HClO}_4$  at  $\nu = 0.02$   $\text{V s}^{-1}$ . (B) Tafel plot of Ohmic drop and mass-transport corrected linear sweep voltammograms in  $\text{O}_2$ -saturated 0.1 M  $\text{HClO}_4$  at  $\nu = 0.005$   $\text{V s}^{-1}$  and  $\omega = 1600$  rpm ( $T = 298$  K, Pt loading =  $20$   $\mu\text{g cm}^{-2}$ ). (C) Nickel atomic content determined by atomic adsorption spectroscopy (AAS). (D) External ( $d_{\text{ext}}$ ) and inner ( $d_{\text{in}}$ ) diameter of the porous hollow PtNi/C NPs synthesized at different temperatures – due to its dual morphology, *i.e.* agglomerates + isolated NPs, only the diameter of the isolated NPs was given for the electrocatalyst synthesized at  $T = 353$  K. (E) HR-TEM micrograph of the electrocatalyst synthesized at  $T = 278$  K. The grain boundaries are highlighted in orange. (F) HR-TEM micrograph of the electrocatalyst synthesized at  $T = 333$  K. The grain boundaries are highlighted in orange.

**Table 2.** Crystallite size ( $d_{\text{XRD}}$ ) for the electrocatalysts synthesized at different temperatures.

	$T = 278 \text{ K}$	$T = 293 \text{ K}$	$T = 313 \text{ K}$	$T = 333 \text{ K}$	$T = 353 \text{ K}$
$d_{\text{XRD}} / \text{nm}$	$1.5 \pm 0.1$	$1.8 \pm 0.1$	$3.2 \pm 0.1$	$3.2 \pm 0.1$	$3.5 \pm 0.1$

The effect of the temperature onto the morphology of the hollow PtNi/C NPs is subtle. It is well-established that  $\text{BH}_4^-$  ions homogeneously decompose into  $\text{BO}_2$  species in water (see **Section III. 3.** and Ref. <sup>321,322</sup>). Hence, aged  $\text{NaBH}_4$  solutions or solutions prepared at pH values < 9 are likely to feature depreciated reducing power. The same holds true for the temperature of the aqueous solvent <sup>321</sup>. Since the hydrolysis rate of the  $\text{BH}_4^-$  ions is slow at low temperature (their half-life time is high), the nucleation of Ni/C NPs on the carbon support is favoured, thereby producing smaller NPs with thinner PtNi shells and, therefore, smaller PtNi crystallites (see **Figure 38** and **Table 2**). Conversely,  $\text{BH}_4^-$  ions decompose rapidly at higher temperatures, resulting in limited number of nuclei on the carbon support, thicker PtNi shells and collapsed and/or aggregated PtNi NPs.

The SA (for the ORR) measured at  $E = 0.95 \text{ V vs. RHE}$  on the porous hollow PtNi/C NPs synthesized at  $T = 333 \text{ K}$  was 7-fold higher than that of a commercial Pt/C and 2.5-fold higher than that of a solid PtNi/C electrocatalyst with identical crystallite size, Ni content and lattice parameter (see **Figure 38B** and **Table 3**). The enhancement of the ORR kinetics was 1.7-fold on the best (electrocatalyst synthesized at  $T = 333 \text{ K}$ ) compared to the less-performing porous hollow NPs (electrocatalyst synthesized at  $T = 278 \text{ K}$ ). Interestingly, this higher ORR activity is correlated to a predominance of the  $\text{CO}_{\text{ads}}$  stripping ‘low-potential’ peak, *i.e.* a higher ratio of the  $\text{CO}_{\text{ads}}$  stripping ‘low-potential’ charge (introduced as  $Q_{\text{pp,CO}}$  in **Section II. 3. 4.**) to the total charge of the  $\text{CO}_{\text{ads}}$  stripping ( $Q_{\text{T,CO}}$ ) (see **Figure 38A**). Some physico-chemical properties of a PtNi/C electrocatalyst, such as the density of structural defects, the Ni content or the Ni-induced strain, can be determined from the  $\text{CO}_{\text{ads}}$  stripping voltammograms. This is especially true for electrocatalysts with a low Ni content, similar crystallite size and Pt-enriched surface.

**Table 3.** Activity for the oxygen reduction reaction – corrected from the Ohmic losses and the diffusion in solution – at  $E = 0.95$  V and  $E = 0.90$  vs. RHE for the electrocatalysts synthesized at  $T = 278, 293, 313, 333$  and  $353$  K and the Pt/C and PtNi/C references. The activities were either given with respect to the electrochemical surface area of the electrocatalysts (specific activity, SA) or to the mass of platinum in the electrocatalyst (mass activity, MA). The Pt specific surface area of the electrocatalysts ( $S_{\text{Pt,CO}}$  in  $\text{m}^2 \text{g}_{\text{Pt}}^{-1}$ ) is also provided.

	$\text{SA}_{0.95}$ / $\mu\text{A cm}_{\text{Pt}}^{-2}$	$\text{MA}_{0.95}$ / $\text{A g}_{\text{Pt}}^{-1}$	$\text{SA}_{0.90}$ / $\mu\text{A cm}_{\text{Pt}}^{-2}$	$\text{MA}_{0.90}$ / $\text{A g}_{\text{Pt}}^{-1}$	$\text{S}_{\text{Pt,CO}}$ / $\text{m}^2 \text{g}_{\text{Pt}}^{-1}$
<b>Pt/C</b>	$26 \pm 3$	$21 \pm 2$	$209 \pm 32$	$166 \pm 30$	$83 \pm 7$
<b>PtNi/C</b>	$70 \pm 20$	$26 \pm 5$	$575 \pm 157$	$215 \pm 41$	$42 \pm 6$
<b><math>T = 278</math> K</b>	$108 \pm 18$	$60 \pm 11$	$1000 \pm 111$	$580 \pm 72$	$56 \pm 8$
<b><math>T = 293</math> K</b>	$119 \pm 31$	$62 \pm 10$	$1328 \pm 146$	$699 \pm 110$	$51 \pm 7$
<b><math>T = 313</math> K</b>	$140 \pm 29$	$53 \pm 6$	$1247 \pm 139$	$496 \pm 40$	$42 \pm 5$
<b><math>T = 333</math> K</b>	$179 \pm 41$	$77 \pm 12$	$1677 \pm 204$	$695 \pm 89$	$41 \pm 3$
<b><math>T = 353</math> K</b>	$170 \pm 48$	$62 \pm 13$	$1498 \pm 148$	$550 \pm 50$	$37 \pm 2$

According to our findings in **Section IV. 2.**, the ‘accessibility’ of the structural defects on the electrocatalyst surface is proportional to the ratio of the electrical charge under the  $\text{CO}_{\text{ads}}$  stripping ‘low-potential’ peak ( $Q_{\text{pp,CO}}$ ) to the total charge of the  $\text{CO}_{\text{ads}}$  stripping ( $Q_{\text{T,CO}}$ ), as the ‘low-potential’ peak is relevant for the  $\text{CO}_{\text{ads}}$  electrooxidation from the structural defects and their neighbouring sites. The electrocatalysts with the highest accessibility to the structural defects also present the highest surface density of structural defects, as evidenced by a visible  $E_{\text{D2}}$  peak (*i.e.* the peak accounting for the oxidation of  $\text{CO}_{\text{ads}}$  adsorbed on the structural defects, see **Section IV. 3.**) for the electrocatalysts synthesized at  $T \geq 333$  K. A straightforward relationship exists between the density of the structural defects ( $Q_{\text{pp,CO}} / Q_{\text{T,CO}}$ ) and the specific activity for the ORR of porous hollow PtNi/C NPs (see **Figure 39A**). The presence of a non-noble metal (PtM,  $M = \text{Fe}, \text{Ni}, \text{Co}, \text{etc.}$ ) in the Pt NCs also influences the  $\text{CO}_{\text{ads}}$  stripping measurements. Recent works from van der Vliet *et al.*<sup>109</sup> and Bandarenka *et al.*<sup>271</sup> have shown that  $\text{Pt}_3\text{Ni}$  skin surfaces and Cu/Pt near surface alloys present a lower overpotential for the  $\text{CO}_{\text{ads}}$  oxidation than pure Pt surfaces. This trend is widely observed in the literature (PdM@PtPd/C core-shell<sup>323</sup>, PtCo and PtNi ribbons<sup>324</sup> or PtNi hollow NPs<sup>84</sup>).

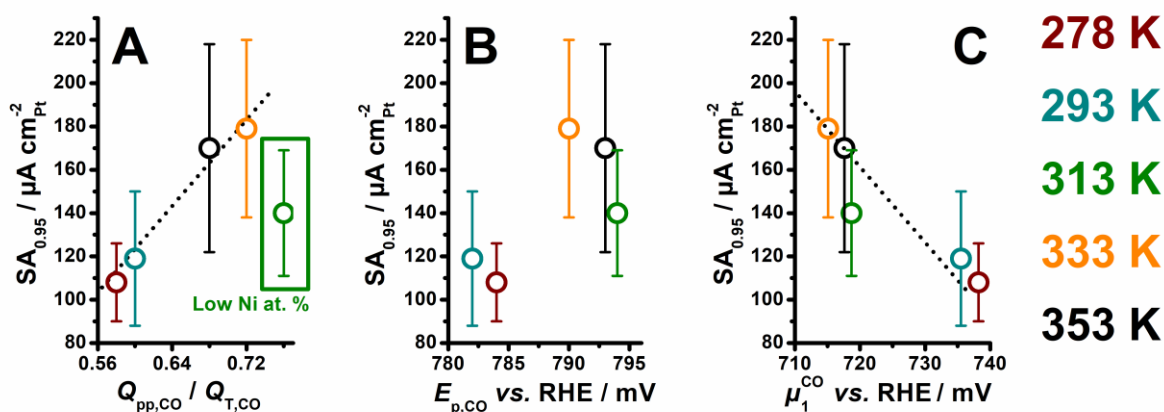


**Figure 39.** Variation of the specific activity for the ORR measured at  $E = 0.95 \text{ V vs. RHE}$  on the porous hollow PtNi/C electrocatalysts synthesized at  $T = 278, 293, 313, 333$  and  $353 \text{ K}$  vs. (A) the ratio of the electrical charge under the ‘low-potential’ peak ( $Q_{pp,CO}$ ) to the total  $\text{CO}_{\text{ads}}$  stripping charge ( $Q_{T,CO}$ ), (B) the potential of the ‘high-potential’ peak of the  $\text{CO}_{\text{ads}}$  stripping ( $E_{p,CO}$ ), (C) the first moment of the potential weight of the  $\text{CO}_{\text{ads}}$  stripping ( $\mu_1^{\text{CO}}$ ).

**Figure 40A** and **Figure 40B** display the changes of the position of the ‘high-potential’ peak of the  $\text{CO}_{\text{ads}}$  stripping ( $E_{p,CO}$ ) vs. the Ni atomic content and vs. the PtNi lattice parameter, respectively. The variations of the ‘low-potential’ of the  $\text{CO}_{\text{ads}}$  stripping ( $E_{pp,CO}$ ) show no direct relationship with the Ni content. In contrast, a linear relationship is observed between  $E_{p,CO}$  and the Ni content (**Figure 40A**). This relationship is even more linear between  $E_{p,CO}$  and the lattice parameter of the electrocatalyst (**Figure 40B**). In conclusion,  $E_{p,CO}$  appears to be a relevant marker to approximate the Ni content and the Ni-induced contraction of the lattice parameter for porous hollow PtNi/C electrocatalysts (and, therefore, the modification of the Pt 5d-band centre by the strain and ligand effects<sup>105–108</sup>).

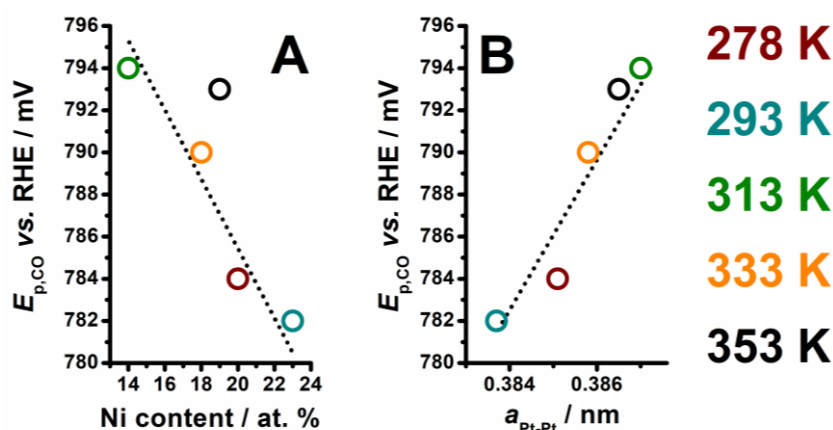


**Figure 40.** Variation of (A) the potential of the high-potential peak of the CO<sub>ads</sub> stripping voltammogram ( $E_{p,CO}$ ) on the porous hollow PtNi/C electrocatalysts synthesized at  $T = 278, 293, 313, 333$  and  $353$  K vs. the nickel atomic content determined by AAS and (B) potential of the ‘high-potential’ peak of the CO<sub>ads</sub> stripping ( $E_{p,CO}$ ) vs. the lattice parameter of the electrocatalysts discussed in this work.

The specific activity for the ORR of porous hollow PtNi/C NPs is thus controlled by the Ni-induced contraction of the lattice parameter and the density of structural defects.  $E_{p,CO}$  and  $Q_{pp,CO}/Q_{T,CO}$  consider these two aspects separately (see **Figure 39A** and **Figure 39B**). Thus, it is essential to use a parameter which describes their synergetic effect on the specific activity for the ORR (**Figure 39C**). The first moment of the potential weight,  $\mu_1^{CO}$  is ideally suited to this purpose. It was introduced by Chattot *et al.*<sup>247</sup> and determines the mean potential of the CO<sub>ads</sub> stripping weighted from the intensity of the ‘low-potential’ and ‘high-potential’ peaks, (see **Equation 23** in **Section II. 3. 4.**) As shown recently, the density of structural defects in an electrocatalyst can also be estimated by the microstrain ( $\mu_\epsilon$ ) derived from Rietveld analysis of X-ray diffraction patterns<sup>234,247</sup>. The microstrain reflects the local variation of the lattice parameter around the mean ( $\mu_\epsilon \propto \Delta a_{Pt-Pt}/a_{Pt-Pt}$ ).

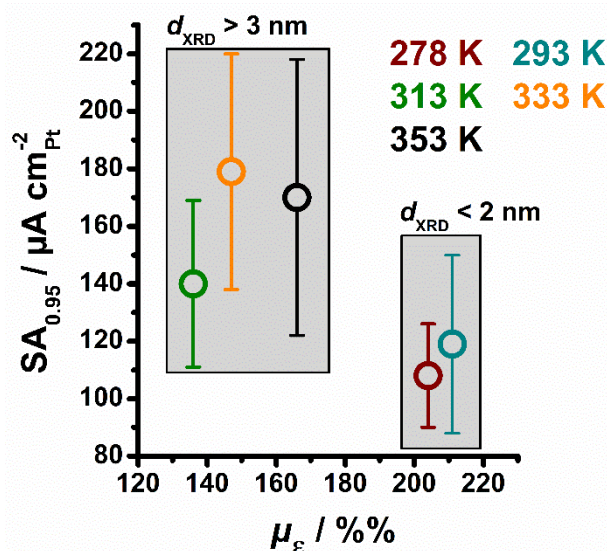


**Figure 41.** Variation of the specific activity for the ORR measured at  $E = 0.95$  V vs. RHE on the porous hollow PtNi/C electrocatalysts synthesized at  $T = 278, 293, 313, 333$  and  $353$  K, vs. the microstrain determined by Rietveld refinement from XRD patterns ( $\mu_\epsilon$ ).

According to the works of Qin *et al.*<sup>293,294</sup>, grain boundaries (GBs) strongly influence the values of the microstrain. Thus, the electrocatalysts with the smallest nanocrystallites, *i.e.* with the highest density of GBs, present the highest microstrain value (see **Figure 41** and **Table 2**). However, the ‘high-microstrain’ / ‘small-crystallites’ porous hollow PtNi/C electrocatalysts, which contain a high density of GBs, are also worst-performing for the ORR (at  $E = 0.95$  V vs. RHE,  $j_k = 108 \pm 18 \mu A cm_{Pt}^{-2}$  for the electrocatalyst synthesized at  $T = 278$  K and  $j_k = 119 \pm 31 \mu A cm_{Pt}^{-2}$  for the electrocatalyst synthesized at  $T = 293$  K, see **Table 3**) as a result of their small crystallite size ( $d_{XRD} < 2$  nm) and their large fraction of low coordinated atoms<sup>49,50</sup>. As observed in **Figure 41**, the surface density of GBs (*i.e.* the microstrain) cannot solely explain the beneficial activity of structural defects, confirming that other defects, such as vacancies, steps, *etc.* impact the specific activity for the ORR and contribute to the  $CO_{ads}$  stripping ‘low-potential’ peak since, despite their higher density in GBs, the electrocatalysts synthesized at  $T = 278$  K and  $T = 293$  K present a depreciated  $CO_{ads}$  peak at  $E \sim 0.7$  V vs. RHE. The enhancement in specific activity observed for the NPs with the biggest crystallites ( $d_{XRD} > 3$  nm) can (in addition to the contribution of the structural defects) be explained in the frame of the particle size effect, *i.e.* smaller crystallites present an increased density of low coordinated atoms with a depreciated activity for the ORR<sup>49,50</sup>.

**IV. 3. 2. The multiplicity of the catalytic sites onto a porous hollow PtNi/C NPs surface**

High structural disorder and thus high values of the microstrain also imply that the lattice of porous hollow PtNi/C NPs comprises a mixture of domains featuring more compressed and more expanded lattice constant values than the average, as evidenced by Dubau *et al.*<sup>234</sup> by HR-TEM (see **Section IV. 1**). In consequence, both oxophilic and oxophobic catalytic sites co-exist on the surface of this nanomaterial. The high structural disorder and the multiplicity of catalytic sites present on porous hollow PtNi/C NPs were recently rationalized by *ab initio* calculations. Le Bacq *et al.*<sup>157</sup> reproduced the highly disordered structure by introducing atomic vacancies into Pt(111) slabs (see **Figure 42A** for an example of a Pt (111) slab with 40% of vacancies randomly introduced). Depending on (i) the concentration and (ii) the spatial distribution of atomic vacancies in the slabs, different bulk and surface arrangements were obtained. Large variations of (i) the in-plane and out-of-plane nearest-neighbour distances around the average value and (ii) of the coordination number of the surface sites were established (see **Figure 42B** and **Figure 42C**). Two families of catalytic sites were found:

- (i) the catalytic sites with a weaker binding of the  $\text{OH}_{\text{ads}}$  intermediates and, to a certain extent, enhanced ORR kinetics *vs.* Pt(111), *i.e.* with a high generalized coordination number<sup>156</sup> or a highly compressed lattice;
- (ii) the catalytic sites with a stronger binding of the  $\text{OH}_{\text{ads}}$  than Pt(111) resulting in depreciated ORR kinetics but enhanced kinetics for electrooxidation reactions, *i.e.* with a low generalized coordination number<sup>156,273</sup> and/or a highly expanded lattice.

Le Bacq *et al.*<sup>157</sup> showed that the binding of  $\text{OH}_{\text{ads}}$  could be *ca.* 0.48 eV stronger or *ca.* 0.25 eV weaker than on Pt (111) surface for two different active sites on the same surface (*e.g.* the surface presented in **Figure 42A**). They also confirmed, by electrochemical measurements, that the porous hollow PtNi/C NPs exhibited both families of catalytic sites and, therefore, an enhanced activity for electrooxidation and electroreduction reactions.

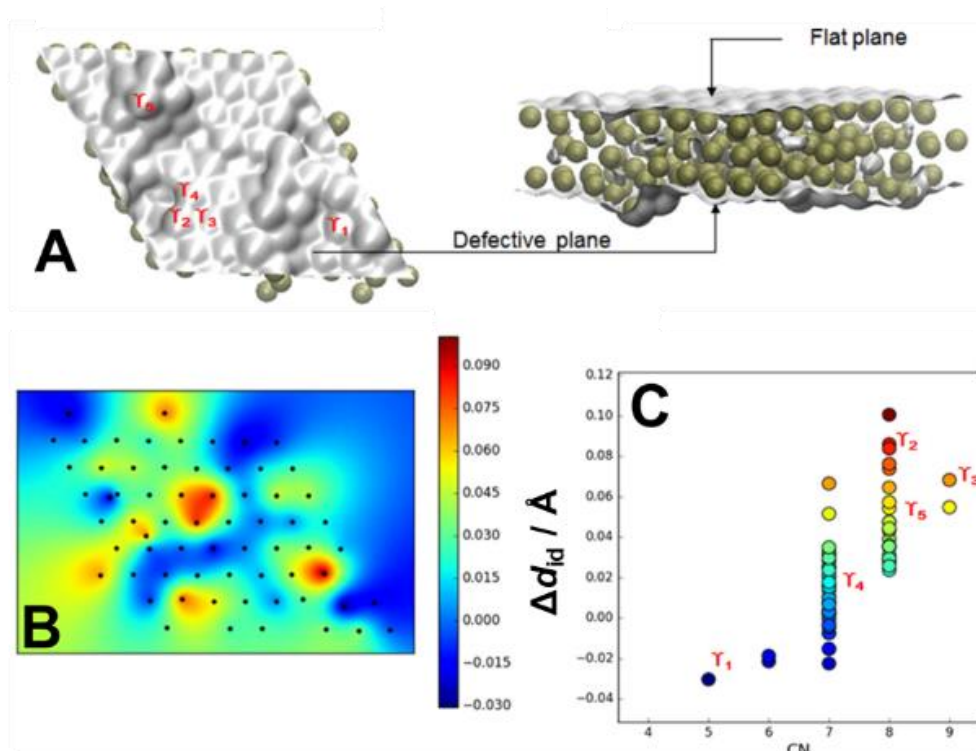


**Figure 42.** (A) Bottom and side view of a 5-layer Pt (111) slab after relaxation for 40% of vacancies randomly introduced. (B) Map of the inner deformation of the defective plane. (C) Deformation index plotted as a function of the coordination number (CN) for each atomic site of the surface displayed in (A). Adapted from Ref. <sup>157</sup>.

#### IV. 4. Extending the synthesis of hollow Pt-based/C nanostructures to other transition metals.

From **Section IV. 1.** to **IV. 3.**, we established the parameters driving the enhanced activity of the porous hollow PtNi/C NPs for the ORR. In the forthcoming sections, we aim at optimizing their electrocatalytic properties (stability, activity) by studying the impact of key parameters of the synthesis, *i.e.* changing the nature of the carbon support or of the sacrificial metal. For that purpose, the synthesis of porous hollow PtM/C NPs was performed, using Co, Cu, Fe and Zn precursors instead of Ni precursors: not only Ni/C NPs can act as a sacrificial template for the deposition of Pt-rich shells (and thus, the formation of porous hollow PtNi/C NPs) but also cobalt (Co) or copper (Cu) NPs (**Figure 43**). This is related to the propensity of these metals to spontaneously form borides <sup>307–312</sup>, *i.e.* to protect the metal cores from oxidation and provide a template for Pt deposition *via* galvanic replacement. The standard potential of the 3d transition metal M appears to be the key of the synthesis of hollow Pt-based/C NPs. Indeed, if the nominal Pt weight fraction (20 wt. %) is achieved for the PtNi/C electrocatalyst, much lower values are observed for others PtM/C electrocatalysts, *e.g.* 1.8 wt. % and 0.2 wt. % for PtFe/C and PtZn/C

electrocatalysts, respectively (see **Figure 43A**). These results indicate that the  $\text{BO}_2/\text{BH}_4^-$  redox pair ( $E^\circ = -0.82 \text{ V vs. SHE at pH} = 7$ <sup>304,305</sup>) cannot reduce 3d transition metal ions with standard potential below  $-0.4 \text{ V vs. SHE}$ . In fact, the best sacrificial templates for the fabrication of hollow Pt-alloy/C NPs feature a standard potential located between  $-0.4 < E^\circ < 0.4 \text{ V vs. NHE}$ <sup>325</sup> (**Table 4**) *i.e.* easy to be reduced by  $\text{BH}_4^-$  ions and easy to be oxidized by  $\text{Pt}^{2+}$  ions *via* galvanic replacement. Interestingly, despite featuring similar standard potential and propensity to form metal borides, very different Pt wt. % were obtained for PtCo/C (5.5 wt. %) and PtNi/C (20.0 wt. %). Such difference underlines the essential role played by the 3d transition metal in the  $\text{Pt}^{2+}$  reduction since, without an appropriate template metal, the adequate Pt loading cannot be reached. Since no particles of zinc or iron were observed on the PtZn/C and PtFe/C electrocatalysts, the residual Zn and Fe at. % observed by Atomic Adsorption Spectroscopy (AAS – **Figure 43A**) were ascribed to traces of the Zn(II) and Fe(II) precursors trapped in the pores of the carbon support. Pronounced differences in size and distribution of the carbon-supported hollow NPs are observed when the nature of the sacrificial template changes (**Figure 43C**). Despite featuring similar standard potential, hollow Pt-rich/C NPs are by far larger ( $d_{\text{ext}} = 158 \pm 76 \text{ nm}$ ,  $d_{\text{in}} = 138 \pm 71 \text{ nm}$ ) when Co instead of Ni atoms ( $d_{\text{ext}} = 11.4 \pm 1.9 \text{ nm}$ ,  $d_{\text{in}} = 6.4 \pm 1.5 \text{ nm}$ ) are used as sacrificial cores. Note also that hollow PtCu/C NPs are strongly agglomerated compared to hollow PtNi/C NPs (see **Figure 43C**). The SA and MA at  $E = 0.95 \text{ V vs. RHE}$  are maintained for the different structures, despite their differences in size and agglomeration (see **Figure 43B**).

The nature of the alloying element plays little role in the activity; indeed, this element is rapidly corroded upon contact with the acidic electrolyte, and the last step of the synthesis was an acid leaching in  $1 \text{ M H}_2\text{SO}_4$  for  $t = 22 \text{ h}$ <sup>83,84</sup>. Its main uses are to provide (i) a sacrificial template for the deposition of  $\text{Pt}^{2+}$  ions and (ii) a mean to contract the Pt lattice constant (strain). However, the final reactivity of the surface will also be influenced by the high structural disorder generated by deposition (and alloying) of Pt ions onto (with) the M-rich/C core. The slight differences observed in specific activity at  $E = 0.95 \text{ V vs. RHE}$  can be explained by the difference in  $\mu_1^{\text{CO}}$  of the electrocatalysts (*i.e.* the density of structural defects and the non-noble metal induced contraction):  $\mu_1^{\text{CO}}(\text{PtNi/C}) = 718 \pm 10 \text{ mV} > \mu_1^{\text{CO}}(\text{PtCu/C}) = 702 \pm 5 \text{ mV} > \mu_1^{\text{CO}}(\text{PtCo/C}) = 665 \pm 15 \text{ mV}$ , *i.e.* the most active electrocatalyst (the porous hollow PtCo/C NPs) is also the electrocatalyst with the lowest  $\mu_1^{\text{CO}}$ .

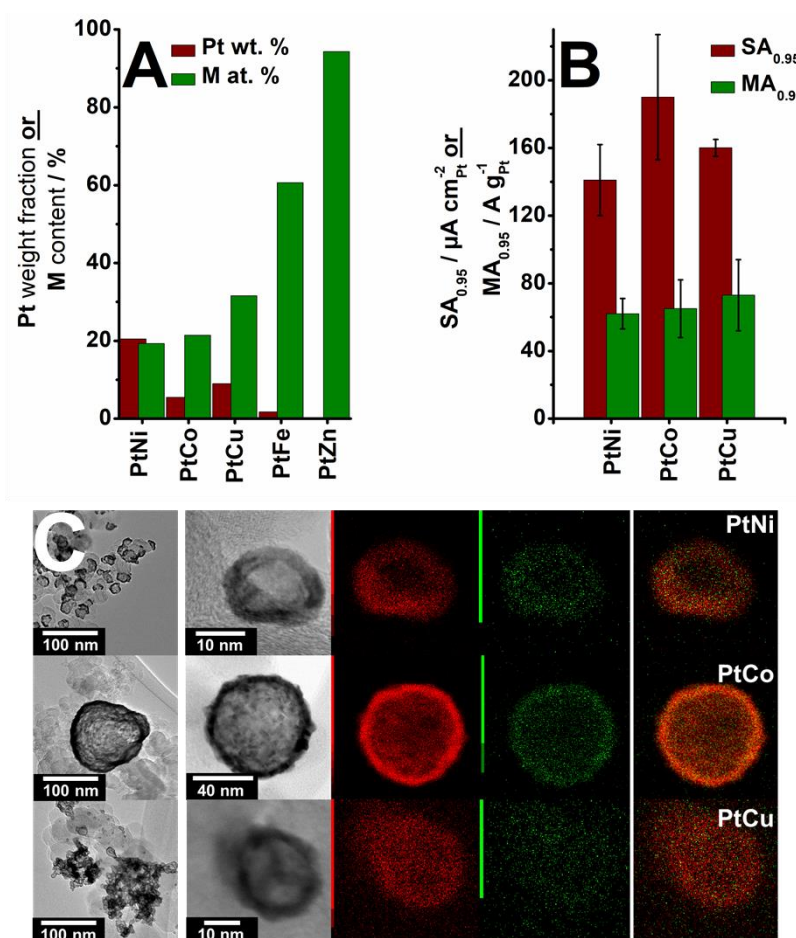


**Figure 43.** Extension of the synthesis of hollow PtM/C NPs to other sacrificial metals, with M = Ni, Co, Cu, Zn and Fe. (A) Pt weight fraction and M content determined by Atomic Absorption Spectroscopy after acid leaching; (B) Specific and mass activity for the ORR at  $E = 0.95$  V vs. RHE ( $SA_{0.95}$  and  $MA_{0.95}$ , respectively) The measurements were performed in an  $\text{O}_2$ -saturated 0.1 M  $\text{HClO}_4$  electrolyte, at a sweep rate  $\nu = 0.005$  V  $\text{s}^{-1}$  and a rotation speed  $\omega = 1600$  rpm. All currents are corrected for Ohmic drop and mass transport. (C) TEM and STEM-EDX micrographs of the PtNi/C, PtCo/C and PtCu/C electrocatalysts (Pt atoms and M atoms are represented in red and green, respectively).

**Table 4.** Standard potential of the  $\text{M}^{2+}/\text{M}$  pair for the 3d transition metal discussed in this work.

M	$E^\circ$ vs. RHE ( $\text{M}^{2+}/\text{M}$ ) / V	Pt weight fraction / %
Fe	- 0.44	1.8
Co	- 0.28	5.5
Ni	- 0.25	20.0
Cu	+ 0.34	9.0
Zn	- 0.76	0.2

## IV. 5. The influence of the carbon support

### IV. 5. 1. Physico-chemical properties of the carbon supports

As mentioned in **Section IV. 2. 2.**, porous hollow PtNi/C<sup>a</sup> NPs were synthesized on seven different carbon supports differing by their physico-chemical properties such as the average crystallite size in the graphene plane ( $L_a$ ), the graphitic domains size perpendicular to the graphene plane ( $L_c$ ), the specific surface, the morphology and the surface functionalization:

- (i) carbon blacks, *i.e.* Vulcan XC72 (XC72 – Cabot), Ketjenblack 600 JD (KJB – Azko Nobel) and YS (YS – Société du Noir d’Acétylène de l’Aubette), a graphitized carbon black;
- (ii) multi walled carbon nanotubes (CNT) synthesized by the sacrificial support method following the procedure described by Andersen *et al* <sup>183</sup>;
- (iii) carbon xerogels (CX), synthesized according to the procedure described by Job *et al.* <sup>186</sup> with a resorcinol / formaldehyde (R/F) ratio of 0.5, a R/Na<sub>2</sub>CO<sub>3</sub> ratio of 1500 and a water / reactants of 5.7;
- (iv) 3D graphene nanosheets (GNS) synthesized by the sacrificial support method following the procedure described by Kabir *et al.* <sup>248,249</sup> and Serov *et al.* <sup>250</sup>. To investigate the effect of the density of oxygen functions onto the carbon surface, GNS surface was functionalized by acid leaching for  $t = 8$  h in 8 M HNO<sub>3</sub>. This carbon is referred to as GNS – AL.

The specific surface areas ( $S_{\text{BET}}$ ) of the different carbon supports were determined by nitrogen adsorption-desorption using the BET equation for data treatment (see **Table 5**). The micropore (*i.e.*  $d_{\text{pores}} < 2$  nm according to the International Union of Pure and Applied Chemistry <sup>171</sup>) surface was calculated using the  $t$ -plot method <sup>282,283</sup>. The  $S_{\text{BET}}$  values range from  $78 \pm 2$  m<sup>2</sup> g<sup>-1</sup> for the CNT to  $1454 \pm 5$  m<sup>2</sup> g<sup>-1</sup> for the KJB. CNT and KJB supports do not present micropores, by opposition to the samples YS, GNS, GNS – AL, XC72 and CX. The specific surfaces excluding micropores ( $S_{\text{BET}} - S_{\text{micropores}}$ ) are reported in **Table 5**. The latter is more representative of the support since, because of their external diameter ( $d_{\text{ext}} \sim 10 - 15$  nm <sup>84</sup>), the porous hollow NPs cannot be formed within micropores.

---

<sup>a</sup>In **Section IV. 5, IV. 6** and **V. 2**, the porous hollow PtNi NPs were synthesized on different carbon supports. As such, the nature of the carbon support is indicated in the discussion. In the other sections, only Vulcan XC72 was used and is there referred as ‘C’.

**Table 5.** Specific surface area values of the carbon supports discussed in this work, calculated by the Brunauer, Emmett and Teller equation, ( $S_{\text{BET}}$ ), surface developed by micropores ( $S_{\text{micropores}}$ ) calculated by the  $t$ -plot method, and difference between the two surfaces ( $S_{\text{BET}} - S_{\text{micropores}}$ ).

	$S_{\text{BET}}$ / $\text{m}^2 \text{g}^{-1}$	$S_{\text{micropores}}$ / $\text{m}^2 \text{g}^{-1}$	$S_{\text{BET}} - S_{\text{micropores}}$ / $\text{m}^2 \text{g}^{-1}$
<b>XC 72</b>	$239 \pm 2$	$88 \pm 2$	$151 \pm 4$
<b>CNT</b>	$78 \pm 2$	*	$78 \pm 2$
<b>YS</b>	$115 \pm 2$	$5 \pm 2$	$110 \pm 4$
<b>GNS</b>	$175 \pm 2$	$40 \pm 2$	$135 \pm 4$
<b>GNS – AL</b>	$165 \pm 2$	$45 \pm 2$	$120 \pm 4$
<b>XG</b>	$548 \pm 5$	$434 \pm 5$	$114 \pm 10$
<b>KJB</b>	$1454 \pm 5$	*	$1454 \pm 5$

\* No microporous surface area was measured on these carbon supports.

The stability of a carbon support is correlated to its structural organization, *i.e.* the average in-plane (the plane being defined as the graphene layer) crystallite size ( $L_a$ ), the average size of the graphitic domain perpendicularly to the plane ( $L_c$ ), the position of the graphite ( $G$ ) band<sup>287</sup> ( $\sim 1585 - 1600 \text{ cm}^{-1}$ ) in the Raman spectra and the interplanar distance perpendicularly to the plane ( $d_{002}$ ) (see **Table 6** and **Figure 44**). The  $L_c$  and  $d_{002}$  values were determined from the analysis of XRD patterns for each carbon support, namely the graphite peak at  $2\theta \sim 26 - 28^\circ$ , using the Scherrer and the Bragg laws, respectively. The  $L_a$  values were determined from Raman spectra using the Knight and White formula (see **Section II. 7.**). The position of the graphite band (see **Table 6**) shifts from  $\nu = 1597 \pm 1 \text{ cm}^{-1}$  for the GNS to  $\nu = 1584 \pm 1 \text{ cm}^{-1}$  for the CNT. According to Lespade *et al.*<sup>287</sup>, the diminution of the  $G$ -band wavenumber corresponds to an increased graphitization of the carbon support because of the diminution of the  $D_2$  band intensity at  $\nu = 1610 \text{ cm}^{-1}$  which corresponds to in-plane surface defects. The CNTs present a well-organized structure (*ca.*  $L_a = 7.0 \text{ nm}$  and  $L_c = 6.3 \text{ nm}$ ), while the carbon blacks show a lower degree of organization in and out of the plane (see **Table 6**). The GNSs present a high  $L_c$  (*ca.*  $12.6 \text{ nm}$ ), resulting from a structure composed of several stacked graphene layers, but a low  $L_a$  (*ca.*  $3.8 \text{ nm}$ ) and a  $G$ -band shifted toward the  $D_2$ -band (*ca.*  $1597 \text{ cm}^{-1}$ ), *i.e.* a disordered structure in the graphene plane. The acid leaching of the GNS produced the GNS-AL catalyst and had no impact on (i) the specific surface area and (ii) the degree of ordering.

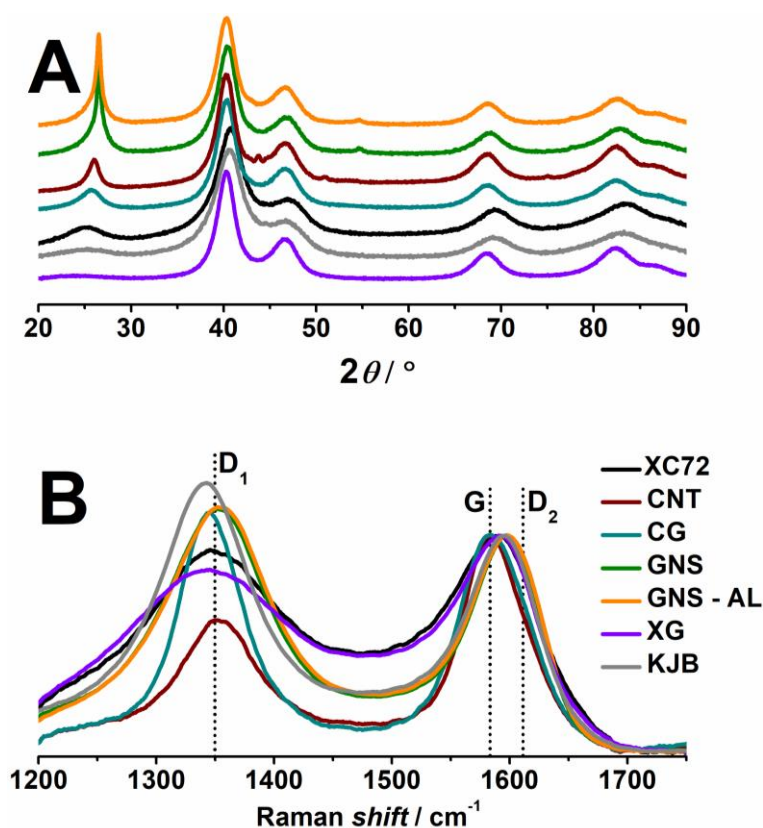


**Figure 44.** (A) XRD patterns measured on the porous hollow PtNi/C NPs synthesized in this work and (B) Raman patterns of the various carbon supports.

**Table 6.** In-plane crystallite size ( $L_a$ ) and size of the graphitic domains perpendicular to the graphite plane ( $L_c$ ), determined by Raman and XRD, respectively, for the different carbon supports discussed in this work.

	$L_a$ / nm	$L_c$ / nm	$d_{002}$ / nm	G-band position / $\text{cm}^{-1}$
<b>XC72</b>	$4.4 \pm 0.1$	$1.9 \pm 0.1$	$0.353 \pm 0.001$	$1588 \pm 1$
<b>CNT</b>	$7.0 \pm 0.1$	$6.3 \pm 0.1$	$0.342 \pm 0.001$	$1583 \pm 1$
<b>YS</b>	$3.8 \pm 0.1$	$3.0 \pm 0.1$	$0.348 \pm 0.001$	$1586 \pm 1$
<b>GNS</b>	$3.8 \pm 0.1$	$12.6 \pm 0.1$	$0.336 \pm 0.001$	$1597 \pm 1$
<b>GNS - AL</b>	$3.8 \pm 0.1$	$12.6 \pm 0.1$	$0.336 \pm 0.001$	$1597 \pm 1$
<b>CX</b>	*	*	*	*
<b>KJB</b>	$3.3 \pm 0.1$	$1.3 \pm 0.1$	$0.359 \pm 0.001$	$1595 \pm 1$

\*No values were determined for the carbon xerogel (CX) because of its amorphous nature (see **Section II. 7**).

The presence of oxygen-containing surface groups (carboxylic, carbonyl, *etc.*) is believed to increase the number of nucleation sites for the formation of NPs, as they act as anchoring sites

for metal precursors<sup>326–328</sup>. Oxygen-containing surface groups also impact on the resistance of the carbon materials to electrochemical corrosion (increased carbon coverage by oxygen results in a decreased stability<sup>192</sup>). Surface analysis was performed with XPS to (i) identify the chemical groups on each substrate by peak-fitting of the C1s spectra and (ii) determine the atomic composition (C, O, N and contamination) by analysing the survey spectra. Atomic percentages associated with each chemical environment of carbon atoms are reported in **Table 7**. The degree of functionalization of the carbon supports was determined by the proportion of carbon atoms forming C-O, C-C=O and O-C=O bonds (*i.e.* the oxygen-containing surface groups) within the C1s spectrum. **Table 7** shows that CNTs display the lowest surface functionalization (23 % of oxygen groups) while the highest coverage with oxygen is reached in CX (42 % of oxygen groups) and XC72 (38.5 % of oxygen groups) supports. The different carbon functionalization is a direct consequence of the synthesis process: for example, lower (32.2 at. % *vs.* 36.5 at. %) total oxygen and nitrogen percentages were found on the GNS sample compared to GNS-AL, *i.e.* the acid treatment (8 M HNO<sub>3</sub> during  $t = 8$  h) increases the oxygen content of the carbon support<sup>326,327,329</sup>; more precisely, it generates 20% more carboxylic acid groups (O – C = O).

**Table 7.** Surface composition of the different carbon substrates as derived from the XPS analysis.

	C-C-H / at. %	C-O, C-N / at. %	C-C=O / at. %	O-C=O / at. %	O / at. %	N / at. %	Other / at. %
<b>XC72</b>	55	21.5	8	9	6.5	*	*
<b>CNT</b>	74	7	11.5	4.5	3	*	*
<b>YS</b>	66	14.5	12.5	4	3	*	*
<b>GNS</b>	64.5	11.5	14.5	3.5	3	2.5	0.5
<b>GNS-AL</b>	59	9.5	15.5	5	6.5	4	0.5
<b>CX</b>	49	24	9	9	9	*	*
<b>KJB</b>	65.5	14.5	12	6	2	*	*

\* No group of this nature was found on the associated support.

#### IV. 5. 2. Morphology and electrochemical activity of porous hollow PtNi/C catalysts

Porous hollow PtNi/C electrocatalysts were successfully synthesized onto different carbon supports, as shown in **Figure 45**. Depending on the support, different external and inner diameters were obtained for the porous hollow NPs (**Figure 45** and **Table 8**). The effect of the oxygen coverage of the carbon support on the final NPs diameter is not straightforward. In fact, different diameters are observed for the NPs synthesized on the XC72 (PtNi/XC72) and the CX (PtNi/CX,  $d_{\text{ext}} = 12.5 \pm 3.5$  nm vs.  $d_{\text{ext}} = 23.1 \pm 7.5$  nm, see **Table 8**) two carbon supports presenting a similar oxygen coverage (% of oxygen groups = 38.5 vs. 42 at. %, see **Table 7**). This suggests that the *relative number* of O (or N) anchoring sites does not control the nucleation of the porous hollow PtNi NPs onto the different carbon supports. An interesting relationship may be established when calculating the specific surface area of macro + mesopores (*i.e.* ignoring the contribution of the micropores,  $S_{\text{BET}} - S_{\text{micropores}}$ ) and correlating it with the external and inner diameters of the NPs (see **Figure 45B**). This can be rationalized owing to the *absolute number* of anchoring sites (*i.e.* the total number of oxygen functions, obtained from the product of the relative number of oxygen functions by the specific surface of the carbon support, micropores excluded). Indeed, KJB features a slightly lower oxygen coverage compared to the XC72 (oxygen groups represent 32.5 at. % of the C1s peak in KJB and 38.5 at. % of the peak in XC72, see **Table 7**) however, the specific surface of KJB is about 6 times larger than that of Vulcan XC72 ( $1454 \pm 5$  vs.  $239 \pm 2$  m<sup>2</sup> g<sup>-1</sup>, as reported in **Table 5**). Therefore, the *absolute number* of available anchoring sites in KJB should roughly be 5 times higher than for the XC72, resulting in an increased number of nucleation sites<sup>326,327</sup> and in the decrease of the external and inner NP diameters.

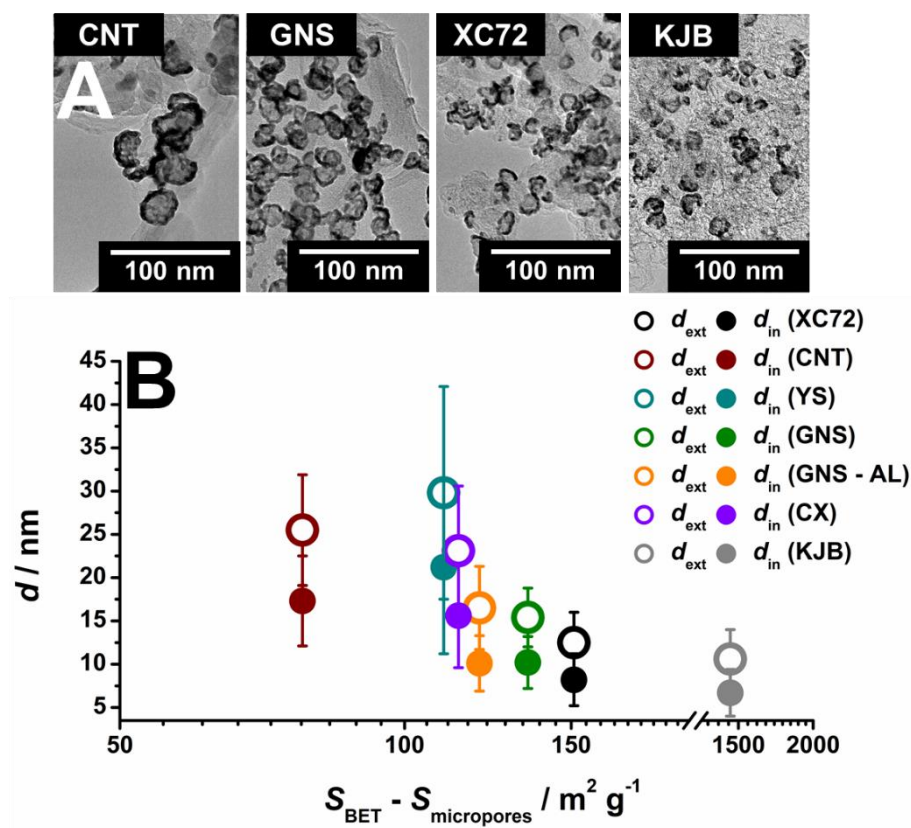


**Figure 45.** (A) Transmission Electron Microscopy micrographs of the porous hollow PtNi/C NPs synthesized on CNT, GNS, XC72 and KJB. (B) Variation of the external and inner diameters of the porous hollow PtNi/C NPs as a function of the BET surface area (micropores excluded) of the different carbon supports.

To sum up:

- (i) The diameter of the porous hollow PtNi NPs decreases with an increase of the specific surface area (micropores excluded) of the carbon support, owing to an increased content in oxygen at the carbon surface acting as nucleation sites for the Ni-rich cores (see **Section III. 2.**);
- (ii) Under the chosen synthesis conditions (ratio between the platinum and nickel precursors equal to 1:3, synthesis at room temperature), the smallest  $d_{ext}$  ( $\sim 10$  nm) was observed for the NPs synthesized on the KJB support. The latter presents a sensibly higher specific surface area (micropores excluded) than the other carbon supports and, thus, a larger absolute number of available oxygen groups;
- (iii) For low specific surface area carbon supports (micropores excluded, *i.e.* YS and CNT), the external diameter of the hollow PtNi NPs tends to stabilize around 30 nm and the inner diameter around 20 nm (see **Figure 45** and **Table 8**).

## Chapter IV. Design of porous hollow PtM nanoparticles for the ORR

**Table 8.** Morphological, physical and electrochemical properties of the porous hollow PtNi/C NPs synthesized on the different carbon supports, *i.e.* the external ( $d_{\text{ext}}$ ) and inner ( $d_{\text{in}}$ ) diameter of the NPs, the Pt weight fraction (Pt wt. %) on the carbon surface, the Ni content (Ni at. %) measured by AAS, the lattice parameter ( $a_{\text{Pt-Pt}}$ ), the mean crystallite size ( $d_{\text{XRD}}$ ) and the first moment of the potential weight of the  $\text{CO}_{\text{ads}}$  stripping voltammogram ( $\mu_1^{\text{CO}}$ ).

	$d_{\text{ext}}$ / nm	$d_{\text{in}}$ / nm	Pt / wt. %	Ni / at. %	$a_{\text{Pt-Pt}}$ / nm	$d_{\text{XRD}}$ / nm	$\mu_1^{\text{CO}}$ / mV vs. RHE
<b>XC72</b>	$12.5 \pm 3.5$	$8.2 \pm 3.0$	$18.2 \pm 0.3$	$23.1 \pm 0.5$	$0.384 \pm 0.001$	$2.3 \pm 0.1$	$718 \pm 10$
<b>CNT</b>	$25.5 \pm 6.4$	$17.3 \pm 5.2$	$23.3 \pm 0.3$	$13.9 \pm 0.3$	$0.388 \pm 0.001$	$3.2 \pm 0.1$	$662 \pm 10$
<b>YS</b>	$29.8 \pm 12.3$	$21.2 \pm 10.0$	$17.7 \pm 0.3$	$19.2 \pm 0.4$	$0.388 \pm 0.001$	$2.8 \pm 0.1$	$693 \pm 5$
<b>GNS</b>	$15.4 \pm 3.4$	$10.2 \pm 3.0$	$18.9 \pm 0.3$	$15.6 \pm 0.3$	$0.387 \pm 0.001$	$2.8 \pm 0.1$	$702 \pm 12$
<b>GNS - AL</b>	$16.5 \pm 4.8$	$10.1 \pm 3.2$	$18.4 \pm 0.3$	$13.6 \pm 0.3$	$0.388 \pm 0.001$	$2.9 \pm 0.1$	$708 \pm 11$
<b>CX</b>	$23.1 \pm 7.5$	$15.6 \pm 6.0$	$16.5 \pm 0.3$	$14.8 \pm 0.3$	$0.388 \pm 0.001$	$3.0 \pm 0.1$	$677 \pm 11$
<b>KJB</b>	$10.6 \pm 3.4$	$6.7 \pm 2.7$	$17.5 \pm 0.3$	$27.9 \pm 0.6$	$0.385 \pm 0.001$	$2.2 \pm 0.1$	$734 \pm 15$

The specific surface area of the carbon supports also controls the final Ni content (see **Table 8**): namely, the NPs synthesized on the substrates having the highest specific surface area (KJB and XC72) display the highest percentage of Ni (*ca.* 27.9 at. % and 23.1 at. %, respectively). This unequivocally results from the higher number of Ni nuclei, which act as sacrificial template for the deposition of Pt<sup>2+</sup> ions *via* galvanic replacement (see **Section III. 2**). Interestingly, porous hollow NPs synthesized on XC72 and KJB feature similar lattice parameter ( $a_{\text{Pt-Pt}} = 0.384 \pm 0.001$  nm *vs.*  $a_{\text{Pt-Pt}} = 0.385 \pm 0.001$  nm), hence suggesting that the higher Ni content (see **Table 8**) measured in the PtNi/KJB is not fully alloyed to Pt. This suggests that Ni atoms may heterogeneously be distributed within the PtNi lattice or that traces of Ni<sup>2+</sup> are trapped within the carbon porosities. The mean lattice parameter ranges from  $a_{\text{Pt-Pt}} = 0.384 \pm 0.001$  nm (XC72) to  $a_{\text{Pt-Pt}} = 0.388 \pm 0.001$  nm (*i.e.* PtNi/CNT, PtNi/YS, PtNi/GNS-AL and PtNi/CX). The crystallite size ranges from  $d_{\text{XRD}} = 2.2 \pm 0.1$  nm (PtNi/KJB) to  $d_{\text{XRD}} = 3.2 \pm 0.1$  nm (PtNi/CNT). Considering that  $d_{\text{ext}} \gg d_{\text{XRD}}$ , the NP morphologies (independently of the carbon support) correspond to Pt-rich polycrystalline porous shells surrounding hollow cores. The electrocatalysts displaying the smallest crystallites (PtNi/XC72 and PtNi/KJB) present a pronounced CO<sub>ads</sub> stripping peak at  $\sim 0.78$  V *vs.* RHE (see **Figure 46**): smaller NPs result in an increased curvature of the inner cavity and, therefore, in a higher proportion of CO<sub>ads</sub> molecule trapped onto highly coordinated Pt sites (see **Section IV. 2**). In addition, the smaller nanocrystallites size might also result in a higher proportion of non-defective NCs facets or NPs. According to **Section IV. 3**, the highest activity should be observed for the electrocatalyst showing the CO<sub>ads</sub> stripping with the lowest first moment of the potential weight of the CO<sub>ads</sub> stripping ( $\mu_1^{\text{CO}}$ , mV *vs.* RHE <sup>247</sup>).

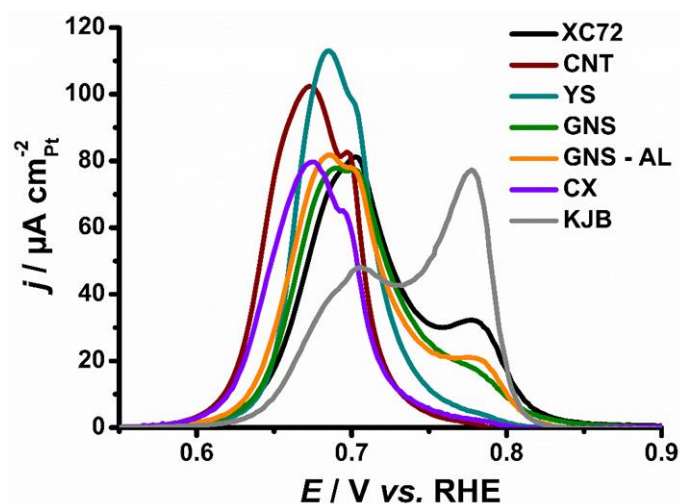


**Figure 46.**  $\text{CO}_{\text{ads}}$  stripping in Ar-saturated 0.1 M  $\text{HClO}_4$  on porous hollow PtNi/C NPs synthesized on different carbon supports, namely: Vulcan XC72 (XC72), carbon nanotubes (CNT), YS (YS), graphene nanosheets (GNS), acid leached graphene nanosheets (GNS – AL), carbon xerogels (CX) and Ketjenblack (KJB) – other conditions:  $\nu = 0.020 \text{ V s}^{-1}$ ,  $T = 298 \pm 1 \text{ K}$ .

The specific activity and the mass activity for the ORR of the different electrocatalysts at  $E = 0.90 \text{ V}$  and  $0.95 \text{ V vs. RHE}$  are shown in **Figure 47**. The ORR specific activities at  $E = 0.95 \text{ V vs. RHE}$  (**Figure 47A**) range from  $136 \pm 18 \mu\text{A cm}^{-2}_{\text{Pt}}$  for the porous hollow PtNi/CX electrocatalyst to  $174 \pm 15 \mu\text{A cm}^{-2}_{\text{Pt}}$  for the porous hollow PtNi/CNT electrocatalyst, indicating a mild influence of the nature of the carbon support. As expected, the electrocatalysts with the lowest  $\mu_1^{\text{CO}}$  values (PtNi/CNT, PtNi/YS, PtNi/GNS–AL and PtNi/GNS) feature the highest specific activity at  $0.95 \text{ V vs. RHE}$  (see **Table 8**). Despite similar  $\mu_1^{\text{CO}}$ , lower performance for the ORR was measured on the PtNi/CX electrocatalyst compared to the PtNi/YS and PtNi/CNT electrocatalysts. The mass activities at  $0.95 \text{ V vs. RHE}$  range from  $40 \pm 2 \text{ A g}^{-1}_{\text{Pt}}$  for PtNi/CG to  $68 \pm 7 \text{ A g}^{-1}_{\text{Pt}}$  PtNi/GNS-AL (see **Figure 47A**). These differences were ascribed to the variation of the Pt specific surface area ( $S_{\text{Pt, CO}}$ ) which is  $\sim 30 \text{ m}^2 \text{ g}^{-1}_{\text{Pt}}$  for the PtNi/CNT, PtNi/YS and PtNi/CX,  $35 \leq S_{\text{Pt, CO}} \leq 41 \text{ m}^2 \text{ g}^{-1}_{\text{Pt}}$  for the PtNi/GNS and PtNi/GNS-AL and more than  $42 \text{ m}^2 \text{ g}^{-1}_{\text{Pt}}$  for the PtNi/XC72 and PtNi/KJB (**Figure 47A**).

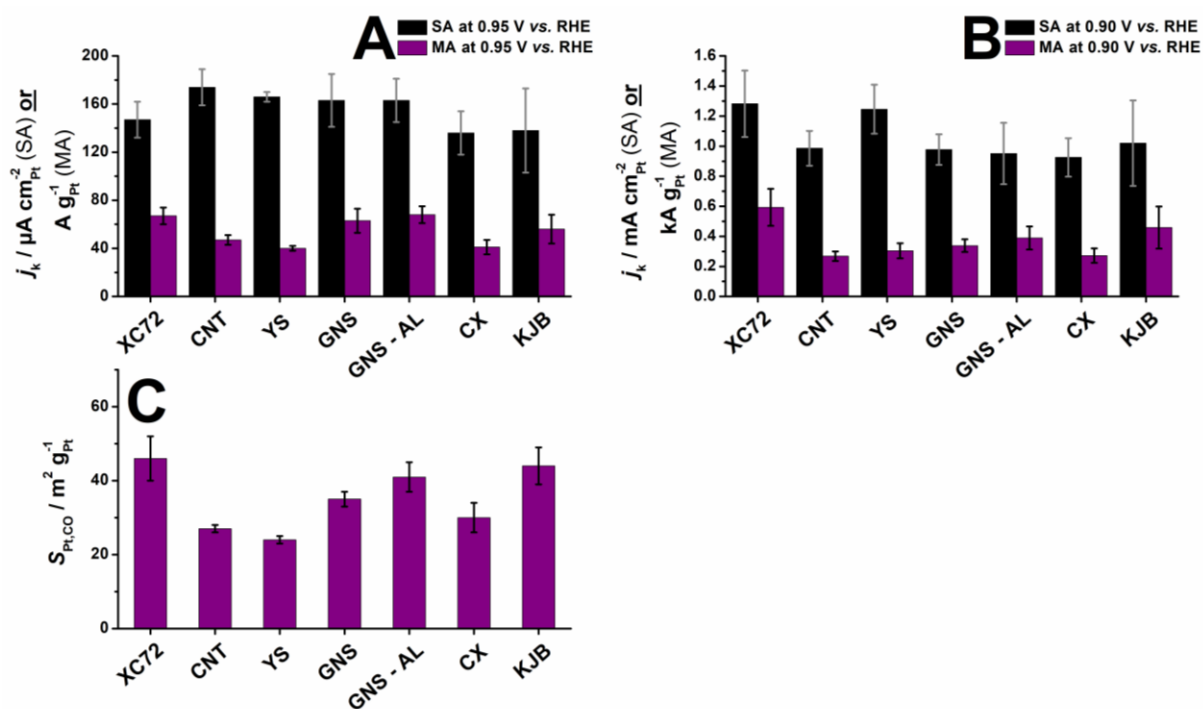


**Figure 47.** Specific activity (SA) and mass activity (MA) in  $\text{O}_2$ -saturated 0.1 M  $\text{HClO}_4$  at (A)  $E = 0.95$  V vs. RHE and (B)  $E = 0.9$  V vs. RHE, corrected for diffusion in solution and Ohmic drop, for the porous hollow PtNi/C NPs synthesized on different carbon supports – other conditions:  $T = 298 \pm 1$  K,  $\omega = 1600$  rpm,  $\nu = 0.005$   $\text{V s}^{-1}$ . (C) Pt specific surface area values determined from the  $\text{CO}_{\text{ads}}$  stripping measurements.

## IV. 6. Conclusions

In summary, we have investigated the effect of several parameters (temperature, nature of the alloying element (Ni, Co, Cu, *etc.*), nature of the carbon support and ratio between the metallic precursors of the synthesis of porous hollow Pt-rich NPs) on the morphology and the electrocatalytic activity of porous hollow PtNi/C NPs. **Figure 48** summarizes the variations of the structural markers of the porous hollow Pt-rich/C NPs to each parameter investigated:

- (i) The diameter of the central cavity (the inner diameter,  $d_{in}$ ) increases with a decrease of the Pt<sup>2+</sup>:Ni<sup>2+</sup> ratio <sup>84</sup>;
- (ii) The mean crystallite size,  $d_{XRD}$ , diminishes with a decrease of the Pt<sup>2+</sup>:Ni<sup>2+</sup> ratio <sup>84</sup>;
- (iii) The mean crystallite size,  $d_{XRD}$ , increases with the increase of the synthesis temperature ( $T_s$ );
- (iv) The external diameter and the inner diameter of the hollow NPs are proportional to the BET specific surface area (see **Table 5**), micropores (pores with width > 2 nm according to the International Union of Pure and Applied Chemistry <sup>171</sup>) excluded, *i.e.* they decrease with an increase of the absolute number of oxygen-based group on the electrocatalyst surface.

The specific activity at  $E = 0.95$  V vs. RHE for the various hollow Pt-rich/CNPs is summarized in **Figure 49**. It ranges from  $109 \pm 12 \mu\text{A cm}^{-2}_{Pt}$  for the PtNi/XC72 electrocatalyst synthesized at  $T = 278$  K to  $190 \pm 30 / 37 \mu\text{A cm}^{-2}_{Pt}$  for the PtNi/XC72 electrocatalyst synthesized at  $T = 333$  K and the PtCo/XC72 electrocatalyst synthesized at room temperature. These comparable ORR activities clearly show that the one-pot synthesis used to synthesize the porous hollow PtNi/C NPs is robust but that the final activity mostly depends on the fine nanostructure of the catalyst.

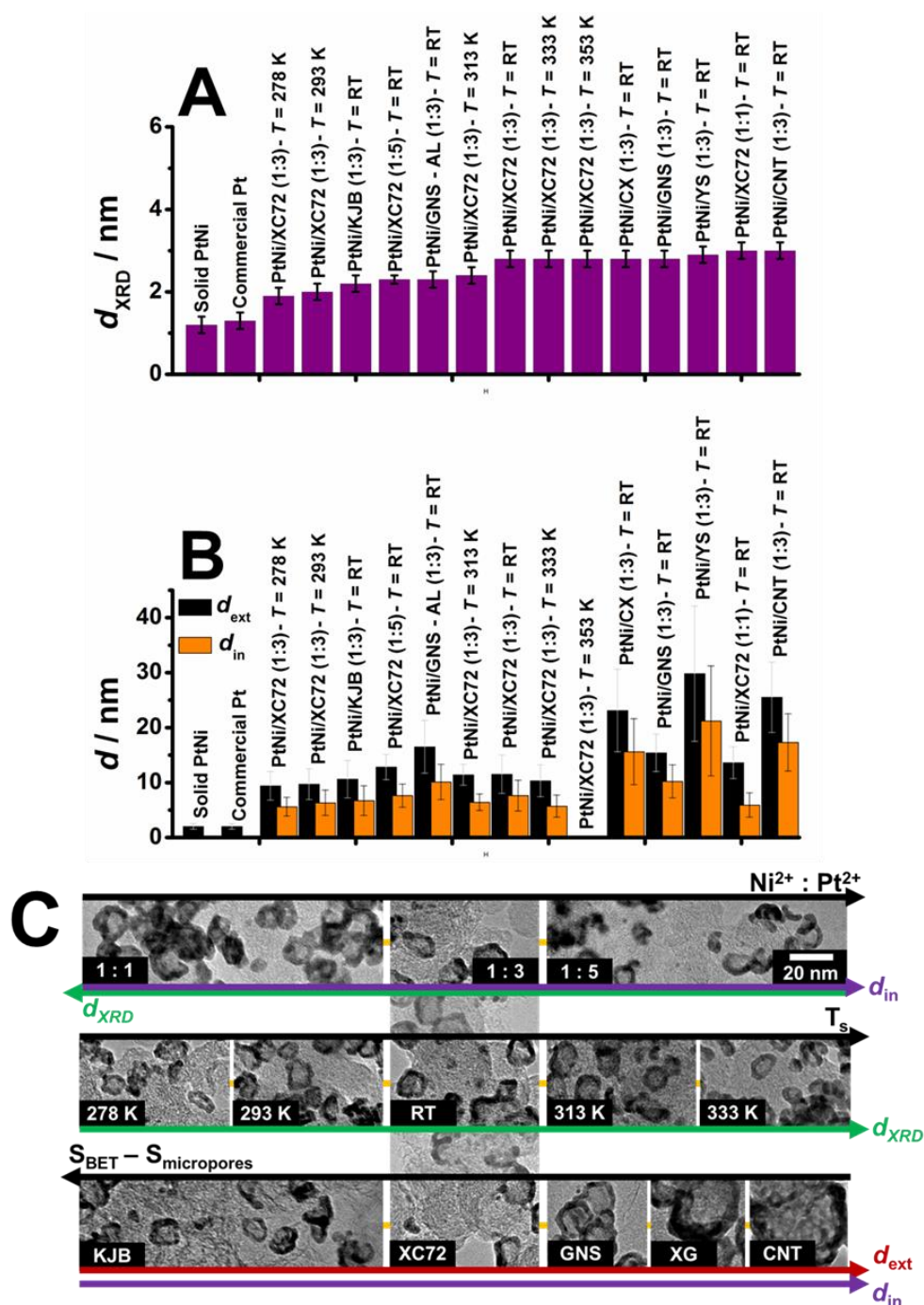


**Figure 48.** Controlling the morphological properties of hollow PtNi/C NPs. The graphs display variations of the mean crystallite size ( $d_{XRD}$ ), the mean outer ( $d_{ext}$ ) and the mean inner ( $d_{in}$ ) diameters measured on hollow PtNi/C NPs synthesized at different temperatures ( $T = 278, 293, 313, 333$  or  $353$  K), with different  $Pt^{2+} : Ni^{2+}$  atomic ratios (1:1, 1:3, 1:5), or supported onto different carbons: carbon black (XC72), Ketjenblack 600 JD (KJB), graphitized carbon (YS), carbon nanotubes (CNT), graphene nanosheets doped with nitrogen before (GNS) or after acid treatment in  $HNO_3$  (GNS – AL) and carbon xerogel (CX). The reference synthesis conditions were: initial  $Pt^{2+} : Ni^{2+}$  atomic ratio of 1:3 and room temperature (RT). (A) Mean crystallite size ( $d_{XRD}$ ), (B) External ( $d_{ext}$ ) and inner ( $d_{in}$ ) diameter of the hollow Pt-based/C NPs synthesized in this work. No inner diameter is given for the commercial solid

Pt/C and the solid PtNi/C, as for the electrocatalyst synthesized at  $T = 353$  K, since they present an agglomerated structure. (C) TEM micrographs of the hollow Pt-based/C NPs synthesized in this work and correlations to the synthesis parameters: the initial  $\text{Pt}^{2+}:\text{Ni}^{2+}$  atomic ratio in the synthesis reactor, the synthesis temperature  $T_s$ , the specific surface area of the support, micropores excluded ( $S_{\text{BET}} - S_{\text{micropores}}$ ).

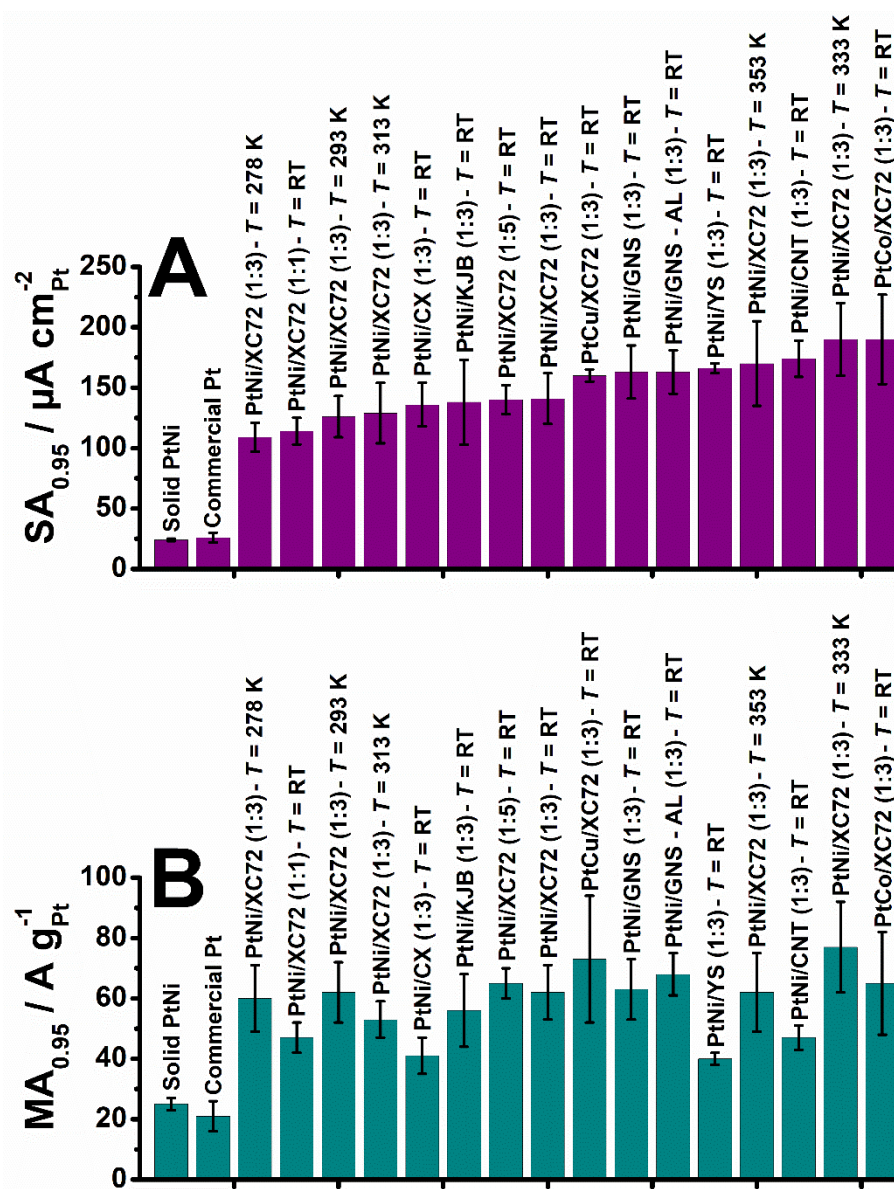


**Figure 49.** Specific and mass activity at  $E = 0.95$  V vs. RHE of porous hollow PtM/C NPs. (A) Specific activity and (B) mass activity measured at  $E = 0.95$  V vs. RHE ( $SA_{0.95}$  and  $MA_{0.95}$ , respectively). The measurements were performed in an  $\text{O}_2$ -saturated 0.1 M  $\text{HClO}_4$  electrolyte, at a sweep rate  $\nu = 0.005$  V  $\text{s}^{-1}$  and a rotation speed  $\omega = 1600$  rpm. All currents are corrected for Ohmic drop and mass transport.

The enhanced electrocatalytic activity of the porous hollow Pt-based/C NPs results from (i) the presence of Ni in the Pt lattice (strain effect), (ii) their open porosity and (iii) their highly defective surface that leads to the presence of active sites both for electroreduction and electrooxidation reactions. The  $\text{CO}_{\text{ads}}$  stripping is impacted by the surface defectivity, resulting in the presence of two peaks, at  $E \sim 0.7 \text{ V vs. RHE}$  and  $E \sim 0.78 \text{ V vs. RHE}$  in  $\text{CO}_{\text{ads}}$  stripping voltammograms. These two electrooxidation peaks are ascribed to (i) the electrooxidation of  $\text{CO}_{\text{ads}}$  adsorbed onto and near the structural defects and (ii) the electrooxidation of the  $\text{CO}_{\text{ads}}$  adsorbed on highly coordinated catalytic sites from which it cannot diffuse to the structural defects. The shape of the  $\text{CO}_{\text{ads}}$  stripping (*i.e.* peak multiplicity, position of the peaks, ratio between the charge under the ‘low-potential’ and the total charge of the  $\text{CO}_{\text{ads}}$  stripping, value of the first moment of the potential weight of the  $\text{CO}_{\text{ads}}$  stripping) was found to be related not only to the density of structural defects, but also to the nickel content, thereby providing tools to predict the electrocatalytic activity for the ORR.



# Chapter V. Stability of the porous hollow PtNi/C NPs during simulated PEMFC operating conditions

**All the results discussed in this chapter have been (or will be) published in:**

(1) Asset, T.; Busby, Y.; Crisci, A.; Martin, V.; Stergiopoulos, V.; Serov, A.; Atanassov, P.; Chattot, R.; Dubau, L.; Maillard, F. and Job, N. Influence of the Carbon Support on the Morphology and Stability of Porous Hollow PtNi/C electrocatalysts, *to be submitted*.

In this article, the contribution of the author of this thesis was (i) the synthesis of the porous hollow PtNi/C NPs on different carbon supports, (ii) the acquisition and analysis of the SAA, of the electrochemical characterization and of the TEM micrographs, (iii) the analysis of the XRD patterns, of the XPS spectra and of the BET specific surface, (iv) the preparation of the samples for the IL-TEM measurements, their acquisition and analysis and (v) the preparation of the manuscript for publication.

(2) Asset, T.; Chattot, R.; Drnec, J.; Bordet, P.; Job, N.; Maillard, F. and Dubau, L. Elucidating the Mechanisms Driving the Ageing of Porous Hollow PtNi/C Nanoparticles by the Means of CO<sub>ads</sub> Stripping, **DOI:** 10.1021/acsami.7b05782.

In this article, the contribution of the author of this thesis was (i) the synthesis of the porous hollow PtNi/C NPs at different temperatures, (ii) the analysis of the XRD patterns, (iii) the acquisition and analysis of the SAA, of the electrochemical characterization and of the TEM micrographs, (iv) the preparation of the samples for the WAXS measurements and the acquisition of the WAXS patterns and (v) the preparation of the manuscript for publication.

(3) Asset, T.; Chattot, R.; Martens, I.; Drnec, J.; Bordet, P.; Nelayah, J.; Job, N.; Maillard, F. and Dubau, L. *In Operando* Study of the Ageing of Porous Hollow PtNi/C NPs, *to be submitted*.

In this article, the contribution of the author of this thesis was (i) the synthesis of the porous hollow PtNi/C NPs at different temperatures, (ii) the preparation of the membrane electrode assemblies for the *in operando* measurements, (iii) the acquisition and analysis of the *in operando* WAXS, the *in operando* SAXS and the electrochemical characterization, (iv) the preparation of the manuscript for publication.

## V. 1. Introduction

The interest of an electrocatalyst for the oxygen reduction reaction (or, *lato sensu*, for every reaction occurring in harsh environmental conditions, *i.e.* high potential, low pH, *etc.*) depends on its electrocatalytic activity but also of its long-term stability. Several nanostructures with high initial activity have been widely discussed in the literature<sup>88,89,129</sup> but the latter shortly depreciates in PEMFCs conditions or during appropriate (*i.e.* at *ca.* 353 K) Accelerated Stress Tests (AST)<sup>280</sup>. Therefore, investigating the stability of an electrocatalyst is essential to foresee its true potential for PEMFCs applications. In this chapter, we address the stability of (i) the porous hollow PtNi NPs and of their carbon supports during AST (see **Section II. 3. 6.**) that simulate the operating conditions of a PEMFC cathode and of (ii) the parameters that drive their enhanced activity for the ORR, *i.e.* the porous architecture, the defective structure and the Ni content (see **Section IV. 1** to **IV. 3**).

Pt-based NPs (*i.e.* PtM NPs, M being a 3d transition metal) suffer from the segregation of the non-noble metal induced by its chemical affinity with the highly oxidizing environment of the PEMFC cathode. Since any M atom reaching the surface is instantaneously corroded into  $M^{z+}$ , the difference in chemical potential between the NCs bulk and their surface is maintained. This causes a continuous dissolution of M associated with a decrease of strain and ligand effects<sup>97,130,215–218</sup>. In addition, the porous hollow Pt-based/C NPs suffer from classical degradation mechanisms, *i.e.* dissolution and redeposition of  $Pt^{z+}$  ions by Ostwald ripening, crystallite migration and coalescence (see **Section I. 6. 2.** and Ref.<sup>198–201</sup>). Gusak *et al.*<sup>330</sup> showed by Monte-Carlo simulation that hollow nanoparticles are not thermodynamically stable and that shrinking time depends on (i) the external diameter of the NPs and the shell thickness, (ii) the presence of an alloyed element (alloyed shells are more stable than pure shells<sup>330</sup>) and (iii) the temperature (*i.e.* increased temperature results in decreased stability<sup>330,331</sup>). This instability was also evidenced by electrochemical means: Dubau *et al.*<sup>331</sup> observed the collapse of porous hollow PtNi/C NPs (precursors ratio = 1:1) after 5,000 cycles between 0.60 and 1.05 V *vs.* RHE at  $T = 353 \pm 1$  K. Another study from Dubau *et al.*<sup>332</sup> on porous hollow PtNi/C NPs (precursors ratio = 1:3), combining HR-TEM, STEM-EDX and electrochemistry showed that, after 5,000 cycles between 0.6 and 1.0 V *vs.* RHE (*i.e.* a different upper potential than in Ref.<sup>331</sup>) at  $T = 353 \pm 1$  K and with  $\nu = 0.050$  V  $s^{-1}$ :

- (i) the activity losses were mainly induced by the nickel dissolution;
- (ii) the activity enhancement factor attributed to structural defects was maintained;

- (iii) the hollow structure was maintained (thus underlining the essential role of the place-exchange mechanism, see **Section I. 6. 2.** onto the NPs collapse observed in Ref. <sup>331</sup>).

In **Section V. 2.**, the ageing of porous hollow PtNi/C electrocatalysts is discussed, up to 20,000 cycles between 0.6 and 1.0 V vs. RHE ( $T = 353 \pm 1$  K,  $\nu = 0.050$  V s<sup>-1</sup>), with various crystallite size and density of structural defects (*i.e.* the materials from **Section IV. 3.**). The ageing of the porous hollow PtNi/C NPs was also investigated by *in operando* X-ray diffraction at the ID 31 beamline of the European Synchrotron Radiation Facility (ESRF) in Grenoble, France (**Section V. 3.**). The *in operando* study was performed by cycling the potential between 0.6 and 1.0 V vs. RHE or between 0.6 and 1.1 V vs. RHE in a liquid electrolyte cell (5,000 cycles,  $T = 353 \pm 1$  K,  $\nu = 0.050$  V s<sup>-1</sup>). Combined to EDX elemental maps and HR-TEM micrographs, these experiments provide a detailed picture of the structural changes of the porous hollow PtNi/C during ageing.

The Pt-based electrocatalysts used to catalyse the ORR operate under harsh conditions, *i.e.* 0.6 V vs. RHE  $< E < 1.0$  V vs. RHE, pH  $\sim 1$ ,  $T = 353$  K, high relative humidity. These conditions promote the degradation of both the Pt-based nanoparticles and of the carbon support. In terms of kinetics, the COR ( $C \rightarrow \text{CO}_{\text{surf}}$  or  $C \rightarrow \text{CO}_2$  <sup>176</sup>) proceeds at potentials  $E > 0.6$  V vs. RHE, starting preferentially on the non-graphitized domains <sup>193</sup> (the graphitized domains starts oxidizing at *ca.* 1.0 V vs. RHE) and, as such, the COR kinetics depends on the carbon structure (carbon crystallite size both in the plane and perpendicular to the plane), on its functionalization <sup>192</sup> and on the weight fraction of Pt-based NPs (the COR is catalysed by Pt <sup>194-196</sup>). Minimizing the corrosion of the carbon support is essential to avoid the detachment of the Pt-based NPs and the carbon support losses of electronic conductivity due to (i) the amorphization of the graphitic domains, especially in the interconnection regions between the carbon particles <sup>333</sup> and (ii) the increase of the surface coverage of oxygen based group (*e.g.* quinone/hydroquinone (Q/HQ)). In **Section V. 4.**, the porous hollow PtNi/C NPs synthesized on different carbon substrates (see **Section IV. 5.**) were aged following a procedure mimicking the potential variations during start-up/shutdown events of a PEMFC cathode <sup>208</sup>. To this goal, a square potential ramp between 1.0 and 1.5 V vs. RHE was used ( $t = 3$  s at each potential,  $T = 353 \pm 1$  K, see **Section II. 3. 6.**). This potential range is much more aggressive for the carbon support than the ‘load-cycling’ potential range (*i.e.* 0.6 – 1.0 or 1.1 V vs. RHE) as it results in the corrosion of both the amorphous and the graphitized domains of the carbon support <sup>193</sup>.

## V. 2. Elucidating the mechanisms driving the ageing of porous hollow PtNi/C nanoparticles by the means of CO<sub>ads</sub> stripping

In this section, we discuss the ageing of hollow porous PtNi/C NPs using a ‘load-cycle’ protocol, *i.e.* 20,000 cycles with a linear profile between 0.6 and 1.0 V *vs.* RHE in 0.1 M HClO<sub>4</sub> at  $\nu = 0.050 \text{ V s}^{-1}$  and  $T = 353 \pm 1 \text{ K}$ , to gain insights onto the durability of the NPs (the stability of the Ni atoms and of the structural defects) without the contribution of the place-exchange mechanism (that occurs at  $E \geq 1.05 \text{ V vs. RHE}$ ). **Figure 50** and **Table 9** summarize the changes of the electrocatalytic properties of the porous hollow PtNi/C nanoparticles synthesized at  $T = 278, 293, 313, 333$  and  $353 \text{ K}$  after 20,000 potential cycles with an intermediate characterisation after 5,000 potential cycles.

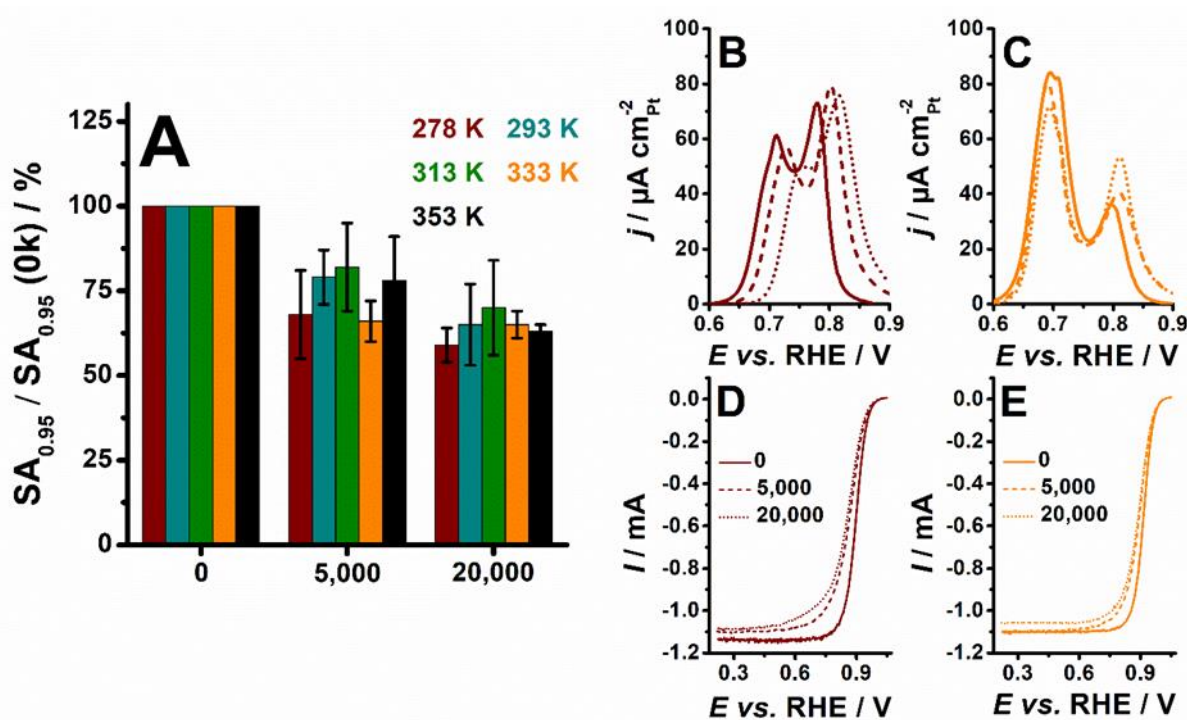


**Figure 50.** (A) Ratio of the specific activity for the ORR measured at  $E = 0.95 \text{ V vs. RHE}$  for the electrocatalysts synthesized at  $T = 278, 293, 313, 333$  and  $353 \text{ K}$  before ( $SA_{0.95}(0k)$ ) and after ( $SA_{0.95}$ ) 5,000 and 20,000 potential cycles with linear profile between  $E = 0.6 \text{ V vs. RHE}$  and  $E = 1.0 \text{ V vs. RHE}$  at  $\nu = 0.05 \text{ V s}^{-1}$  and  $T = 353 \text{ K}$  in Ar-saturated 0.1 M HClO<sub>4</sub>; (B – C) Background-subtracted CO<sub>ads</sub> stripping voltammograms measured before and after 5,000 and 20,000 potential cycles with linear profile for the porous hollow PtNi/C electrocatalysts synthesized at (B)  $T = 278 \text{ K}$  and (C)  $T = 333 \text{ K}$ ; (D – E) Ohmic drop corrected polarization curves in O<sub>2</sub> saturated 0.1 M HClO<sub>4</sub> before and after 5,000 and 20,000 potential cycles with linear profile for the porous hollow PtNi/C electrocatalysts synthesized at (D)  $T = 278 \text{ K}$  and (E)  $T = 333 \text{ K}$ .

## Chapter V. Stability of the porous hollow PtNi/C NPs during simulated PEMFC operating conditions

After 20,000 potential cycles, a 30 to 40 % loss of the specific activity for the ORR at  $E = 0.95$  V vs. RHE is reported (**Figure 50A**), the most stable electrocatalyst being that synthesized at  $T = 313$  K ( $j_k = 140 \pm 29 \mu\text{A cm}_{\text{Pt}}^{-2}$  before ageing and  $98 \pm 20 \mu\text{A cm}_{\text{Pt}}^{-2}$  after 20,000 potential cycles) and the least stable that synthesized at  $T = 278$  K ( $j_k = 108 \pm 18 \mu\text{A cm}_{\text{Pt}}^{-2}$  before ageing and  $73 \pm 13 \mu\text{A cm}_{\text{Pt}}^{-2}$  after 20,000 potential cycles, see **Table 9**). A mass activity loss approaching 60 % is also observed for the electrocatalyst synthesized at  $T = 278$  K after 20,000 potential cycles (**Table 9**). The specific and mass activities for the ORR measured at  $E = 0.95$  V and 0.90 V vs. RHE after 5,000 and 20,000 potential cycles are provided in **Table 9**.

**Table 9.** Specific and mass activities for the ORR (corrected for the Ohmic losses and oxygen diffusion in solution) measured at  $E = 0.95$  V vs. RHE or  $E = 0.90$  vs. RHE for the electrocatalysts synthesized at  $T = 278, 293, 313, 333$  and  $353$  K before and after 5,000 and 20,000 potential cycles between  $E = 0.6$  V vs. RHE and  $E = 1$  V vs. RHE at  $\nu = 0.05$  V s<sup>-1</sup>,  $T = 353$  K in an Ar-saturated 0.1 M HClO<sub>4</sub> electrolyte. The electrocatalytic activities are normalized by the electrochemically active surface area (specific activity, SA) or by the mass of Pt (mass activity, MA).

	SA <sub>0.95</sub> / $\mu\text{A cm}_{\text{Pt}}^{-2}$			MA <sub>0.95</sub> / $\text{A g}_{\text{Pt}}^{-1}$			SA <sub>0.90</sub> / $\mu\text{A cm}_{\text{Pt}}^{-2}$			MA <sub>0.90</sub> / $\text{A g}_{\text{Pt}}^{-1}$		
	0k	5k	20k	0k	5k	20k	0k	5k	20k	0k	5k	20k
<b>Pt/C</b>	26 ± 3	27 ± 2	37 ± 3	21 ± 2	20 ± 2	27 ± 2	209 ± 32	183 ± 10	218 ± 15	166 ± 30	127 ± 8	159 ± 9
<b>T = 278 K</b>	108 ± 18	77 ± 15	65 ± 5	60 ± 11	29 ± 2	23 ± 1	1000 ± 111	438 ± 33	341 ± 36	580 ± 72	159 ± 6	123 ± 3
<b>T = 293 K</b>	119 ± 31	89 ± 9	73 ± 13	62 ± 10	38 ± 2	30 ± 3	1328 ± 146	532 ± 8	398 ± 70	699 ± 110	222 ± 37	163 ± 14
<b>T = 313 K</b>	140 ± 29	115 ± 18	98 ± 20	53 ± 6	41 ± 3	32 ± 5	1247 ± 139	561 ± 24	395 ± 45	496 ± 40	227 ± 9	154 ± 30
<b>T = 333 K</b>	179 ± 41	123 ± 12	120 ± 7	77 ± 12	40 ± 5	39 ± 5	1677 ± 204	687 ± 202	604 ± 143	695 ± 89	223 ± 73	195 ± 57
<b>T = 353 K</b>	170 ± 48	135 ± 23	109 ± 4	62 ± 13	35 ± 1	31 ± 1	1498 ± 148	640 ± 108	517 ± 30	550 ± 50	168 ± 7	147 ± 5

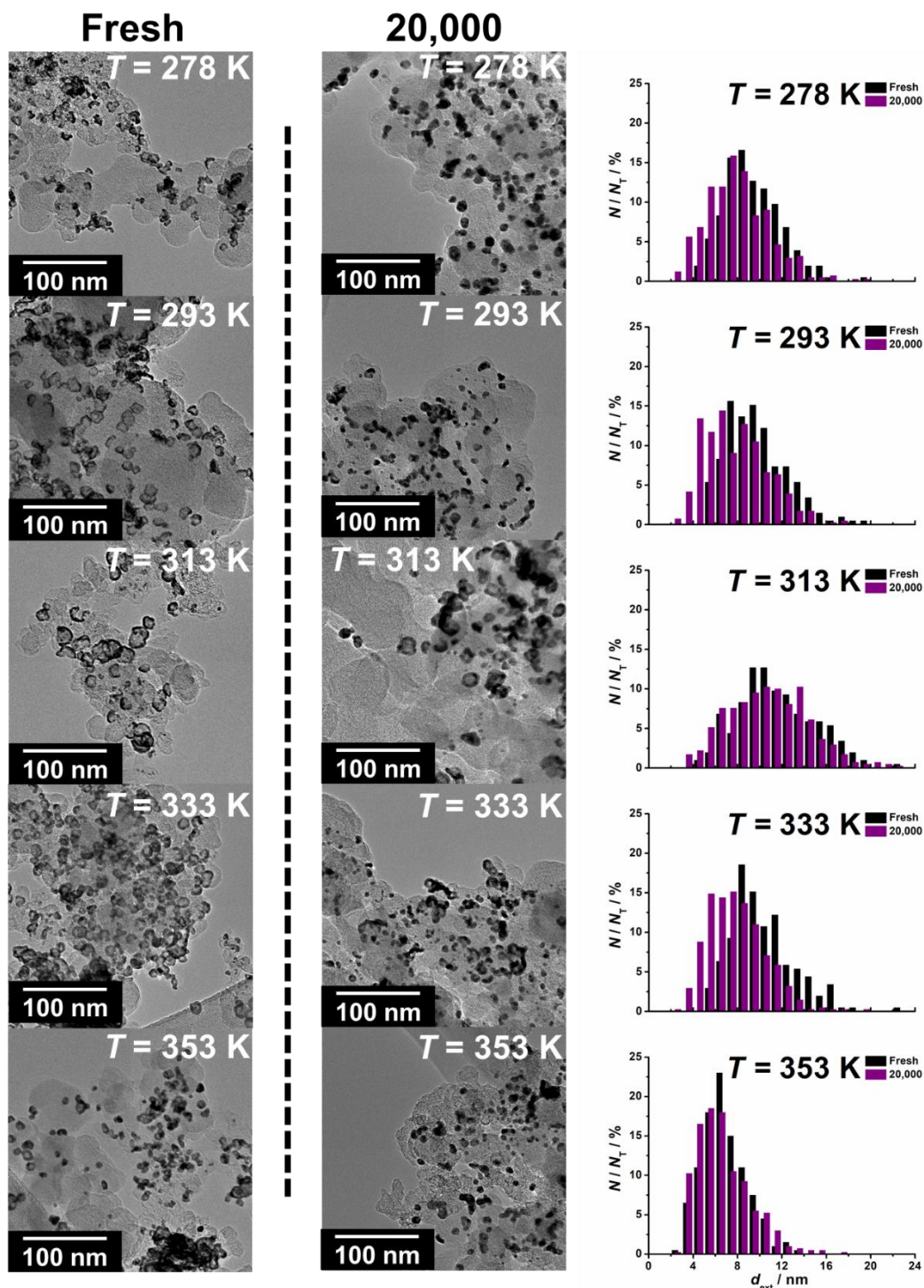


**Figure 51.** Representative TEM micrographs of the porous hollow PtNi/C electrocatalysts studied in this work before and after 20,000 potential cycles between  $E = 0.6 \text{ V vs. RHE}$  and  $E = 1.0 \text{ V vs. RHE}$  at  $\nu = 0.05 \text{ V s}^{-1}$  and  $T = 353 \text{ K}$  in Ar-saturated  $0.1 \text{ M HClO}_4$  electrolyte. The particle size distributions have been built from the external diameters ( $d_{ext}$ ) of the NPs before and after 20,000 potential cycles (note that the electrocatalyst synthesized at  $T = 353 \text{ K}$  initially presented a partly agglomerated shape: only the  $d_{ext}$  of the isolated particles is provided in the particle size distribution).

**Figure 51** shows that the hollow nanostructure is not maintained during the AST, with the notable exception of the electrocatalyst synthesized at  $T = 313$  K which remains partly hollow-shaped. The central cavity collapses, leading to the formation of 7 – 10 nm solid nanoparticles. The losses in ORR specific activity can be correlated to the changes of the  $\text{CO}_{\text{ads}}$  stripping voltammograms. As observed in **Figure 50B** and **Figure 50C** for the electrocatalysts synthesized at  $T = 278$  K and  $T = 333$  K, the losses in ORR specific activity (see **Figure 50D** and **Figure 50E**) are associated with a decrease in intensity of the  $\text{CO}_{\text{ads}}$  stripping ‘low-potential’ peak (*i.e.* a diminution of  $Q_{\text{pp,CO}} / Q_{\text{T,CO}}$ ) and an increase in potential of the  $\text{CO}_{\text{ads}}$  stripping peaks (*i.e.* an increase of  $E_{\text{pp,CO}}$  and  $E_{\text{p,CO}}$  and, thus, a decrease of  $\mu_1^{\text{CO}}$ , see **Figure 52**).

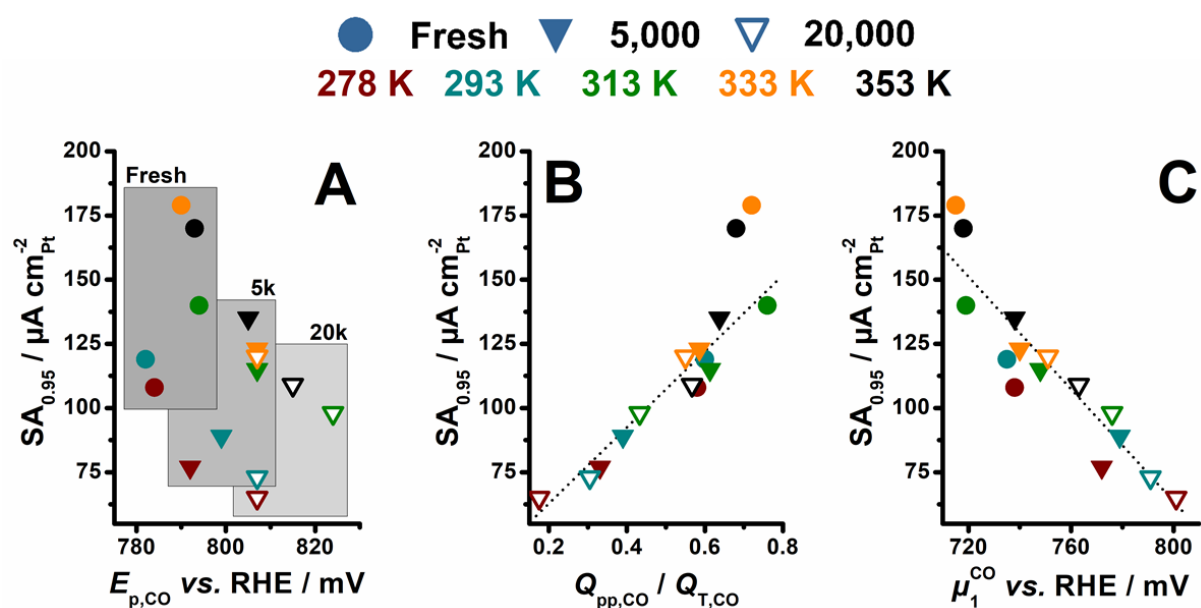


**Figure 52.** Variation of the specific activity for the ORR measured at  $E = 0.95$  V vs. RHE for the porous hollow PtNi/C electrocatalysts synthesized at  $T = 278, 293, 313, 333$  and  $353$  K before (Fresh) and after 5,000 and 20,000 potential cycles with linear profile between  $E = 0.6$  V vs. RHE and  $E = 1.0$  V vs. RHE in Ar-saturated 0.1 M  $\text{HClO}_4$  at  $v = 0.05$  V  $\text{s}^{-1}$  and  $T = 353$  K vs. (A) the potential of the ‘high-potential’ peak in  $\text{CO}_{\text{ads}}$  stripping voltammograms ( $E_{\text{p,CO}}$ ); (B) the ratio of the electrical charge under the ‘low-potential’ ( $Q_{\text{pp,CO}}$ ) to the total electrical charge of the  $\text{CO}_{\text{ads}}$  stripping voltammogram ( $Q_{\text{T,CO}}$ ); (C) the first moment of the potential weight of the  $\text{CO}_{\text{ads}}$  stripping ( $\mu_1^{\text{CO}}$ ).

The average value of  $E_{\text{p,CO}}$  shifts from  $E_{\text{p,CO}} = 789$  mV vs. RHE before ageing to  $E_{\text{p,CO}} = 802$  mV vs. RHE and  $E_{\text{p,CO}} = 812$  mV vs. RHE after 5,000 and 20,000 potential cycles, respectively (see **Figure 52**). This relaxation is associated with a diminution of the Ni content of the electrocatalysts synthesized at  $T = 278$  K and  $T = 333$  K as determined from the STEM-EDX micrographs (see **Figure 53**). In contrast to AAS analyses, STEM-EDX analyses are performed

on single nanoparticles: this may account for the difference between the values reported in **Figure 53** and **Figure 38**. The depletion in Ni and the subsequent relaxation of the lattice parameter, predicted by the change of  $E_{p,CO}$ , (*i.e.* disappearance of the Ni-induced lattice parameter contraction) are in agreement with the literature results for PtM electrocatalysts<sup>215,243,332,334,335</sup>.

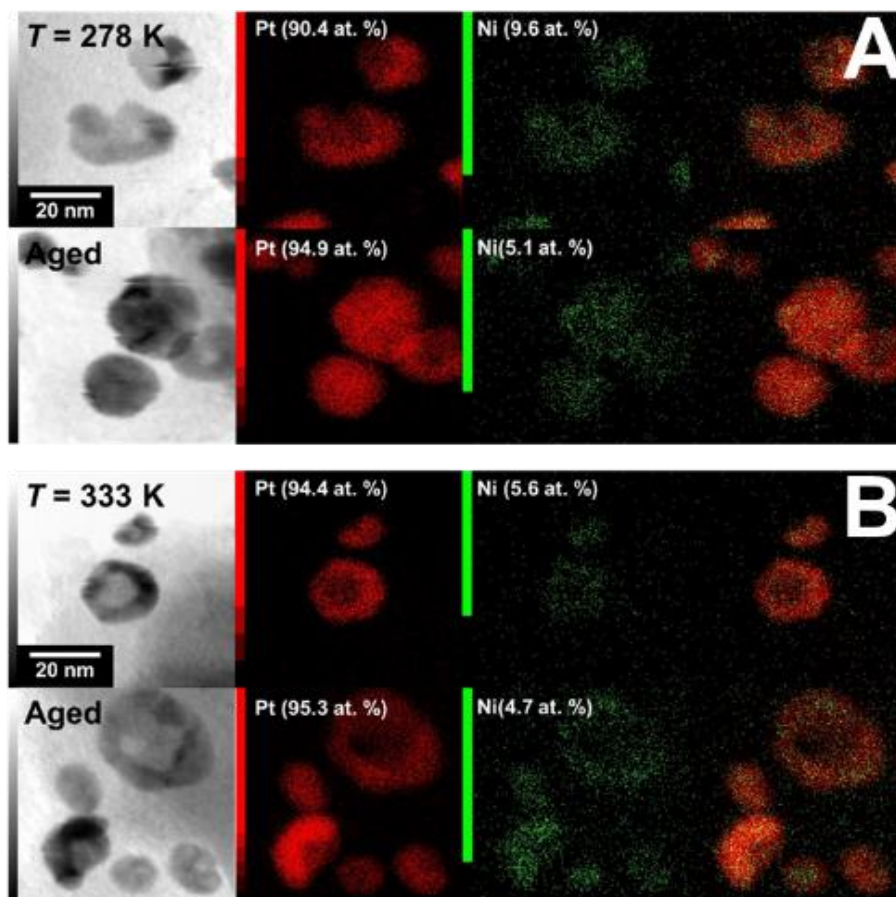


**Figure 53.** Variation of the composition measured by STEM-EDX for the electrocatalysts synthesized at  $T = 278$  K and  $T = 333$  K before and after 20,000 potential cycles between  $E = 0.6$  V vs. RHE and  $E = 1.0$  V vs. RHE at  $\nu = 0.05$  V s<sup>-1</sup>,  $T = 353$  K in an Ar-saturated 0.1 M HClO<sub>4</sub> electrolyte.

**Table 10.** Variation of the microstrain ( $\mu_\varepsilon$ ), the mean crystallite size ( $d_{\text{XRD}}$ ) for the electrocatalysts synthesized at  $T = 278$  and  $333$  K before (prior to the electrochemical characterisation, *i.e.* ‘Fresh’) and after electrochemical characterisation (‘Fresh + ORR’) and after 5,000 and 20,000 potential cycles between  $E = 0.6$  V *vs.* RHE and  $E = 1.0$  V *vs.* RHE in Ar-saturated  $0.1$  M  $\text{HClO}_4$  at  $\nu = 0.05$  V  $\text{s}^{-1}$  and  $T = 353$  K.

		$\mu_\varepsilon / \%$	$d_{\text{XRD}} / \text{nm}$
<b><math>T = 278</math> K</b>	Fresh	204	$1.5 \pm 0.1$
	Fresh + ORR	91	$3.5 \pm 0.2$
	5,000	16	$4.2 \pm 0.3$
	20,000	19	$3.9 \pm 0.3$
<b><math>T = 333</math> K</b>	Fresh	147	$3.2 \pm 0.1$
	Fresh + ORR	81	$4.0 \pm 0.3$
	5,000	65	$5.2 \pm 0.7$
	20,000	44	$4.6 \pm 0.6$

The physical properties of the electrocatalysts synthesized at  $T = 298$  K and  $T = 333$  K after electrochemical characterisation (*i.e.*  $\text{CO}_{\text{ads}}$  stripping + 6 cycles between  $E = 0.2$  V *vs.* RHE and  $E = 1.0$  V *vs.* RHE at  $\nu = 0.005$  V  $\text{s}^{-1}$  in an  $\text{O}_2$ -saturated  $0.1$  M  $\text{HClO}_4$  electrolyte) but before ageing are provided in **Table 10** as ‘Fresh + ORR’. Interestingly, the electrocatalysts suffer dramatic structural modification after the initial electrochemical characterisation. For the electrocatalyst synthesized at  $T = 278$  K, the microstrain shifts from  $\mu_\varepsilon = 204$  % to  $\mu_\varepsilon = 91$  % and the crystallite size shifts from  $d_{\text{XRD}} = 1.48$  nm to  $d_{\text{XRD}} = 3.5$  nm. Castanheira *et al.*<sup>203</sup> underlined the impact of intermediate characterizations of a Pt/HSAC electrocatalyst during its ageing in an Ar-saturated electrolyte, focusing on the impact of  $\text{CO}_{\text{ads}}$  stripping and cyclic voltammograms. They showed that intermediate characterizations intensify the degradation of the Pt/HSAC ECSA<sup>203</sup>. Here, it appears that the measurement of the ORR activity in  $\text{O}_2$ -saturated electrolyte also results in modification of the electrocatalysts morphology, likely because of the shift between a reductive atmosphere (CO) and an oxidant atmosphere ( $\text{O}_2$ ). This is confirmed by the changes of the  $\text{CO}_{\text{ads}}$  stripping voltammograms before and after the ORR (see **Figure 54**). A diminution of the contribution of the ‘low-potential’ peak of the  $\text{CO}_{\text{ads}}$  stripping is observed for the electrocatalyst synthesized at  $T = 278$  K (while being less visible for the electro-

catalyst synthesized at  $T = 333$  K) concomitantly with a shift of the  $E_{p,CO}$  toward higher electrode potentials accounting for the diminution of both the density of structural defects and the Ni content in the electrocatalyst.

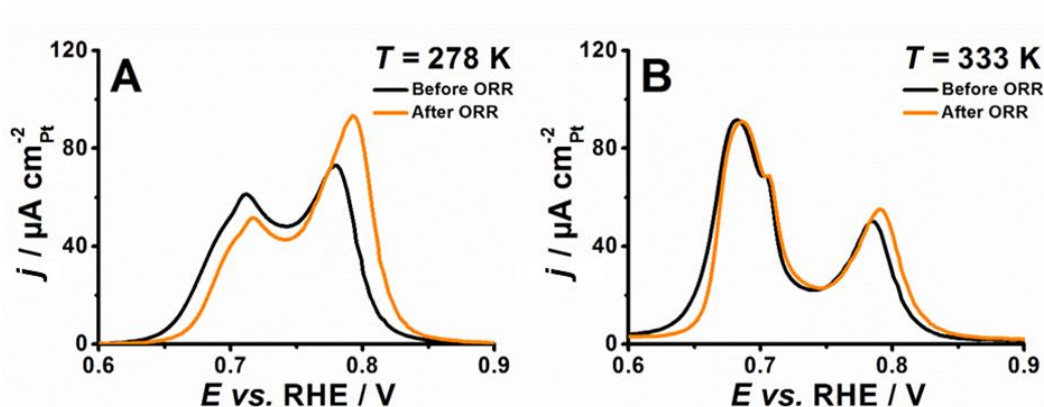


**Figure 54.** Variation of the  $\text{CO}_{\text{ads}}$  stripping voltammograms performed in an Ar-saturated 0.1 M  $\text{HClO}_4$  electrolyte ( $\nu = 0.020$  V  $\text{s}^{-1}$ ,  $T = 298$  K) before and after measurement of the ORR activity for the electrocatalysts synthesized at (A)  $T = 298$  K and (B)  $T = 333$  K.

Simultaneously to the increase of  $E_{p,CO}$ , a decrease of ratio of the  $Q_{pp,CO} / Q_{T,CO}$  and a dramatic decrease of the microstrain ( $\mu_\epsilon$ ) are observed for the electrocatalysts synthesized at  $T = 278$  K and  $T = 333$  K during ageing (see **Figure 52B** and **Table 10**). This is in agreement with the increase of the average crystallite size ( $d_{\text{XRD}}$ ) determined from the XRD patterns during the first 5,000 potential cycles (**Table 10**) resulting from Ostwald ripening and/or crystallite migration/coalescence<sup>199</sup>. Note that the variation of the PtNi crystallite size observed between 5,000 and 20,000 cycles ( $d_{\text{XRD}} = 4.2 \pm 0.3$  nm at 5,000 cycles and  $d_{\text{XRD}} = 3.9 \pm 0.3$  nm at 20,000 cycles for the electrocatalyst synthesized at  $T = 278$  K) remains within the error bar of the measurement and was thus considered as non-significant. Depending on their initial morphology ('nanocrystallites (NCs) < 2nm' / 'high-microstrain' or 'NCs > 3 nm' / 'low-microstrain'), the NPs suffer different fates. For the electrocatalysts where the density of grain boundaries (GBs) was the highest (*i.e.* the electrocatalysts synthesized at  $T = 278$  K and  $T = 293$  K), a dramatic decrease of the microstrain (see **Table 10** for the electrocatalyst synthesized at  $T = 278$  K), of  $Q_{pp,CO} / Q_{T,CO}$  (**Figure 52B**) and of the specific activity for the ORR at  $E = 0.95$  V vs. RHE is noticed. However, for the electrocatalysts that presented a NCs diameter > 3 nm and an initial  $Q_{pp,CO} / Q_{T,CO} > 0.68$ , *i.e.* the electrocatalysts where the GBs are not the main type of structural defects, the losses in specific activity for the ORR are far less severe. Consequently,

on electrocatalysts displaying initial ORR activity controlled by the density of structural defects, a value of  $d_{\text{XRD}} > 3$  nm (and therefore, stable structural defects) is a pre-requisite to stable ORR activity during ageing. The morphological and structural changes of the electrocatalysts (*i.e.*  $\mu_{\text{e}}$ ,  $d_{\text{XRD}}$ ,  $a_{\text{Pt-Pt}}$ , *etc.*) slow down between 5,000 and 20,000 potential cycles (see **Figure 52**). Therefore, (i) most of the electrocatalysts degradation occurs during the 5,000 first cycles between  $E = 0.6$  V and  $E = 1.0$  V *vs.* RHE at  $T = 353$  K and (ii) the losses in the density of structural defects which occurs between 5,000 and 20,000 cycles do not impact the NPs size. The density of GBs remains identical and other types of structural defects are likely impacted (such as the concavity of the internal surface during the collapsing of the nanoparticles, see **Figure 51**).

Combining high resolution TEM and electrochemistry, Dubau *et al.*<sup>332</sup> recently reported that the depletion in Ni was the main cause of the decline in ORR activity for porous hollow and solid PtNi/C NPs. The electrocatalysts discussed by Dubau *et al.*<sup>332</sup> presented a  $d_{\text{XRD}} > 3$  nm<sup>234</sup>, therefore supporting the results discussed in this section, *i.e.* porous hollow and solid PtNi/C structures with a  $d_{\text{XRD}} > 3$  nm do not suffer dramatic losses in structural defects density during ageing. Most of their activity losses result from the dissolution of the Ni atoms from the PtNi shell (see **Figure 52**, **Figure 53** and Ref.<sup>332</sup>). **Figure 52C** shows that the first moment of the potential weight of the electrocatalysts discussed in this work ( $\mu_1^{\text{CO}}$ ) is directly correlated to the changes of ORR specific activity at  $E = 0.95$  V *vs.* RHE. This clearly confirms that the losses in ORR specific activity for the ORR are induced by the combination of the relaxation of the lattice parameter, *i.e.* the diminution of the Ni-induced lattice contraction, and a decrease of the density of structural defects.

### V. 3. *In operando* study of the ageing of the porous hollow PtNi/C NPs

Porous hollow PtNi/C NPs were also aged in the electrochemical flow cell described in **Section II. 3. 7** coupled with *in operando* wide angle X-ray scattering (WAXS) measurements. The electrocatalyst used in this section was synthesized at room temperature with a 1:3 atomic ratio between the metallic precursors and supported onto Vulcan XC72. The initial crystallite size was  $d_{\text{XRD}} = 2.4 \pm 0.1$  nm and the electrocatalyst was aged during 5,000 potential cycles between 0.6 and 1.0 or 1.1 V *vs.* RHE at  $\nu = 0.05$  V s<sup>-1</sup>, both in classic four-electrode cell (see **Figure 55**) and in the *in operando* WAXS cell.

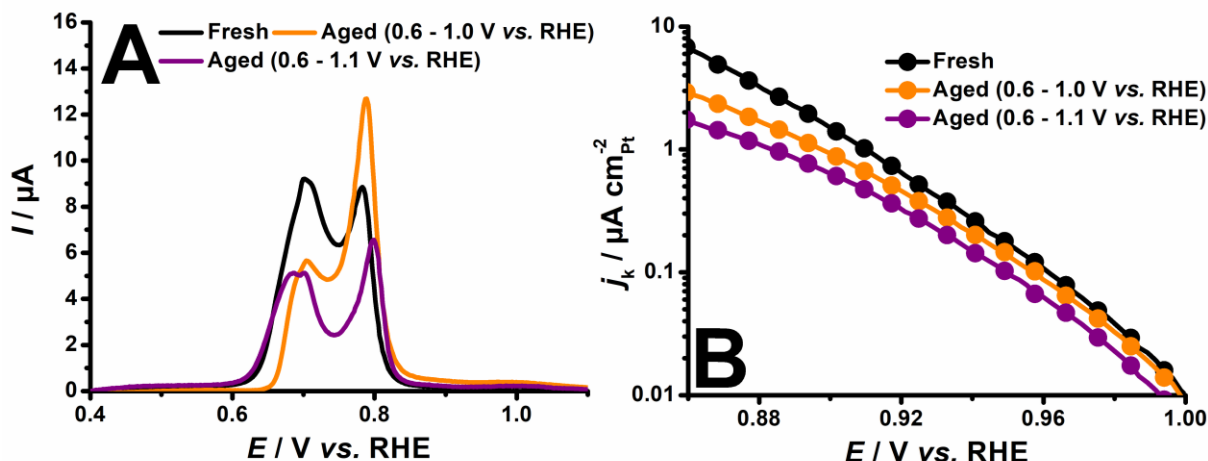


**Figure 55.** Electrochemical properties of the porous hollow PtNi/C electrocatalyst discussed in this section before and after 5,000 potential cycles in Ar-saturated 0.1 M HClO<sub>4</sub> between 0.6 and 1.0 V vs. RHE or 1.1 V vs. RHE ( $\nu = 0.05 \text{ V s}^{-1}$  and  $T = 353 \pm 1 \text{ K}$ ). **(A)** CO<sub>ads</sub> stripping ( $\nu = 0.020 \text{ V s}^{-1}$ , electrolyte = Ar-saturated 0.1 M HClO<sub>4</sub>,  $T = 298 \pm 1 \text{ K}$ ). **(B)** Linear sweep voltammograms in O<sub>2</sub>-saturated 0.1 M HClO<sub>4</sub> in Tafel representation, corrected from the diffusion in solution and the Ohmic drop ( $\nu = 0.005 \text{ V s}^{-1}$ ,  $\omega = 1600 \text{ rpm}$ ).

The post-ageing CO<sub>ads</sub> stripping is highly dependent on the upper potential chosen for the ageing (1.0 or 1.1 V vs. RHE, see **Figure 55**). For  $E_{\text{upper}} = 1.0 \text{ V vs. RHE}$ , the intensity under the ‘low-potential’ peak decreases with respect to what was observed in **Section V. 2**. The electrocatalyst suffers from a decrease of its Ni content, as evidenced by the shift of  $E_{\text{p,CO}}$  toward higher potentials (from 0.78 to 0.79 V vs. RHE). These Ni losses are more pronounced for  $E_{\text{upper}} = 1.1 \text{ V vs. RHE}$  ( $E_{\text{p,CO}} = 0.80 \text{ V vs. RHE}$  after ageing). The first moment of the potential weight ( $\mu_1^{\text{CO}}$ , see **Equation 24**) increases if  $E_{\text{upper}} = 1.0 \text{ V vs. RHE}$  ( $\mu_1^{\text{CO}}(\text{fresh}) = 734 \text{ mV vs. RHE vs. } \mu_1^{\text{CO}}(\text{aged}) = 767 \text{ mV vs. RHE}$ ) but remains nearly constant if  $E_{\text{upper}} = 1.1 \text{ V vs. RHE}$  ( $\mu_1^{\text{CO}}(\text{fresh}) = 734 \text{ mV vs. RHE vs. } \mu_1^{\text{CO}}(\text{aged}) = 737 \text{ mV vs. RHE}$ ). However, the electrocatalyst aged up to  $E = 1.1 \text{ V vs. RHE}$  presented a depreciated SA at  $E = 0.95 \text{ V vs. RHE}$  compared to the electrocatalyst aged up to  $E = 1.0 \text{ V vs. RHE}$  and the fresh electrocatalyst ( $\text{SA}_{0.95} = 92 \mu\text{A cm}_{\text{Pt}}^{-2}$  vs. 137 and 154  $\mu\text{A cm}_{\text{Pt}}^{-2}$ , respectively, see **Table 11**), by opposition to what was observed in **Section IV. 3**, *i.e.* a decreased  $\mu_1^{\text{CO}}$  results in an increased specific activity at  $E = 0.95 \text{ V vs. RHE}$ .

Chapter V. Stability of the porous hollow PtNi/C NPs during simulated PEMFC operating conditions

**Table 11.** Physical, chemical and electrochemical properties of the hollow PtNi/C electrocatalyst used in the *in operando* WAXS measurements.

	<b>Fresh</b>	<b>0.6 – 1.0 V vs. RHE</b>	<b>0.6 – 1.1 V vs. RHE</b>
<b>Pt</b> / wt. %	20.3 ± 0.5	*	*
<b>Ni<sub>AAS</sub></b> / at %	20 ± 0.5	*	*
<b>S<sub>Pt, CO</sub></b> / m <sup>2</sup> g <sub>Pt</sub> <sup>-1</sup>	42.6 ± 5	31.6 **	24.5 **
<b>SA<sub>0.95</sub></b> / μA cm <sub>Pt</sub> <sup>-2</sup>	154 ± 14	129	92
<b>SA<sub>0.90</sub></b> / μA cm <sub>Pt</sub> <sup>-2</sup>	1287 ± 63	816	536
<b>MA<sub>0.95</sub></b> / μA cm <sub>Pt</sub> <sup>-2</sup>	65.5 ± 1	40	23
<b>MA<sub>0.90</sub></b> / μA cm <sub>Pt</sub> <sup>-2</sup>	546 ± 30	259	134

\* The determination of the Pt weight fraction and the Ni content from the AAS was not possible, owing to the extremely small amount of electrocatalyst obtained after the accelerated stress test (3.92 μg of Pt per electrode).

\*\* S<sub>Pt, CO</sub> was determined using the initial Pt weight fraction on the electrode.

The changes in the NPs morphology were also investigated by analyzing the electrocatalysts before and after the ageing in the WAXS electrochemical cell by TEM and STEM-EDX and HR-TEM (see **Figure 56**, **Figure 57** and **Figure 58**).

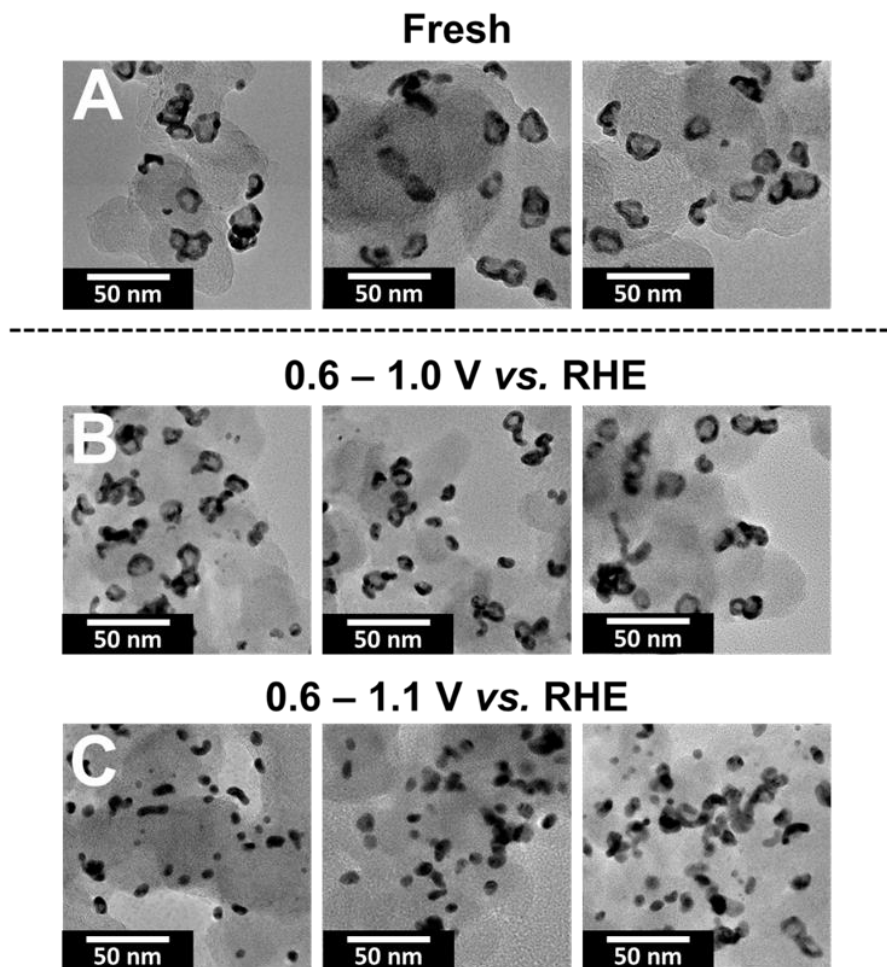


**Figure 56.** TEM micrographs of the gas diffusion electrode (GDE) (A) before and after 5,000 cycles in Ar-saturated 0.1 M HClO<sub>4</sub> between 0.6 and (B) 1.0 V vs. RHE or (C) 1.1 V vs. RHE. Other conditions:  $\nu = 0.050 \text{ V s}^{-1}$  and  $T = 353 \pm 1 \text{ K}$ .

At  $E_{\text{upper}} = 1.1 \text{ V vs. RHE}$ , the hollow nanostructure mainly collapses after 5,000 cycles (**Figure 56C**), by opposition to  $E_{\text{upper}} = 1.0 \text{ V vs. RHE}$  (in this case, the collapse of the nanostructure was observed after 20,000 cycles, see **Section V. 2.**). This confirms that the increase of the upper potential of the ageing exacerbates the rate of degradation mechanisms at stake. Deeper insights obtained by STEM-EDX (**Figure 57**) show that the electrocatalyst aged between 0.6 and 1.1 V vs. RHE presents two distinct structures: (i) porous hollow PtNi/C NPs with a slightly decreased Ni content ( $7.3 \pm 0.6 \text{ at. \% vs. } 9.8 \pm 0.8 \text{ at. \%}$  before ageing, see **Figure 57C**) and (ii) solid PtNi/C NPs with a low Ni content ( $3.9 \pm 0.9 \text{ at. \%}$ , see **Figure 57D**). By opposition, the electrocatalyst aged between 0.6 and 1.0 V vs. RHE only contains porous hollow PtNi/C NPs with a Ni content of  $6.3 \pm 0.7 \text{ at. \%}$  (**Figure 56** and **Figure 57B**).

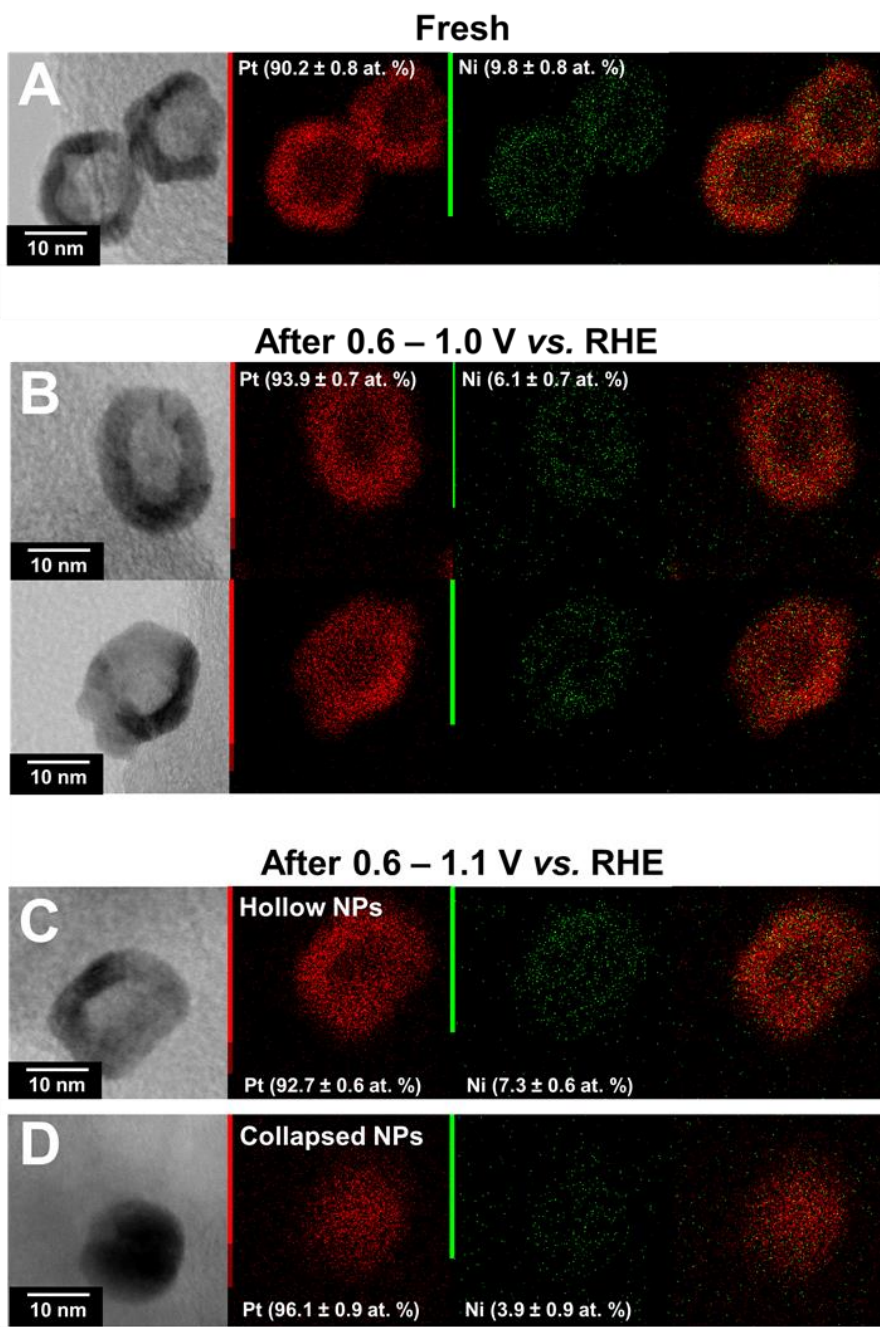


**Figure 57.** EDX elemental mapping of the gas diffusion electrode (A) before and after 5,000 cycles in Ar-saturated 0.1 M HClO<sub>4</sub> between 0.6 and (B) 1.0 V vs. RHE or (C - D) 1.1 V vs. RHE. Other conditions:  $\nu = 0.050 \text{ V s}^{-1}$  and  $T = 353 \pm 1 \text{ K}$ .

The heterogeneity in structure observed for the electrocatalyst aged with  $E_{\text{upper}} = 1.1 \text{ V vs. RHE}$  was assumed to originate from the difference in diameter (and shell thickness) of the initial porous hollow NPs ( $d_{\text{ext}} = 11.4 \pm 1.9 \text{ nm}$ ), the smaller NPs collapsing while the biggest NPs maintained their hollow nanostructure<sup>330</sup>. The HR-TEM micrographs indicates that the polycrystallinity and the hollow shape of the electrocatalysts aged with  $E_{\text{upper}} = 1.0 \text{ V vs. RHE}$  is

maintained (see **Figure 58B**), similarly to the porous hollow NPs observed on the electrocatalyst aged with  $E_{\text{upper}} = 1.1 \text{ V vs. RHE}$ . But collapsed NPs composed of only one nanocrystallite were also found (see **Figure 58C**).

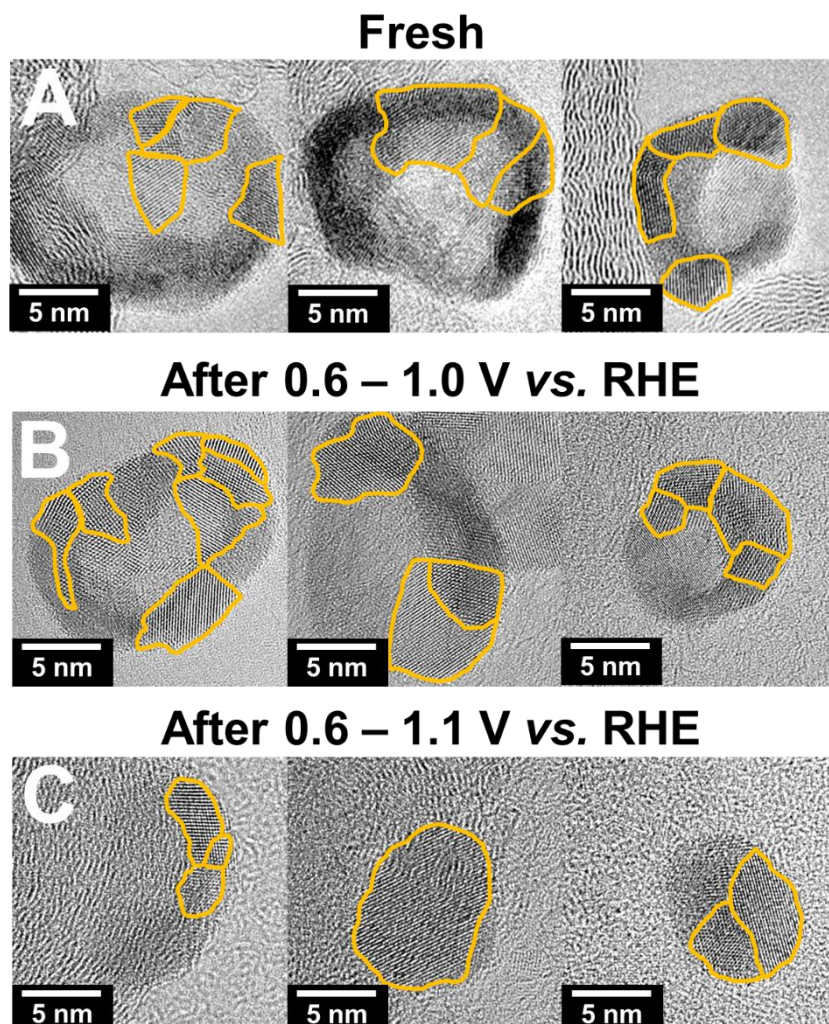


**Figure 58.** High resolution TEM of the gas diffusion electrode (A) before and after 5,000 cycles in Ar-saturated 0.1 M HClO<sub>4</sub> between 0.6 and (B) 1.0 V vs. RHE or (C) 1.1 V vs. RHE. Other conditions:  $\nu = 0.050 \text{ V s}^{-1}$  and  $T = 353 \pm 1 \text{ K}$ .

The electrocatalyst aged between 0.6 and 1.1 V vs. RHE thus presents a dual morphology, similarly to the nanostructures discussed by Maillard *et al.*<sup>149,264</sup>, *i.e.* polycrystalline NPs (*e.g.* agglomerated or hollow NPs) and monocrystalline NPs (with a low Ni-content, therefore explaining the positive shift of  $E_{\text{p,CO}}$ ). This explains the shape of its CO<sub>ads</sub> stripping (see **Figure 55B**), *i.e.* close to the CO<sub>ads</sub> of the fresh electrocatalyst despite their different morphologies.

As discussed in **Section IV. 2.**, the ‘high-potential’ peak of the CO<sub>ads</sub> stripping of the porous hollow PtNi/C results from the electrooxidation of the CO adsorbed on high-coordination sites from which they cannot diffuse to structural defects beneficial to the CO<sub>ads</sub> electrooxidation. Those sites are prone to disappear during the collapse of the hollow nanostructure. Therefore, the CO<sub>ads</sub> stripping of the aged electrocatalyst should be a unique ‘low-potential’ peak if the aged electrocatalyst was only composed of polycrystalline, highly defective NPs. **Figure 58B** shows that it is not always the case, *i.e.* some of the collapsed NPs are monocrystalline. On monocrystalline NPs, the CO<sub>ads</sub> cannot diffuse to the GBs (that present a highly expanded lattice thus nucleating OH at low potential values and facilitating the CO<sub>ads</sub> electrooxidation<sup>293,294</sup>) and is forced to oxidize within the ‘high-potential peak’. Consequently, the ‘high-potential’ peak observed on the CO<sub>ads</sub> stripping of the porous hollow PtNi/C NPs after ageing (see **Section V. 2.** and **Figure 55A**) does not result of the highly coordinated sites, but of (i) the collapsed monocrystalline NPs formed by NCs coalescence during ageing and (ii) of the NCs facets from which the CO<sub>ads</sub> cannot diffuse to a structural defect beneficial for the CO<sub>ads</sub> electrooxidation.

In summary, during ageing, the nature of the ‘high-potential’ peak of the CO<sub>ads</sub> stripping evolves from being representative of highly-coordinated sites to being representative of the monocrystalline nanostructures and defect-free facets, *i.e.* the nature discussed in **Section V. 3.** to the nature evidenced by Maillard *et al.*<sup>149,264</sup>. Then, different nanostructures can exhibit the same CO<sub>ads</sub> stripping (**Figure 55A**). This result also underlines the limits of the structural interpretations based on the CO<sub>ads</sub> stripping as the hollow porous PtNi/C NPs before and after the 0.6 – 1.1 V *vs.* RHE display similar  $\mu_1^{\text{CO}}$  but not the same SA at  $E = 0.95$  V *vs.* RHE.

*In operando* WAXS provided information on the changes of the physical parameters defining the NPs morphology, *i.e.* the mean crystallite size ( $d_{\text{XRD}}$ ), the average lattice parameter ( $a_{\text{Pt-Pt}}$ ) and the microstrain ( $\mu_\epsilon$ ). **Figure 59** presents the changes of the spectra of the porous hollow PtNi/C electrocatalysts during *in operando* ageing with  $E_{\text{upper}} = 1.0$  V *vs.* RHE (**Figure 59A**) and  $E_{\text{upper}} = 1.1$  V *vs.* RHE (**Figure 59B**). The patterns were collected in three regions of the gas diffusion electrode (GDE):

- (i) a region constantly exposed to the synchrotron beam;
- (ii) a region exposed to the beam during *ca.* 1 % of the experiment time;
- (iii) a region only exposed to the beam at the beginning and at the end of the experiment.

The spectra and values of the parameters presented in **Figure 59** and **Figure 60** have been obtained in the ‘low-radiation’ region (exposure during *ca.* 1 % of the experiment time) to minimize the modifications induced by exposure of the electrocatalyst to the X-ray beam. The X-ray patterns only provide mild variations of the electrocatalyst structure even if the influence of  $E_{\text{upper}}$  is shown:

- (i) for  $E_{\text{upper}} = 1.1$  V vs. RHE, a diminution of  $2\theta$  is observed for the Pt (111) peak ( $4.08^\circ$  before ageing vs.  $4.06^\circ$  after, see **Figure 59B**), the latter remaining constant for  $E_{\text{upper}} = 1.0$  V vs. RHE;
- (ii) for  $E_{\text{upper}} = 1.1$  V vs. RHE, the XRD peaks sharpen during the first 2,000 seconds, thereby signing an increase of the crystallite size in agreement with the coalescence process previously discussed (see **Figure 59B**).

Further insights into the variation of the NPs structure were obtained by refining the X-ray patterns by the Rietveld method which allows monitoring the variations of the lattice parameter, the average crystallite size and the microstrain (see **Figure 60**).

The sudden changes (*i.e.* the large standard deviation) of the normalized  $d_{\text{XRD}}$  and the normalized  $\mu_\varepsilon$  (**Figure 60B** and **Figure 60C**) are directly linked to *in operando* measurements. Indeed, during the measurements, gas bubbles form in the GDE or at the interface between the Kapton film and the GDE (see **Section II. 3. 7.**) modify the thickness of the electrolyte film by a few micrometers.

During the 5,000 potential cycles ageing, several features were observed:

- (i) a progressive decrease of the lattice parameter, *ca.* – 10 % of the initial contraction after the 0.6 – 1.0 V vs. RHE ageing protocol and *ca.* – 25 % after the 0.6 – 1.1 V vs. RHE ageing protocol (see **Figure 60A**);
- (ii) a sudden and fast increase of the crystallite size ( $\times 1.15$ ) at the beginning of the ageing protocol (see **Figure 60B**) for  $E_{\text{upper}} = 1.1$  V vs. RHE;
- (iii) a negligible diminution of the microstrain during the ageing with  $E_{\text{upper}} = 1.0$  vs. RHE (see **Figure 60B** and **Figure 60C**), while being more important (up to *ca.* – 15 % of the initial microstrain) for  $E_{\text{upper}} = 1.1$  V vs. RHE.

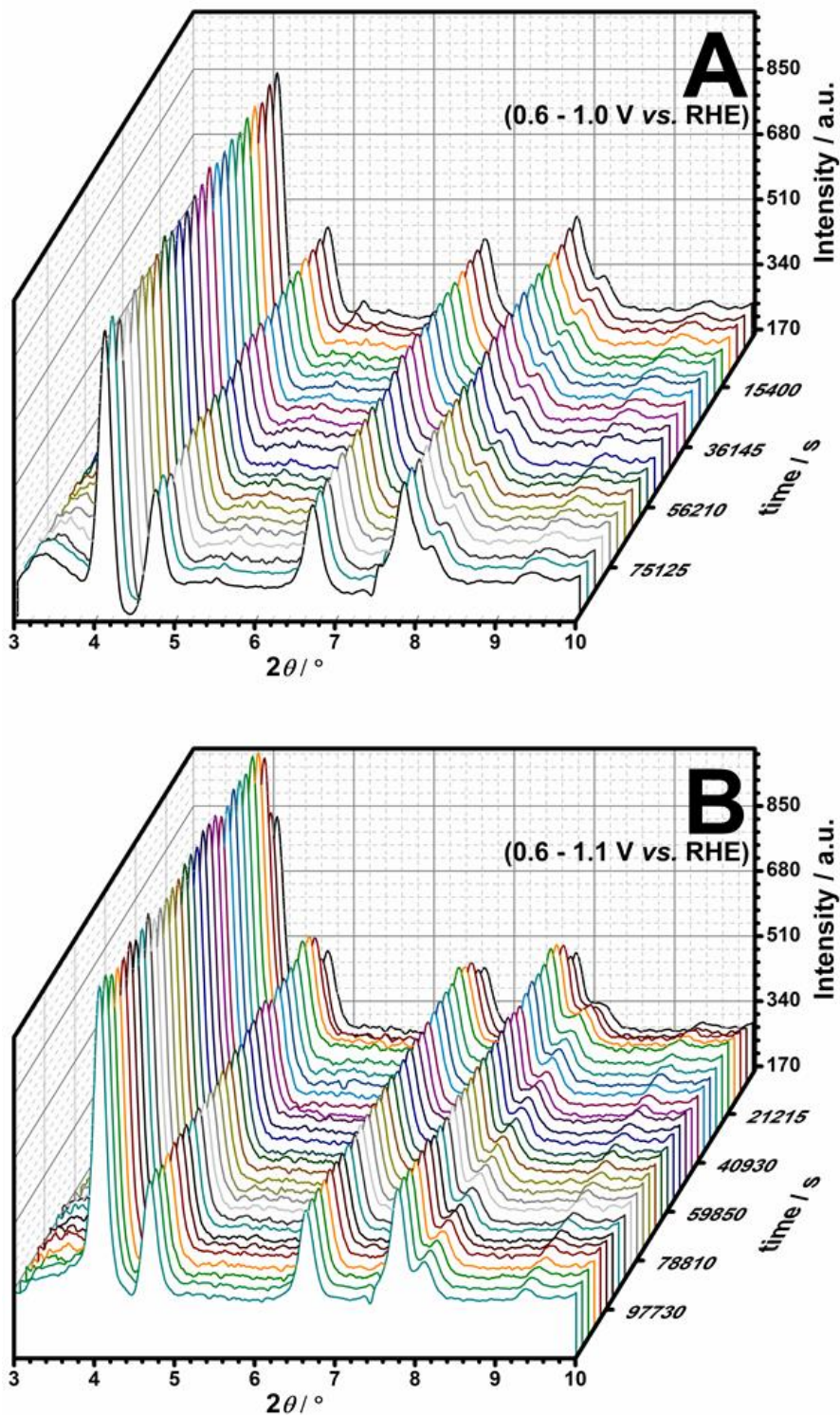


**Figure 59.** Variations of the X-ray patterns recorded onto a porous hollow PtNi/C electrocatalyst during 5,000 cycles in Ar-saturated 0.1 M HClO<sub>4</sub> between (A) 0.6 and 1.0 V vs. RHE or (B) 1.1 V vs. RHE ( $v = 0.050 \text{ V s}^{-1}$  and  $T = 353 \pm 1 \text{ K}$ ).

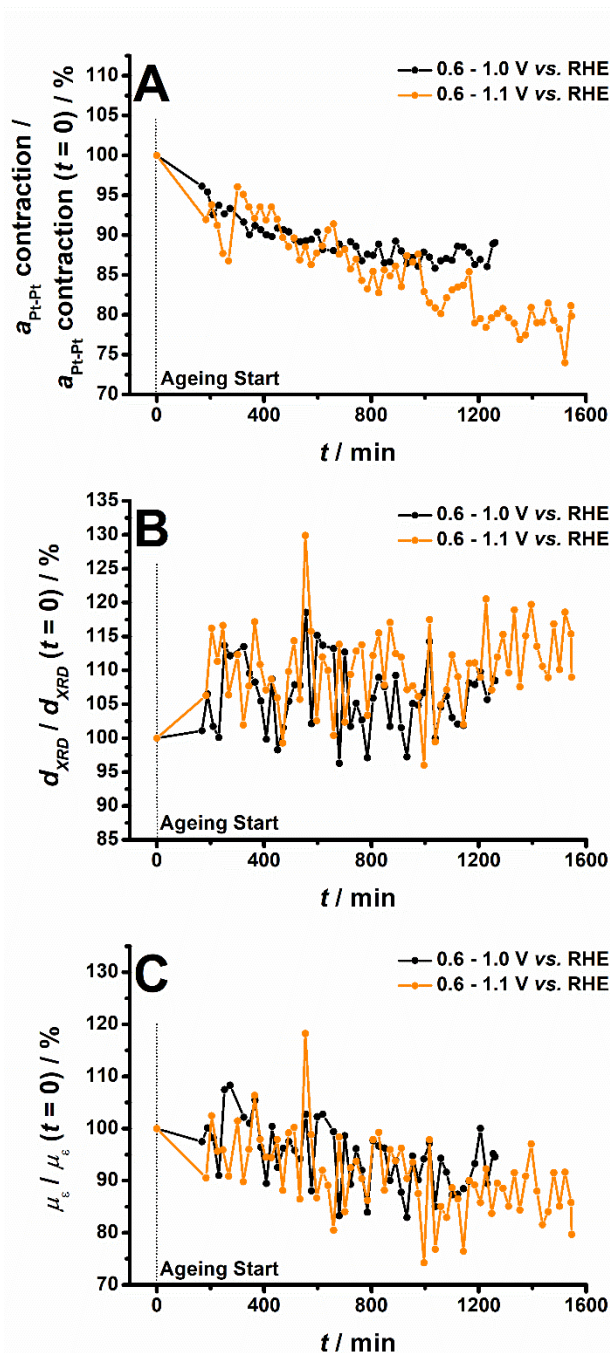


**Figure 60.** Variations of structural parameters extracted from Rietveld refinement of XRD patterns measured on porous hollow PtNi/C electrocatalyst during 5,000 potential cycles in Ar-saturated 0.1 M HClO<sub>4</sub> between 0.6 and 1.0 V vs. RHE or 1.1 V vs. RHE ( $v = 0.050 \text{ V s}^{-1}$  and  $T = 353 \pm 1 \text{ K}$ ). (A) Normalized variation of the contraction (vs. the lattice parameter of Pt/C) of the lattice parameter,  $a_{\text{Pt-Pt}}$  vs. the lattice parameter of Pt/C, in the low radiation area, (B) normalized variation of the average crystallite size,  $d_{\text{XRD}}$  and (C) normalized variation of the microstrain,  $\mu_e$ . Since the number of potential cycles was kept constant, the AST between 0.6 and 1.1 V vs. RHE was 20% longer than the AST between 0.6 and 1.0 V vs. RHE.

## Chapter V. Stability of the porous hollow PtNi/C NPs during simulated PEMFC operating conditions

The stability of the microstrain and of the crystallite size for  $E_{\text{upper}} = 1.0 \text{ V vs. RHE}$  confirms the observations of Dubau *et al.*<sup>332</sup>, *i.e.* that the depletion in Ni is the main reason of the ORR activity losses for highly defective electrocatalysts (as porous hollow PtNi/C NPs) with  $d_{\text{XRD}} \geq 3 \text{ nm}$ . Note that the electrocatalysts did not undergo intermediate characterization during the *in operando* ageing, thus resulting in less degradation than observed in **Section V. 3**.

The losses in Ni are *ca.* 3 – 4 times higher than the diminution of the lattice contraction (*vs.* the lattice parameter of Pt/C) (**Figure 57** and **Figure 60A**):

- *ca.* 40 % of Ni losses *vs.* a *ca.* 10 % decrease of the lattice contraction of the electrocatalysts aged between 0.6 V and 1.0 V *vs.* RHE
- *ca.* 60 % of Ni losses (for the collapsed NPs) *vs.* a *ca.* 20 % decrease of the lattice contraction of the electrocatalysts aged between 0.6 V and 1.1 V *vs.* RHE.

This means that part of the lattice contraction results of the structural defects (*e.g.* missing atoms, nanovoids, *etc.*) and not of the Ni content. For the electrocatalyst aged with  $E_{\text{upper}} = 1.0 \text{ V vs. RHE}$ , the *ca.* 10 % decrease of the lattice contraction correspond to *ca.* 16 % of SA losses at  $E = 0.95 \text{ V vs. RHE}$  (**Table 11**). The SA losses observed in **Table 11** were aggravated because of the characterizations under  $\text{O}_2$  (see **Section V. 2.**) that were not performed during the *in operando* ageing. It is likely that most of the electrocatalytic activity losses during 5,000 cycles between 0.6 and 1.0 V *vs.* RHE at  $T = 353 \text{ K}$  results from the Ni segregation and dissolution, therefore confirming the work of Dubau *et al.*<sup>332</sup>. However, the ageing with  $E_{\text{upper}} = 1.1 \text{ V vs. RHE}$  also affects the structural defects: the electrocatalyst suffers 40 % losses in  $\text{SA}_{0.95}$  while losing only *ca.* 20 % of its Ni content (but, in addition, *ca.* 15 % of its microstrain).

#### V. 4. Stability of the carbon supports

In this section, the electrocatalysts were aged by the procedure mimicking the start-up/shut-down event of a PEMFC (*i.e.* square potential ramp between  $E = 1.0$  V and  $E = 1.5$  V *vs.* RHE with  $t = 3$  s at each potential, see **Figure 19**) to mainly assess the durability of the carbon support<sup>193</sup>. Fresh and 500-cycle aged electrocatalysts were characterized by electrochemical measurements and IL-TEM (see **Figure 61** to **Figure 66**).

Base and CO<sub>ads</sub> stripping (**Figure 61** and **Figure 62**) voltammograms show:

- (i) the formation of carbon surface oxides (CO<sub>surf</sub>) during the AST for the electrocatalysts based on KJB, XC72, GNS, GNS-AL and CX. This is illustrated by the increasing charge under the Q/HQ<sup>176</sup> in the potential region  $0.4 < E < 0.8$  V *vs.* RHE (**Figure 61**);
- (ii) the increase of the double layer capacitance ( $C_{dl}$ ) for the electrocatalysts supported on CNT and carbon blacks. This suggests larger carbon support specific surface area and increased oxygen content<sup>193,336</sup>;
- (iii) the decrease of  $C_{dl}$  for the electrocatalysts supported on GNS, GNS-AL and CX. This suggests complete oxidation of carbon into CO<sub>2</sub><sup>336</sup>, *i.e.* a decrease of the carbon specific surface area;
- (iv) the decrease of the electrical charge required to adsorb/desorb under-potentially deposited hydrogen ( $H_{upd}$ ) or to electrooxidize a CO<sub>ads</sub> monolayer, due to the ECSA losses, especially for the electrocatalysts synthesized on GNS, GNS-AL and CX;
- (v) the decrease of the CO<sub>ads</sub> stripping peak intensity at  $E = 0.7$  V *vs.* RHE (for the electrocatalysts synthesized on KJB and XC72), which is ascribed to the decrease of the density of structural defects<sup>149,232,234,247</sup>.

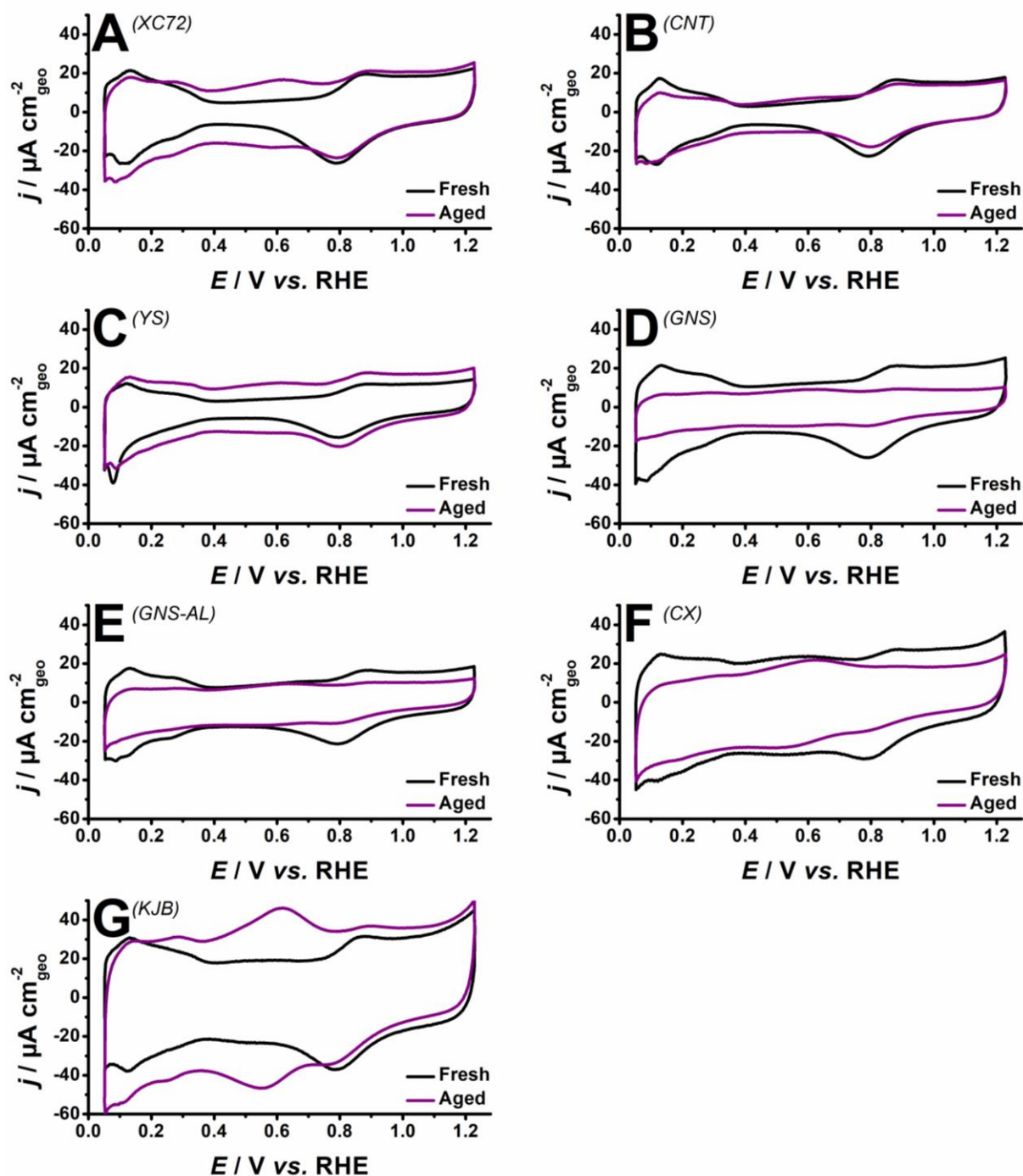


**Figure 61.** Cyclic voltammograms measured between  $E = 0.05$  and  $1.23$  V vs. RHE at  $\nu = 0.020$  V s<sup>-1</sup> and  $T = 298 \pm 1$  K in Ar-saturated  $0.1$  M HClO<sub>4</sub>, normalized to the geometric surface of the electrode ( $0.196$  cm<sup>2</sup>), for the porous hollow PtNi/C electrocatalysts synthesized on different carbon supports: (A) Vulcan XC72, (B) carbon nanotubes, (C) YS, (D) graphene nanosheets, (E) acid leached graphene Nanosheets, (F) carbon xerogels, (G) Ketjenblack. All the results were obtained before and after an accelerated stress test protocol mimicking potential variations during start-up/shutdown of a PEMFC cathode (500 steps at  $T = 353$  K between  $1.0$  V vs. RHE ( $t = 3$  s) and  $1.5$  V vs. RHE ( $t = 3$  s)).

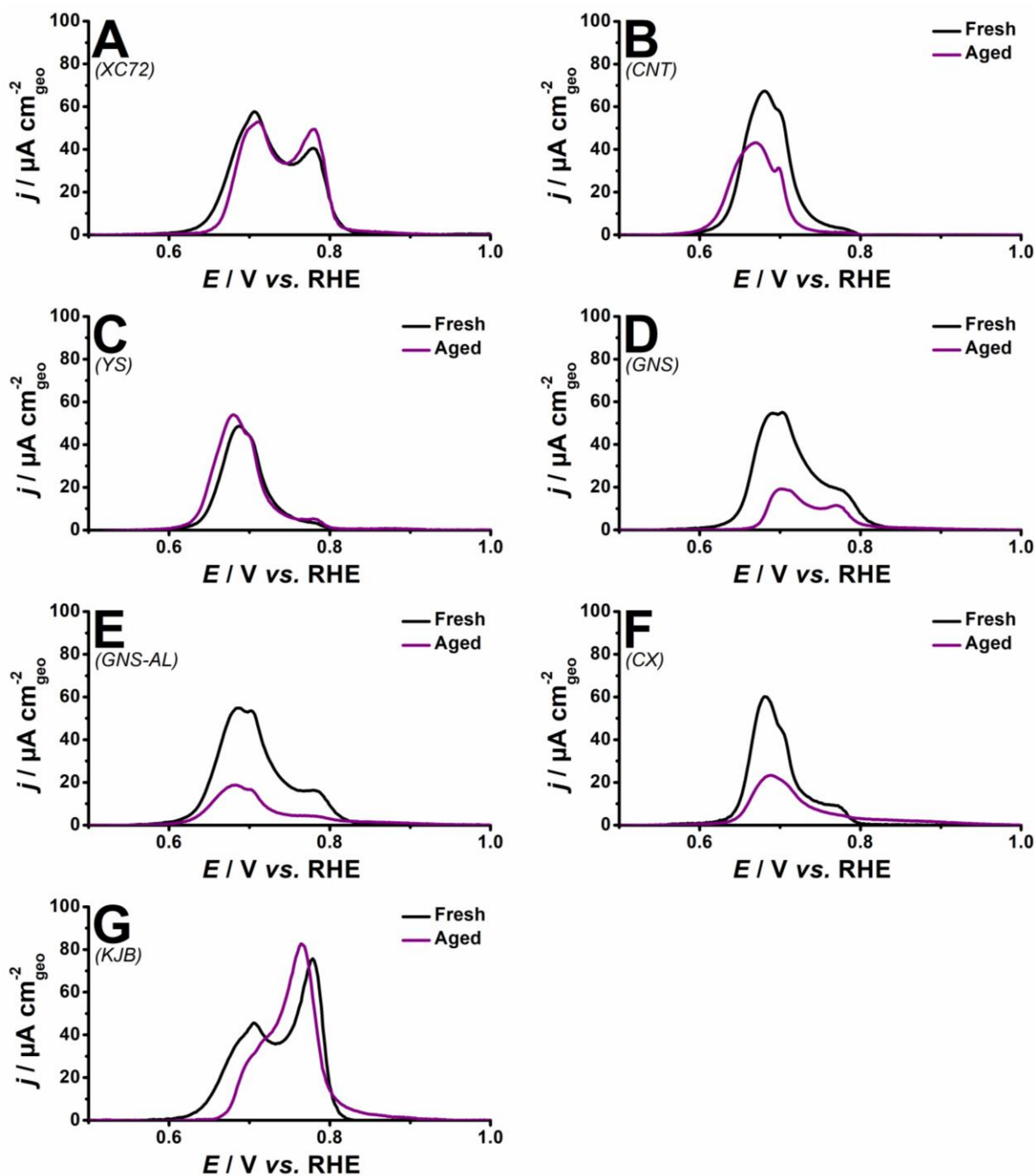


**Figure 62.** Electrooxidation of a  $\text{CO}_{\text{ads}}$  monolayer between  $E = 0.05$  and  $1.23$  V vs. RHE at  $\nu = 0.020$  V  $\text{s}^{-1}$  and  $T = 298 \pm 1$  K in Ar-saturated  $0.1$  M  $\text{HClO}_4$ , normalized by the geometric surface of the electrode ( $0.196$   $\text{cm}^2$ ), for the porous hollow PtNi/C electrocatalysts synthesized on different carbon supports: (A) Vulcan XC72, (B) carbon nanotubes, (C) YS, (D) graphene nanosheets, (E) acid leached graphene nanosheets, (F) carbon xerogels, (G) Ketjenblack. All the results were obtained before and after an accelerated stress test protocol mimicking potential variations during start-up/shutdown of a PEMFC cathode (500 steps at  $T = 353$  K between  $1.0$  V vs. RHE ( $t = 3$  s) and  $1.5$  V vs. RHE ( $t = 3$  s)).

On PtNi/GNS, PtNi/GNS-AL and PtNi/CX, the COR kinetics seems to be very pronounced as illustrated by the decrease of (i) the double layer current, (ii) the electrical charge in the  $H_{\text{upd}}$  region and (iii) the intensity of the  $\text{CO}_{\text{ads}}$  stripping peaks (*i.e.* a decrease of the  $S_{\text{Pt,CO}}$ , see **Figure 64**), relevant for a pronounced detachment of metal NPs. This behaviour is explained by (i) the amorphous structure of the CX, which allows the COR to start at a potential value as low as 0.6 V *vs.* RHE<sup>193</sup>, (ii) the disordered GNS and GNS-AL crystallites in the plane ( $G$ -band position =  $1597 \pm 1 \text{ cm}^{-1}$  and  $L_a = 3.8 \text{ nm}$ , see **Table 6**, and (iii) the highly functionalized surface of the CX, GNS-AL and GNS supports<sup>192</sup>. Since GNS and GNS-AL possess the highest size of the crystallite domains perpendicular to the plane ( $L_c = 12.6 \text{ nm}$ ), this indicates that mostly  $L_a$ , and not  $L_c$ , drives the stability of the carbon supports discussed in this work, this being explained by the fact that carbon essentially corrodes from the edges of the graphene planes. While a moderate NPs detachment is observed on PtNi/CNT (see **Figure 62C**), this effect is negligible on carbon blacks. Since the PtNi/CNT sample does not show carbon corrosion (see **Figure 61C**), its NPs detachment can be ascribed to a weaker bonding of NPs due to the low surface functionalization (23% of oxygen groups, see **Table 7**). Carbon blacks show an increase of the Q/HQ peak and of  $C_{\text{dl}}$  upon cycling (**Figure 61**): the electrical charge at the Q/HQ peak depends on the specific surface area of the carbon support, given in **Table 5**; KJB presents 6 (14) times higher specific surface than XC72 (YS), resulting in a higher absolute Q/HQ value. A decrease of the density of structural defects (*i.e.* a higher charge under the peak at  $E = 0.8 \text{ V vs. RHE}$ ) is observed on the PtNi/KJB and PtNi/XC72 electrocatalysts, *i.e.* the electrocatalysts with the smallest crystallite sizes.

Carbon corrosion and detachment of NPs were observed on the IL-TEM micrographs of the GNS, the GNS-AL and, to a lower extent, on the CX, the CNT and the KJB (**Figure 63**), therefore confirming the information derived from electrochemical measurements (**Figure 61** and **Figure 62**). However, the ageing of the electrocatalysts by IL-TEM is much less aggravating than by electrochemistry (*i.e.* few particles detachment, *etc.* see **Figure 63**), this being ascribed to (i) the absence of characterisation before and after the ageing (see **Section V. 2**) and (ii) the fact that IL-TEM provides local information, by opposition to electrochemistry. It is then important to consider IL-TEM data qualitatively, to observe the trends in degradation (*e.g.* carbon corrosion for the GNS and GNS-AL) but not to assess quantitatively the degradation processes. Moreover, IL-TEM was performed at  $T = 353 \text{ K}$  between 1.0 and 1.5 V *vs.* RHE, *i.e.* under harsh conditions for gold TEM grids; as a result, gold re-deposition was sometimes observed, especially on PtNi/CG (**Figure 63**).

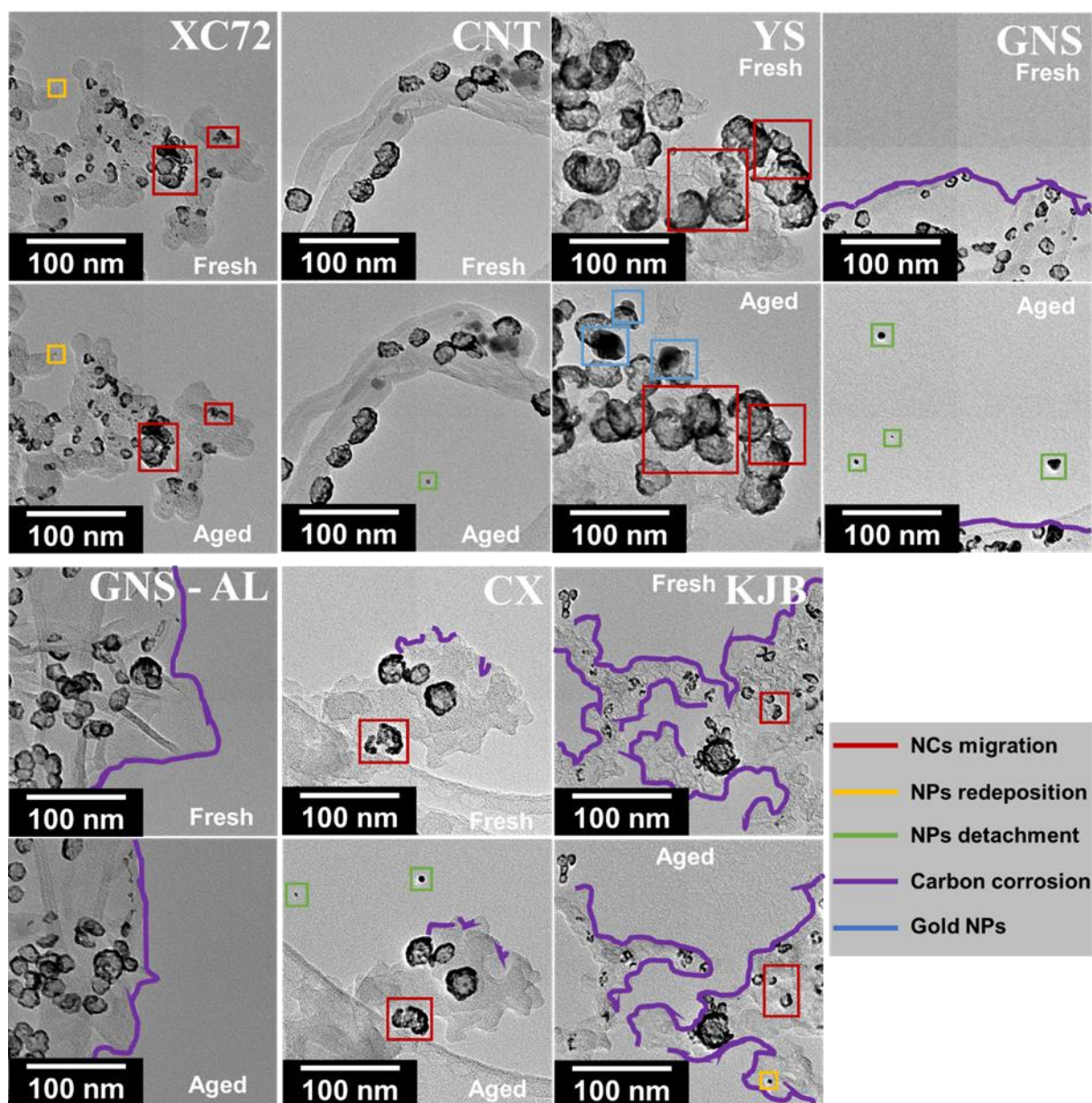


**Figure 63.** IL-TEM for the porous hollow PtNi/C NPs synthesized on different carbon supports: Vulcan XC72, carbon nanotubes, YS, graphene nanosheets, acid leached graphene nanosheets, carbon xerogels and Ketjenblack before and after an accelerated stress test protocol mimicking potential variations during start-up/shutdown of a PEMFC cathode (500 steps at  $T = 353$  K between 1.0 V vs. RHE ( $t = 3$  s) and 1.5 V vs. RHE ( $t = 3$  s)).

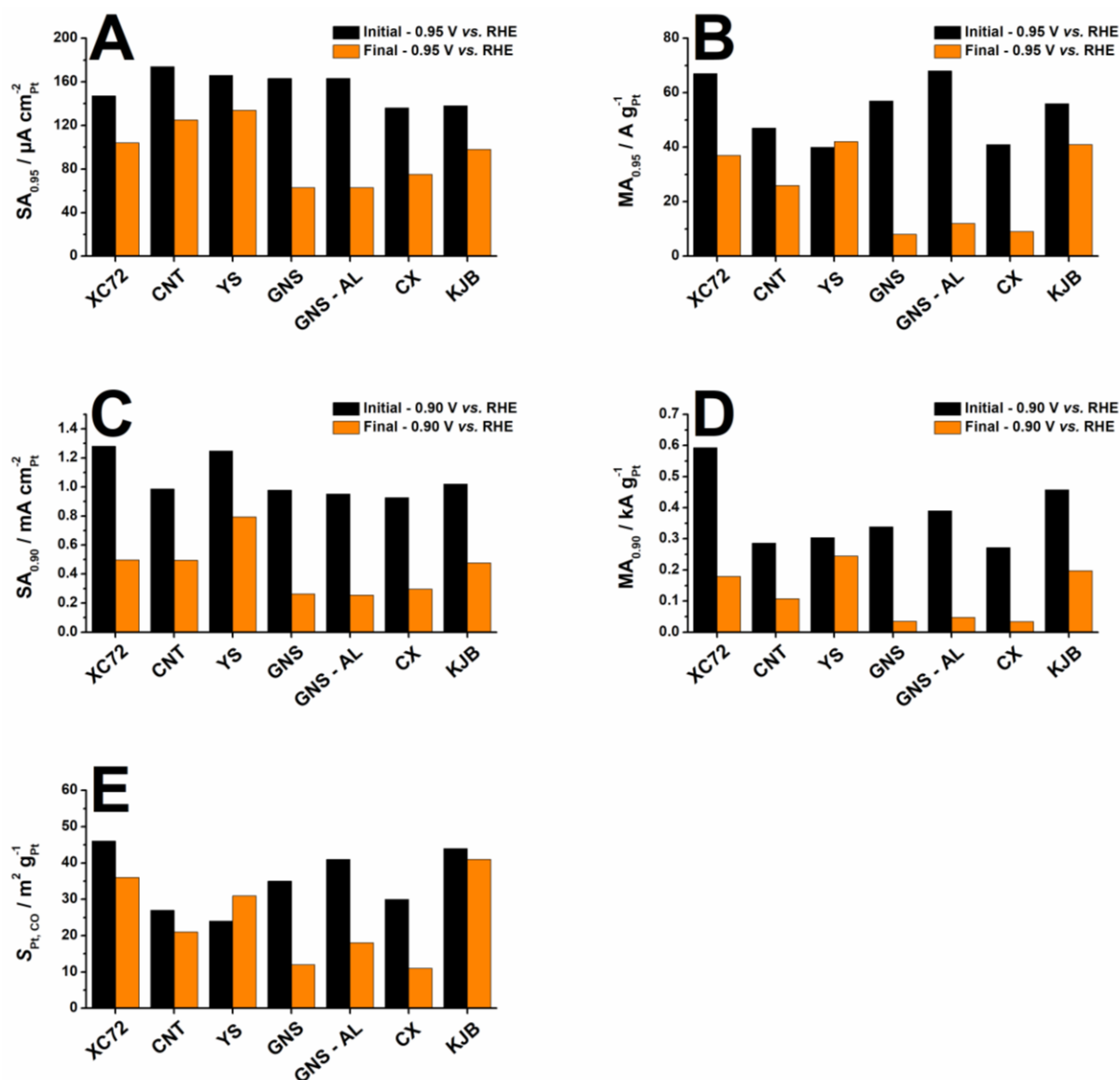


**Figure 64.** (A) Specific and (B) Mass activity for the ORR in O<sub>2</sub>-saturated 0.1 M HClO<sub>4</sub> at  $E = 0.95$  V vs. RHE, (C) specific and (D) mass activity in O<sub>2</sub>-saturated 0.1 M HClO<sub>4</sub> at  $E = 0.90$  V vs. RHE – corrected for diffusion in solution and Ohmic drop,  $T = 298 \pm 1$  K,  $\omega = 1600$  rpm,  $\nu = 0.005$  V s<sup>-1</sup> and (E) Pt specific surface area determined from the CO<sub>ad</sub> stripping experiments for the porous hollow PtNi/C NPs synthesized on different carbon supports before and after an accelerated stress test protocol mimicking potential variations during start-up/shutdown of a PEMFC cathode (500 steps at  $T = 353$  K between 1.0 V vs. RHE ( $t = 3$  s) and 1.5 V vs. RHE ( $t = 3$  s)).

## Chapter V. Stability of the porous hollow PtNi/C NPs during simulated PEMFC operating conditions

The losses in Pt specific surface area (up to *ca.* 65 % for the PtNi/GNS) induced by the particle detachment and the carbon corrosion cannot solely explain the dramatic diminution of the ORR specific activity at  $E = 0.90$  and  $0.95$  V *vs.* RHE. After ageing, the specific activity at  $E = 0.95$  V *vs.* RHE ( $SA_{0.95}$ , **Figure 64A**) undergoes a 62% decrease in the PtNi/GNS and about 19% decrease for the PtNi/CNT. **Figure 65** presents the ORR linear sweep voltammograms after correction of the Ohmic drop and the diffusion of oxygen in solution.

The potential difference ( $\Delta E$ ) between the  $j_k$  of the fresh electrocatalysts and the  $j_k$  of the aged electrocatalyst is presented in **Figure 66** (for  $-0.1 < j_k < -1$  mA cm<sup>-2</sup><sub>Pt</sub>). In this potential range,  $\Delta E$  evolves linearly with  $j_k$ , suggesting that the electrocatalytic losses partially result from Ohmic losses due to the increase of the system resistance upon ageing. The electrochemical system (*i.e.* a glassy carbon (GC) electrode covered by a catalytic film immersed in an electrolyte) correspond to a complex equivalent circuit that forbids the simultaneous determination of all the resistances (the resistance of the electrolyte, the resistance of the carbon and the resistance of the glassy carbon)<sup>333,337–340</sup>, both in nature and value.

The electrolyte properties were identical before and after ageing (the electrolyte was removed and replaced by a fresh electrolyte and the cell was washed with MilliQ water; therefore, its resistance was *ca.* 20  $\Omega$ ) and the resistance of the GC is negligible, owing to its high conductivity<sup>333</sup>. Thus, the increase of the system resistance (related to the slope  $R_k$ , the latter being an arbitrary value extracted from **Figure 66**, see **Table 12**) was ascribed to the decreased electrical conductivity of the catalytic layer following the electrochemical amorphization of the graphitic regions, especially in the interconnection regions between the elementary carbon particles<sup>333</sup>, and to the increase of the Q/HQ surface content (**Figure 61**). This degradation (*i.e.* the higher  $R_k$ ) was the most important for the GNS, GNS-AL and the CX, accordingly to the results of **Figure 65** and **Figure 66**, followed by the XC72, the CNT and the YS. The resistance of the PtNi/KJB did not increase during ageing (see **Figure 66**): its activity losses mainly result from the decrease of the density of structural defects (see **Section V. 2**).

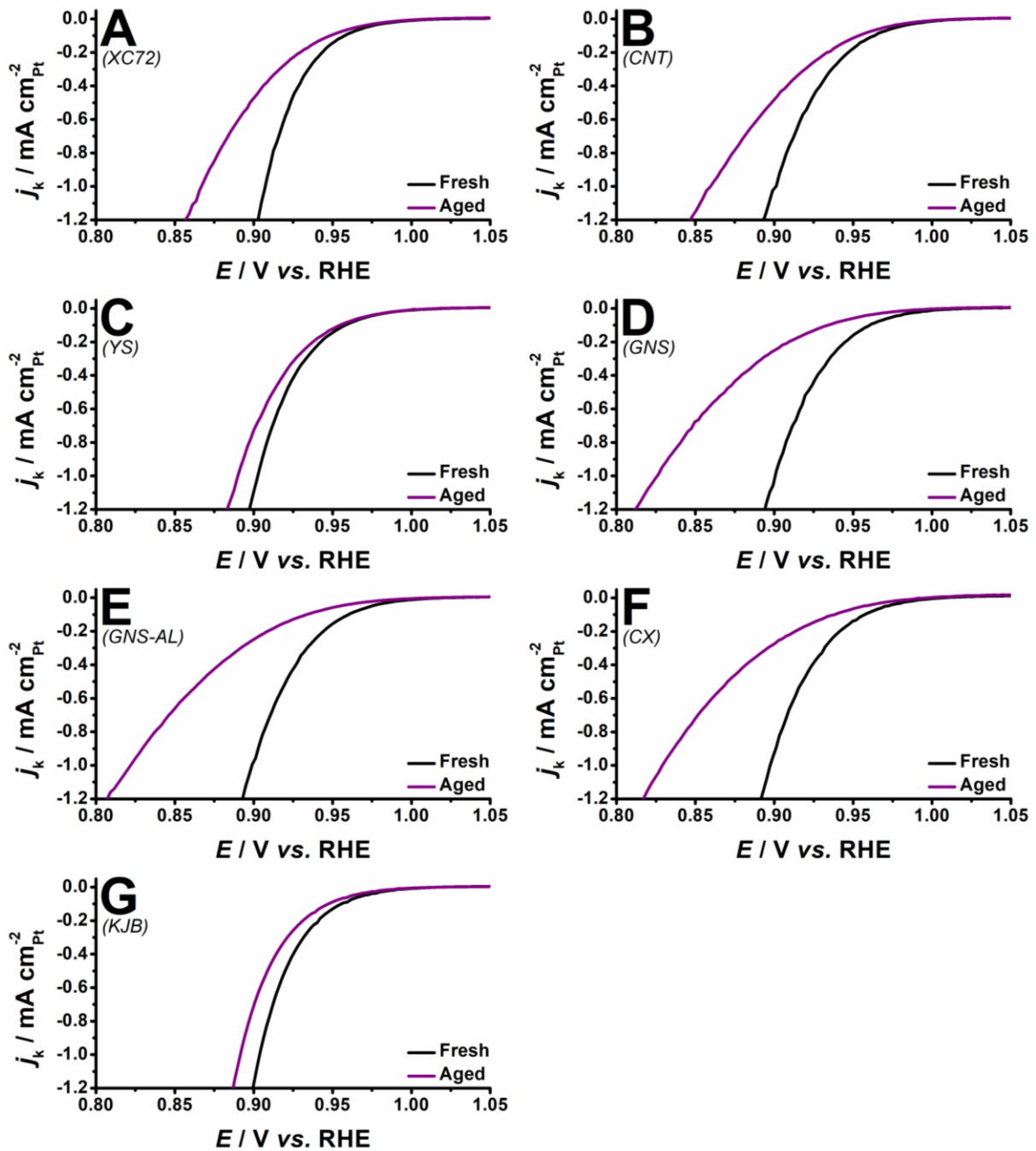


**Figure 65.** Linear sweep voltammograms corrected from the Ohmic drop and from oxygen diffusion in solution measured at  $\nu = 0.005 \text{ V s}^{-1}$  in  $\text{O}_2$ -saturated  $0.1 \text{ M HClO}_4$  on porous hollow PtNi/C electrocatalysts synthesized on different carbon supports: (A) Vulcan XC72, (B) carbon nanotubes, (C) YS, (D) graphene nanosheets, (E) acid leached graphene nanosheets, (F) xerogels, (G) Ketjenblack. The kinetic current is normalized to the Pt ECSA. All the results were obtained before and after an accelerated stress test protocol mimicking potential variations during start-up/shutdown of a PEMFC cathode (500 steps at  $T = 353 \text{ K}$  between  $1.0 \text{ V vs. RHE}$  ( $t = 3 \text{ s}$ ) and  $1.5 \text{ V vs. RHE}$  ( $t = 3 \text{ s}$ )).

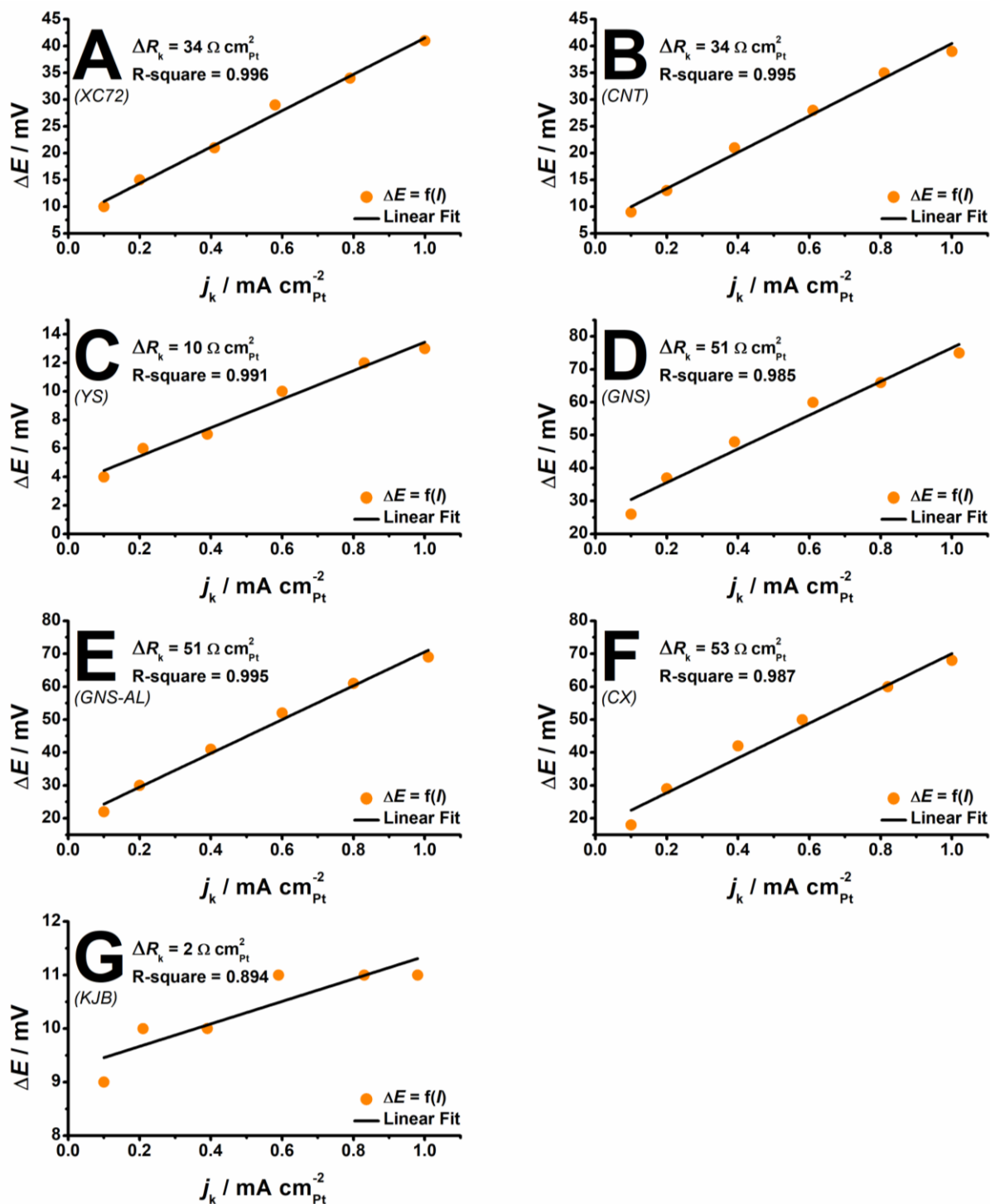


**Figure 66.** Linear fits of the difference of potential ( $\Delta E$ ) as a function of the kinetic current ( $j_k$ ) for the porous hollow PtNi/C electrocatalysts synthesized on (A) Vulcan XC72, (B) carbon nanotubes, (C) YS, (D) graphene nanosheets, (E) acid leached graphene nanosheets, (F) Xerogel and (G) Ketjenblack before and after an accelerated stress test protocol mimicking potential variations during start-up/shutdown of a PEMFC cathode (500 steps at  $T = 353 \text{ K}$  between  $1.0 \text{ V vs. RHE}$  ( $t = 3 \text{ s}$ ) and  $1.5 \text{ V vs. RHE}$  ( $t = 3 \text{ s}$ )).

**Table 12.** Slopes ( $R_k$ ) determined from the fits of the curves presented in **Figure 66** by a linear equation for the different carbon substrates and effective resistances ( $R_{eff}$ ) determined from the cyclic voltammetry using **Equation 41**.

	$R_k$ ( $\Omega \text{ cm}^2_{Pt}$ )	$R_{eff}$ ( $\Omega \text{ cm}^2_{geo}$ )
<b>XC72</b>	34	$575 \pm 10$
<b>CNT</b>	34	*
<b>CG</b>	10	*
<b>GNS</b>	51	$3500 \pm 100$
<b>GNS – AL</b>	51	$4200 \pm 100$
<b>CX</b>	53	$1800 \pm 100$
<b>KJB</b>	2	$355 \pm 10$

\*The cathodic Q/HQ peak was not observable, resulting in an impossibility to calculate  $R_{eff}$ .

Recently, Gribov *et al.*<sup>333</sup> proposed a method to estimate the effective resistance ( $R_{eff}$ ) of a carbon supported electrocatalyst based on the post-ageing CVs and, more specifically, on the potential shift of the Q/HQ peak, according to **Equation 41**.

$$R_{eff} = \frac{(E_{a,QHQ} - E_{c,QHQ}) - 0,028}{i_{a,QHQ} - i_{c,QHQ}} \quad (Eq. 41)$$

where  $E_{a,QHQ}$  and  $E_{c,QHQ}$  are the potential of the anodic and cathodic peak of the Q/HQ couple, and  $i_{a,QHQ}$  and  $i_{c,QHQ}$  are their respective intensity.  $R_{eff}$  corresponds to the serial connection of the resistance of the GC, of the electrolyte and of the carbon support. As such, a high  $R_{eff}$  (see **Table 12**) indicates an increase of the carbon support resistance, thus confirming the results obtained using  $R_k$  (*i.e.* highest  $R_{eff}$  for the GNS and GNS – AL, then CX and XC72). The initial  $R_{eff}$  was not calculated, as the Q/HQ peaks were not visible on the base voltammogram of the non-aged electrocatalysts (**Figure 61**).

The losses in ORR specific activity measured at 0.90 V vs. RHE vary from 74 % in PtNi/GNS to 36 % in PtNi/YS (**Figure 64**). These higher losses (compared to what was measured at 0.95 V vs. RHE) result:

- (i) from the increased contribution of the ohmic drop to the ORR kinetic current ( $j_k$ );
- (ii) from an increased effect of the diffusion limitations into the catalytic layer.

For each catalyst, the losses in mass activity for the ORR (**Figure 64B** and **Figure 64D**) are more pronounced than the losses in specific activity. This relates to the dramatic losses in Pt specific surface area upon ageing (see **Figure 64E**), which are particularly marked for PtNi/CX, PtNi/GNS and PtNi/GNS-AL (*ca.* 64%, 65% and 56%, respectively). The losses in mass activity amount up to 90 % for PtNi/GNS.

YS and KJB appears to be promising as support for the porous hollow PtNi/C NPs. They present, by far, the highest durability (*i.e.* slight increase of the support resistance, minor decrease in activity, *etc.*). Furthermore, the NPs supported on KJB have a  $d_{\text{ext}} = 10.6 \pm 3.4$  nm, resulting in a  $S_{\text{Pt,CO}} = 45 \pm 5$  m<sup>2</sup> g<sub>Pt</sub><sup>-1</sup> and, therefore, an increased initial mass activity compared to PtNi/YS ( $\text{MA}_{0.95} = 56 \pm 12$  A g<sub>Pt</sub><sup>-1</sup> *vs.*  $40 \pm 2$  A g<sub>Pt</sub><sup>-1</sup>, see **Section IV. 5**). The only drawback of the PtNi/KJB electrocatalyst is its lower initial specific activity, *i.e.*  $138 \pm 35$  μA cm<sup>-2</sup> at  $E = 0.95$  V *vs.* RHE, resulting of its small crystallite size and its low density of structural defects, therefore implying that those two parameters should be improved (*e.g.* by performing the synthesis at higher temperature on KJB).

## V. 5. Conclusions

In this chapter, we provided insights on the structural and electrochemical changes of the porous hollow PtNi/C NPs and of their support during accelerated stress tests (ASTs):

- (i) composed of 5,000 or 20,000 potential cycles in the  $E = 0.6 - 1.0$  V *vs.* RHE potential range to focus on the structural changes of the porous hollow PtNi/C NPs;
- (ii) composed of 5,000 potential cycles in the  $E = 0.6 - 1.1$  V *vs.* RHE potential range to focus on the effect of the place-exchange mechanism onto the structure of the porous hollow PtNi/C NPs;
- (iii) composed of 500 potential cycles in the  $E = 1.0 - 1.5$  V *vs.* RHE potential range to focus on the degradation of the carbon support.

The texture, the structure and the chemistry of the different carbon supports were crucial during AST. Electrochemical and IL-TEM analysis on aged electrocatalysts showed pronounced detachment of NPs and degradation of the carbon support (detachment, complete and partial corrosion, *etc.*) for the electrocatalysts supported on graphene nanosheets and on carbon xerogel while the electrocatalysts supported on carbon blacks reported an incomplete oxidation of the surface (formation of CO<sub>surf</sub>). Overall, the degradation of the carbon support resulted in losses

in the Pt specific surface area, mass activity and specific activity for the ORR, as the result of the increase of the resistance of the catalytic layers.

Using the tools described in **Section IV. 3.** ( $Q_{pp,CO} / Q_{T,CO}$ ,  $E_{p,CO}$ ,  $\mu_{1^{CO}}$  and  $\mu_{\epsilon}$ ), we observed that the losses in ORR specific activity of the porous hollow PtNi/C NPs in the ‘load-cycling’ protocol (20,000 potential cycles between 0.6 and 1.0 V vs. RHE at  $v = 50 \text{ mV s}^{-1}$ ) resulted from a combination of losses in Ni-induced lattice contraction and an increase of the crystallite size, resulting in the diminution of the density of grain boundaries. The electrocatalysts that presented an initial nanocrystallite size  $d_{XRD} > 3 \text{ nm}$  presented a higher stability than the one with a  $d_{XRD} < 2 \text{ nm}$ . We also noticed that intermediate characterisations in O<sub>2</sub>-saturated electrolyte resulted in aggravated changes of the electrocatalyst morphology. These changes in nanostructure were confirmed using *in operando* WAXS measurements. The diminution of the Ni content occurred gradually during the AST, while the crystallite size increased during the first 2,000 seconds (for an upper potential of 1.1 V vs. RHE). The structural changes were by far more severe when the upper potential limit reached 1.1 V vs. RHE: this is believed to arise from the place-exchange mechanism.

# **Chapter VI. General Conclusion and Perspectives**

The Earth depletion in fossil fuels, the global warming and the resulting need in green energies devices, such as proton exchange membrane fuel cells (PEMFCs), are driving forces for the design, synthesis and characterisation of nanostructured electrocatalysts. The ORR is the electrocatalytic reaction limiting the performance of PEMFCs (the oxidation of di-hydrogen on Pt/C being much faster<sup>58</sup>). Enhancement of the ORR mass activity is requested for PEMFC to be economically viable. During the last decade, a wide range of nanomaterials were synthesized, presenting 20-fold enhancement of the SA for the ORR vs. Pt/C (flat-annealed surfaces)<sup>158</sup>, 55-fold enhancement in SA vs. Pt/C (highly defective nanowires<sup>143</sup>) and up to 90-fold enhancement of the SA for the ORR vs. Pt/C (Pt<sub>3</sub>Ni (111) extended surfaces<sup>138</sup>). The electrocatalytic activity enhancement was achieved by (i) alloying the Pt with other elements, either 3d-transition metals or rare-Earth elements, to modify the Pt 5d band centre and, therefore, the adsorption strength of the ORR intermediates<sup>54,136</sup>, (ii) diminishing the number of Pt atoms that are not involved in the electrocatalytic reaction (*e.g.* core@shell and hollow nanostructures<sup>72,85,223</sup>) and (iii) increasing the density of highly active facets (*e.g.* (111), see octahedral nanostructures<sup>88,89</sup>). In this work, we opened a new path to design and synthesize a novel class of nanocatalysts (hollow PtNi/C nanoparticles) that fulfill cost (*i.e.* by increasing the mass activity and, therefore, diminishing the amount of Pt used), performance and stability requirements of PEMFC cathodes. These nanomaterials can be synthesized using the galvanic replacement of a transition metal M by Pt, and the nanoscale Kirkendall effect. In their final form, they feature a highly polycrystalline metal shell (shell thickness = 2 – 3 nm) surrounding a hollow core.

To establish the mechanisms driving the formation and growth of the porous hollow PtNi/C NPs, we used a combination of:

- (i) *in operando* WAXS measurements to identify the phases in presence (Pt, Ni, C and Ni<sub>x</sub>B<sub>y</sub>O<sub>z</sub>) and to determine the variations of the interatomic distances. The chemical nature of these phases was further discussed with the help of X-ray photoelectron spectroscopy measurements;
- (ii) *in operando* SAXS measurements to follow the change of the scattering length density in the core and in the metal shell and thus provide physical evidence of the nanoscale Kirkendall effect<sup>219</sup>;
- (iii) scanning TEM and Energy Dispersive X-ray maps to observe the variation of the composition of the nanoparticles during the synthesis;
- (iv) conventional TEM and high-resolution TEM to gather further insights into the fine nanostructure of the nanoparticles.

Our work shows that:

- (i) Ni-rich cores *ca.* 2 – 3 nm in size form first before being rapidly embedded into a  $\text{Ni}_x\text{B}_y\text{O}_z$  shell at  $t = 2$  min after addition of the first drop of reducing agent ( $\text{NaBH}_4$ );
- (ii) Pt atoms are deposited *via* galvanic replacement onto the  $\text{Ni}_x\text{B}_y\text{O}_z$  shell (the  $\text{Ni}_x\text{B}_y\text{O}_z$  shell acts as a template) resulting into the formation of Ni-rich core@Pt-rich shell structure at  $t = 20$  min;
- (iii) Hollow PtNi/C NPs are formed between  $20 < t < 60$  min due to the nanoscale Kirkendall effect.

In addition to the precise description of the formation and growth mechanism, this work also provides a methodology to identify the various synthesis intermediates forming during the synthesis of *e.g.* preferentially-shaped NPs<sup>88,90</sup>, sea-sponges,<sup>247</sup> or core@shell<sup>72</sup> NPs. Whatever the temperature of the synthesis, the initial Pt:M stoichiometry or the carbon support, the resulting PtM/C NPs were then acid-leached during  $t = 22$  h in 1 M  $\text{H}_2\text{SO}_4$  resulting into the appearance of a central void with molecular accessibility.

The surface reactivity and the electrocatalytic activity for the ORR of the porous hollow PtM/C NPs were then investigated. The best porous hollow nanocatalyst, PtNi/C NPs, achieved 6-fold and 9-fold enhancement in mass and specific activity for the ORR, respectively, over standard solid Pt/C nanocrystallites of the same size. The catalytic enhancement was 4-fold and 3-fold in mass and specific activity, respectively, over solid PtNi/C nanocrystallites with similar chemical composition, PtNi lattice contraction and crystallite size. This enhanced catalytic performance has been ascribed to the weakened chemisorption of oxygenated species induced by the contraction of the lattice parameter (the lattice parameter was *ca.* 0.385 nm on porous hollow PtNi/C NPs compared to 0.393 nm for Pt/C) and to the high density of surface structural defects. Density functional theory calculations by Le Bacq *et al.*<sup>157</sup> showed that the surface of hollow NPs is jagged and composed of domains with expanded and contracted lattice parameter (with respect to the average value determined by XRD). Depending on the density of atomic vacancies formed within the nanoparticle during its synthesis, catalytic sites with very high and very low coordination numbers co-exist at the NP surface. The individual PtM nanocrystallites are also connected to each other *via* grain boundaries.

This high density of structural defects provides the surface with both oxophilic and oxophobic catalytic sites. Oxophobic catalytic sites feature, to a certain extent, the optimal properties (coordination number, degree of contraction of the lattice parameter) and thus, the optimal turnover frequency for the ORR, being responsible for the 9-fold enhancement in specific activity<sup>84</sup>, while others bind oxygenated species much more strongly and thus feature enhanced activity for electrooxidation reactions ( $\text{CO}_{\text{ads}}$  stripping, alcohol oxidation reactions<sup>157</sup>).

The effect of the nature of the sacrificial atoms and of the carbon support was also discussed. The best sacrificial templates feature a standard potential comprised between  $-0.4 < E^\circ < 0.4$  V vs. NHE<sup>325</sup> (Ni, Cu, Co), *i.e.* can be reduced by  $\text{BH}_4^-$  ions and be oxidized by  $\text{Pt}^{2+}$  ions *via* galvanic replacement. The absolute number oxygen-containing surface groups on the carbon support was found to control the external and inner diameter of the M-rich NPs, *i.e.* the increase of the absolute number of oxygen-containing surface groups results in a diminution of the NPs size.

Finally, the stability of the porous hollow metal NPs and of the carbon support were investigated, owing to three different ageing protocols:

- (i) potential cycling between 1.0 and 1.5 V vs. RHE to investigate the degradation of the carbon support during start-up/shutdown events;
- (ii) potential cycling between 0.6 and 1.0 V vs. RHE to investigate the structural and chemical changes of the porous hollow PtM/C NPs during load cycling;
- (iii) potential cycling between 0.6 and 1.1 V vs. RHE to gain insights on the effect of the place-exchange mechanism on the structural and chemical changes of the porous hollow PtM/C NPs.

The robustness of the carbon supports was related to (i) their degree of graphitization and (ii) to the relative functionalization of the surface (*i.e.* the number of oxygen surface groups per carbon atom). The carbon support that presented the lowest graphitization degree and the highest relative functionalization suffered dramatic corrosion, which caused detachment of the hollow metal NPs. In contrast, highly graphitic carbon supports were only partially corroded and maintained a higher specific activity for the ORR (*e.g.* 19 % and 62 % of the initial  $\text{SA}_{0.95}$  were lost on the PtNi/CNT and the PtNi/GNS nanoparticles, respectively). An overall increase of the catalytic layer resistance, due to the carbon degradation of the carbon support, was also observed.

A severe diminution of the Ni atomic content (determined by STEM-EDX elemental maps and the position of the  $\text{CO}_{\text{ads}}$  stripping peak) was noticed during the load-cycling protocol. For the electrocatalysts presenting an initial crystallite size  $d_{\text{XRD}} < 2$  nm, collapse of the hollow nanostructure and the associated crystallite growth were severe and resulted in a pronounced diminution of structural defects, as presented in **Figure 67**. Electrochemical characterization (such as cyclic voltammograms in Ar-saturated electrolyte,  $\text{CO}_{\text{ads}}$  stripping and ORR measurements) accelerated the changes in structure (*i.e.* increase of the crystallite size, decrease of the concentration of structural defects, *etc.*).

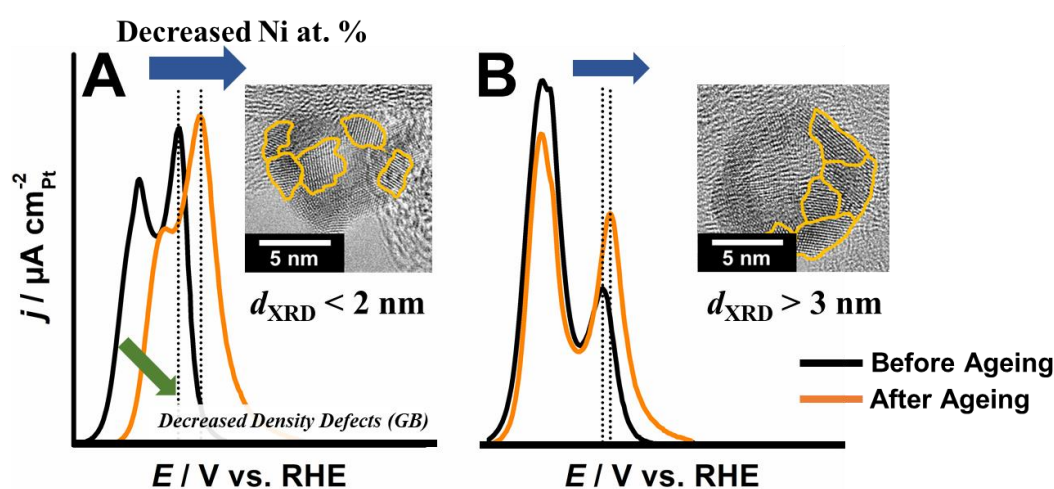


**Figure 67.** Variation of  $\text{CO}_{\text{ads}}$  stripping voltammograms before and after 20,000 potential cycles between 0.6 and 1.0 V vs. RHE at  $T = 353$  K and  $\nu = 50$   $\text{mV s}^{-1}$  for porous hollow PtNi/C nanoparticles with a crystallite size (A)  $d_{\text{XRD}} < 2$  nm and (B)  $d_{\text{XRD}} > 3$  nm.

The structural and chemical modifications of hollow PtNi/C NPs were also investigated in the 0.6 – 1.0 V vs. RHE and the 0.6 – 1.1 V vs. RHE potential ranges using *in operando* WAXS, HR-TEM and STEM-EDX measurements. In both cases, a continuous decrease of the lattice parameter contraction was noticed following Ni depletion. However, the hollow nanostructure, the crystallite size and the concentration of structural defects were found nearly constant after 2,000 s in the 0.6 – 1.0 V vs. RHE potential range. Conversely, the hollow nanostructure partly collapsed after 5,000 cycles<sup>332</sup>, the crystallite size increased significantly (*i.e.* monocrystalline collapsed NPs were formed), the microstrain value diminished and most of the initial Ni atoms were dissolved after potential cycling in the 0.6 – 1.1 V vs. RHE potential range. Those phenomena were ascribed to the place exchange mechanism<sup>209,210</sup>, *i.e.* the faster dissolution of the

Pt surface atoms due to the formation of a PtO oxide layer with oxygen atoms replacing Pt atoms in the first two atomic layers.

*This story might come to an end, but many stones remain unturned.*

The structural defects and their activity for the oxygen reduction reaction have been thoroughly discussed in this manuscript, as well as physical and electrochemical markers of their density (microstrain value, number, position and shape of CO<sub>ads</sub> stripping peaks). However, they have been only discussed for porous hollow PtNi/C NPs and an extension to other catalytic surfaces, as introduced by Chattot *et al.*<sup>247</sup>, is essential. The accelerated stress test performed between 0.6 and 1.1 V *vs.* RHE also showed the limitation of the CO<sub>ads</sub> stripping as a mean to predict the ORR activity, inducing that the exact nature of the structural defects remains unclear. In this work, we showed that structural defects cause the formation of domains featuring either relaxed (*e.g.* near the grain boundaries<sup>293,294</sup>) or contracted lattice constant, but little is known on how these domains impact the electronic structure of the Pt surface atoms. This may be investigated using density functional theory calculations<sup>341</sup>.

Another aspect to discuss is the large-scale production of porous hollow PtNi/C NPs. However, in the frame of a collaboration between the French Alternative Energy and Atomic Energy Commission (CEA) and LEPMI, the synthesis was up-scaled (up to 10 g per synthesis) without any modification of the morphology (see **Figure 68A**) and the electrocatalytic activity for the ORR (see **Figure 68B – Figure 68D**).

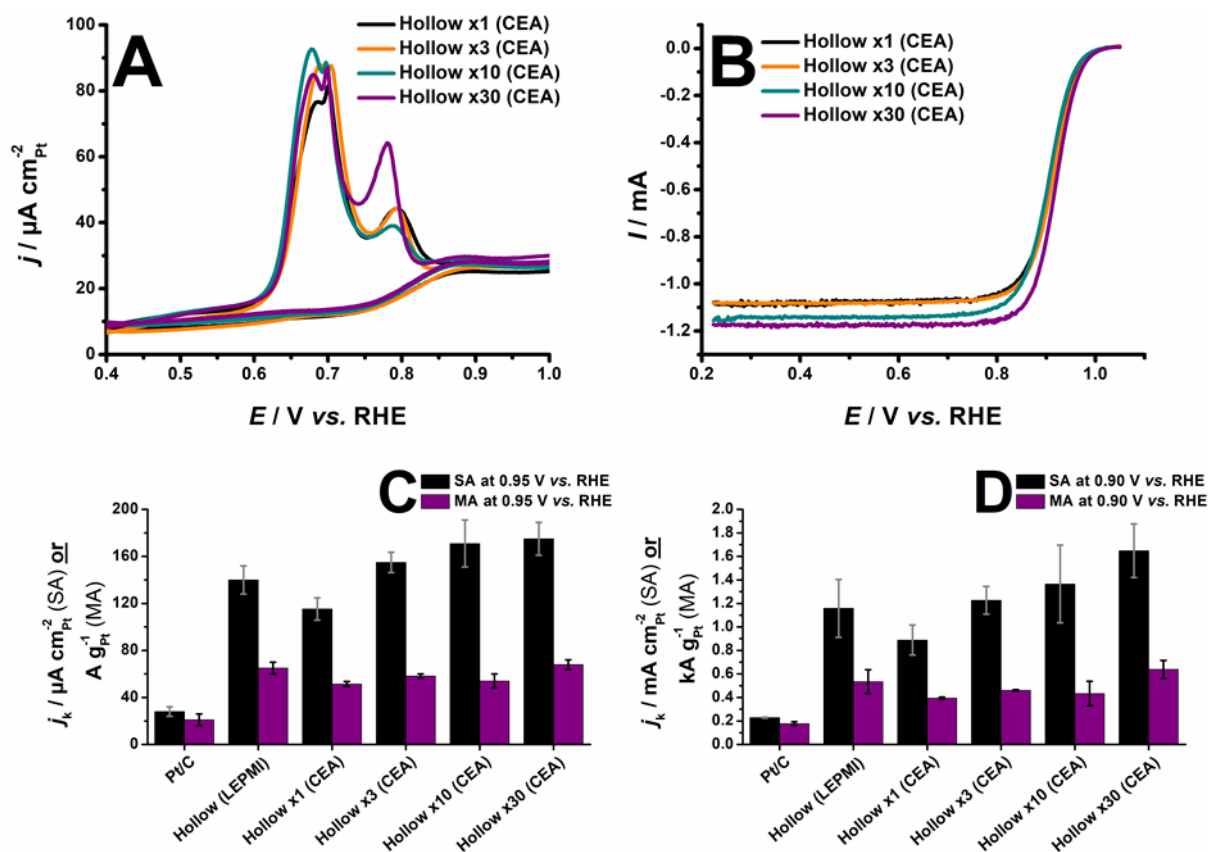


**Figure 68.** Electrochemical properties of porous hollow PtNi/C NPs synthesized at LEPMI or in large-scale reactors by CEA (from *ca.* 350 mg to *ca.* 10 g), with an initial ratio  $\text{Pt}^{2+}:\text{Ni}^{2+}$  of 1:5. **(A)**  $\text{CO}_{\text{ads}}$  stripping voltammogram ( $v = 0.020 \text{ V s}^{-1}$ , Ar-saturated 0.1 M  $\text{HClO}_4$ ). **(B)** Ohmic drop corrected linear sweep voltammograms ( $v = 0.005 \text{ V s}^{-1}$ , electrolyte =  $\text{O}_2$ -saturated 0.1 M  $\text{HClO}_4$ ,  $\omega = 1600 \text{ rpm}$ ). Mass-transport and Ohmic drop corrected specific activity (SA) and mass activity (MA) measured in  $\text{O}_2$ -saturated 0.1 M  $\text{HClO}_4$  at **(C)**  $E = 0.95 \text{ V vs. RHE}$  and **(D)**  $E = 0.9 \text{ V vs. RHE}$ .

The porous hollow PtNi/C NPs were tested in MEA to check if their activity enhancement relative to Pt/C and their stability is maintained in real PEMFC conditions, where the conditions and limitations are quite different from liquid electrolyte<sup>58</sup> (*i.e.* coverage of the electrocatalyst by a solid electrolyte, diffusion of the gases to the catalytic sites, *etc.*). The results are presented in **Figure 69**.

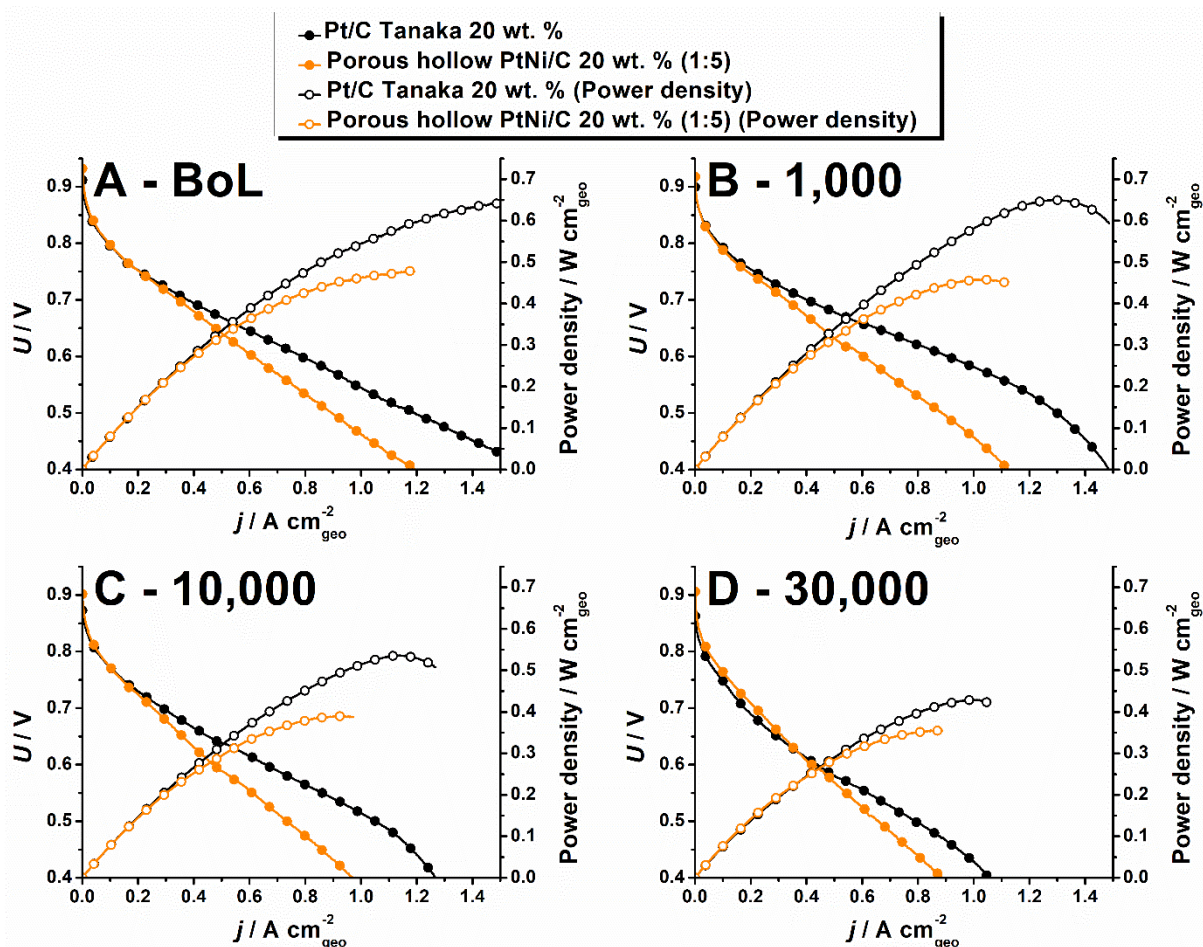


**Figure 69.** Performances of MEA (anode: 50 wt. % commercial Pt/C –  $0.2 \text{ mg cm}_{\text{geo}}^{-2}$ , cathode: porous hollow PtNi/C or commercial Pt/C –  $0.2 \text{ mg cm}_{\text{geo}}^{-2}$ , surface of the MEA:  $25 \text{ cm}^2$ ) at  $T = 353 \text{ K}$ , with a relative humidity of 50 % both for the  $\text{H}_2$  ( $P = 1.5 \text{ bar}$ , stoichiometry 1.5) and the air ( $P = 1.5 \text{ bar}$ , stoichiometry 2). (A) Beginning of life, after activation, (B) after 1,000 potential cycles between 0.6 and 1.0 V at  $\nu = 0.050 \text{ V s}^{-1}$  (C) after 10,000 potential cycles and (D) after 30,000 potential cycles.

The superior activity of the porous hollow NPs is not initially maintained in MEA, *i.e.* the performances are close to the performances of a commercial Pt/C for  $U = 0.70 - 0.90 \text{ V}$  and are depreciated at lower potential, *i.e.* in the diffusion-limited current area (**Figure 69A**). This lower enhancement factor is partly induced by the decreased Pt specific surface of the porous hollow NPs in MEA, *i.e.*  $ca. 20 \text{ m}^2 \text{ g}_{\text{Pt}}^{-1}$  vs.  $ca. 45 \text{ m}^2 \text{ g}_{\text{Pt}}^{-1}$  in RDE experiments. Optimizing the ink formulation and the dispersion of the porous hollow PtNi/C NPs on the carbon support is then essential to ensure a better activity and, therefore, a suitable activity for PEMFC applications. **Figure 69B** to **Figure 69D** shows the MEA performances after 1,000, 10,000 and 30,000 cycles between 0.6 and 1.0 V at  $\nu = 0.050 \text{ V s}^{-1}$ . An interesting feature stemming from those results is that, after 30,000 cycles, the porous hollow NPs presents an enhanced activity vs. commercial Pt/C in the 0.60 – 0.85 V potential range, *i.e.* that the porous hollow NPs present

an enhanced stability in MEA than the commercial Pt/C, resulting from lower losses in specific surface (see **Figure 70**).

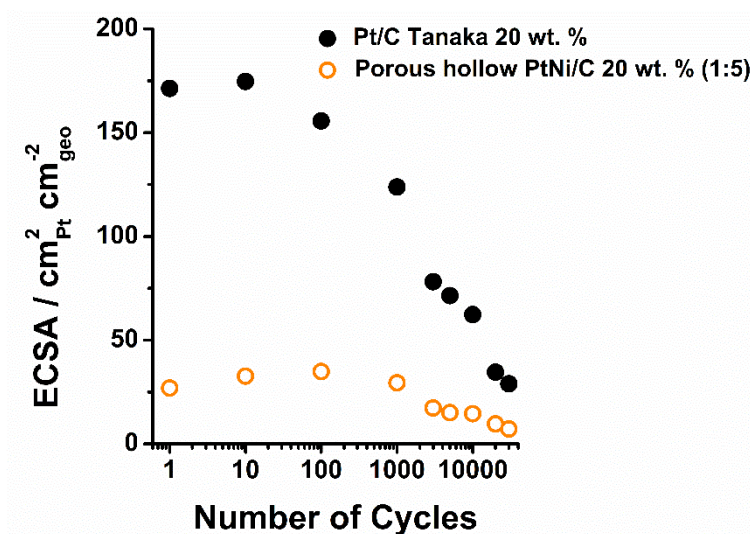


**Figure 70.** Evolution of the Pt specific surface (in  $\text{cm}_{\text{Pt}}^2 \text{cm}_{\text{geo}}^{-2}$ ) in MEA for a commercial Pt/C cathode or a porous hollow PtNi/C cathode ( $0.20 \text{ mg cm}_{\text{geo}}^{-2}$ ).

Understanding the parameters that limit the activity of the porous hollow PtNi/C NPs in MEA configuration (*i.e.* in solid electrolyte, *etc.*), and, *lato sensu*, of the ‘exotic’ Pt-based electrocatalysts (*e.g.* PtNi nanoframes<sup>129</sup>) is essential to consider them as a suitable replacement Pt and Pt-based NPs ( $d \sim 2 - 3 \text{ nm}$ ) in PEMFC applications. Further characterizations in large single-cell and short stack configurations are programmed, in collaboration with the CEA, for the porous hollow PtNi/C NPs.



# **Chapter VII. References**

## Chapter VII. References

- (1) McDougall, I.; Brown, F. H.; Fleagle, J. G. Stratigraphic Placement and Age of Modern Humans from Kibish, Ethiopia. *Nature* **2005**, *433* (7027), 733–736.
- (2) Hublin, J.-J.; Ben-Ncer, A.; Bailey, S. E.; Freidline, S. E.; Neubauer, S.; Skinner, M. M.; Bergmann, I.; Le Cabec, A.; Benazzi, S.; Harvati, K.; Gunz, P. New Fossils from Jebel Irhoud, Morocco and the Pan-African Origin of Homo Sapiens. *Nature* **2017**, *546*, 289–292.
- (3) Berna, F.; Goldberg, P.; Horwitz, L. K.; Brink, J.; Holt, S.; Bamford, M.; Chazan, M. Microstratigraphic Evidence of in Situ Fire in the Acheulean Strata of Wonderwerk Cave, Northern Cape Province, South Africa. *Proc. Natl. Acad. Sci.* **2012**, *109* (20), E1215–E1220.
- (4) Reed, D. L.; Smith, V. S.; Hammond, S. L.; Rogers, A. R.; Clayton, D. H. Genetic Analysis of Lice Supports Direct Contact between Modern and Archaic Humans. *PLoS Biol.* **2004**, *2* (11), 1972–1983.
- (5) Radivojević, M.; Rehren, T.; Pernicka, E.; Šljivar, D.; Brauns, M.; Borić, D. On the Origins of Extractive Metallurgy: New Evidence from Europe. *J. Archaeol. Sci.* **2010**, *37* (11), 2775–2787.
- (6) Dodson, J.; Li, X.; Sun, N.; Atahan, P.; Zhou, X.; Liu, H.; Zhao, K.; Hu, S.; Yvang, Z. Use of Coal in the Bronze Age in China. *The Holocene* **2014**, *24* (5), 525–530.
- (7) Mattusch, C. Metalworking and Tools. In *The Oxford Handbook of Engineering and Technology in the Classical World*; Oleson, J. P., Ed.; Oxford University Press, 2008; pp 418–438.
- (8) Morris, C. R. *The Dawn of Innovation*, PublicAffa.; New York, 2012.
- (9) US\_Census. World Population Summary <https://www.census.gov/population/international/data/> (accessed May 2, 2017).
- (10) International Energy Agency. *Energy and Climate Change*; 2015.
- (11) International Energy Agency. *CO2 Emissions from Fuel Combustion*; 2016.
- (12) Heinberg, R. *The End Of Growth*; New Society: Canada, 2011.
- (13) Global Resources Stock Check <http://www.bbc.com/future/story/20120618-global-resources-stock-check> (accessed Apr 16, 2017).
- (14) Darras, C.; Muselli, M.; Poggi, P.; Voyant, C.; Hogue, J.-C.; Montignac, F. PV Output Power Fluctuations Smoothing : The MYRTE Platform Experience. *Int. J. Hydrogen Energy* **2012**, *37*, 14015–14025.
- (15) Vielstich, W.; Lamm, A.; Gaseiger, H. A. Handbook of Fuel Cells—Fundamentals, Technology and Applications. *Handb. Fuel Cells—Fundamentals, Technol. Appl.* **2003**, *3*, 145–217.
- (16) Grove, W. On the Gas Voltaic Battery. Experiments Made with a View of Ascertaining the Rationale of Its Action and Its Application to Eudiometry. *Philos. Trans. R. Soc. London* **1843**, *133* (January), 91–112.
- (17) Schumm, B. Fuel Cell <https://www.britannica.com/technology/fuel-cell> (accessed May 3, 2017).
- (18) Dicks, A. L. Molten Carbonate Fuel Cells. *Curr. Opin. Solid State Mater. Sci.* **2004**, *8* (5), 379–383.
- (19) Klingele, M.; Breitwieser, M.; Zengerle, R.; Thiele, S. Direct Deposition of Proton Exchange

## Chapter VII. References

- Membranes Enabling High Performance Hydrogen Fuel Cells. *J. Mater. Chem. A* **2015**, *3* (21), 11239–11245.
- (20) de Chialvo, M. R. G.; Chialvo, A. C. Hydrogen Evolution Reaction: Analysis of the Volmer-Heyrovsky-Tafel Mechanism with a Generalized Adsorption Model. *J. Electroanal. Chem.* **1994**, *372* (1–2), 209–223.
- (21) Conway, B. E.; Salomon, M. Electrochemical Reaction Orders : Applications To the Hydrogen- and Oxygen-Evolution Reactions\*. *Electrochimica Acta* **1964**, *9* (January), 1599–1615.
- (22) Bockris, J. O.; Reddy, A. K. N.; Gamboa-Aldeco, M. *Modern Electrochemistry, Second Edition: Fundamentals of Electrode Processes*; Plenum Publishers: New York, 2000.
- (23) Gennero De Chialvo, M. R.; Chialvo, A. C. Hydrogen Diffusion Effects on the Kinetics of the Hydrogen Electrode Reaction. Part I. Theoretical Aspects. *Phys. Chem. Chem. Phys.* **2004**, *6* (15), 4009–4017.
- (24) Wang, J. X.; Springer, T. E.; Adzic, R. A. Dual-Pathway Kinetic Equation for the Hydrogen Oxidation Reaction on Pt Electrodes. *J. Electrochem. Soc.* **2006**, *153*, A1732–A1740.
- (25) Quaino, P. M.; Fernández, J. L.; Gennero de Chialvo, M. R.; Chialvo, A. C. Hydrogen Oxidation Reaction on Microelectrodes: Analysis of the Contribution of the Kinetic Routes. *J. Mol. Catal. A Chem.* **2006**, *252* (1–2), 156–162.
- (26) Bonnefont, A.; Simonov, A. N.; Pronkin, S. N.; Gerasimov, E. Y.; Pyrjaev, P. A.; Parmon, V. N.; Savinova, E. R. Hydrogen Electrooxidation on PdAu Supported Nanoparticles: An Experimental RDE and Kinetic Modeling Study. *Catal. Today* **2013**, *202* (1), 70–78.
- (27) Pronkin, S. N.; Bonnefont, A.; Ruvinskiy, P. S.; Savinova, E. R. Hydrogen Oxidation Kinetics on Model Pd/C Electrodes: Electrochemical Impedance Spectroscopy and Rotating Disk Electrode Study. *Electrochim. Acta* **2010**, *55*, 3312–3323.
- (28) Sheng, W.; Gasteiger, H. A.; Shao-Horn, Y. Hydrogen Oxidation and Evolution Reaction Kinetics on Platinum: Acid vs Alkaline Electrolytes. *J. Electrochem. Soc.* **2010**, *157* (11), B1529.
- (29) Gennero de Chialvo, M. R.; Chialvo, A. C. Kinetics of Hydrogen Evolution Reaction with Frumkin Adsorption: Re-Examination of the Volmer–Heyrovsky and Volmer–Tafel Routes. *Electrochim. Acta* **1998**, *44* (5), 841–851.
- (30) Quaino, P. M.; Gennero de Chialvo, M. R.; Chialvo, A. C. Hydrogen Electrode Reaction: A Complete Kinetic Description. *Electrochim. Acta* **2007**, *52* (25), 7396–7403.
- (31) Zolfaghari, A.; Jerkiewicz, G. Temperature-Dependent Research on Pt(111) and Pt(100) Electrodes in Aqueous H<sub>2</sub>SO<sub>4</sub>. *J. Electroanal. Chem.* **1999**, *467* (1), 177–185.
- (32) Kunimatsu, K.; Senzaki, T.; Samjeské, G.; Tsushima, M.; Osawa, M. Hydrogen Adsorption and Hydrogen Evolution Reaction on a Polycrystalline Pt Electrode Studied by Surface-Enhanced Infrared Absorption Spectroscopy. *Electrochim. Acta* **2007**, *52* (18), 5715–5724.
- (33) Conway, B. E.; Jerkiewicz, G. Relation of Energies and Coverages of Underpotential and Overpotential Deposited H at Pt and Other Metals to the 'volcano Curve' for Cathodic H<sub>2</sub>

## Chapter VII. References

- Evolution Kinetics. *Electrochim. Acta* **2000**, *45* (25–26), 4075–4083.
- (34) Stamenković, V.; Schmidt, T. J.; Ross, P. N.; Marković, N. M. Surface Composition Effects in Electrocatalysis: Kinetics of Oxygen Reduction on Well-Defined Pt 3 Ni and Pt 3 Co Alloy Surfaces. *J. Phys. Chem. B* **2002**, *106* (46), 11970–11979.
- (35) Damjanovic, A.; Genshaw, M. A.; Bockris, J. O. Distinction between Intermediates Produced in Main and Side Electrode Reactions. *J. Chem. Phys.* **1966**, *45*, 4057–4059.
- (36) Damjanovic, A.; Genshaw, M. A.; Bockris, J. O. The Role of Hydrogen Peroxide in Oxygen Reduction at Platinum in H<sub>2</sub>SO<sub>4</sub> Solution. *J. Electrochem. Soc.* **1967**, *114*, 466–472.
- (37) Damjanovic, A.; Genshaw, M. A.; Bockris, J. O. The Mechanism of Oxygen Reduction at Pt in Alkaline Solution with Special Reference to H<sub>2</sub>O<sub>2</sub>. *J. Electrochem. Soc.* **1967**, *114*, 1107–1112.
- (38) Damjanovic, A.; Brusic, V. Electrode Kinetics of Oxygen Reduction on Oxide-Free Platinum Electrodes. *Electrochim. Acta* **1967**, *12*, 615–628.
- (39) Shao, M. H.; Liu, P.; Adzic, R. R. Superoxide Anion Is the Intermediate in the Oxygen Reduction Reaction on Platinum Electrodes. *J. Am. Chem. Soc.* **2006**, *128* (23), 7408–7409.
- (40) El Kadiri, F.; Faure, R.; Durand, R. Electrochemical Reduction of Molecular Oxygen on Platinum Single Crystals. *J. Electroanal. Chem.* **1991**, *301*, 177–188.
- (41) Gamez, A.; Richard, D.; Gallezot, P.; Gloaguen, F.; Faure, R.; Durand, R. Oxygen Reduction on Well-Defined Platinum Nanoparticles inside Recast Ionomer. *Electrochim. Acta* **1996**, *41*, 307–314.
- (42) Antoine, O.; Durand, R. RRDE Study of Oxygen Reduction on Pt Nanoparticles inside Nafion: H<sub>2</sub>O<sub>2</sub> Production in PEMFC Cathode Conditions. *J. Appl. Electrochem.* **2000**, *30*, 839–844.
- (43) Antoine, O.; Bultel, Y.; Durand, R. Oxygen Reduction Reaction Kinetics and Mechanism on Platinum Nanoparticles inside Nafion. *J. Electroanal. Chem.* **2001**, *499*, 85–94.
- (44) Wroblowa, H. S.; Pan, Y. C.; Razumney, G. Electroreduction of Oxygen: A New Mechanistic Criterion. *J. Electroanal. Chem. Interfacial Electrochem.* **1976**, *69* (2), 195–201.
- (45) Anastasijević, N. A.; Vesović, V.; Adžić, R. R. Determination of the Kinetic Parameters of the Oxygen Reduction Reaction Using the Rotating Ring-Disk Electrode: Part I. Theory. *J. Electroanal. Chem. Interfacial Electrochem.* **1987**, *229*, 305–316.
- (46) Anastasijević, N. A.; Vesović, V.; Adžić, R. R. Determination of the Kinetic Parameters of the Oxygen Reduction Reaction Using the Rotating Ring-Disk Electrode: Part II. Applications. *J. Electroanal. Chem. Interfacial Electrochem.* **1987**, *229*, 317–325.
- (47) Markovic, N. M.; Adzic, R. R.; Cahan, B. D.; Yeager, E. B. Structural Effects in Electrocatalysis - Oxygen Reduction on Platinum Low-Index Single-Crystal Surfaces in Perchloric-Acid Solutions. *J. Electroanal. Chem.* **1994**, *377* (1–2), 249–259.
- (48) Maillard, F.; Martin, M.; Gloaguen, F.; Léger, J. M. Oxygen Electroreduction on Carbon-Supported Platinum Catalysts. Particle-Size Effect on the Tolerance to Methanol Competition. *Electrochim. Acta* **2002**, *47* (21), 3431–3440.

## Chapter VII. References

- (49) Shao, M.; Peles, A.; Shoemaker, K. Electrocatalysis on Platinum Nanoparticles : Particle Size Effect on Oxygen Reduction Reaction Activity. *Nano Lett.* **2011**, *11*, 3714–3719.
- (50) Perez-Alonso, F. J.; McCarthy, D. N.; Nierhoff, A.; Hernandez-Fernandez, P.; Strebel, C.; Stephens, I. E. L.; Nielsen, J. H.; Chorkendorff, I. The Effect of Size on the Oxygen Electroreduction Activity of Mass-Selected Platinum Nanoparticles. *Angew. Chem., Int. Ed.* **2012**, *51* (19), 4641–4643.
- (51) Stamenkovic, V.; Markovic, N. M.; Ross, P. N. Structure-Relationships in Electrocatalysis: Oxygen Reduction and Hydrogen Oxidation Reactions on Pt(111) and Pt(100) in Solutions Containing Chloride Ions. *J. Electroanal. Chem.* **2001**, *500* (1–2), 44–51.
- (52) Marković, N. M.; Gasteiger, H. A.; Grgur, B. N.; Ross, P. N. Oxygen Reduction Reaction on Pt(111): Effects of Bromide. *J. Electroanal. Chem.* **1999**, *467*, 157–163.
- (53) Wang, J. X.; Zhang, J.; Adzic, R. R. Double-Trap Kinetic Equation for the Oxygen Reduction Reaction on pt(111) in Acidic Media. *J. Phys. Chem. A* **2007**, *111* (49), 12702–12710.
- (54) Stephens, I. E. L.; Bondarenko, A. S.; Grønbjerg, U.; Rossmeisl, J.; Chorkendorff, I. Understanding the Electrocatalysis of Oxygen Reduction on Platinum and Its Alloys. *Energy Environ. Sci.* **2012**, *5* (5), 6744–6762.
- (55) Greeley, J.; Stephens, I. E. L.; Bondarenko, S.; Johansson, T. P.; Hansen, H. A.; Jaramillo, T. F.; Rossmeisl, J.; Chorkendorff, I.; Nørskov, J. K.; Bondarenko, A. S.; Johansson, T. P.; Hansen, H. A.; Jaramillo, T. F.; Rossmeisl, J.; Chorkendorff, I.; Nørskov, J. K. Alloys of Platinum and Early Transition Metals as Oxygen Reduction Electrocatalysts. *Nat. Chem.* **2009**, *1* (7), 552–558.
- (56) Rossmeisl, J.; Logadottir, A.; Nørskov, J. K. Electrolysis of Water on (Oxidized) Metal Surfaces. *Chem. Phys.* **2005**, *319* (1–3), 178–184.
- (57) Nørskov, J. K.; Rossmeisl, J.; Logadottir, A.; Lindqvist, L.; Lyngby, D.; Jo, H.; Kitchin, J. R.; Bligaard, T. Origin of the Overpotential for Oxygen Reduction at a Fuel-Cell Cathode. *J. Phys. Chem. B* **2004**, *108*, 17886–17892.
- (58) Gasteiger, H. A.; Kocha, S. S.; Sompalli, B.; Wagner, F. T. Activity Benchmarks and Requirements for Pt, Pt-Alloy, and Non-Pt Oxygen Reduction Catalysts for PEMFCs. *Appl. Catal. B Environ.* **2005**, *56* (1–2), 9–35.
- (59) Lefevre, M.; Proietti, E.; Jaouen, F.; Dodelet, J.-P. Iron-Based Catalysts with Improved Oxygen Reduction Activity in Polymer Electrolyte Fuel Cells. *Science (80-. )*. **2009**, *324* (5923), 71–74.
- (60) Jaouen, F.; Proietti, E.; Lefèvre, M.; Chenitz, R.; Dodelet, J.-P.; Wu, G.; Chung, H. T.; Johnston, C. M.; Zelenay, P. Recent Advances in Non-Precious Metal Catalysis for Oxygen-Reduction Reaction in Polymer Electrolyte Fuel Cells. *Energy Environ. Sci.* **2011**, *4* (1), 114–130.
- (61) Jaouen, F.; Herranz, J.; Lefevre, M.; Dodelet, J. P.; Kramm, U. I.; Herrmann, I.; Bogdanoff, P.; Maruyama, J.; Nagaoka, T.; Garsuch, A.; Dahn, J. R.; Olson, T.; Pylypenko, S.; Atanassov, P.; Ustinov, E. A. Cross-Laboratory Experimental Study of Non-Noble-Metal Electrocatalysts for the Oxygen Reduction Reaction. *ACS Appl. Mater. Interfaces* **2009**, *1* (8), 1623–1639.

## Chapter VII. References

- (62) Wu, G.; More, K. L.; Johnston, C. M.; Zelenay, P. High-Performance Electrocatalysts for Oxygen Reduction Derived from Polyaniline, Iron and Cobalt. *Science* (80-. ). **2011**, *332*, 443–448.
- (63) Bashyam, R.; Zelenay, P. A Class of Non-Precious Metal Composite Catalysts for Fuel Cells. *Nature* **2006**, *443* (7107), 63–66.
- (64) Lopez-Haro, M.; Guétaz, L.; Printemps, T.; Morin, A.; Escribano, S.; Jouneau, P.-H.; Bayle-Guillemaud, P.; Chandezon, F.; Gebel, G. Three-Dimensional Analysis of Nafion Layers in Fuel Cell Electrodes. *Nat. Commun.* **2014**, *5*, 5229–5334.
- (65) Xie, J.; Xu, F.; Wood, D. L.; More, K. L.; Zawodzinski, T.; Smith, W. H. Influence of Ionomer Content on the Structure and Performance of PEFC Membrane Electrode Assemblies. *Electrochim. Acta* **2010**, *55* (24), 7404–7412.
- (66) Locating the World's Minerals and Mines <http://www.mining.com/infographic-where-the-minerals-are-82638/> (accessed May 3, 2017).
- (67) Stephens, I. E. L.; Rossmeisl, J.; Chorkendorff, I. Toward Sustainable Fuel Cells. *Science* (80-. ). **2016**, *354*, 1378–1379.
- (68) Wang, C.; Markovic, N. M.; Stamenkovic, V. R. Advanced Platinum Alloy Electrocatalysts for the Oxygen Reduction Reaction. *ACS Catal.* **2012**, *2* (5), 891–898.
- (69) Wang, C.; Vliet, D. Van Der; Chang, K.; You, H.; Strmcnik, D.; Schlueter, J. A.; Markovic, N. M.; Stamenkovic, V. R.; Van der Vliet, D.; Chang, K.; You, H.; Strmcnik, D.; Schlueter, J. A.; Markovic, N. M.; Stamenkovic, V. R. Monodisperse Pt<sub>3</sub>Co Nanoparticles as a Catalyst for the Oxygen Reduction Reaction: Size-Dependent Activity. *J. Phys. Chem. C Lett.* **2009**, *113*, 19365–19368.
- (70) Paulus, U. A.; Wokaun, A.; Scherer, G. G.; Schmidt, T. J.; Stamenkovic, V.; Markovic, N. M.; Ross, P. N. Oxygen Reduction on High Surface Area Pt-Based Alloy Catalysts in Comparison to Well Defined Smooth Bulk Alloy Electrodes. *Electrochim. Acta* **2002**, *47* (22–23), 3787–3798.
- (71) Paulus, U. a; Wokaun, a; Scherer, G. G.; Institut, P. S.; Psi, C.-V. Oxygen Reduction on Carbon-Supported Pt - Ni and Pt - Co Alloy Catalysts. *J. Phys. Chem. B* **2002**, *106* (41), 4181–4191.
- (72) Oezaslan, M.; Hasché, F.; Strasser, P. Pt-Based Core–Shell Catalyst Architectures for Oxygen Fuel Cell Electrodes. *J. Phys. Chem. Lett.* **2013**, *4* (19), 3273–3291.
- (73) Oezaslan, M.; Hasché, F.; Strasser, P. Oxygen Electroreduction on PtCo<sub>3</sub>, PtCo and Pt<sub>3</sub>Co Alloy Nanoparticles for Alkaline and Acidic PEM Fuel Cells. *J. Electrochem. Soc.* **2012**, *159* (4), B394–B405.
- (74) Oezaslan, M.; Strasser, P. Activity of Dealloyed PtCo<sub>3</sub> and PtCu<sub>3</sub> Nanoparticle Electrocatalyst for Oxygen Reduction Reaction in Polymer Electrolyte Membrane Fuel Cell. *J. Power Sources* **2011**, *196* (12), 5240–5249.
- (75) Hasché, F.; Oezaslan, M.; Strasser, P. Activity and Structure of Dealloyed PtNi<sub>3</sub> Nanoparticle

## Chapter VII. References

- Electrocatalyst for Oxygen Reduction Reaction in PEMFC. *ECS Trans.* **2011**, *41* (1), 1079–1088.
- (76) Kuttiyiel, K.; Sasaki, K.; Su, D.; Vukmirovic, M. B.; Marinkovic, N. S.; Adzic, R. R. Pt Monolayer on Au-Stabilized PdNi Core-shell Nanoparticles for Oxygen Reduction Reaction. *Electrochim. Acta* **2013**, *110*, 267–272.
- (77) Sasaki, K.; Naohara, H.; Cai, Y.; Choi, Y. M.; Liu, P.; Vukmirovic, M. B.; Wang, J. X.; Adzic, R. R. Core-Protected Platinum Monolayer Shell High-Stability Electrocatalysts for Fuel-Cell Cathodes. *Angew. Chemie - Int. Ed.* **2010**, *49*, 8602–8607.
- (78) Gong, K.; Su, D.; Adzic, R. R. Platinum-Monolayer Shell on AuNi 0.5 Fe Nanoparticle Core Electrocatalyst with High Activity and Stability for the Oxygen Reduction Reaction. *J. Am. Chem. Soc.* **2010**, *132*, 14364–14366.
- (79) Zhang, J.; Lima, F. H. B.; Shao, M. H.; Sasaki, K.; Wang, J. X.; Hanson, J.; Adzic, R. R. Platinum Monolayer on Nonnoble Metal-Noble Metal Core-Shell Nanoparticle Electrocatalysts for O<sub>2</sub> Reduction. *J. Phys. Chem. B* **2005**, *109* (48), 22701–22704.
- (80) Sasaki, K.; Naohara, H.; Choi, Y.; Cai, Y.; Chen, W.-F.; Liu, P.; Adzic, R. R. Highly Stable Pt Monolayer on PdAu Nanoparticle Electrocatalysts for the Oxygen Reduction Reaction. *Nat Commun* **2012**, *3*, 1–5.
- (81) Snyder, J.; McCue, I.; Livi, K.; Erlebacher, J. Structure/Processing/Properties Relationships in Nanoporous Nanoparticles as Applied to Catalysis of the Cathodic Oxygen Reduction Reaction. *J. Am. Chem. Soc.* **2012**, *134* (20), 8633–8645.
- (82) Snyder, J.; Livi, K.; Erlebacher, J. Oxygen Reduction Reaction Performance of [MTBD][beti]-Encapsulated Nanoporous NiPt Alloy Nanoparticles. *Adv. Funct. Mater.* **2013**, *23* (44), 5494–5501.
- (83) Dubau, L.; Lopez-Haro, M.; Durst, J.; Guétaz, L.; Bayle-Guillemaud, P.; Chatenet, M.; Maillard, F. Beyond Conventional Electrocatalysts: Hollow Nanoparticles for Improved and Sustainable Oxygen Reduction Reaction Activity. *J. Mater. Chem. A* **2014**, *2* (43), 18497–18507.
- (84) Dubau, L.; Asset, T.; Chattot, R. R.; Bonnaud, C. C.; Vanpeene, V.; Maillard, F. F.; Nelayah, J.; Maillard, F. F. Tuning the Performance and the Stability of Porous Hollow PtNi/C Nanostructures for the Oxygen Reduction Reaction. *ACS Catal.* **2015**, *5* (9), 5333–5341.
- (85) Zhang, Y.; Ma, C.; Zhu, Y.; Si, R.; Cai, Y.; Wang, J. X.; Adzic, R. R. Hollow Core Supported Pt Monolayer Catalysts for Oxygen Reduction. *Catal. Today* **2013**, *202*, 50–54.
- (86) Mayers, B.; Jiang, X.; Sunderland, D.; Cattle, B.; Xia, Y. Hollow Nanostructures of Platinum with Controllable Dimensions Can Be Synthesized by Templating against Selenium Nanowires and Colloids. *J. Am. Chem. Soc.* **2003**, *125* (44), 13364–13365.
- (87) Bu, L.; Zhang, N.; Guo, S.; Zhang, X.; Li, J.; Yao, J.; Wu, T.; Lu, G.; Ma, J.-Y.; Su, D.; Huang, X. Biaxially Strained PtPb/Pt Core/shell Nanoplate Boosts Oxygen Reduction Catalysis. *Science* (80-. ). **2016**, *354*, 1410–1414.
- (88) Cui, C.; Gan, L.; Li, H.-H.; Yu, S.-H.; Heggen, M.; Strasser, P. Octahedral PtNi Nanoparticle

## Chapter VII. References

- Catalysts: Exceptional Oxygen Reduction Activity by Tuning the Alloy Particle Surface Composition. *Nano Lett.* **2012**, *12* (11), 5885–5889.
- (89) Beermann, V.; Gocyla, M.; Willinger, E.; Rudi, S.; Heggen, M.; Dunin-Borkowski, R. E.; Willinger, M.-G.; Strasser, P. Rh-Doped Pt-Ni Octahedral Nanoparticles: Understanding the Correlation between Elemental Distribution, Oxygen Reduction Reaction, and Shape Stability. *Nano Lett.* **2016**, *16* (3), 1719–1725.
- (90) Wu, J.; Zhang, J.; Peng, Z.; Yang, S.; Wagner, F. T.; Yang, H. Truncated Octahedral Pt<sub>3</sub>Ni Oxygen Reduction Reaction Electrocatalysts. *J. Am. Chem. Soc.* **2010**, *132* (14), 4984–4985.
- (91) Wang, X.; Vara, M.; Luo, M.; Huang, H.; Ruditskiy, A.; Park, J.; Bao, S.; Liu, J.; Howe, J.; Chi, M.; Xie, Z.; Xia, Y. Pd@Pt Core-Shell Concave Decahedra: A Class of Catalysts for the Oxygen Reduction Reaction with Enhanced Activity and Durability. *J. Am. Chem. Soc.* **2015**, *137* (47), 15036–15042.
- (92) Samjeske, G.; Xiao, X.; Baltruschat, H. Ru Decoration of Stepped Pt Single Crystals and the Role of the Terrace Width on the Electrocatalytic CO Oxidation. **2002**, No. 13, 4659–4666.
- (93) Hammer, B.; Nørskov, J. K. Electronic Factors Determining the Reactivity of Metal Surfaces. *Surf. Sci.* **1995**, *343* (3), 211–220.
- (94) Hammer, B.; Morikawa, Y.; Nørskov, J. K. CO Chemisorption at Metal Surfaces and Overlayers. *Phys. Rev. Lett.* **1996**, *76* (12), 2141–2144.
- (95) Pedersen, A. F.; Ulrikkeholm, E. T.; Escudero-Escribano, M.; Johansson, T. P.; Malacrida, P.; Pedersen, C. M.; Hansen, M. H.; Jensen, K. D.; Rossmeisl, J.; Friebel, D.; Nilsson, A.; Chorkendorff, I.; Stephens, I. E. L. Probing the Nanoscale Structure of the Catalytically Active Overlayer on Pt Alloys with Rare Earths. *Nano Energy* **2016**, *29*, 249–260.
- (96) Ulrikkeholm, E. T.; Pedersen, A. F.; Vej-Hansen, U. G.; Escudero-Escribano, M.; Stephens, I. E. L.; Friebel, D.; Mehta, A.; Schiøtz, J.; Feidenhansl, R. K.; Nilsson, A.; Chorkendorff, I. Pt<sub>x</sub>Gd Alloy Formation on Pt(111): Preparation and Structural Characterization. *Surf. Sci.* **2016**, *652*, 114–122.
- (97) Dubau, L.; Maillard, F.; Chatenet, M.; André, J.; Rossinot, E. Nanoscale Compositional Changes and Modification of the Surface Reactivity of Pt<sub>3</sub>Co/C Nanoparticles during Proton-Exchange Membrane Fuel Cell Operation. *Electrochim. Acta* **2010**, *56* (2), 776–783.
- (98) Stamenkovic, V. R.; Mun, B. S.; Arenz, M.; Mayrhofer, K. J. J.; Lucas, C. A.; Wang, G.; Ross, P. N.; Markovic, N. M. Trends in Electrocatalysis on Extended and Nanoscale Pt-Bimetallic Alloy Surfaces. *Nat. Mater.* **2007**, *6*, 241–247.
- (99) Chen, S.; Kucernak, A. Electrocatalysis under Conditions of High Mass Transport Rate: Oxygen Reduction on Single Submicrometer-Sized Pt Particles Supported on Carbon. *J. Phys. Chem. B* **2004**, *108*, 3262–3276.
- (100) Stamenkovic, V.; Mun, B. S.; Mayrhofer, K. J. J.; Ross, P. N.; Markovic, N. M.; Rossmeisl, J.; Greeley, J.; Nørskov, J. K. Changing the Activity of Electrocatalysts for Oxygen Reduction by

## Chapter VII. References

- Tuning the Surface Electronic Structure. *Angew. Chemie - Int. Ed.* **2006**, *45* (18), 2897–2901.
- (101) Bligaard, T.; Nørskov, J. K. Ligand Effects in Heterogeneous Catalysis and Electrochemistry. *Electrochim. Acta* **2007**, *52*, 5512–5516.
- (102) Greeley, J.; Nørskov, J. K. Combinatorial Density Functional Theory-Based Screening of Surface Alloys for the Oxygen Reduction Reaction. *J. Phys. Chem. C* **2009**, *113* (12), 4932–4939.
- (103) Viswanathan, V.; Hansen, H. A.; Rossmeisl, J.; Nørskov, J. K. Universality in Oxygen Reduction Electrocatalysis on Metal Surfaces. *ACS Catal.* **2012**, *2* (8), 1654–1660.
- (104) Kitchin, J. R.; Nørskov, J. K.; Barteau, M. A.; Chen, J. G. Modification of the Surface Electronic and Chemical Properties of Pt (111) by Subsurface 3d Transition Metals. *J. Chem. Phys.* **2004**, *120* (21), 10240–10246.
- (105) Mavrikakis, M.; Hammer, B.; Nørskov, J. K. Effect of Strain on the Reactivity of Metal Surfaces. *Phys. Rev. Lett.* **1998**, *81* (13), 2819–2822.
- (106) Strasser, P.; Koh, S.; Anniyev, T.; Greeley, J.; More, K.; Yu, C.; Liu, Z.; Kaya, S.; Nordlund, D.; Ogasawara, H.; Toney, M. F.; Nilsson, A. Lattice-Strain Control of the Activity in Dealloyed Core-Shell Fuel Cell Catalysts. *Nat Chem* **2010**, *2* (6), 454–460.
- (107) Zhang, J.; Vukmirovic, M. B.; Xu, Y.; Mavrikakis, M.; Adzic, R. R. Controlling the Catalytic Activity of Platinum-Monolayer Electrocatalysts for Oxygen Reduction with Different Substrates. *Angew. Chem., Int. Ed.* **2005**, *44* (14), 2132–2135.
- (108) Suo, Y.; Zhuang, L.; Lu, J. First-Principles Considerations in the Design of Pd-Alloy Catalysts for Oxygen Reduction. *Angew. Chem., Int. Ed.* **2007**, *46* (16), 2862–2864.
- (109) Van Der Vliet, D. F.; Wang, C.; Li, D.; Paulikas, A. P.; Greeley, J.; Rankin, R. B.; Strmcnik, D.; Tripkovic, D.; Markovic, N. M.; Stamenkovic, V. R. Unique Electrochemical Adsorption Properties of Pt-Skin Surfaces. *Angew. Chem., Int. Ed.* **2012**, *51* (13), 3139–3142.
- (110) Stamenkovic, V. R.; Mun, B. S.; Mayrhofer, K. J. J.; Ross, P. N.; Markovic, N. M. Effect of Surface Composition on Electronic Structure, Stability, and Electrocatalytic Properties of Pt-Transition Metal Alloys: Pt-Skin versus Pt-Skeleton Surfaces. *J. Am. Chem. Soc.* **2006**, *128* (27), 8813–8819.
- (111) Kang, Y.; Snyder, J.; Chi, M.; Li, D.; More, K. L.; Markovic, N. M.; Stamenkovic, V. R. Multimetallic Core/Interlayer/Shell Nanostructures as Advanced Electrocatalysts. *Nano Lett.* **2014**, *14* (11), 6361–6367.
- (112) Wang, C.; Vliet, D. Van Der; More, K. L.; Zaluzec, N. J.; Peng, S.; Sun, S.; Daimon, H.; Wang, G.; Pearson, J.; Paulikas, A. P.; Karapetrov, G.; Strmcnik, D.; Markovic, N. M.; Stamenkovic, V. R. Multimetallic Au/FePt<sub>3</sub> Nanoparticles as Highly Durable Electrocatalyst. *Nano Lett.* **2011**, 919–926.
- (113) Rossmeisl, J.; Karlberg, G. S.; Jaramillo, T.; Nørskov, J. K. Steady State Oxygen Reduction Reaction and Cyclic Voltammetry. *Faraday Discuss.* **2008**, *140*, 337–346.

## Chapter VII. References

- (114) Adzic, R. R.; Zhang, J.; Sasaki, K.; Vukmirovic, M. B.; Shao, M.; Wang, J. X.; Nilekar, A. U.; Mavrikakis, M.; Valerio, J. A.; Uribe, F. Platinum Monolayer Fuel Cell Electrocatalysts. *Top. Catal.* **2007**, *46* (3–4), 249–262.
- (115) Zhang, J.; Mo, Y.; Vukmirovic, M. B.; Klie, R.; Sasaki, K.; Adzic, R. R. Platinum Monolayer Electrocatalysts for O<sub>2</sub> Reduction: Pt Monolayer on Pd(111) and on Carbon-Supported Pd Nanoparticles. *J. Phys. Chem. B* **2004**, *108* (30), 10955–10964.
- (116) Neimark, A. V.; Kheifez, L. I.; Fenelonov, V. B. Theory of Preparation of Supported Catalysts. *Ind. Eng. Chem. Prod. Res. Dev.* **1981**, *20*, 439–450.
- (117) Qian, L.; Zhang, H. Controlled Freezing and Freeze Drying: A Versatile Route for Porous and Micro-/nano-Structured Materials. *J. Chem. Technol. Biotechnol.* **2011**, *86* (2), 172–184.
- (118) Mani, P.; Srivastava, R.; Strasser, P. Dealloyed Binary PtM<sub>3</sub> (M=Cu, Co, Ni) and Ternary PtNi<sub>3</sub>M (M=Cu, Co, Fe, Cr) Electrocatalysts for the Oxygen Reduction Reaction: Performance in Polymer Electrolyte Membrane Fuel Cells. *J. Power Sources* **2011**, *196* (2), 666–673.
- (119) Oezaslan, M.; Hasché, F.; Strasser, P. In Situ Observation of Bimetallic Alloy Nanoparticle Formation and Growth Using High-Temperature XRD. *Chem. Mater.* **2011**, *23* (8), 2159–2165.
- (120) Mani, P.; Srivastava, R.; Strasser, P. Dealloyed Pt-Cu Core-Shell Nanoparticle Electrocatalysts for Use in PEM Fuel Cell Cathodes. *J. Phys. Chem. C* **2008**, *112* (7), 2770–2778.
- (121) Rudi, S.; Tuaeov, X.; Strasser, P. Electrocatalytic Oxygen Reduction on Dealloyed Pt<sub>1-x</sub>Ni<sub>x</sub> Alloy Nanoparticle Electrocatalysts. *Electrocatalysis* **2012**, *3* (3), 265–273.
- (122) Srivastava, R.; Mani, P.; Hahn, N.; Strasser, P. Efficient Oxygen Reduction Fuel Cell Electrocatalysis on Voltammetrically Dealloyed Pt-Cu-Co Nanoparticles. *Angew. Chemie - Int. Ed.* **2007**, *46* (47), 8988–8991.
- (123) Heggen, M.; Oezaslan, M.; Houben, L.; Strasser, P. Formation and Analysis of Core-Shell Fine Structures in Pt Bimetallic Nanoparticle Fuel Cell Electrocatalysts. *J. Phys. Chem. C* **2012**, *116* (36), 19073–19083.
- (124) Gan, L.; Heggen, M.; Rudi, S.; Strasser, P. Core-Shell Compositional Fine Structures of Dealloyed Pt<sub>x</sub>Ni<sub>1-x</sub> Nanoparticles and Their Impact on Oxygen Reduction Catalysis. *Nano Lett.* **2012**, *12* (10), 5423–5430.
- (125) Strasser, P. Dealloyed Core-Shell Fuel Cell Electrocatalysts. *Rev. Chem. Eng.* **2009**, *25* (4), 255–295.
- (126) Oezaslan, M.; Heggen, M.; Strasser, P. Size-Dependent Morphology of Dealloyed Bimetallic Catalysts: Linking the Nano to the Macro Scale. *J. Am. Chem. Soc.* **2012**, *134* (1), 514–524.
- (127) Gan, L.; Heggen, M.; O'Malley, R.; Theobald, B.; Strasser, P.; Malley, R. O.; Theobald, B. Understanding and Controlling Nanoporosity Formation for Improving the Stability of Bimetallic Fuel Cell Catalysts. *Nano Lett.* **2013**, *13* (3), 1131–1138.
- (128) Gan, L.; Cui, C.; Rudi, S.; Strasser, P. Core-Shell and Nanoporous Particle Architectures and Their Effect on the Activity and Stability of Pt ORR Electrocatalysts. *Top. Catal.* **2014**, *57* (1–

- 4), 236–244.
- (129) Chen, C.; Kang, Y.; Huo, Z.; Zhu, Z.; Huang, W.; Xin, H. L.; Snyder, J. D.; Li, D.; Herron, J. A.; Mavrikakis, M.; Chi, M.; More, K. L.; Li, Y.; Markovic, N. M.; Somorjai, G. A.; Yang, P.; Stamenkovic, V. R.; Samorjai, G. A.; Yang, P.; Stamenkovic, V. R.; Somorjai, G. A.; Yang, P.; Stamenkovic, V. R. Highly Crystalline Multimetallic Nanoframes with Three-Dimensional Electrocatalytic Surfaces. *Science* **2014**, *343*, 1339–1343.
- (130) Maillard, F.; Dubau, L.; Durst, J.; Chatenet, M.; André, J.; Rossinot, E. Durability of Pt<sub>3</sub>Co/C Nanoparticles in a Proton-Exchange Membrane Fuel Cell: Direct Evidence of Bulk Co Segregation to the Surface. *Electrochem. commun.* **2010**, *12* (9), 1161–1164.
- (131) Lopez-Haro, M.; Dubau, L.; Guétaz, L.; Bayle-Guillemaud, P.; André, J.; Caqué, N.; Rossinot, E.; Maillard, F. Atomic-Scale Structure and Composition of Pt<sub>3</sub>Co/C Nanocrystallites during a 3422 H PEMFC Aging Test: A STEM-EELS Study. *Appl. Catal. B Environ.* **2014**, *152–153*, 300–308.
- (132) Carlton, C. E.; Chen, S.; Ferreira, P. J.; Allard, L. F.; Shao-Horn, Y. Sub-Nanometer-Resolution Elemental Mapping of “Pt<sub>3</sub>Co” Nanoparticle Catalyst Degradation in Proton-Exchange Membrane Fuel Cells. *J. Phys. Chem. Lett.* **2012**, *3*, 161–166.
- (133) Durst, J.; Lopez-Haro, M.; Dubau, L.; Chatenet, M.; Soldo-Olivier, Y.; Guétaz, L.; Bayle-Guillemaud, P.; Maillard, F. Reversibility of Pt-Skin and Pt-Skeleton Nanostructures in Acidic Media. *J. Phys. Chem. Lett.* **2014**, *5*, 434–439.
- (134) Escudero-Escribano, M.; Malacrida, P.; Hansen, M. H.; Vej-Hansen, U. G.; Velázquez-Palenzuela, A.; Tripkovic, V.; Schiøtz, J.; Rossmeisl, J.; Stephens, I. E. L.; Chorkendorff, I. Tuning the Activity of Pt Alloy Electrocatalysts by Means of the Lanthanide Contraction. *Science (80-. )*. **2016**, *352* (6281), 73–76.
- (135) Escudero-Escribano, M.; Verdaguer-Casadevall, A.; Malacrida, P.; Grønbjerg, U.; Knudsen, B. P.; Jepsen, A. K.; Rossmeisl, J.; Stephens, I. E. L.; Chorkendorff, I. Pt<sub>5</sub>Gd as a Highly Active and Stable Catalyst for Oxygen Electroreduction. *J. Am. Chem. Soc.* **2012**, *134*, 16476–16479.
- (136) Čolić, V.; Bandarenka, A. S. Pt Alloy Electrocatalysts for the Oxygen Reduction Reaction: From Model Surfaces to Nanostructured Systems. *ACS Catal.* **2016**, *6* (8), 5378–5385.
- (137) Markovic, N. M.; Adzi, R. R.; Cahan, B. D.; Yeager, E. B. Structural Effects in Electrocatalysis: Oxygen Reduction on Platinum Low Index Single-Crystal Surfaces in Perchloric Acid Solutions. **1994**, *377*, 249–259.
- (138) Stamenkovic, V. R.; Fowler, B.; Mun, B. S.; Wang, G.; Ross, P. N.; Lucas, C. A.; Markovic, N. M. Improved Oxygen Reduction Activity on Pt<sub>3</sub>Ni (111) via Increased Surface Site Availability. *Science (80-. )*. **2007**, *315* (5811), 493–497.
- (139) Cui, C.; Gan, L.; Heggen, M.; Rudi, S.; Strasser, P. Compositional Segregation in Shaped Pt Alloy Nanoparticles and Their Structural Behaviour during Electrocatalysis. *Nat. Mater.* **2013**, *12* (8), 765–771.

## Chapter VII. References

- (140) Huang, X.; Zhao, Z.; Cao, L.; Chen, Y.; Zhu, E.; Lin, Z.; Li, M.; Yan, A.; Zettl, A.; Wang, Y. M.; Duan, X.; Mueller, T.; Huang, Y. High-Performance Transition Metal – Doped Pt<sub>3</sub>Ni Octahedra for Oxygen Reduction Reaction. *Science* (80-. ). **2015**, *348* (2009), 1230–1234.
- (141) Wu, J.; Gross, A.; Yang, H. Shape and Composition-Controlled Platinum Alloy Nanocrystals Using Carbon Monoxide as Reducing Agent. *Nano Lett.* **2011**, *11* (2), 798–802.
- (142) Fortunelli, A.; Goddard III, W. A.; Sementa, L.; Barcaro, G.; Negreiros, F. R.; Jaramillo-Botero, A. The Atomistic Origin of the Extraordinary Oxygen Reduction Activity of Pt<sub>3</sub>Ni<sub>7</sub> Fuel Cell Catalysts. *Chem. Sci.* **2015**, *6* (7), 3915–3925.
- (143) Li, M.; Zhao, Z.; Cheng, T.; Fortunelli, A.; Chen, C.-Y.; Yu, R.; Zhang, Q.; Gu, L.; Merinov, B. V.; Lin, Z.; Zhu, E.; Yu, T.; Jia, Q.; Guo, J.; Zhang, L.; Goddard, W. A.; Huang, Y.; Duan, X. Ultrafine Jagged Platinum Nanowires Enable Ultrahigh Mass Activity for the Oxygen Reduction Reaction. *Science* (80-. ). **2016**, *354* (6318), 1414–1419.
- (144) Lebedeva, N. P.; Rodes, A.; Feliu, J. M.; Koper, M. T. M.; van Santen, R. A. Role of Crystalline Defects in Electrocatalysis: CO Adsorption and Oxidation on Stepped Platinum Electrodes As Studied by in Situ Infrared Spectroscopy. *J. Phys. Chem. B* **2002**, *106* (38), 9863–9872.
- (145) Lebedeva, N. P.; Koper, M. T. M.; Feliu, J. M.; Van Santen, R. Role of Crystalline Defects in Electrocatalysis: Mechanism and Kinetics of CO Adlayer Oxidation on Stepped Platinum Electrodes. *J. Phys. Chem. B* **2002**, *106* (50), 12938–12947.
- (146) Lebedeva, N. .; Koper, M. T. .; Feliu, J. .; Van Santen, R. Mechanism and Kinetics of the Electrochemical CO Adlayer Oxidation on Pt(111). *J. Electroanal. Chem.* **2002**, *524–525*, 242–251.
- (147) Lebedeva, N. P.; Koper, M. T. M.; Herrero, E.; Feliu, J. .; Van Santen, R. Cooxidation on Stepped Pt[n(111)×(111)] Electrodes. *J. Electroanal. Chem.* **2000**, *487* (1), 37–44.
- (148) Cherstiouk, O. V.; Simonov, P. A.; Savinova, E. R. Model Approach to Evaluate Particle Size Effects in Electrocatalysis: Preparation and Properties of Pt Nanoparticles Supported on GC and HOPG. *Electrochim. Acta* **2003**, *48*, 3851–3860.
- (149) Maillard, F.; Schreier, S.; Hanzlik, M.; Savinova, E. R.; Weinkauf, S.; Stimming, U. Influence of Particle Agglomeration on the Catalytic Activity of Carbon-Supported Pt Nanoparticles in CO Monolayer Oxidation. *Phys. Chem. Chem. Phys.* **2005**, *7* (2), 385–393.
- (150) Hitotsuyanagi, A.; Nakamura, M.; Hoshi, N. Structural Effects on the Activity for the Oxygen Reduction Reaction on n(111)–(100) Series of Pt: Correlation with the Oxide Film Formation. *Electrochim. Acta* **2012**, *82*, 512–516.
- (151) Kuzume, A.; Herrero, E.; Feliu, J. M. Oxygen Reduction on Stepped Platinum Surfaces in Acidic Media. *J. Electroanal. Chem.* **2007**, *599* (2), 333–343.
- (152) Bandarenka, A. S.; Hansen, H.; Rossmeisl, J.; Stephens, I. E. L. Elucidating the Activity of Stepped Pt Single Crystals for Oxygen Reduction. *Phys. Chem. Chem. Phys.* **2014**, *16* (27), 13625–13629.

## Chapter VII. References

- (153) Pohl, M. D.; Colic, V.; Scieszka, D.; Bandarenka, A. S. Elucidation of Adsorption Processes at the Surface of Pt(331) Model Electrocatalysts in Acidic Aqueous Media. *Phys. Chem. Chem. Phys.* **2016**, *18*, 10792–10799.
- (154) Casalongue, H. S.; Kaya, S.; Viswanathan, V.; Miller, D. J.; Friebel, D.; Hansen, H.; Nørskov, J. K.; Nilsson, A.; Ogasawara, H. Direct Observation of the Oxygenated Species during Oxygen Reduction on a Platinum Fuel Cell Cathode. *Nat. Commun.* **2013**, *4* (May), 2817–2823.
- (155) Calle-Vallejo, F.; Martínez, J. I.; García-Lastra, J. M.; Sautet, P.; Loffreda, D. Fast Prediction of Adsorption Properties for Platinum Nanocatalysts with Generalized Coordination Numbers. *Angew. Chem., Int. Ed.* **2014**, *53* (32), 8316–8319.
- (156) Calle-Vallejo, F.; Tymoczko, J.; Colic, V.; Vu, Q. H.; Pohl, M. D.; Morgenstern, K.; Loffreda, D.; Sautet, P.; Schuhmann, W.; Bandarenka, A. S. Finding Optimal Surface Sites on Heterogeneous Catalysts by Counting Nearest Neighbors. *Science (80-. )*. **2015**, *350* (6257), 185–189.
- (157) Le Bacq, O.; Pasturel, A.; Chattot, R.; Previdello, B.; Nelayah, J.; Asset, T.; Dubau, L.; Maillard, F. Effect of Atomic Vacancies on the Structure and the Electrocatalytic Activity of Pt-rich/C Nanoparticles: A Combined Experimental and Density Functional Theory Study. *ChemCatChem* **2017**, *9*, 2324–2338.
- (158) van der Vliet, D. F.; Wang, C.; Tripkovic, D.; Strmcnik, D.; Zhang, X. F.; Debe, M. K.; Atanoski, R. T.; Markovic, N. M.; Stamenkovic, V. R. Mesostructured Thin Films as Electrocatalysts with Tunable Composition and Surface Morphology. *Nat. Mater.* **2012**, *11* (12), 1051–1058.
- (159) Henning, S.; Kühn, L.; Herranz, J.; Durst, J.; Binninger, T.; Nachttegaal, M.; Werheid, M.; Liu, W.; Adam, M.; Kaskel, S.; Eychmüller, A.; Schmidt, T. J. Pt-Ni Aerogels as Unsupported Electrocatalysts for the Oxygen Reduction Reaction. *J. Electrochem. Soc.* **2016**, *163*, F998–F1003.
- (160) Henning, S.; Ishikawa, H.; Kuhn, L.; Herranz, J.; Müller, E.; Eychmüller, A.; Schmidt, T. J. Unsupported Pt-Ni Aerogels with Enhanced High Current Performance and Durability in Fuel Cell Cathodes. *Angew. Chemie Int. Ed.* **2017**.
- (161) Liu, W.; Rodriguez, P.; Borchardt, L.; Foelske, A.; Yuan, J.; Herrmann, A. K.; Geiger, D.; Zheng, Z.; Kaskel, S.; Gaponik, N.; Kötz, R.; Schmidt, T. J.; Eychmüller, A. Bimetallic Aerogels: High-Performance Electrocatalysts for the Oxygen Reduction Reaction. *Angew. Chemie - Int. Ed.* **2013**, *52*, 9849–9852.
- (162) Liu, W.; Herrmann, A. K.; Bigall, N. C.; Rodriguez, P.; Wen, D.; Oezaslan, M.; Schmidt, T. J.; Gaponik, N.; Eychmüller, A. Noble Metal Aerogels-Synthesis, Characterization, and Application as Electrocatalysts. *Acc. Chem. Res.* **2015**, *48*, 154–162.
- (163) Lim, B.; Jiang, M.; Camargo, P. H. C.; Cho, E. C.; Tao, J.; Lu, X.; Zhu, Y.; Xia, Y. Pd-Pt Bimetallic Nanodendrites with High Activity for the Oxygen Reduction. *Science (80-. )*. **2009**,

- 324, 1302–1305.
- (164) Liang, H. W.; Cao, X.; Zhou, F.; Cui, C. H.; Zhang, W. J.; Yu, S. H. A Free-Standing Pt-Nanowire Membrane as a Highly Stable Electrocatalyst for the Oxygen Reduction Reaction. *Adv. Mater.* **2011**, *23* (12), 1467–1471.
- (165) Kibsgaard, J.; Gorlin, Y.; Chen, Z.; Jaramillo, T. F. Meso-Structured Platinum Thin Films : Active and Stable Electrocatalysts for the Oxygen Reduction Reaction. **2012**, 1–4.
- (166) Kongkanand, A.; Kuwabata, S.; Girishkumar, G.; Kamat, P. Single-Wall Carbon Nanotubes Supported Platinum Nanoparticles with Improved Electrocatalytic Activity for Oxygen Reduction Reaction. *Langmuir* **2006**, *22* (5), 2392–2396.
- (167) Cavaliere, S.; Subianto, S.; Chevallier, L.; Jones, D. J.; Rozière, J. Single Step Elaboration of Size-Tuned Pt Loaded Titania Nanofibres. *Chem. Commun. (Camb)*. **2011**, *47* (24), 6834–6836.
- (168) Cavaliere, S.; Subianto, S.; Savych, I.; Tillard, M.; Jones, D. J.; Rozière, J. Dopant-Driven Nanostructured Loose-Tube SnO<sub>2</sub> Architectures: Alternative Electrocatalyst Supports for Proton Exchange Membrane Fuel Cells. *J. Phys. Chem. C* **2013**, *117* (36), 18298–18307.
- (169) Cognard, G.; Ozouf, G.; Beauger, C.; Berthomé, G.; Riassetto, D.; Dubau, L.; Chattot, R.; Chatenet, M.; Maillard, F. Benefits and Limitations of Pt Nanoparticles Supported on Highly Porous Antimony-Doped Tin Dioxide Aerogel as Alternative Cathode Material for Proton-Exchange Membrane Fuel Cells. *Appl. Catal. B Environ.* **2017**, *201*, 381–390.
- (170) Fabbri, E.; Rabis, A.; Kötz, R.; Schmidt, T. J. Pt Nanoparticles Supported on Sb-Doped SnO<sub>2</sub> Porous Structures: Developments and Issues. *Phys. Chem. Chem. Phys.* **2014**, *16* (27), 13672–13681.
- (171) Rouquerol, J.; Avnir, D.; Fairbridge, C. W.; Everett, D. H.; Haynes, J. H.; Pernicone, N.; Ramsay, J. D. F.; Sind, K. S. W.; Unger, K. K. Recommendation for the Porous Solids. *Pure Appl. Chem.* **1994**, *66* (8), 1739–1758.
- (172) Ferrari, A. C.; Robertson, J. Interpretation of Raman Spectra of Disordered and Amorphous Carbon. *Phys. Rev. B* **2000**, *61* (20), 14095–14107.
- (173) Cherstiouk, O. V.; Simonov, A. N.; Moseva, N. S.; Cherepanova, S. V.; Simonov, P. A.; Zaikovskii, V. I.; Savinova, E. R. Microstructure Effects on the Electrochemical Corrosion of Carbon Materials and Carbon-Supported Pt Catalysts. *Electrochim. Acta* **2010**, *55* (28), 8453–8460.
- (174) Katsnelson, M. I. Graphene: Carbon in Two Dimensions. *Mater. Today* **2007**, *10* (1–2), 20–27.
- (175) Guo, H.; Wang, X.; Qian, Q.; Wang, F.; Xia, X. A Green Approach to the Synthesis of Graphene Nanosheets. *ACS Nano* **2009**, *3* (9), 2653–2659.
- (176) Kinoshita, K. *Carbon - Electrochemical and Physicochemical Properties*, John Wiley.; John Wiley & Sons: New York, 1987.
- (177) Wissler, M. Graphite and Carbon Powders for Electrochemical Applications. *J. Power Sources* **2006**, *156* (2), 142–150.

## Chapter VII. References

- (178) Maillard, F.; Simonov, P. A.; Savinova, E. R. Carbon Materials as Supports for Fuel Cells Electrocatalysts. In *Carbon Materials for Catalysis*; Serp, P., Figueiredo, J. L., Eds.; Hoboken, 2009; pp 439–480.
- (179) Rodríguez-Reinoso, F. The Role of Carbon Materials in Heterogeneous Catalysis. *Carbon N. Y.* **1998**, *36* (3), 159–175.
- (180) Iijima, S. Helical Microtubes of Graphitic Carbon. *Nature* **1991**, *354*, 56–58.
- (181) Radushkevich, L. V.; Lukyanovich, V. M. O Strukture Ugleroda, Obrazujucesja Pri Termiceskom Razlozenii Okisi Ugleroda Na Zeleznom Kontakte. *Zurn Fis. Chim* **1952**, *26*, 88–95.
- (182) Thostenson, E. T.; Ren, Z.; Chou, T.-W. Advances in the Science and Technology of Carbon Nanotubes and Their Composites: A Review. *Compos. Sci. Technol.* **2001**, *61* (13), 1899–1912.
- (183) Andersen, N. I.; Serov, A.; Atanassov, P. Metal oxides/CNT Nano-Composite Catalysts for Oxygen Reduction/oxygen Evolution in Alkaline Media. *Appl. Catal. B Environ.* **2015**, *163*, 623–627.
- (184) Pekala, R. W. Organic Aerogels from the Polycondensation of Resorcinol with Formaldehyde. *J. Mater. Sci.* **1989**, *24* (9), 3221–3227.
- (185) Job, N.; Pirard, R.; Marien, J.; Pirard, J. P. Porous Carbon Xerogels with Texture Tailored by pH Control during Sol-Gel Process. *Carbon N. Y.* **2004**, *42* (3), 619–628.
- (186) Job, N.; Théry, A.; Pirard, R.; Marien, J.; Kocon, L.; Rouzaud, J. N.; Béguin, F.; Pirard, J. P. Carbon Aerogels, Cryogels and Xerogels: Influence of the Drying Method on the Textural Properties of Porous Carbon Materials. *Carbon N. Y.* **2005**, *43* (12), 2481–2494.
- (187) Piedboeuf, M. L. C.; Léonard, A. F.; Traina, K.; Job, N. Influence of the Textural Parameters of Resorcinol-Formaldehyde Dry Polymers and Carbon Xerogels on Particle Sizes upon Mechanical Milling. *Colloids Surfaces A Physicochem. Eng. Asp.* **2015**, *471*, 124–132.
- (188) Kinoshita, K.; Bett, J. Electrochemical Oxidation of Carbon Black in Concentrated Phosphoric Acid at 135 °C. *Carbon N. Y.* **1973**, *11* (3), 237–247.
- (189) Donnet, J. B.; Ehrburger, P.; Voet, A. Etude Du Mécanisme d'Oxydation Des Noirs de Carbone Par l'Ozone En Milieu Aqueux. *Carbon N. Y.* **1972**, *10* (6), 737–746.
- (190) Mathias, M. F.; Makharia, R.; Gasteiger, H. a.; Conley, J. J.; Fuller, T. J.; Gittleman, C. J.; Kocha, S. S.; Miller, D. P.; Mittelsteadt, C. K.; Xie, T.; Yan, S. G.; Yu, P. T. Two Fuel Cell Cars in Every Garage? *Electrochem. Soc. Interface* **2005**, *14*, 24–35.
- (191) Makharia, R.; Kocha, S.; Yu, P.; Sweikart, M. A.; Gu, W.; Wagner, F.; Gasteiger, H. A. Durable PEM Fuel Cell Electrode Materials: Requirements and Benchmarking Methodologies. *ECS Trans.* **2006**, *1* (8), 3–18.
- (192) Artyushkova, K.; Pylypenko, S.; Dowlapalli, M.; Atanassov, P. Structure-to-Property Relationships in Fuel Cell Catalyst Supports: Correlation of Surface Chemistry and Morphology with Oxidation Resistance of Carbon Blacks. *J. Power Sources* **2012**, *214*, 303–313.

## Chapter VII. References

- (193) Castanheira, L.; Dubau, L.; Mermoux, M.; Berthome, G.; Caque, N.; Rossinot, E.; Chatenet, M.; Maillard, F. Carbon Corrosion in Proton-Exchange Membrane Fuel Cells: From Model Experiments to Real-Life Operation in Membrane Electrode Assemblies. *ACS Catal.* **2014**, *4*, 2258–2267.
- (194) Passalacqua, E.; Antonucci, P. L.; Vivaldi, M.; Patti, A.; Antonucci, V.; Giordano, N.; Kinoshita, K. The Influence of Pt on the Electrooxidation Behaviour of Carbon in Phosphoric Acid. *Electrochim. Acta* **1992**, *37* (15), 2725–2730.
- (195) Linse, N.; Gubler, L.; Scherer, G. G.; Wokaun, A. The Effect of Platinum on Carbon Corrosion Behavior in Polymer Electrolyte Fuel Cells. *Electrochim. Acta* **2011**, *56* (22), 7541–7549.
- (196) Maillard, F.; Bonnefont, A.; Micoud, F. An EC-FTIR Study on the Catalytic Role of Pt in Carbon Corrosion. *Electrochem. Commun.* **2011**, *13* (10), 1109–1111.
- (197) Sihvonen, V. The Influence Of Keto- And Ketene Groups, Adsorbed Molecules And Ions On The Mechanism Of Carbon Oxidation. *Faraday Soc.* **1938**, *34*, 1062–1074.
- (198) Borup, R.; Meyers, J.; Pivovar, B.; Kim, Y. S.; Mukundan, R.; Garland, N.; Myers, D.; Wilson, M.; Garzon, F.; Wood, D.; Zelenay, P.; More, K.; Stroh, K.; Zawodzinski, T.; Boncella, J.; Mcgrath, J. E.; Inaba, M.; Miyatake, K.; Hori, M.; Ota, K.; Ogumi, Z.; Miyata, S.; Nishikata, A.; Siroma, Z.; Uchimoto, Y.; Yasuda, K.; Kimijima, K.; Iwashita, N. Scientific Aspects of Polymer Electrolyte Fuel Cell Durability and Degradation. *Chem. Rev.* **2007**, *107*, 3904–3951.
- (199) Shao-Horn, Y.; Sheng, W. C.; Chen, S.; Ferreira, P. J.; Holby, E. F.; Morgan, D. Instability of Supported Platinum Nanoparticles in Low-Temperature Fuel Cells. *Top. Catal.* **2007**, *46* (3–4), 285–305.
- (200) Ferreira, P. J.; la O', G. J.; Shao-Horn, Y.; Morgan, D.; Makharia, R.; Kocha, S.; Gasteiger, H. a. Instability of Pt/C Electrocatalysts in Proton Exchange Membrane Fuel Cells. *J. Electrochem. Soc.* **2005**, *152* (11), A2256–A2271.
- (201) Meier, J. C.; Galeano, C.; Katsounaros, I.; Topalov, A. A.; Kostka, A.; Schu, F.; Mayrhofer, K. J. J. Degradation Mechanisms of Pt/C Fuel Cell Catalysts under Simulated Start – Stop Conditions. **2012**.
- (202) Sheng, W.; Chen, S.; Vescovo, E.; Shao-Horn, Y. Size Influence on the Oxygen Reduction Reaction Activity and Instability of Supported Pt Nanoparticles. *J. Electrochem. Soc.* **2012**, *159* (2), B96.
- (203) Castanheira, L.; Dubau, L.; Maillard, F. Accelerated Stress Tests of Pt/HSAC Electrocatalysts: An Identical-Location Transmission Electron Microscopy Study on the Influence of Intermediate Characterizations. *Electrocatalysis* **2014**, *5* (2), 125–135.
- (204) Perez-Alonso, F. J.; Elkjær, C. F.; Shim, S. S.; Abrams, B. L.; Stephens, I. E. L.; Chorkendorff, I. B. Identical Locations Transmission Electron Microscopy Study of Pt/C Electrocatalyst Degradation during Oxygen Reduction Reaction. *J. Power Sources* **2011**, *196* (15), 6085–6091.
- (205) Topalov, A. A.; Katsounaros, I.; Auinger, M.; Cherevko, S.; Meier, J. C.; Klemm, S. O.;

## Chapter VII. References

- Mayrhofer, K. J. J. Dissolution of Platinum: Limits for the Deployment of Electrochemical Energy Conversion? *Angew. Chemie - Int. Ed.* **2012**, *51* (50), 12613–12615.
- (206) Dubau, L.; Castanheira, L.; Berthomé, G.; Maillard, F. An Identical-Location Transmission Electron Microscopy Study on the Degradation of Pt/C Nanoparticles under Oxidizing, Reducing and Neutral Atmosphere. *Electrochim. Acta* **2013**, *110*, 273–281.
- (207) Darling, R., Meyers, J. Kinetic Model of Platinum Dissolution in PEMFCs. *J. Electrochem. Soc.* **2003**, *150*, A1523–A1527.
- (208) Ohma, A.; Shinohara, K.; Iiyama, A.; Yoshida, T.; Daimaru, A. Membrane and Catalyst Performance Targets for Automotive Fuel Cells by FCCJ Membrane, Catalyst, MEA WG. *ECS Trans.* **2010**, *41* (1), 775–784.
- (209) Ruge, M.; Drnec, J.; Rahn, B.; Reikowski, F.; Harrington, D. A.; Carla, F.; Felici, R.; Stettner, J.; Magnussen, O. M. Structural Reorganization of Pt(111) Electrodes by Electrochemical Oxidation and Reduction. *J. Am. Chem. Soc.* **2017**, *139* (12), 4532–4539.
- (210) Drnec, J.; Ruge, M.; Reikowski, F.; Rahn, B.; Carla, F.; Felici, R.; Stettner, J.; Magnussen, O. M.; Harrington, D. A. Initial Stages of Pt(111) Electrooxidation: Dynamic and Structural Studies by Surface X-Ray Diffraction. *Electrochim. Acta* **2017**, *224*, 220–227.
- (211) Conway, B. E. Electrochemical At Noble Metals Oxide Film Formation As a Surface-Chemical Process. *Prog. Surf. Sci.* **1995**, *49* (95), 331–452.
- (212) Jerkiewicz, G.; Vatankhah, G.; Lessard, J.; Soriaga, M. P.; Park, Y. S. Surface-Oxide Growth at Platinum Electrodes in Aqueous H<sub>2</sub>SO<sub>4</sub> Reexamination of Its Mechanism through Combined Cyclic-Voltammetry, Electrochemical Quartz-Crystal Nanobalance, and Auger Electron Spectroscopy Measurements. *Electrochim. Acta* **2004**, *49* (9–10), 1451–1459.
- (213) Birss, V. I.; Chang, M.; Segal, J. Platinum Oxide Film Formation-Reduction : Measurement Study an in-Situ Mass Measurement Study. *J. Electroanal. Chem.* **1993**, *355*, 181.
- (214) Yu, Y.; Xin, H. L.; Hovden, R.; Wang, D.; Rus, E. D.; Mundy, J. A.; Muller, D. A.; Abruna, H. D. Three-Dimensional Tracking and Visualization of Hundreds of Pt – Co Fuel Cell Nanocatalysts During Electrochemical Aging. *Nano Lett.* **2011**, *12* (9), 4417–4423.
- (215) Dubau, L.; Lopez-Haro, M.; Castanheira, L.; Durst, J.; Chatenet, M.; Bayle-Guillemaud, P.; Guétaz, L.; Caqué, N.; Rossinot, E.; Maillard, F. Probing the Structure, the Composition and the ORR Activity of Pt<sub>3</sub>Co/C Nanocrystallites during a 3422h PEMFC Ageing Test. *Appl. Catal., B* **2013**, *142–143*, 801–808.
- (216) Dubau, L.; Durst, J.; Maillard, F.; Guétaz, L.; Chatenet, M.; André, J.; Rossinot, E. Further Insights into the Durability of Pt<sub>3</sub>Co/C Electrocatalysts: Formation of “hollow” Pt Nanoparticles Induced by the Kirkendall Effect. *Electrochim. Acta* **2011**, *56* (28), 10658–10667.
- (217) Dubau, L.; Maillard, F.; Chatenet, M.; Guetaz, L.; André, J.; Rossinot, E. Durability of Pt[sub 3]Co/C Cathodes in a 16 Cell PEMFC Stack: Macro/Microstructural Changes and Degradation Mechanisms. *J. Electrochem. Soc.* **2010**, *157* (12), B1887.

## Chapter VII. References

- (218) Lopez-Haro, M.; Dubau, L.; Guétaz, L.; Bayle-Guillemaud, P.; Chatenet, M.; André, J.; Caqué, N.; Rossinot, E.; Maillard, F. Atomic-Scale Structure and Composition of Pt<sub>3</sub>Co/C Nanocrystallites during Real PEMFC Operation: A STEM–EELS Study. *Appl. Catal. B Environ.* **2014**, *152–153*, 300–308.
- (219) Yin, Y.; Rioux, R. M.; Erdonmez, C. K.; Hughes, S.; Somorjai, G.; Alivisatos, A. P. Formation of Hollow Nanocrystals through the Nanoscale Kirkendall Effect. *Science* **2004**, *304*, 711–714.
- (220) Yin, Y.; Erdonmez, C. K.; Cabot, A.; Hughes, S.; Alivisatos, A. P. Colloidal Synthesis of Hollow Cobalt Sulfide Nanocrystals. *Adv. Funct. Mater.* **2006**, *16* (11), 1389–1399.
- (221) Cabot, A.; Iba, M.; Guardia, P.; Alivisatos, A. P. Reaction Regimes on the Synthesis of Hollow Particles by the Kirkendall. *J. Am. Chem. Soc.* **2009**, *131*, 11326–11328.
- (222) Nakajima, H. The Discovery and Acceptance of the Kirkendall Effect : The Result of a Short Research Career. *JOM* **2011**, *49* (6), 15–19.
- (223) Wang, J. X.; Ma, C.; Choi, Y.; Su, D.; Zhu, Y.; Liu, P.; Si, R.; Vukmirovic, M. B.; Zhang, Y.; Adzic, R. R. Kirkendall Effect and Lattice Contraction in Nanocatalysts: A New Strategy to Enhance Sustainable Activity. *J. Am. Chem. Soc.* **2011**, *133* (34), 13551–13557.
- (224) González, E.; Arbiol, J.; Puentes, V. F. Carving at the Nanoscale: Sequential Galvanic Exchange and Kirkendall Growth at Room Temperature. *Science* **2011**, *334* (6061), 1377–1380.
- (225) Shan, A.; Chen, Z.; Li, B.; Chen, C.; Wang, R. Monodispersed, Ultrathin NiPt Hollow Nanospheres with Tunable Diameter and Composition via a Green Chemical Synthesis. *J. Mater. Chem. A* **2015**, *3* (3), 1031–1036.
- (226) Sun, Y.; Xia, Y. Shape-Controlled Synthesis of Gold and Silver Nanoparticles. *Science* **2002**, *298* (5601), 2176–2179.
- (227) Zhang, L.; Roling, L. T.; Wang, X.; Vara, M.; Chi, M.; Liu, J.; Choi, S.; Park, J.; Herron, J. A.; Xie, Z.; Mavrikakis, M.; Xia, Y. Platinum Based Nanocages with Subnanometer-Thick Walls and Well Defined, Controllable Facets. *Science* **2015**, *349* (6246), 412–416.
- (228) Sun, Y.; Mayers, B.; Xia, Y. Metal Nanostructures with Hollow Interiors. *Adv. Mater.* **2003**, *15* (78), 641–646.
- (229) Chen, G.; Xia, D.; Nie, Z.; Wang, Z.; Wang, L.; Zhang, L. Facile Synthesis of Co - Pt Hollow Sphere Electrocatalyst. **2007**, No. 3, 1840–1844.
- (230) Xia, X.; Wang, Y.; Ruditskiy, A.; Xia, Y. 25th Anniversary Article: Galvanic Replacement: A Simple and Versatile Route To Hollow Nanostructures With Tunable and Well-Controlled Properties. *Adv. Mater.* **2013**, *25* (44), 6313–6333.
- (231) Bae, S. J.; Yoo, S. J.; Lim, Y. Y.; Kim, S. S.-K.; Lim, Y. Y.; Choi, J.; Nahm, K. S.; Hwang, S. J.; Lim, T.-H.; Kim, S. S.-K.; Kim, P. Facile Preparation of Carbon-Supported PtNi Hollow Nanoparticles with High Electrochemical Performance. *J. Mater. Chem.* **2012**, *22* (18), 8820–8825.
- (232) Asset, T.; Chattot, R.; Nelayah, J.; Job, N.; Dubau, L.; Maillard, F. Structure-Activity

## Chapter VII. References

- Relationships for the Oxygen Reduction Reaction in Porous Hollow PtNi/C Nanoparticles. *ChemElectroChem* **2016**, 3 (10), 1591–1600.
- (233) Shan, A.; Cheng, M.; Fan, H.; Chen, Z.; Wang, R.; Chen, C. NiPt Hollow Nanocatalyst: Green Synthesis, Size Control and Electrocatalysis. *Prog. Nat. Sci. Mater. Int.* **2014**, 24 (2), 175–178.
- (234) Dubau, L.; Nelayah, J.; Moldovan, S.; Ersen, O.; Bordet, P.; Drnec, J.; Asset, T.; Chattot, R. R.; Maillard, F. F. Defects Do Catalysis: CO Monolayer Oxidation and Oxygen Reduction Reaction on Hollow PtNi/C Nanoparticles. *ACS Catal.* **2016**, 6 (7), 4673–4684.
- (235) Mori, D.; Hirose, K. Recent Challenges of Hydrogen Storage Technologies for Fuel Cell Vehicles. *Int. J. Hydrogen Energy* **2009**, 34, 4569–4574.
- (236) Ross, D. K. Hydrogen Storage: The Major Technological Barrier to the Development of Hydrogen Fuel Cell Cars. *Vacuum* **2006**, 80, 1084–1089.
- (237) Sharaf, O. Z.; Orhan, M. F. An Overview of Fuel Cell Technology: Fundamentals and Applications. *Renew. Sustain. Energy Rev.* **2014**, 32, 810–853.
- (238) Turner, J. A. Sustainable Hydrogen Production. *Science (80-. )*. **2004**, 305, 972–974.
- (239) Barbir, F. PEM Electrolysis for Production of Hydrogen from Renewable Energy Sources. *Sol. Energy* **2005**, 78 (5), 661–669.
- (240) Ursua, A.; Gandia, L. M.; Sanchis, P. Hydrogen Production From Water Electrolysis: Current Status and Future Trends. *Proc. IEEE* **2012**, 100, 410–426.
- (241) Kraysberg, A.; Ein-Eli, Y. Review of Advanced Materials for Proton Exchange Membrane Fuel Cells. *Energy & Fuels* **2014**, 28, 7303–7330.
- (242) Peighambardoust, S. J.; Rowshanzamir, S.; Amjadi, M. *Review of the Proton Exchange Membranes for Fuel Cell Applications*; Elsevier Ltd, 2010; Vol. 35.
- (243) Dubau, L.; Castanheira, L.; Maillard, F.; Chatenet, M.; Lottin, O.; Maranzana, G.; Dillet, J.; Lamibrac, A.; Perrin, J.-C. C.; Moukheiber, E.; Elkaddouri, A.; De Moor, G.; Bas, C.; Flandin, L.; Caqué, N. A Review of PEM Fuel Cell Durability: Materials Degradation, Local Heterogeneities of Aging and Possible Mitigation Strategies. *Wiley Interdiscip. Rev. Energy Environ.* **2014**, 3 (6), 540–560.
- (244) Oezaslan, M.; Hasché, F.; Strasser, P. Pt-Based Core-Shell Catalyst Architectures for Oxygen Fuel Cell Electrodes. *J. Phys. Chem. Lett.* **2013**, 4 (19), 3273–3291.
- (245) Liang, H.-P. P.; Zhang, H.-M. M.; Hu, J.-S. S.; Guo, Y.-G. G.; Wan, L.-J. J.; Bai, C.-L. L. Pt Hollow Nanospheres: Facile Synthesis and Enhanced Electrocatalysts. *Angew. Chemie - Int. Ed.* **2004**, 43 (12), 1540–1543.
- (246) Liang, H.-P.; Guo, Y.-G.; Zhang, H.-M.; Hu, J.-S.; Wan, L.-J.; Bai, C.-L. Controllable AuPt Bimetallic Hollow Nanostructures. *Chem. Commun. (Camb)*. **2004**, No. 13, 1496–1497.
- (247) Chattot, R.; Asset, T.; Bordet, P.; Drnec, J.; Dubau, L.; Maillard, F. Beyond Alloying Effects: Microstrain-Induced Enhancement of the Oxygen Reduction Reaction Kinetics on Various PtNi/C Nanostructures. *ACS Catal.* **2017**, 7 (1), 398–408.

## Chapter VII. References

- (248) Kabir, S.; Serov, A.; Atanassov, P. Palladium Nanoparticles Supported on 3D-Graphene Nanosheets for Oxygen Reduction Reactions in Alkaline Media. *ECS Trans.* **2016**, 72 (29), 39–47.
- (249) Kabir, S.; Serov, A.; Artyushkova, K.; Atanassov, P. Design of Novel Graphene Materials as a Support for Palladium Nanoparticles: Highly Active Catalysts towards Ethanol Electrooxidation. *Electrochim. Acta* **2016**, 203, 144–153.
- (250) Serov, A.; Andersen, N. I.; Kabir, S. A.; Roy, A.; Asset, T.; Chatenet, M.; Maillard, F.; Atanassov, P. Palladium Supported on 3D Graphene as an Active Catalyst for Alcohols Electrooxidation. *J. Electrochem. Soc.* **2015**, 162 (12), F1305–F1309.
- (251) Pylypenko, S.; Mukherjee, S.; Olson, T. S.; Atanassov, P. Non-Platinum Oxygen Reduction Electrocatalysts Based on Pyrolyzed Transition Metal Macrocycles. *Electrochim. Acta* **2008**, 53 (27), 7875–7883.
- (252) Serov, A.; Artyushkova, K.; Andersen, N. I.; Stariha, S.; Atanassov, P. Original Mechanochemical Synthesis of Non-Platinum Group Metals Oxygen Reduction Reaction Catalysts Assisted by Sacrificial Support Method. *Electrochim. Acta* **2015**, 179, 154–160.
- (253) Hummers Jr, W. S.; Offeman, R. E. Preparation of Graphitic Oxide. *J. Am. Chem. Soc.* **1958**, 80 (6), 1339–1339.
- (254) Shinozaki, K.; Zack, J. W.; Richards, R. M.; Pivovar, B. S.; Kocha, S. S. Oxygen Reduction Reaction Measurements on Platinum Electrocatalysts Utilizing Rotating Disk Electrode Technique. *J. Electrochem. Soc.* **2015**, 162 (10), F1144–F1158.
- (255) Markovic, N. M.; Marinkovic, N. S.; Adzic, R. R. Electrosorption of Hydrogen and Sulphuric Acid Anions on Single-Crystal Platinum Stepped Surfaces. Part I. The [110] Zone. *J. Electroanal. Chem.* **1988**, 241 (1–2), 309–328.
- (256) Markovic, N. M.; Marinkovic, N. S.; Adzic, R. R. Electrosorption of Hydrogen and Sulfuric Acid Anions on Single Crystal Platinum Stepped Surfaces. Part II. The [1-10] Zone. *J. Electroanal. Chem.* **1991**, 314 (1–2), 289–306.
- (257) Herrmann, C.; Perrault, G.; Pilla, A. Dual Reference Electrode for Electrochemical Pulse Studies. *Anal. Chem.* **1968**, 40 (7), 1173–1174.
- (258) Castanheira, L. *Corrosion of High Surface Area Carbon Supports Used in Proton Exchange Membrane Fuel Cell Electrodes*; 2014.
- (259) Garsany, Y.; Baturina, O. A.; Swider-Lyons, K. E.; Kocha, S. S. Experimental Methods for Quantifying the Activity of Platinum Electrocatalysts for the Oxygen Reduction Reaction. *Anal. Chem.* **2010**, 82 (15), 6321–6328.
- (260) Garsany, Y.; Singer, I. L.; Swider-Lyons, K. E. Impact of Film Drying Procedures on RDE Characterization of Pt/VC Electrocatalysts. *J. Electroanal. Chem.* **2011**, 662 (2), 396–406.
- (261) Strmcnik, D.; Tripkovic, D.; van der Vliet, D.; Stamenkovic, V.; Marković, N. M. Adsorption of Hydrogen on Pt(1 1 1) and Pt(1 0 0) Surfaces and Its Role in the HOR. *Electrochem. commun.*

- 2008**, *10* (10), 1602–1605.
- (262) Markovic, N. M.; Gasteiger, H.; Ross, P. N. Oxygen Reduction on Platinum Low-Index Single-Crystal Surfaces in Sulfuric Acid Solution: Rotating Ring-Pt(hkl) Disk Studies. *J. Phys. Chem.* **1995**, *99* (11), 3411–3416.
- (263) Maillard, F.; Pronkin, S.; Savinova, E. R. Size Effects in Electrocatalysis of Fuel Cells Reactions on Supported Metal Nanoparticles. In *Fuel cell catalysis: a surface science approach*; Koper, M. T. M., Ed.; John Wiley & Sons, Inc.: New York, 2009; pp 507–566.
- (264) Maillard, F.; Savinova, E. R.; Stimming, U. CO Monolayer Oxidation on Pt Nanoparticles: Further Insights into the Particle Size Effects. *J. Electroanal. Chem.* **2007**, *599* (2), 221–232.
- (265) Maillard, F.; Eikerling, M.; Cherstiouk, O. V.; Schreier, S.; Savinova, E.; Stimming, U. Size Effects on Reactivity of Pt Nanoparticles in CO Monolayer Oxidation: The Role of Surface Mobility. *Faraday Discuss.* **2004**, *125*, 357–377.
- (266) Yeager, E.; O’Grady, W. E.; Woo, M. Y. C.; Hagans, P. Hydrogen Adsorption on Single Crystal Platinum. *J. Electrochem. Soc.* **1978**, *125*, 348–349.
- (267) Clavilier, J.; Faure, R.; Guinet, G.; Durand, R. Preparation of Monocrystalline Pt Microelectrodes and Electrochemical Study of the Plane Surfaces Cut in the Direction of the {111} and {110} Planes. *J. Electroanal. Chem.* **1979**, *107*, 205–209.
- (268) Clavilier, J. The Role of Anion of the Electrochemical Behaviour of a (111) Platinum Surface: An Unusual Splitting of the Voltammogram in the Hydrogen Region. *J. Electroanal. Chem.* **1980**, *107*, 211–216.
- (269) Clavilier, J.; Armand, D.; Sun, S. G.; Petit, M. Electrochemical Adsorption Behaviour of Platinum Stepped Surfaces in Sulphuric Acid Solutions. *J. Electroanal. Chem.* **1986**, *205*, 267–277.
- (270) Marković, N. M.; Grgur, B. N.; Ross, P. N. Temperature-Dependent Hydrogen Electrochemistry on Platinum Low-Index Single-Crystal Surfaces in Acid Solutions. *J. Phys. Chem. B* **1997**, *101* (27), 5405–5413.
- (271) Bandarenka, A. S.; Varela, A. S.; Karamad, M.; Calle-Vallejo, F.; Bech, L.; Perez-Alonso, F. J.; Rossmeisl, J.; Stephens, I. E. L.; Chorkendorff, I. Design of an Active Site towards Optimal Electrocatalysis: Overlayers, Surface Alloys and near-Surface Alloys of Cu/Pt(111). *Angew. Chem., Int. Ed.* **2012**, *51* (47), 11845–11848.
- (272) Koper, M. T. M.; Lebedeva, N. P.; Hermse, C. G. M. Dynamics of CO at the Solid/Liquid Interface Studied by Modeling and Simulation of CO Electro-Oxidation on Pt and PtRu Electrodes. *Faraday Discuss.* **2002**, *121*, 301–311.
- (273) Calle-Vallejo, F.; Pohl, M. D.; Bandarenka, A. S. Quantitative Coordination–Activity Relations for the Design of Enhanced Pt Catalysts for CO Electro-Oxidation. *ACS Catal.* **2017**, *7* (7), 4355–4359.
- (274) Koper, M. T. M.; Jansen, A. P. J.; Van Santen, R. A.; Lukkien, J. J.; Hilbers, P. A. J. Monte Carlo

## Chapter VII. References

- Simulations of a Simple Model for the Electrocatalytic CO Oxidation on Platinum. *J. Chem. Phys.* **1998**, *109* (14), 6051–6062.
- (275) Arenz, M.; Mayrhofer, K. J. J.; Stamenkovic, V.; Blizanac, B. B.; Tomoyuki, T.; Ross, P. N.; Markovic, N. M. The Effect of the Particle Size on the Kinetics of CO Electrooxidation on High Surface Area Pt Catalysts. *J. Am. Chem. Soc.* **2005**, *127* (18), 6819–6829.
- (276) Maillard, F.; Savinova, E. R.; Simonov, P. A.; Zaikovskii, V. I.; Stimming, U. Infrared Spectroscopic Study of CO Adsorption and Electro-Oxidation on. *J. Phys. Chem. B* **2004**, *108*, 17893–17904.
- (277) Hodnik, N.; Baldizzone, C.; Cherevko, S.; Zeradjanin, A.; Mayrhofer, K. J. J. The Effect of the Voltage Scan Rate on the Determination of the Oxygen Reduction Activity of Pt/C Fuel Cell Catalyst. *Electrocatalysis* **2015**, *6*, 237–241.
- (278) Vidal-Iglesias, F. J.; Solla-Gullón, J.; Montiel, V.; Aldaz, A. Errors in the Use of the Koutecky-Levich Plots. *Electrochem. commun.* **2012**, *15* (1), 42–45.
- (279) Mayrhofer, K. J. J.; Strmcnik, D.; Blizanac, B. B.; Stamenkovic, V.; Arenz, M.; Markovic, N. M. Measurement of Oxygen Reduction Activities via the Rotating Disc Electrode Method: From Pt Model Surfaces to Carbon-Supported High Surface Area Catalysts. *Electrochim. Acta* **2008**, *53* (7), 3181–3188.
- (280) Dubau, L.; Maillard, F. Unveiling the Crucial Role of Temperature on the Stability of Oxygen Reduction Reaction Electrocatalysts. *Electrochem. commun.* **2016**, *63*, 65–69.
- (281) Brunauer, S.; Emmett, P. H.; Teller, E. Adsorption of Gases in Multimolecular Layers. *J. Am. Chem. Soc.* **1938**, *60* (2), 309–319.
- (282) Lippens, B. C.; de Boer, J. H. Studies on Pore Systems in Catalysts: V. The T Method. *J. Catal.* **1965**, *4* (3), 319–323.
- (283) de Boer, J. H.; Lippens, B. C.; Linsen, B. G.; Broekhoff, J. C. P.; van den Heuvel, A.; Osinga, T. J. Thet-Curve of Multimolecular N<sub>2</sub>-Adsorption. *J. Colloid Interface Sci.* **1966**, *21* (4), 405–414.
- (284) Mayrhofer, K. J. J.; Ashton, S. J.; Meier, J. C.; Wiberg, G. K. H.; Hanzlik, M.; Arenz, M. Non-Destructive Transmission Electron Microscopy Study of Catalyst Degradation under Electrochemical Treatment. *J. Power Sources* **2008**, *185* (2), 734–739.
- (285) Hartl, K.; Hanzlik, M.; Arenz, M. IL-TEM Investigations on the Degradation Mechanism of Pt/C Electrocatalysts with Different Carbon Supports. *Energy Environ. Sci.* **2011**, *4* (1), 234–238.
- (286) Schlögl, K.; Mayrhofer, K. J. J.; Hanzlik, M.; Arenz, M. Identical-Location TEM Investigations of Pt/C Electrocatalyst Degradation at Elevated Temperatures. *J. Electroanal. Chem.* **2011**, *662* (2), 355–360.
- (287) Lespade, P.; Marchand, A.; Couzi, M.; Cruege, F. Characterisation de Matériaux Carbones Par Microspectrométrie Raman. *Carbon N. Y.* **1984**, *22* (4–5), 375–385.
- (288) Sadezky, A.; Muckenhuber, H.; Grothe, H.; Niessner, R.; Pöschl, U. Raman Microspectroscopy

## Chapter VII. References

- of Soot and Related Carbonaceous Materials: Spectral Analysis and Structural Information. *Carbon N. Y.* **2005**, *43* (8), 1731–1742.
- (289) Knight, D. S.; White, W. B. Characterization of Diamond Films by Raman Spectroscopy. *J. Mater. Res.* **1989**, *4* (2), 385–393.
- (290) Vidano, R. P.; Fischbach, D. B.; Willis, L. J.; Loehr, T. M. Observation of Raman Band Shifting with Excitation Wavelength for Carbons and Graphites. *Solid State Commun.* **1981**, *39* (2), 341–344.
- (291) Mernagh, T. P.; Cooney, R. P.; Johnson, R. A. Raman Spectra of Graphon Carbon Black. *Carbon N. Y.* **1984**, *22* (1), 39–42.
- (292) Matthews, M.; Pimenta, M.; Dresselhaus, G.; Dresselhaus, M.; Endo, M. Origin of Dispersive Effects of the Raman D Band in Carbon Materials. *Phys. Rev. B* **1999**, *59* (10), R6585–R6588.
- (293) Qin, W.; Szipunar, J. A. Origin of Lattice Strain in Nanocrystalline Materials. *Philos. Mag. Lett.* **2005**, *85* (12), 649–656.
- (294) Qin, W.; Nagase, T.; Umakoshi, Y.; Szipunar, J. A. Relationship between Microstrain and Lattice Parameter Change in Nanocrystalline Materials. *Philos. Mag. Lett.* **2008**, *88* (3), 169–179.
- (295) Ashiotis, G.; Deschildre, A.; Nawaz, Z.; Wright, J. P.; Karkoulis, D.; Picca, F. E.; Kieffer, J. The Fast Azimuthal Integration Python Library: PyFAI. *J. Appl. Crystallogr.* **2015**, *48*, 510–519.
- (296) Knorr, K.; Henrichsen, B. *Determination of Pair Distribution Functions (PDF)*; 2009.
- (297) Juhás, P.; Davis, T.; Farrow, C. L.; Billinge, S. J. L. PDFgetX3: A Rapid and Highly Automatable Program for Processing Powder Diffraction Data into Total Scattering Pair Distribution Functions. *J. Appl. Crystallogr.* **2013**, *46* (2), 560–566.
- (298) Farrow, C. L.; Juhas, P.; Liu, J. W.; Bryndin, D.; Božin, E. S.; Bloch, J.; Proffen, T.; Billinge, S. J. L. PDFfit2 and PDFgui: Computer Programs for Studying Nanostructure in Crystals. *J. Phys. Condens. Matter* **2007**, *19* (33), 335219–335226.
- (299) Li, T.; Senesi, A. J.; Lee, B. Small Angle X-Ray Scattering for Nanoparticle Research. *Chem. Rev.* **2016**, *116* (18), 11128–11180.
- (300) Bartlett, P.; Ottewill, R. H. A Neutron Scattering Study of the Structure of a Bimodal Colloidal Crystal. *J. Chem. Phys.* **1992**, *96* (4), 3306–3318.
- (301) Chattot, R.; Asset, T.; Drnec, J.; Bordet, P.; Dubau, L.; Maillard, F.; Drnec, J.; Dubau, L.; Maillard, F. Atomic Scale Snapshots of the Growth Mechanism of Hollow PtNi/C Nanocatalysts for Oxygen Reduction Reaction. *Nano Lett* **2017**, *17* (4), 2447–2453.
- (302) Zhao, J.; Chen, W.; Zheng, Y.; Li, X. Novel Carbon Supported Hollow Pt Nanospheres for Methanol Electrooxidation. *J. Power Sources* **2006**, *162* (1), 168–172.
- (303) Liu, B.; Li, H. Y.; Die, L.; Zhang, X. H.; Fan, Z.; Chen, J. H. Carbon Nanotubes Supported PtPd Hollow Nanospheres for Formic Acid Electrooxidation. *J. Power Sources* **2009**, *186* (1), 62–66.
- (304) Pecsok, R. L. Polarographic Studies on the Oxidation and Hydrolysis of Sodium Borohydride. *J. Am. Chem. Soc.* **1953**, *75*, 2862–2864.

## Chapter VII. References

- (305) Stockmayer, W. H.; Rice, D. W.; Stephenson, C. C. Thermodynamic Properties of Sodium Borohydride and Aqueous Borohydride Ion. *J. Am. Chem. Soc.* **1955**, *77*, 1980–1983.
- (306) Caputo, R.; Guzzetta, F.; Angerhofer, A. Room-Temperature Synthesis of Nickel Borides via Decomposition of NaBH<sub>4</sub> Promoted by Nickel Bromide. *Inorg. Chem.* **2010**, *49* (19), 8756–8762.
- (307) Glavee, G. N.; Klabunde, K. J.; Sorensen, C. M.; Hadjipanayis, G. C. Borohydride Reduction of Nickel and Copper Ions in Aqueous and Nonaqueous Media. Controllable Chemistry Leading to Nanoscale Metal and Metal Boride Particles. *Langmuir* **1994**, *10* (12), 4726–4730.
- (308) Glavee, G. N.; Klabunde, K. J.; Sorensen, C. M.; Hadjipanayis, G. C. Borohydride Reduction of Cobalt Ions in Water. Chemistry Leading to Nanoscale Metal, Boride, or Borate Particles. *Langmuir* **1993**, *9* (1), 162–169.
- (309) Glavee, G. N.; Klabunde, K. J.; Sorensen, C. M.; Hadjipanayis, G. C. Chemistry of Borohydride Reduction of Iron(II) and Iron(III) Ions in Aqueous and Nonaqueous Media. Formation of Nanoscale Fe, FeB, and Fe<sub>2</sub>B Powders. *Inorg. Chem.* **1995**, *34* (1), 28–35.
- (310) Glavee, G. N.; Klabunde, K. J.; Sorensen, C. M.; Hadjipanayis, G. C. Sodium Borohydride Reduction of Cobalt Ions in Nonaqueous Media. Formation of Ultrafine Particles (Nanoscale) of Cobalt Metal. *Inorg. Chem.* **1993**, *32* (4), 474–477.
- (311) Glavee, G. N.; Klabunde, K. J.; Sorensen, C. M.; Hadjipanayis, G. C. Borohydride Reductions of Metal Ions. A New Understanding of the Chemistry Leading to Nanoscale Particles of Metals, Borides, and Metal Borates. *Langmuir* **1992**, *8* (3), 771–773.
- (312) Carenco, S.; Portehault, D.; Boissière, C.; Mézailles, N.; Sanchez, C. Nanoscaled Metal Borides and Phosphides: Recent Developments and Perspectives. *Chem. Rev.* **2013**, *113* (10), 7981–8065.
- (313) Arzac, G. M.; Rojas, T. C.; Fernández, A. Boron Compounds as Stabilizers of a Complex Microstructure in a Co-B-Based Catalyst for NaBH<sub>4</sub> Hydrolysis. *ChemCatChem* **2011**, *3* (8), 1305–1313.
- (314) Geng, J.; Jefferson, D. Al; Johnson, B. F. G. The Unusual Nanostructure of Nickel-Boron Catalyst. *Chem. Commun.* **2007**, 969–971.
- (315) Li, H. H.; Li, H. H.; Dai, W. L.; Wang, W.; Fang, Z.; Deng, J. F. XPS Studies on Surface Electronic Characteristics of Ni-B and Ni-P Amorphous Alloy and Its Correlation to Their Catalytic Properties. *Appl. Surf. Sci.* **1999**, *152* (1), 25–34.
- (316) Li, H.; Li, H.; Dai, W.; Qiao, M. Preparation of the Ni-B Amorphous Alloys with Variable Boron Content and Its Correlation to the Hydrogenation Activity. *Appl. Catal. A Gen.* **2002**, *238* (1), 119–130.
- (317) Hasché, F.; Oezaslan, M.; Strasser, P.; Hasché, F.; Oezaslan, M.; Strasser, P.; Hasché, F.; Oezaslan, M.; Strasser, P. Activity, Structure and Degradation of Dealloyed PtNi<sub>3</sub> Nanoparticle Electrocatalyst for the Oxygen Reduction Reaction in PEMFC. *J. Electrochem. Soc.* **2012**, *159*

## Chapter VII. References

- (1), B25–B34.
- (318) Montejano-Carrizales, J. M.; Morán-López, J. L. Geometrical Characteristics of Compact Nanoclusters. *Nanostructured Mater.* **1992**, *1* (5), 397–409.
- (319) Montejano-Carrizales, J. M.; Aguilera-Granja, F.; Morán-López, J. L. Direct Enumeration of the Geometrical Characteristics of Clusters. *Nanostructured Mater.* **1997**, *8* (3), 269–287.
- (320) Urchaga, P.; Baranton, S.; Coutanceau, C.; Jerkiewicz, G. Electro-Oxidation of CO Chem on Pt Nanosurfaces: Solution of the Peak Multiplicity Puzzle. *Langmuir* **2012**, *28* (7), 3658–3663.
- (321) Minkina, V. G.; Shabunya, S. I.; Kalinin, V. I.; Martynenko, V. V. Stability of Aqueous-Alkaline Sodium Borohydride Formulations. *Russ. J. Appl. Chem.* **2008**, *81* (3), 380–385.
- (322) Mochalov, K. .; Khain, V. .; Gil'manshin, G. . Generalized Scheme for the Hydrolysis of the Borhydride Ions and Diborane. *Dokl. Akad. Nauk SSSR* **1965**, *162* (3), 613–616.
- (323) Trinh, Q. T.; Yang, J.; Lee, J. Y.; Saeys, M. Computational and Experimental Study of the Volcano Behavior of the Oxygen Reduction Activity of PdM@PdPt/C (M = Pt, Ni, Co, Fe, and Cr) Core-Shell Electrocatalysts. *J. Catal.* **2012**, *291*, 26–35.
- (324) Xu, C.; Hou, J.; Pang, X.; Li, X.; Zhu, M.; Tang, B. Nanoporous PtCo and PtNi Alloy Ribbons for Methanol Electrooxidation. *Int. J. Hydrogen Energy* **2012**, *37* (14), 10489–10498.
- (325) Standard Reduction Potentials In Aqueous Solution at 25°C  
<http://www.chemeddl.org/services/moodle/media/QBank/GenChem/Tables/EStandardTable.htm> (accessed Apr 16, 2017).
- (326) Giordano, R.; Serp, P.; Kalck, P.; Kihn, Y.; Schreiber, J.; Marhic, C.; Duvail, J. L. Preparation of Rhodium Catalysts Supported on Carbon Nanotubes by a Surface Mediated Organometallic Reaction. *Eur. J. Inorg. Chem.* **2003**, No. 4, 610–617.
- (327) Solhy, A.; Machado, B. F.; Beausoleil, J.; Kihn, Y.; Gonçalves, F.; Pereira, M. F. R.; Órfão, J. J. M.; Figueiredo, J. L.; Faria, J. L.; Serp, P. MWCNT Activation and Its Influence on the Catalytic Performance of Pt/MWCNT Catalysts for Selective Hydrogenation. *Carbon N. Y.* **2008**, *46* (9), 1194–1207.
- (328) Laurent-Brocq, M.; Job, N.; Eskenazi, D.; Pireaux, J.-J. Pt/C Catalyst for PEM Fuel Cells: Control of Pt Nanoparticles Characteristics through a Novel Plasma Deposition Method. *Appl. Catal. B Environ.* **2014**, *147*, 453–463.
- (329) Silva, A. M. T.; Machado, B. F.; Figueiredo, J. L.; Faria, J. L. Controlling the Surface Chemistry of Carbon Xerogels Using HNO<sub>3</sub>-Hydrothermal Oxidation. *Carbon N. Y.* **2009**, *47* (7), 1670–1679.
- (330) Gusak, A. M.; Zaporozhets, T. V.; Tu, K. N.; Gösele, U. Kinetic Analysis of the Instability of Hollow Nanoparticles. *Philos. Mag.* **2005**, *85* (36), 4445–4464.
- (331) Dubau, L.; Lopez-Haro, M.; Durst, J.; Maillard, F. Atomic-Scale Restructuring of Hollow PtNi/C Electrocatalysts during Accelerated Stress Tests. *Catal. Today* **2016**, *262*, 146–154.
- (332) Dubau, L.; Nelayah, J.; Asset, T.; Chattot, R.; Maillard, F. Implementing Structural Defects as a

## Chapter VII. References

- New Direction to Improve the Durability of PtNi/C Nanoparticles. *ACS Catal.* **2017**, 7 (4), 3072–3081.
- (333) Gribov, E. N.; Maltseva, N. V.; Golovin, V. A.; Okunev, A. G. A Simple Method for Estimating the Electrochemical Stability of the Carbon Materials. *Int. J. Hydrogen Energy* **2016**, 41 (40), 18207–18213.
- (334) Zignani, S. C.; Antolini, E.; Gonzalez, E. R. Stability of Pt-Ni/C (1:1) and Pt/C Electrocatalysts as Cathode Materials for Polymer Electrolyte Fuel Cells: Effect of Ageing Tests. *J. Power Sources* **2009**, 191 (2), 344–350.
- (335) Antolini, E.; Salgado, J. R. C.; Gonzalez, E. R. The Stability of Pt-M (M = First Row Transition Metal) Alloy Catalysts and Its Effect on the Activity in Low Temperature Fuel Cells. A Literature Review and Tests on a Pt-Co Catalyst. *J. Power Sources* **2006**, 160, 957–968.
- (336) Yoda, T.; Uchida, H.; Watanabe, M. Effects of Operating Potential and Temperature on Degradation of Electrocatalyst Layer for PEMFCs. *Electrochim. Acta* **2007**, 52 (19), 5997–6005.
- (337) Saab, A. P.; Garzon, F. H.; Zawodzinski, T. A. Determination of Ionic and Electronic Resistivities in Carbon/Polyelectrolyte Fuel-Cell Composite Electrodes. *J. Electrochem. Soc.* **2002**, 149 (12), A1541–A1546.
- (338) Siroma, Z.; Hagiwara, J.; Yasuda, K.; Inaba, M.; Tasaka, A. Simultaneous Measurement of the Effective Ionic Conductivity and Effective Electronic Conductivity in a Porous Electrode Film Impregnated with Electrolyte. *J. Electroanal. Chem.* **2010**, 648 (2), 92–97.
- (339) Shetzline, J. A.; Creager, S. E. Quantifying Electronic and Ionic Conductivity Contributions in Carbon/Polyelectrolyte Composite Thin Films. *J. Electrochem. Soc.* **2014**, 161 (14), H917–H923.
- (340) Jang, J. H.; Jeon, S.; Cho, J. H.; Kim, S.-K.; Lee, S.-Y.; Cho, E.; Kim, H.-J.; Han, J.; Lim, T.-H. Complex Capacitance Analysis of Ionic Resistance and Interfacial Capacitance in PEMFC and DMFC Catalyst Layers. *J. Electrochem. Soc.* **2009**, 156 (11), B1293–B1300.
- (341) Greeley, J.; Nørskov, J. K.; Mavrikakis, M. Electronic Structure and Catalysis on Metal Surfaces. *Annu. Rev. Phys. Chem.* **2002**, 53, 319–348.



## Abstract

This Ph.D. thesis investigates the mechanisms driving the formation, the enhanced activity for the oxygen reduction reaction (ORR) and the durability of porous hollow PtM/C nanoparticles (NPs) for proton exchange membrane fuel cell (PEMFC) applications. The formation and growth of the NPs, synthesized by a ‘one-pot’ process, were discussed in the light of microscopic, *operando* X-ray and electron-based techniques, unveiling the different intermediate steps of the synthesis. The synthesis process was extended to different non-noble metals (M = Ni, Co, Cu, Zn and Fe) and to different carbon supports. The enhanced activity for the ORR resulted from (i) the contraction of the lattice parameter by the non-noble metal (the final NPs contains *ca.* 15 – 20 at. % of M), (ii) the open porosity and (iii) the density of structural defects at the surface of the NPs, which was semi-quantitatively estimated by COads stripping measurements and Rietveld analysis of wide-angle X-ray scattering patterns. The non-noble metal was found to be annealed (dissolved) faster than the structural defects during the accelerated stress tests.

Key words: Proton Exchange Membrane Fuel Cell, Porous Hollow PtM Nanoparticles, Oxygen Reduction Reaction.

## Résumé

Cette thèse s’intéresse aux mécanismes de formation, à l’activité électrocatalytique pour la réduction de l’oxygène (ORR) et à la stabilité de nanoparticules (NPs) creuses à base de Pt supportées sur carbone pour des applications en pile à combustible à membrane échangeuse de protons (PEMFC). La formation et la croissance des NPs, synthétisées par une méthode dite ‘one-pot’, ont été étudiées grâce à des techniques utilisant les rayons X ou les électrons, nous permettant ainsi de mettre en évidence les différentes étapes de la synthèse. Le procédé de synthèse a été étendu à différents métaux non nobles (M = Ni, Co, Cu, Zn and Fe) et à différents supports carbonés. L’activité supérieure des NPs pour l’ORR résulte (i) de la contraction du paramètre de maille induit par la présence du métal non-noble, (ii) de leur porosité ouverte et (iii) de la densité de défauts structuraux à la surface des NPs (estimée de façon semi-quantitative via mesures COads stripping et analyse Rietveld de données de diffusion des rayons X aux grands angles). Les défauts structuraux sont plus stables que le métal non-noble durant les tests de vieillissement accéléré.

Mots clés : Pile à Combustible à Membrane Echangeuse de Protons, Nanoparticules Creuses de PtM, Réduction de l’Oxygène.

